Durability Testing of an Aircraft Structural Health Monitoring System

by

Jeffrey Thomas Chambers

B.S. Mechanical Engineering
University of California, 2004

Submitted to the Department of Aeronautics and Astronautics
in partial fulfillment of the requirements for the degree of

Master of Science in Aeronautics and Astronautics

at the

MASSACHUSETTS INSTITUTE OF TECHNOLOGY

September 2006

Author .....
Department of Aeronautics and Astronautics
August 18, 2006

Certified by .....
Professor Brian L. Wardle
Boeing Assistant Professor of Aeronautics and Astronautics
Thesis Supervisor

Accepted by .....
Professor Jaime Peraire
Professor of Aeronautics and Astronautics
Chair, Committee on Graduate Students

Durability Testing of an Aircraft Structural Health Monitoring System

by

Jeffrey Thomas Chambers

Submitted to the Department of Aeronautics and Astronautics
on August 18, 2006, in partial fulfillment of the
requirements for the degree of
Master of Science in Aeronautics and Astronautics

Abstract

Structural health monitoring (SHM) is an emerging technology leading to systems capable of continuously monitoring structures for damage. Aerospace structures have one of the highest payoffs for SHM systems because damage can lead to catastrophic and expensive failures. Prior work in SHM has focused on damage detection methods and sensor optimization, however, the topics of durability, reliability, and longevity of these systems has not been addressed. A framework for developing SHM durability test standards for aerospace vehicles is offered. Existing standards for the durability of commercial and military aircraft avionics are identified, and the relation to SHM systems is described. Using these existing standards, a test matrix and testing specifics are developed to assess the durability of SHM systems. Careful consideration is necessary in defining the 'system' under testing. Criteria are defined to establish whether a sensor/structural system has been affected by the various environments. Extensive experimental results from durability testing of a surface-mounted piezoelectric Lamb-wave SHM system are presented. Environments tested include temperature extremes, humidity, fluid susceptibility, altitude, and mechanical strain. A voltage change criteria, which measures pre- vs. post-test sensed wave amplitude, proved useful in assessing the SHM system's performance. All sensors survived the tested environments, with an average voltage degradation of -16%. The high-temperature, humidity, and water-based fluids susceptibility tests had the greatest influence on the sensors, with an average voltage degradation of -38%. In several of the tests, the sensors had significant voltage degradation during environmental exposure, which recovered somewhat in most cases after ambient conditions were reestablished. A clear need exists for a supplemental standard geared specifically towards smart structure technologies that would address SHM and other embedded or surface mounted smart structure components and systems. Additional testing of the Lamb-wave sensors, including consideration of ultrasonic fatigue, is recommended.

Thesis Supervisor: Brian L. Wardle
Title: Boeing Assistant Professor of Aeronautics and Astronautics

Acknowledgments

I must give thanks to many people for contributing to this thesis in their own way.

First, to my advisor, Prof. Brian Wardle, for the help he has given me during the course of this research. He has been a colleague and friend throughout the project. Thank you for guiding me down the correct paths and for the countless hours spent correcting this thesis.

Second, to Dr. Seth Kessler for providing this research opportunity to MIT. It has been a pleasure working with you, and I wish the best for Metis Design.

To all the people who have helped with this research: Prof. Paul Lagacé for providing insight on testing standards and certifications, John Kane for always having creative solutions to testing problems, Dave Robertson for spending his time helping me fix machines, and all my friends in TELAMS for providing a fun and productive workspace. Special thanks to my UROP, James Miller, who put in countless hours down in the lab setting up and running the experiments.

And to Danielle, for making MIT a fun experience. I never knew how much there was to experience in this world until I met you. Thank you for your patience and support.

This thesis is dedicated to my amazing family, all of whom have contributed to the person I have become. Most of all, I must thank my parents, Tom and Sue Chambers, who have presented me every opportunity I could desire. Without their support and encouragement over the years this would not have been possible.

Contents

1 Introduction **23**

2 Background **27**

2.1 Existing Mechanical and Environmental Test Standards 27

2.2 Lamb-wave Sensors 28

3 Approach **33**

3.1 Framework for SHM Durability Testing 34

3.2 Use of Existing Aerospace Standards 35

3.3 Test Matrix 38

3.4 SHM System Definition 40

3.5 Metric Selection 42

4 Experimental Procedures **47**

4.1 Specimen Description and Preparation 48

4.2 Data-Acquisition System 52

4.3 Testing Procedures 54

4.3.1 High-temperature 55

4.3.2 Low-temperature 58

4.3.3 Thermal Shock 61

4.3.4 Humidity 63

4.3.5 Fluid Susceptibility 66

4.3.6 Altitude (Pressure) 69

4.3.7 Static Strain 73

5 Results and Discussion **75**

5.1 High-temperature Test Results 79

5.2 Low-temperature Test Results 81

5.3 Thermal Shock Test Results 83

5.4 Humidity Test Results 84

5.5 Oil-based Fluids Susceptibility Test Results 85

5.6 Water-based Fluids Susceptibility Test Results 87

5.7 Altitude (Low-pressure) Test Results 88

5.8 Decompression Test Results 89

5.9 Overpressure Test Results 90

5.10 Static-strain Test Results 91

5.11 Test Result Summary and Discussion 92

6 Conclusions and Recommendations **97**

6.1 Conclusions 97

6.2 Recommendations 100

References **103**

Appendix A Experimental Testing Profiles **107**

Appendix B Experimental Test Signals and Metrics **125**

Appendix C Material Properties of 2024-T3 Aluminum Coupons **183**

Appendix D AE-10 Epoxy Properties **187**

Appendix E Shear Gel Properties **189**

Appendix F MATLAB Code for Data Analysis **191**

List of Figures

2-1 Illustration of antisymmetric and symmetric Lamb waves 31

2-2 Dispersion curves for Lamb waves in a 3.175 *mm* thick 2024-T3 aluminum plate 32

3-1 Framework for identifying SHM and smart structure testing standards. 34

3-2 Test coupon with node and boundary clamps. Defined SHM system inside box. 41

3-3 Example sensed signal. 43

3-4 Wave path illustration of SHM node asymmetrically mounted between boundary clamps 44

4-1 Exploded view of M.E.T.I.-Disk 2 node. 49

4-2 Digital M.E.T.I.-Disk 3 node with USB connection. 49

4-3 'SHM system' used in all tests: asymmetrically-mounted node, aluminum coupon (structure), and boundary clamps. 51

4-4 Screenshot of M.E.T.I.-System software. 52

4-5 M.E.T.I.-System software settings. 53

4-6 Nominal high-temperature test profile. 55

4-7 ATS oven/cooling chamber with test specimen installed. 56

4-8 Experimental high-temperature test profile for node 0041. 57

4-9 Nominal low-temperature test profile. 58

4-10 ATS chamber with Omega CN2024 controller. 59

4-11 Experimental low-temperature test profile for node 0068. 60

4-12 Nominal thermal shock test profile (1 of 2 required cycles). 62

4-13 Experimental thermal shock test cycle (1 of 2 cycles) for node 0061. . 62
4-14 Nominal humidity test profile (1 of 10 cycles required). 63
4-15 Experimental humidity single cycle profile for nodes 0016, 0021, and 0060. 65
4-16 Experimental humidity test profile for nodes 0016, 0021, and 0060. . . 66
4-17 Nominal fluid susceptibility test profile. 67
4-18 Fluid susceptibility test basin. 68
4-19 Nominal altitude test profile. 70
4-20 Nominal decompression test profile. 70
4-21 Nominal overpressure test profile. 71
4-22 Low-pressure and rapid decompression test setup. 72
4-23 Experimental overpressure test profile for nodes 0011, 2586, and 2601. 73
4-24 MTS testing machine with Instron controller. Test specimen is loaded in the test machine's hydraulic grips. 74
4-25 Experimental static-strain loading profile of node 0017. 74

5-1 Sample CSV data file from the M.E.T.I.-System software. 76
5-2 Example test signal plots. 78
5-3 Example envelope plot. 79
5-4 Example pulse and sensed signal. 80
5-5 High-temperature test envelopes. 81
5-6 Low-temperature test envelopes. 82
5-7 Thermal shock test envelopes. 83
5-8 Humidity test envelopes. 85
5-9 Oil-based fluids susceptibility test envelopes. 86
5-10 Water-based fluids susceptibility test envelopes. 87
5-11 Altitude (low-pressure) test envelopes. 88
5-12 Decompression test envelopes. 90
5-13 Overpressure test envelopes. 91
5-14 Static-strain test envelopes. 92

A-1 Experimental high-temperature test profile for node 0026. 107
A-2 Experimental high-temperature test profile for node 0036. 108
A-3 Experimental high-temperature test profile for node 0041. 108
A-4 Experimental low-temperature test profile for node 0029. 109
A-5 Experimental low-temperature test profile for node 0049. 109
A-6 Experimental low-temperature test profile for node 0068. 110
A-7 Experimental thermal shock test profile for node 0034. 110
A-8 Experimental thermal shock test profile for node 0046. 111
A-9 Experimental thermal shock test profile for node 0061, incomplete. . . 111
A-10 Experimental thermal shock test profile for node 0061, ran after previous cycles shown in Fig. A-9. 112
A-11 Experimental humidity test profile for nodes 0016, 0021, and 0060. . . 113
A-12 Experimental humidity test profile, cycle 1, for nodes 0016, 0021, and 0060. 114
A-13 Experimental humidity test profile, cycle 2, for nodes 0016, 0021, and 0060. 114
A-14 Experimental humidity test profile, cycle 3, for nodes 0016, 0021, and 0060. 115
A-15 Experimental humidity test profile, cycle 4, for nodes 0016, 0021, and 0060. 115
A-16 Experimental humidity test profile, cycle 5, for nodes 0016, 0021, and 0060. 116
A-17 Experimental humidity test profile, cycle 6, for nodes 0016, 0021, and 0060. 116
A-18 Experimental humidity test profile, cycle 7, for nodes 0016, 0021, and 0060. 117
A-19 Experimental humidity test profile, cycle 8, for nodes 0016, 0021, and 0060. 117
A-20 Experimental humidity test profile, cycle 9, for nodes 0016, 0021, and 0060. 118

A-21 Experimental humidity test profile, cycle 10, for nodes 0016, 0021, and 0060. 118
A-22 Experimental oil-based fluid susceptibility test profile for nodes 0010, 0015, and 0052. 119
A-23 Experimental water-based fluid susceptibility test profile for nodes 0012, 0203, and 2598. 119
A-24 Experimental altitude test profile for node 2555. 120
A-25 Experimental altitude test profile for node 2557. 120
A-26 Experimental altitude test profile for node 2595. 121
A-27 Experimental decompression test profile for node 0204. 121
A-28 Experimental decompression test profile for node 2575. 122
A-29 Experimental decompression test profile for node 2578. 122
A-30 Experimental overpressure test profile for nodes 0011, 2586, and 2601. 123
A-31 Experimental static-strain test profile for node 0017. 123

B-1 High-temperature averaged test signals for node 0026 127
B-2 High-temperature test signal envelopes for node 0026. 128
B-3 High-temperature averaged test signals for node 0036 129
B-4 High-temperature test signal envelopes for node 0036. 130
B-5 High-temperature averaged test signals for node 0041 131
B-6 High-temperature test signal envelopes for node 0041. 132
B-7 Low-temperature test signals for node 0029 133
B-8 Low-temperature test signal envelopes for node 0029. 134
B-9 Low-temperature test signals for node 0049 135
B-10 Low-temperature test signal envelopes for node 0049. 136
B-11 Low-temperature test signals for node 0068 137
B-12 Low-temperature test signal envelopes for node 0068. 138
B-13 Thermal shock test signals for node 0034 139
B-14 Thermal shock test signal envelopes for node 0034. 140
B-15 Thermal shock test signals for node 0046 141

B-16 Thermal shock test signal envelopes for node 0046. 142
B-17 Thermal shock test signals for node 0061 143
B-18 Thermal shock test signal envelopes for node 0061. 144
B-19 Humidity test signals for node 0016 145
B-20 Humidity test signal envelopes for node 0016. 146
B-21 Humidity test signals for node 0021 147
B-22 Humidity test signal envelopes for node 0021. 148
B-23 Humidity test signals for node 0060 149
B-24 Humidity test signal envelopes for node 0060. 150
B-25 Oil-based fluid susceptibility test signals for node 0010 151
B-26 Oil-based fluid susceptibility test signal envelopes for node 0010. . . . 152
B-27 Oil-based fluid susceptibility test signals for node 0015 153
B-28 Oil-based fluid susceptibility test signal envelopes for node 0015. . . . 154
B-29 Oil-based fluid susceptibility test signals for node 0052 155
B-30 Oil-based fluid susceptibility test signal envelopes for node 0052. . . . 156
B-31 Water-based fluid susceptibility test signals for node 0012 157
B-32 Water-based fluid susceptibility test signal envelopes for node 0012. . 158
B-33 Water-based fluid susceptibility test signals for node 0203 159
B-34 Water-based fluid susceptibility test signal envelopes for node 0203. . 160
B-35 Water-based fluid susceptibility test signals for node 2598 161
B-36 Water-based fluid susceptibility test signal envelopes for node 2598. . 162
B-37 Altitude test signals for node 2555 163
B-38 Altitude test signal envelopes for node 2555. 164
B-39 Altitude test signals for node 2557 165
B-40 Altitude test signal envelopes for node 2557. 166
B-41 Altitude test signals for node 2595 167
B-42 Altitude test signal envelopes for node 2595. 168
B-43 Decompression test signals for node 0204 169
B-44 Decompression test signal envelopes for node 0204. 170
B-45 Decompression test signals for node 2575 171

B-46 Decompression test signal envelopes for node 2575. 172
B-47 Decompression test signals for node 2578 173
B-48 Decompression test signal envelopes for node 2578. 174
B-49 Overpressure test signals for node 0011 175
B-50 Overpressure test signal envelopes for node 0011. 176
B-51 Overpressure test signals for node 2586 177
B-52 Overpressure test signal envelopes for node 2586. 178
B-53 Overpressure test signals for node 2601 179
B-54 Overpressure test signal envelopes for node 2601. 180
B-55 Static-strain test signals for node 0017 181
B-56 Static-strain test signal envelopes for node 0017. 182

C-1 Experimental stress-strain curves of three aluminum samples. 184
C-2 Experimental transverse stain vs. longitudinal strain of three aluminum samples. 184
C-3 Certified inspection report for 2024-T3 aluminum from Alcoa. 185

D-1 AE-10 cure time vs. cure temperature. 187

List of Tables

3.1 Testing standards defined by RTCA/DO-160E. 37
3.2 Testing standards defined by MIL-STD-810F. 37
3.3 SHM durability test matrix for Lamb-wave nodes. 38

5.1 Summary of averaged metrics (post-test compared to baseline) for all testing. 95
5.2 Estimated number of excitation fatigue cycles of nodes for each test. . 95

B.1 Metric values and differences (deltas) of node 0026 for the high-temperature test. 128
B.2 Metric values and differences (deltas) of node 0036 for the high-temperature test. 130
B.3 Metric values and differences (deltas) of node 0041 for the high-temperature test. 132
B.4 Metric values and differences (deltas) of node 0029 for the low-temperature test. 134
B.5 Metric values and differences (deltas) of node 0049 for the low-temperature test. 136
B.6 Metric values and differences (deltas) of node 0068 for the low-temperature test. 138
B.7 Metric values and differences (deltas) of node 0034 for the thermal shock test. 140
B.8 Metric values and differences (deltas) of node 0046 for the thermal shock test. 142

B.9 Metric values and differences (deltas) of node 0061 for the thermal shock test. 144
B.10 Metric values and differences (deltas) of node 0016 for the humidity test. 146
B.11 Metric values and differences (deltas) of node 0021 for the humidity test. 148
B.12 Metric values and differences (deltas) of node 0060 for the humidity test. 150
B.13 Metric values and differences (deltas) of node 0010 for the oil-based fluid susceptibility test. 152
B.14 Metric values and differences (deltas) of node 0015 for the oil-based fluid susceptibility test. 154
B.15 Metric values and differences (deltas) of node 0052 for the oil-based fluid susceptibility test. 156
B.16 Metric values and differences (deltas) of node 0012 for the water-based fluid susceptibility test. 158
B.17 Metric values and differences (deltas) of node 0203 for the water-based fluid susceptibility test. 160
B.18 Metric values and differences (deltas) of node 2598 for the water-based fluid susceptibility test. 162
B.19 Metric values and differences (deltas) of node 2555 for the altitude test. 164
B.20 Metric values and differences (deltas) of node 2557 for the altitude test. 166
B.21 Metric values and differences (deltas) of node 2595 for the altitude test. 168
B.22 Metric values and differences (deltas) of node 0204 for the decompression test. 170
B.23 Metric values and differences (deltas) of node 2575 for the decompression test. 172
B.24 Metric values and differences (deltas) of node 2578 for the decompression test. 174
B.25 Metric values and differences (deltas) of node 0011 for the overpressure test. 176
B.26 Metric values and differences (deltas) of node 2586 for the overpressure test. 178

B.27 Metric values and differences (deltas) of node 2601 for the overpressure test. 180
B.28 Metric values and differences (deltas) of node 0017 for the static-strain test. 182

C.1 Experimental material properties of 2024-T3 aluminum samples. . . . 183

Nomenclature

A_0	-	first antisymmetric Lamb-wave mode
c_g	-	group velocity of Lamb-wave
$c_{g_{A_0}}$	-	group velocity of first antisymmetric Lamb-wave
c_L	-	longitudinal velocity
c_p	-	phase velocity of Lamb-wave
c_R	-	Rayleigh velocity
c_T	-	transverse velocity
d	-	plate thickness
d_{node}	-	diameter of SHM transceiver node
E	-	Young's modulus
f	-	excitation frequency
h	-	half-thickness of plate
k	-	wavenumber
L_{near}	-	distance from node center to the near edge of near boundary clamp
TOF_{min}	-	minimum time-of-flight of first reflected wavepacket
TOF_{max}	-	maximum time-of-flight of first reflected wavepacket
w_{BC}	-	width of boundary clamp
λ	-	first Lamé constant
μ	-	second Lamé constant
ν	-	Poisson's ratio
ρ	-	density
ω	-	angular frequency of excitation

Chapter 1

Introduction

Structural health monitoring (SHM) has been defined in the literature as the acquisition, validation, and analysis of technical data to facilitate life-cycle management decisions [1]. Aerospace structures have one of the highest payoffs for SHM systems since damage can lead to catastrophic and expensive failures, and the vehicles involved undergo regular costly inspections. The field of structural health monitoring has been expanding rapidly, both in the number of applications as well as the number of technologies. As more systems become available and continue to mature, it is important to define testing standards to address how SHM devices will be commercialized and certified especially in the aerospace industry. Most prior research on the topic of SHM has been focused on the development of new detection methods and optimization of systems, but has not yet addressed the commercial aircraft certification process.

The aircraft component manufacturing and integration industry in general is well developed with regard to certification and standards. However, there is a need for standards specifically for SHM technologies in order to comprehensively address all of the regulatory concerns typical of aircraft. Recently, certification guidance for rotorcraft health and usage monitoring systems (HUMS) have been developed [2]. HUMS consist of similar components (sensors and data acquisition systems) as SHM systems, however, HUMS typically solely record peak values (e.g., force, strain, acceleration) experienced by sensors during operation. By contrast, SHM is based on nondestruc-

tive inspection (NDI) techniques that examine for damage within the structure (and away from the sensor). SHM systems integrate one or more nondestructive testing methods into a vehicle in order to facilitate quick and accurate damage detection with minimal human intervention. It is important to define testing standards and certification procedures to validate SHM systems. The testing procedures will be similar to the existing avionics standards (the components will experience similar operational conditions) with additional considerations needed because the structure becomes part of the tested 'system.' Also, the conditions necessary for the SHM system to prove compliance with these standards will be unique to the operating mode of the system (ground based monitoring versus in-situ monitoring), and surface-mounted versus embedded sensors.

Typical NDI techniques include visual inspection, X-radiography, strain gauge, optical fiber, ultrasonic (A-, B-, and C-scans), eddy current, and vibration-based methods. However, not all of these techniques are ideal for SHM due to the required equipment size, weight, cost, or power consumption. Currently, the most widely used NDI techniques for SHM include optical fiber and vibration-based methods [3]. The SHM system used for this work utilizes a vibration-based method. Using surface-mounted piezoelectric nodes (transceivers), ultrasonic Lamb-waves are produced in the structure being monitored. For this study, the nodes were used in a pulse-echo configuration requiring only one node per specimen. The node produces ultrasonic Lamb-waves in the structure and then 'listens' for reflections. These nodes can also be used in a pitch-catch configuration with multiple nodes, where one node actuates the Lamb-waves and the other nodes sense the disturbances. In both configurations, changes in received signal characteristics can be used to identify location and mode of damage to the structure.

Several viable SHM systems have been demonstrated in laboratory conditions and are beginning to operate on experimental flight tests [3–11]. It is necessary to form testing standards so these systems can be utilized in prognostic applications for commercial use. As no SHM standards currently exist, applicable existing standards for commercial and military aircraft were consulted to assist in forming SHM spe-

cific standards. The most similar components with existing standards are avionics (electrical and electronic devices used in aircraft, such as cockpit gauges and controls systems). The avionic standards address susceptibility to environmental conditions, mechanical durability, and electro-magnetic interference (EMI), as well as a host of other extreme aircraft conditions (shock, vibration, fluids, *etc.*). These standards were tailored and a test matrix was formed including the environments most likely to strongly affect the SHM nodes.

The overall goal of this project is to assess the topics of durability, reliability, and longevity of Lamb wave-based sensor nodes and formulate guidance to help form SHM testing standards. The main tasks to accomplish this goal are:

- Create a framework for creating SHM durability test standards.
- Modify existing standards to test the specific SHM system in this work (Lamb wave-based surface-mounted transceivers).
- Define criteria to assess the performance of the Lamb wave-based SHM system.
- Perform durability tests and apply the criteria to assess SHM system performance.

The approach taken for meeting these goals is largely experimental. Existing standards for the durability, reliability, and longevity of commercial and military aircraft components are identified, and the relation of those standards to SHM systems is discussed. A framework for developing SHM standards based on these existing standards is formed. Using this framework, modified testing procedures (specific to SHM systems) are developed and a test matrix to assess the durability of the Lamb-wave sensors is constructed. Criteria (metrics) for assessing whether the sensor's performance is affected by the particular environment or loading are defined. The results from the tests are analyzed and discussed before making recommendations on furthering the creation of SHM standards and extending understanding durability of the specific SHM system tested.

Existing avionic standards are presented, nondestructive testing methods used in SHM are discussed, and the ultrasonic Lamb-wave technique behind the SHM system used for this work is explained in Chapter 2. In Chapter 3, a framework for developing durability and reliability standards for SHM systems is offered. The tailoring of existing avionic standards to pertain to SHM systems is discussed, the test matrix used for this work is presented, the definition of the SHM 'system' is provided, and the criteria (metrics) for assessing system performance are defined. The experimental procedures and setups for each of the environmental and structural tests are presented in Chapter 4. SHM specific testing procedures are formed and realized experimentally. The specimens (sensor node plus structure) are described and the data-acquisition system is presented. Environmental survivability of the nodes is discussed in Chapter 5. The environmental extremes tested in this work include high-temperature, low-temperature, thermal shock, high humidity, fluids (water- and oil-based) susceptibility, altitude (low-pressure), rapid decompression, over pressurization, and structural static-strain. Results from each test are presented and discussed. Finally, Chapter 6 concludes the findings of this work and recommends future work and testing to be included in SHM and smart structure durability standards.

Chapter 2

Background

In this chapter, background is given on the existing test standards and Lamb wave techniques that are the basis of the SHM system studied in this work. A basic Lamb-wave theory is reviewed at the end of the chapter including an analytical calculation of the first antisymmetric Lamb group velocity. It appears that there has been no previous work on defining SHM durability standards. Researchers and companies developing SHM systems have realized the necessity to conduct durability tests [12–14], however, the tests are non-existent and/or non-standardized.

2.1 Existing Mechanical and Environmental Test Standards

Current standards exist that define test methods used for certifying structures and avionic equipment for commercial aircraft. The existing standards are well developed and have been refined over many years. While these standards do not cover the full spectrum required for SHM, they serve as a good foundation from which to build a framework for SHM standards and certifications. There is a breadth of testing standards applicable to the aircraft industry. Some standards identify critical operating environments while some require proof of compliance as rules for certification. The Federal Aviation Administration (FAA) has identified RTCA/DO-160E as an

acceptable test standard for environmental qualifications to show compliance with certain airworthiness requirements [2]. Other relevant standards include MIL-STD-810F (environmental testing), MIL-STD-461E (electromagnetic interference, EMI, testing), and MIL-STD-310 (global climatic data) [15–18]. Each standard defines a minimum environmental qualification process to be used for avionic equipment. RTCA/DO-160E is largely based on the information found in MIL-STD-810F and defines testing profiles and extreme conditions for the equipment to be tested. Standards used in meeting certification criteria (e.g., ASTM, MIL-STDs, and industry standards) for aerospace structures serve as the best basis to build on for identifying/developing SHM standards to address structural aspects of SHM durability. Tailoring of these existing standards for use in SHM durability tests in this work is undertaken in Sections 3.2 and 3.3.

2.2 Lamb-wave Sensors

Nondestructive inspection (NDI) techniques are used to inspect structures without damaging the structure or impacting its serviceability. The goal of NDI is to detect damage or flaws within a component. Visual inspection methods are the most basic form of NDI. A trained technician inspects the part using various techniques from the use of a microscope to examination by eye. This method is extremely dependent on the level of training of the technician and can be inefficient for large structures. Strain gauge methods may be the most widely used NDI technique. Many civil structures, such as bridges and buildings, are monitored using strain gauges. The system is relatively inexpensive, but the strain gauges can only monitor the area directly under the gauge. Optical fiber methods involve embedding or affixing optical fibers to a structure. Light is pulsed through the fiber and reflected by gratings along the length of the fiber. The time it takes the light to be reflected is measured, and as the structure is strained, the fiber changes length and the time it takes the light to reflect changes. This method is prone to shear-lag effects that make accurate measurements difficult. Ultrasonic methods (A-, B-, and C-scans) have been widely

used in the aerospace industry, however, typically both sides of the structure must be accessible. Vibration-based methods are also common in the aerospace industry and include modal response, acoustic emission, and ultrasonic techniques [3].

The SHM system studied in this work uses ultrasonic Lamb waves to monitor structures for damage. The system is composed of nodes (transceivers), software, and the structure. The nodes are bonded directly to the surface of the structure being monitored and can detect damage away from the node. The software allows a user to setup the system and then the software collects information from the nodes to be used in assessing the state of the structure. Ultrasonic wave methods are coupled to the structure being monitored, and therefore the structure itself becomes a component of the SHM system: the structure is the solid media that the Lamb waves propagate within. Using wave theories, algorithms have been developed to process the collected data and determine the state of the structure, including damage location and type [7]. The remainder of the section discusses the basic Lamb-wave theory.

Lamb waves are a form of elastic perturbation that can propagate in solid plates. Lord Rayleigh and Horacc Lamb were the first to describe elastic waves in solid plates [19]. Following the work presented by Lamb in 1917 [20], J.L. Rose discusses the wave characteristics of Lamb waves. The Rayleigh–Lamb frequency equation in a thin isotropic solid elastic media is [21]:

$$\frac{\tan qh}{\tan ph} + \left(\frac{4k^2pq}{(q^2-k^2)^2} \right)^{\pm 1} = 0 \quad \begin{cases} +1 = symmetric \\ -1 = antisymmetric \end{cases} \tag{2.1}$$

where the parameters are:

$$p^2 = \frac{\omega^2}{c_L^2} - k^2, \quad q^2 = \frac{\omega^2}{c_T^2} - k^2, \quad k = \frac{\omega}{c_p} \tag{2.2}$$

The wavenumber (k) is equal to the actuating frequency (ω) divided by the phase velocity (c_p). h is the half-thickness of the plate. The transverse (c_T), longitudinal

(c_L), and Rayleigh (c_R) wave velocities are:

$$c_T = \sqrt{\frac{\mu}{\rho}}, \quad c_L = \sqrt{\frac{\lambda + 2\mu}{\rho}}, \quad c_R = c_T \left(\frac{0.87 + 1.12\nu}{1 + \nu} \right) \tag{2.3}$$

where λ and μ are the Lamé constants and ν is the Poisson's ratio. Transverse waves (S waves) have particle motion perpendicular to the direction of wave propagation. A typical example of a transverse wave is a wave in a string. Longitudinal waves (P waves) or compressive waves have particle motion along or parallel to the motion of the wave. Sound waves are an example of a longitudinal wave. Rayleigh waves, existing in semi-infinite media (half-spaces), are a type of dispersive surface wave. When waves are dispersive, it means that the wave velocity is dependent on the wave frequency. The higher-frequency waves propagate through the media faster than the lower-frequency waves. In the limiting case where the semi-infinite media becomes a thin plate, the Rayleigh waves propagate through the thickness of the material. These types of waves are called Rayleigh-Lamb waves (or just Lamb waves). The dispersive nature of Lamb waves is quite complex, but closed-form expressions (eqs. 2.1 to 2.3) exist that relate the material properties of the media, the frequency of the waves, and the wave speeds.

The Rayleigh-Lamb frequency equation has two groups corresponding to symmetric and antisymmetric waves. When solving the symmetric case, the +1 exponent of Eqn. 2.1 is used and the -1 exponent is used to solve the antisymmetric case. A graphical representation of these two types of waves is shown in Fig. 2-1. The nodes used for this work excite primarily the antisymmetric A_0 mode.

The phase velocities are functions of the driving frequency ($f = \frac{\omega}{2\pi}$) and the half-thickness of the plate (h). The phase velocity is the rate at which the phase of the wave propagates through space. The group velocities are determined using the relation:

$$c_g = \frac{c_p^2}{c_p - \omega \frac{\partial c_p}{\partial \omega}} \tag{2.4}$$

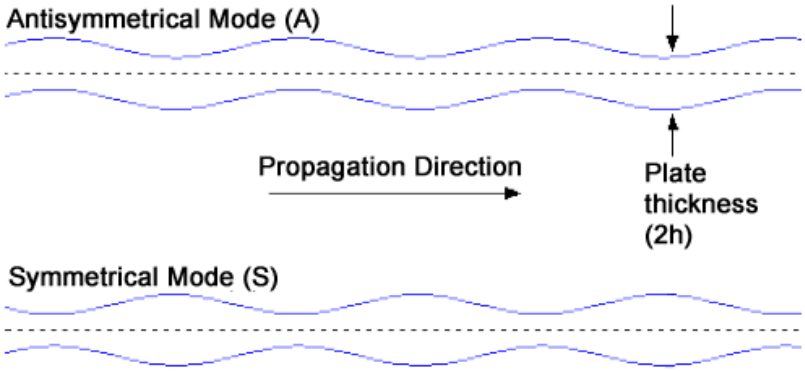

Figure 2-1: Illustration of antisymmetric and symmetric Lamb waves propagating on a plate of thickness 2h, adapted from [3].

The group velocity is the speed that the wavepacket (see Section 3.5 for examples of wavepackets) propagates along the plate (see Fig. 2-1). This velocity is a function of the driving frequency and the phase velocity (which is also a function of the driving frequency). Dispersion curves are typically created to show the relation between the phase velocity and driving frequency and the group velocity and driving frequency.

The dispersion curves for the aluminum coupon used in this study, using the experimental material properties, are shown in Fig. 2-2. The curves are created using MATLAB to numerically solve the roots of the Rayleigh-Lamb frequency equations to determine the phase velocities of both the symmetric (S) and antisymmetric (A) modes. The experimental Young's modulus (74.9 GPa) and Poisson's ratio (0.33), density ($2767\frac{kg}{m^3}$), and plate thickness ($d = 3.175\ mm$) were used to solve Eqn. 2.1. The density was taken from MIL-HDBK-5J [22]. The resulting parameters from the analysis where:

$$c_T = 3.2\frac{mm}{\mu s}, \quad c_L = 6.3\frac{mm}{\mu s}, \quad c_R = 3.0\frac{mm}{\mu s} \tag{2.5}$$

The phase velocity and driving frequency were incremented independently to solve the transcendental Rayleigh-Lamb frequency equation (2.1) for the symmetric and antisymmetric phase velocities. Once the phase velocities of the first four modes were solved as functions of frequency, the group velocities were determined. The

frequency-thickness ($f \cdot d$, where $d = 2h$) product used in this work is 0.19 $MHz \cdot mm$ at the excitation frequency of 60 kHz. As can be seen by the dispersion curves, only the first mode of the symmetric (S_0) and antisymmetric (A_0) waves are present at frequencies below 1.8 $MHz \cdot mm$, the first cutoff frequency. V. Giurgiutiu has shown analytically and experimentally that frequency tuning can be used to selectively excite modes of Lamb waves [10]. The nodes used for this work have been tuned to produce a dominant A_0 mode, with the S_0 mode present, but weak. The group velocity calculated for the first antisymmetric mode with the excitation frequency of 60 kHz is $c_{g_{A_0}} = 2.3\frac{mm}{\mu s}$. This group velocity is used in the time-of-flight calculations of the sensed signal reflections in Chapter 3.

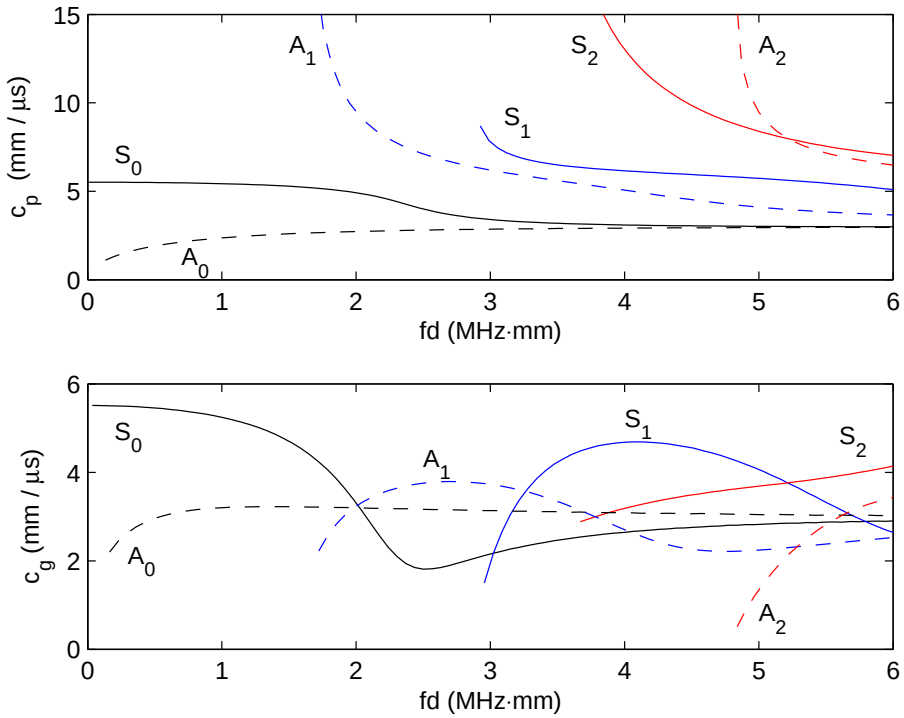

Figure 2-2: Dispersion curves for Lamb waves in a 3.175 mm thick 2024-T3 aluminum plate: a) Phase velocity dispersion curves for first three symmetric and antisymmetric modes. b) Group velocity dispersion curves for the first three symmetric and antisymmetric modes. Symmetric modes shown as solid lines, antisymmetric modes shown as dashed lines.

Chapter 3

Approach

There are currently no standards established for durability testing or certification of SHM (or smart structure) systems for commercial or military aircraft. In order to create such standards, one must address the complete process of health monitoring: installation, credit validation, and instructions for continued airworthiness. A standard for testing health usage monitoring (HUMS) and SHM systems in rotorcraft is in provisional form as part of FAA Advisory Circular (AC) 29-2C [23]. The void in SHM standards stems in part from the difficulty in identifying what the system is, and what it is not: in many cases, even the simplest actuator/sensor is integrally connected to the structure (or embedded in the structure) such that durability testing becomes a subcomponent testing task. In the case of the surface-mounted Lamb-wave type sensors considered here, the sensor's performance requires an integral connection to the structure: the Lamb waves are initiated at the sensor/actuator, propagate through the structure, and return to the sensor/actuator. Clearly, the structure itself (in this work, a narrow aluminum plate) is part of the SHM system in conjunction with the sensor node. Further, the bondline between the sensor node and the structure as well as the electrical connections and software for processing data forms part of the SHM system. In this chapter, a framework for developing SHM durability standards is presented utilizing existing avionics and structural standards, and the SHM system is rigorously defined. The test matrix for this work is presented, as well as a discussion of metrics used to quantitatively assess SHM system performance.

3.1 Framework for SHM Durability Testing

A practical approach to developing a durability standard for aircraft SHM (and smart structures in general) should make use of existing standards, but require additional development to recognize that the SHM system is both sensor and structure [12, 13]. Taking such a view, a durability standard for SHM systems will borrow from (at least) existing standards for structures (Structural Design Standards) and avionic equipment / electronic components (Environmental Standards) following the suggested framework shown in Fig. 3-1. As recommended by the FAA recently, environmental standards are best considered through RTCA/DO-160E "Environmental Conditions and Test Procedures for Airborne Equipment" [2], and both military and commercial structural standards exist or are evolving to meet certification requirements (*e.g.,* FARs) for both metal and composite structures (*e.g.,* ASTM, MIL-STD, and industry proprietary standards). The intersection between the Environmental and Structural Design spaces has, and continues to be, a point of difficulty for assessing performance of structures, and this is no less difficult for SHM systems. Combined environmental excursions and mechanical loading, especially over extended time

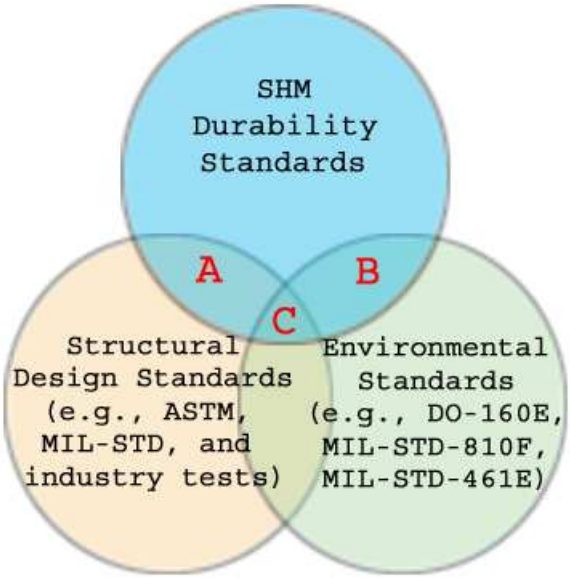

Figure 3-1: Framework for identifying SHM and smart structure testing standards. Regions A and B are the focus of the current work.

frames such as the operational life of commercial transports, are both difficult to achieve experimentally (therefore accelerated testing approaches) and are known to produce interactive effects beyond simple superposition. The framework in Fig. 3-1 recognizes this intersection as also being important for SHM systems, but also clearly shows the need for additional considerations beyond the existing standards.

This work focuses on the overlaps in Fig. 3-1 between the SHM durability and environmental standards (region B) and the SHM durability and structural design standards (region A). Existing environmental and structural design standards have been tailored in this work to define the appropriate tests and conditions to assess SHM system durability. The focus here is decoupled environmental and structural tests, regions A and B in Fig. 3-1, as a good starting point for both evolving the SHM durability framework and evaluating the Lamb-wave based SHM system particular to this work. The upper region of SHM Durability Standards in Fig. 3-1 will contain requirements specific to SHM systems. An example is the need to define the 'operating' state of SHM systems. Most avionic gauges are 'operating' when power is applied, however, SHM systems can be powered but not actively monitoring the structure. Eventually the center overlap, region C of Fig. 3-1, will have to be addressed to fully define durability standards for SHM systems.

3.2 Use of Existing Aerospace Standards

Utilizing the framework discussed in the previous section, the existing standards presented in Chapter 2 have been down-selected to craft a SHM durability standard. Because of the similarities between SHM systems and traditional avionic equipment (both have electrical components used in/on aircraft), the avionic environmental standards formed a starting point to developing testing criteria and procedures. The testing categories from DO-160E and MIL-STD-810F are summarized in Tables 3.1 and 3.2. As the work herein appears to be the first to explore SHM system durability, the tests were down-selected to tests which are likely first-order critical to the SHM system performance - these tests are highlighted in Tables 3.1 and 3.2. The selected

categories provide the foundation of the test matrix for this research discussed in the next section. Also considered when forming the test matrix were structural design standards ASTM D 950-03 and ASTM E 466-96. These standards define testing procedures for impact strength of adhesive bonds and uniaxial fatigue testing of metallic materials, respectively. However, these tests did not make the first-order critical test matrix. Eventually, all the test categories in Tables 3.1 and 3.2, additional structural tests, and SHM-specific tests should be considered following Fig. 3-1.

Table 3.1: Testing standards defined by RTCA/DO-160E. Gray shading indicates tests selected for this work.

Section	Test Title
4.0	Temperature and Altitude
5.0	Temperature Variation
6.0	Humidity
7.0	Shock
8.0	Vibration
9.0	Explosion Proofness
10.0	Waterproofness
11.0	Fluids Susceptibility
12.0	Sand and Dust
13.0	Fungus Resistance
14.0	Salt Spray
15.0	Magnetic Effect
16.0	Power Input
17.0	Voltage Spike Conducted
18.0	Audio Frequency Conducted Susceptibility
19.0	Induced Signal Susceptibility
20.0	RF Susceptibility
21.0	Emission of RF Energy
22.0	Lightning Induced Transient Susceptibility
23.0	Lightning Direct Effects
24.0	Icing
25.0	Electro-Static Discharge
26.0	Fire, Flammability
27.0	Smoke Density, Toxicity

Table 3.2: Testing standards defined by MIL-STD-810F. Gray shading indicates tests selected for this work.

Section	Test Title
500	Low Pressure (Altitude)
501	High Temperature
502	Low Temperature
503	Temperature Shock
504	Contamination by Fluids
505	Solar Radiation (Sunshine)
506	Rain
507	Humidity
508	Fungus
509	Salt Fog
510	Sand and Dust
511	Explosive Atmosphere
512	Immersion
513	Acceleration
514	Vibration
515	Acoustic Noise
516	Shock
517	Pyroshock
518	Acidic Atmosphere
519	Gunfire Vibration
520	Temperature, Humidity, Vibration, and Altitude
521	Icing/Freezing Rain
522	Ballistic Shock
523	Vibro-Acoustic/Temperature

3.3 Test Matrix

The test matrix in this work was formed as a starting point for SHM durability testing. Not all environments necessary to fully test SHM systems are included in this matrix. The standards discussed in the previous section formed the foundation for this matrix. RTCA/DO-160E contains many of the same tests and extreme values as MIL-STD-810F and has been referenced by the FAA as a means for environmental qualification. The testing procedures and extreme conditions were thus largely based on RTCA/DO-160E. The test matrix used for this work is shown in Table 3.3. The test extreme is listed as well as the number of specimens to be tested per environment. The last column of the table lists the section from DO-160E that forms the basis of the test. Details on the test procedures used in this work for each environment can be found in Chapter 4.

Table 3.3: SHM durability test matrix for Lamb-wave nodes.

Environment	**Extreme Condition**	**Samples/ Test Type**	**DO-160E Section**
High Temperature	$85°C$ operating high temp	3	4.5.4
Low Temperature	$-55°C$ operating low temp	3	4.5.2
Thermal Shock	$10\frac{°C}{min}$ minimum change rate	3	5
Humidity	Pure water, $65°C$, 95%RH	3	6.3.2
Oil-based Fluids Susceptibility	24 hour immersion in fluids	3	11.4
Water-based Fluids Susceptibility	24 hour immersion in fluids	3	11.4
Altitude (Low-pressure)	Altitude of $21,336\ m$ ($4.4\ kPa$)	3	4.6.1
Decompression	Rapid decompression to $21,336\ m$	3	4.6.2
Overpressure	Pressurize to $-4,572\ m$ ($170\ kPa$)	3	4.6.3
Static-strain	Strain coupon to near yield	1	-
Total	**-**	**28**	**-**

Specifics of the existing standards used herein are described below. In all cases, extreme conditions (*e.g.,* high-temperature of $85°C$) in the standards were selected.

- The high-temperature test procedure described in Section 4.3.1 is based on the "Operating High Temperature Test" in Section 4.5.4 of DO-160E. The extreme temperature condition of $85°C$ ($185°F$) was selected from the short-time operating high-temperature test. The test qualifies the equipment to be installed in non-temperature controlled locations of the aircraft.

- The low-temperature test procedure described in Section 4.3.2 is based on the

"Operating Low Temperature Test" in Section 4.5.2 of DO-160E. The extreme temperature condition is defined as $-55°C$ $(-67°F)$. The test qualifies the equipment to be installed in non-temperature controlled locations of the aircraft.

- The thermal shock test procedure described in Section 4.3.3 is based on Section 5, "Temperature Variation," of DO-160E. The extreme rate of change greater than $10°C$ $(18°F)$ per minute was selected. This qualifies the equipment for installation external or internal to the aircraft.

- The humidity test procedure described in Section 4.3.4 is based on Section 6.3.2, "Severe Humidity Environment," of DO-160E. The procedure was modified to have the equipment operating (SHM nodes actuating) the entire test. The test qualifies the equipment to be used on aircraft that may experience natural or induced humid atmospheres.

- The fluid susceptibility test procedure described in Section 4.3.5 is based on Section 11.4 of DO-160E. The test exposes the equipment to common fluids used in (or on) aircraft. The test qualifies the equipment to be installed in areas where fluid contamination could be commonly encountered.

- The altitude (low-pressure) test procedure described in Section 4.3.6 is based on Section 4.6.1 of DO-160E. The extreme altitude of $21,300$ m $(70,000$ $ft)$, equivalent to an absolute pressure of 4.4 kPa $(0.6$ $psia)$, was selected. The test qualifies the equipment to be installed in non-pressurized locations on aircraft that are operated up to $21,300$ m $(70,000$ $ft)$.

- The decompression test procedure described in Section 4.3.6 is based on Section 4.6.2 of DO-160E. The extreme case calls for an instantaneous (but no longer that 15 s) decompression from 75.3 kPa to 4.4 kPa (10.9 $psia$ to 0.6 $psia$), equivalent to an altitude of $2,400$ m to $21,300$ m $(8,000$ ft to $70,000$ $ft)$, respectively. The test qualifies equipment installed in pressurized areas on the aircraft required to operate during and following an emergency descent (in case loss of pressurization occurs at altitude).

- The overpressure test procedure described in Section 4.3.6 is based on Section 4.6.3 of DO-160E. The test requires the equipment to withstand an absolute pressure of 170 kPa (24.7 $psia$), equivalent to $-4,600$ m ($-15,000$ ft). The test qualifies the equipment to be installed in pressurized areas of the aircraft that are exposed to routine pressurization and pressurization system testing.

- The static-strain test procedure described in Section 4.3.7 was formed to simulate normal strain levels experienced in aircraft structural components. The extreme level of strain should be based on the design of the structure being monitored, and was chosen here to be near the structure's (in this work an aluminum coupon) yield stress.

The tests above are considered extreme cases for all categories based on the existing standards, and are intended to explore the SHM system's durability under the most extreme expected conditions.

3.4 SHM System Definition

Standards specific to SHM and smart structures are needed to address the fact that the structure is an integral part of the system as discussed earlier. An example, utilizing the ultrasonic Lamb-wave sensors that are the focus of this work, is the issue of modulus change of a composite structure with environmental aging that will change/degrade the propagation characteristics of the Lamb waves. The change can be associated with polymer aging and may (or may not) be considered damage. A more subtle example is the possibility that the ultrasonic excitation initiates, or propagates over time, cracks in a composite material/laminate. While this seems unlikely for the sensors considered here, it certainly is a possibility for embedded smart/active structures.

For this work, the SHM system is defined as the SHM node and connector, the aluminum coupon (structure) between the two boundary clamps, the adhesive bonding the node to the coupon, the boundary clamps, and the shear gel between the

boundary clamps and coupon, shown in Fig. 3-2. The SHM node and adhesive were supplied by MDC. 2024-T3 aluminum produced by Alcoa was selected as the test structure because of its isotropic wave propagation properties and its usage history in aircraft applications. 2024-T3 sheet aluminum has been extensively used in commercial and military aircraft for fuselage and wing skins [24] and has well-characterized thermomechanical properties. The thickness of the aluminum coupons was selected based on typical fuselage and skin thicknesses. The width of the coupon was selected to be the same width as the node to create a near 1-dimensional wave propagation. The length was limited based on testing equipment constraints. The boundary clamps and shear gel were used to define the extent of the system. The additional aluminum material past the clamps was intended to allow the coupons to be installed in test fixtures without influencing the defined system. Additional detail on the SHM system used throughout this work is presented in Section 4.1.

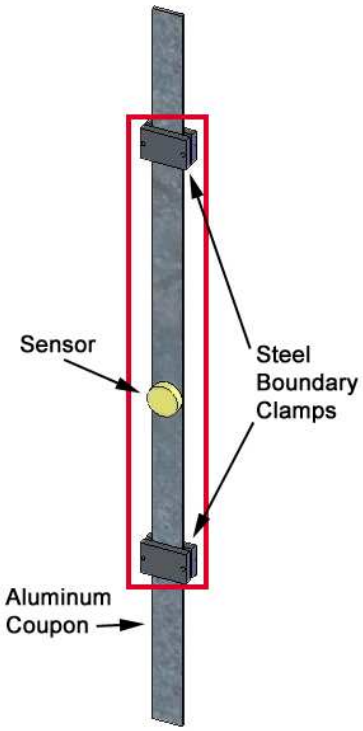

Figure 3-2: Test coupon with node and boundary clamps. Defined SHM system inside box.

3.5 Metric Selection

A critical component to forming SHM testing standards is clearly defining criteria to judge the system's performance. Because of the different techniques used for various SHM systems, it is likely that the criteria will be unique for each system. These criteria will likely need to be specified by the manufacturer based on system requirements to accurately monitor the structure.

The criteria formed for the Lamb wave-based nodes used in this work is based on two difference/change metrics; a time-of-flight metric and a peak voltage metric. MDC (the equipment manufacturer) agreed with these metrics to assess the performance of the nodes. These metrics were selected after studying the operation of the SHM nodes. The system's operating principle is based on sending and receiving ultrasonic wavepackets propagating through the structure (aluminum coupon). The ultrasonic elastic Lamb-waves are initiated by applying a voltage signal to the actuator of the node. The excitation signal and actuator geometry have been designed to create the desired Lamb-wave packet [3]. By selecting the appropriate frequency (effectively the $f \cdot d$ product discussed in Section 2.2), certain Lamb-wave modes can be excited. For this work, 60 kHz was selected as the driving frequency to produce antisymmetric (A_0) wavepackets. This frequency resulted in clearly separated reflected wavepackets for the system tested based on initial testing.

The wavepacket propagates through the structure until it encounters a discontinuity. Depending on the type of discontinuity (*e.g.,* inclusion, free-edge, clamped-edge), the wavepacket (or part of the wavepacket) may reflect and travel back to the node. As the waves pass under the node they strain the piezoelectric elements. The piezoelectric elements convert the elastic disturbance of the waves into electrical signals measured by the electronics in the node. The signal voltage produced is proportional to the amount of strain experienced by the sensing element. Recording this signal over time enables one to capture wavepackets as they travel under the node. An example sensed signal with the direct path, first reflected, and second reflected wavepackets circled is shown in Fig. 3-3. Further discussion on the recorded signals is included in

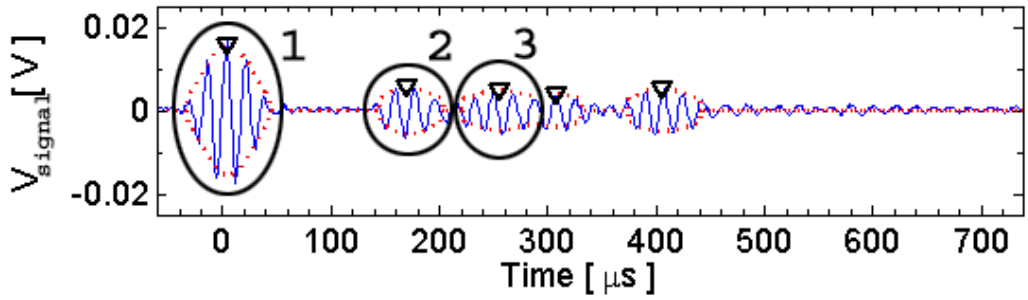

Figure 3-3: Example sensed signal. Labeled are the direct path (1), first reflection (2), and second reflection (3) wavepackets.

At the start of the work, the metrics were applied to the wavepackets from the first and second reflections (labeled 2 and 3 in Fig. 3-3). A discrepancy was found between the analytical and experimental TOF of the second reflection. This was likely due to the complexities of multiple Lamb-wave modes interacting within wavepackets as they passed through other wavepackets. To avoid this complexity, the metrics are applied to the first two wavepackets (labeled 1 and 2 in Fig. 3-3) only. These wavepackets nominally have no interference from other wavepackets before being sensed. An illustration showing the location of wavepackets at successive time steps is shown in Fig. 3-4. In the figure, the initial pulse produces wavepackets in both directions. These wavepackets propagate through the structure until they reach the boundary clamps, where they are reflected. Note, the illustration assumes total reflection from the boundary clamps, this is likely not the case. In the last step (d), the wavepackets are shown interfering with each other.

The first reflected wavepacket's experimental TOF (171 μs on average) disagrees with the analytical TOF. However, for the specimens tested without boundary clamps, the distance the first reflected wavepacket travels is twice as long and the experimental TOF nearly doubles (327 μs on average). This confirms the first reflected wavepacket is identified correctly, but the analytical model used is not properly predicting the group velocity. Using the first antisymmetric group velocity ($c_{g_{A_0}}$) from Section 2.2,

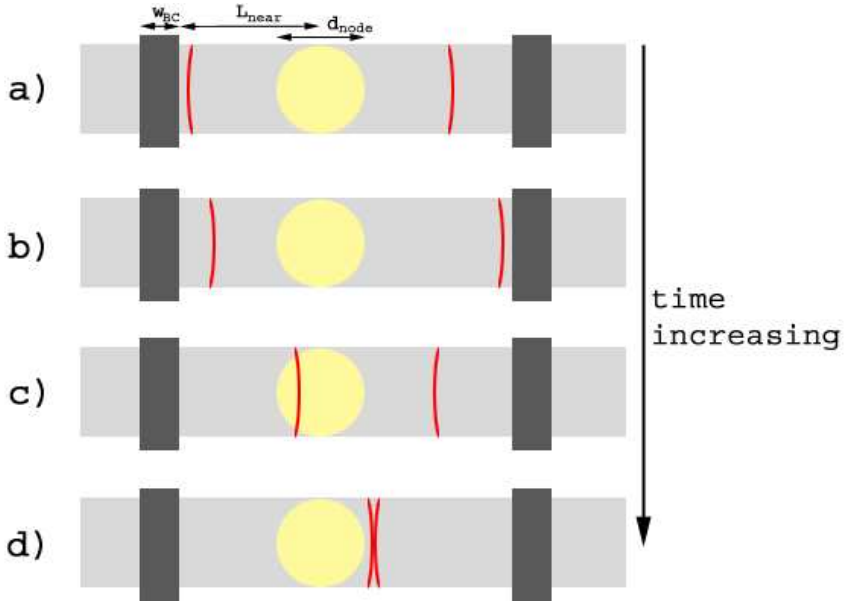

Figure 3-4: Wave path illustration of SHM node asymmetrically mounted between boundary clamps. a) wavepackets propagating away from node. b) first wavepacket reflection from near (left) boundary clamp. c) first reflected wavepacket sensed by node. d) wavepackets interfering. (Not drawn to scale).

the analytical TOF calculations are:

$$TOF_{min} = \frac{2L_{near}}{c_{g_{A_0}}} - \frac{d_{node}}{2c_{g_{A_0}}} = \frac{2 * 127\ mm}{2.27\frac{mm}{\mu s}} - \frac{25.4\ mm}{2 * 2.27\frac{mm}{\mu s}} = 106\ \mu s$$

$$TOF_{max} = \frac{2L_{near}}{c_{g_{A_0}}} + \frac{d_{node}}{2c_{g_{A_0}}} + \frac{w_{B.C.}}{c_{g_{A_0}}} = \frac{2 * 127\ mm}{2.27\frac{mm}{\mu s}} + \frac{25.4\ mm}{2 * 2.27\frac{mm}{\mu s}} + \frac{25.4\ mm}{2.27\frac{mm}{\mu s}} = 129\ \mu s$$

The range of time (min to max) comes from the wave propagation characteristics of Lamb-waves. The first term in both equation is twice the distance from the node center to the near edge of the boundary clamp (L_{near}). The second term accounts for the width of the node (d_{node}). The Lamb-waves may not always be sensed at the center of the node, however they will be sensed between the near ($-12.5\ mm$) and far ($+12.5\ mm$) node edges. In the second equation, the third term (w_{BC}) accounts for the distance the wavepacket travels before it encounters the boundary clamp. Ideally, the wavepacket will reflect from the near edge, however, there is a possibility that the wavepacket could travel some distance below the boundary clamp before being reflected.

The metrics used to assess the performance of the node assess four points in the sensed signals (refer to Fig. 3-3), the TOF and peak voltage of the first two wavepackets. A baseline signal of each specimen is taken at ambient conditions before testing. Operational (during test) signals are acquired throughout the test and a post-test signal is collected once ambient conditions are reestablished. These signals are compared to the baseline and the differences in the TOFs and peak voltages are calculated. To normalize these values for all tests, a percent change from the baseline values are calculated. Based on these four metrics, the performance of the SHM system is assessed as discussed in Chapter 5.

Chapter 4

Experimental Procedures

The experimental testing procedures were formed largely from DO-160E and MIL-STD-810F [15, 16]. Each environmental condition described in these standards has categories defining the severity of environment the tested equipment is expected to be regularly exposed to throughout it's lifetime. The qualification category is to be specified by the equipment supplier and is application dependent. When choosing operational categories to operate the system for this research, the extreme categories were selected in all cases. For the purpose of all testing, ambient conditions are defined as a temperature from $+15°C$ to $+35°C$, a pressure from 84 to 107 kPa (equivalent to an altitude from $+1,525\ m$ to $-460\ m$), and a humidity not greater than $85\%RH$. Before each test, baseline sensor signals were recorded at ambient conditions. The first baseline signal was without boundary clamps and the second was with boundary clamps. These baselines were used for comparison to the signals recorded during and after testing to determine the performance of the node by assessing differences (deltas) in the signal characteristics. Two delta metrics were used to determine the sensor's performance: a time-of-flight (TOF) metric of the first two wavepackets, and a maximum voltage (within each wavepacket) metric. The signals and metrics will be discused in the next chapter.

4.1 Specimen Description and Preparation

The definition of the SHM system from a durability testing standpoint is discussed in Section 3.4. The coupon material (underlying structure being assessed with the SHM node) was chosen as 2024-T3 aluminum, a commonly used aerospace alloy [24]. Aluminum was chosen because of the well-characterized material properties and the less complicated wave propagation through the nominally isotropic material. The dimensions of each rectangular cross-section aluminum bar were 609.6 mm (24 $in.$) long by 25.4 mm (1 $in.$) wide by 3.175 mm ($\frac{1}{8}$ $in.$) thick. The experimental modulus and Poisson's ratio of three aluminum coupons were determined from tensile tests. Two strain gauges were attached to blank (no nodes) coupons and the samples were loaded in a MTS uniaxial testing machine. The resulting modulus, Poisson's ratio, and yield stress were compared to the values listed in MIL-HDBK-5J and were found equivalent [22]: $E_{exp} = 74.9\ GPa$, $E_{MIL} = 72.4\ GPa$, $\nu_{exp} = 0.33$, $\nu_{MIL} = 0.33$, $\sigma_{y_{exp}} = 314\ MPa$, $\sigma_{y_{MIL}} = 324\ MPa$.

The SHM nodes were supplied by MDC as Monitoring and Evaluation Technology Integration Disk 3 (M.E.T.I.-Disk 3). An exploded view of an early version of the M.E.T.I.-Disk node (M.E.T.I.-Disk 2) is shown in Fig. 4-1, and the digital node used in this work is shown in Fig. 4-2. The nodes have concentric piezoceramic (PZT) sensor and actuator elements labeled 'piezo' in Fig. 4-1. The analog M.E.T.I.-Disk 2 node has a multiple part design and two SMB (SubMiniature version B) connections (one to the actuating element and one to the sensing element). The digital node (M.E.T.I.-Disk 3) has a printed-circuit board that is encapsulated in urethane for durability and has a mini-USB connector for power and data transfer. The node has 2 channels with a maximum 1 MHz 16-bit ADC and $1,000,000\frac{sample}{s}$ 8-bit DAC. The node is 9 mm (0.35 $in.$) tall and has a diameter of 25.4 mm (1 $in.$). The digital node is a single-piece construction that is bonded directly to the structure to be monitored.

The nodes were bonded to the aluminum samples with AE-10 epoxy, a general-purpose adhesive that is highly resistant to moisture and most chemicals. The as-received adhesive is packaged in a two part sachet that was broken in the middle

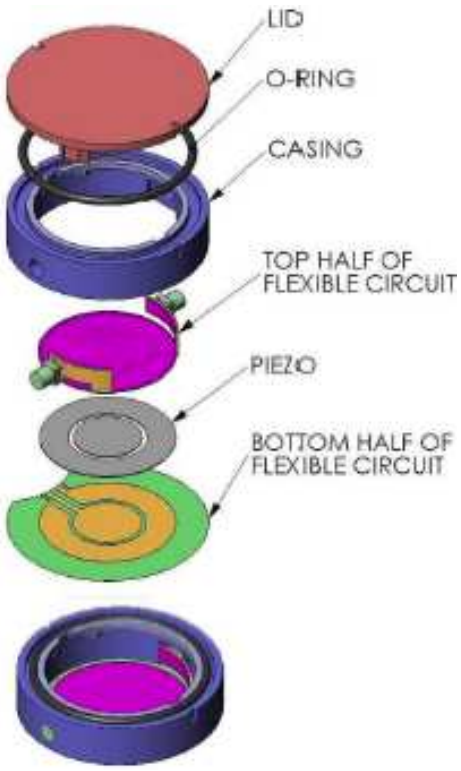

Figure 4-1: Exploded view of M.E.T.I.-Disk 2 node.

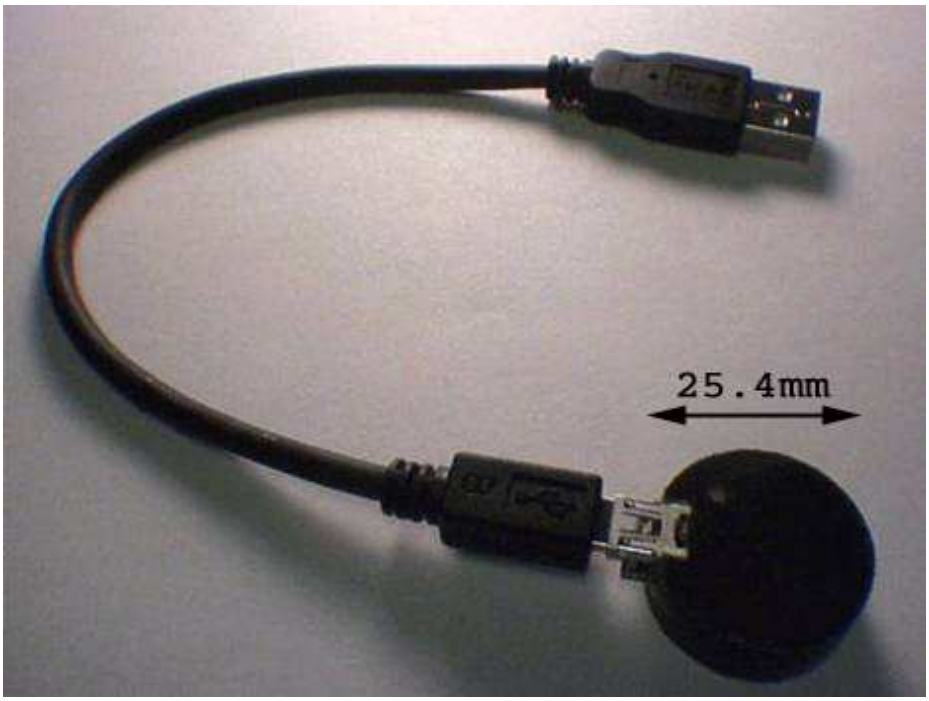

Figure 4-2: Digital M.E.T.I.-Disk 3 node with USB connection.

to allow the parts to mix before application. The epoxy has a working time of 15 minutes and a cure time at room temperature of 24 to 48 hours. The manufacturer's listed operating temperature range was $-196°C$ to $95°C$ ($-320°F$ to $200°F$). The surface of the aluminum sample was prepared for node placement by hand sanding the application area with 600-grit sandpaper and then cleaning the surface with isopropyl alcohol. The adhesive was mixed and applied directly from the sachet to the bottom of the sensor and to the mounting surface of the aluminum, taking care to avoid bubbles. The sensor was then placed on the aluminum sample and worked around by hand to force out any air bubbles. The node was centered (side-to-side) on the aluminum and the vertical alignment was verified with a ruler. The first four samples (nodes 0017, 0026, 0041, and 0058) had 5.44 kg (12 $lbs.$) of dead weight rested upon the top of each node, with the aluminum samples on a level bench. Due to difficulty balancing the dead weight on the nodes, Hargrave No. 2 spring clamps were used for all remaining nodes. The spring clamps provided a load of 7.62 kg (16.8 $lbs.$). A 6.35 mm ($\frac{1}{4}$ $in.$) thick, 25.4 mm (1 $in.$) square foam pad was placed on top of the node and a 25.4 mm (1 $in.$) diameter, 2 mm (0.08 $in.$) thick steel washer was placed on the foam. The clamp was then applied, with it's jaws making contact with the bottom of the aluminum sample and the steel washer. The washer and foam were used to apply uniform pressure to the node. Excess adhesive was immediately removed using a cotton swab, and then the adhesive was allowed to cure at room temperature for 48+ hours.

The nodes were bonded asymmetrically with respect to the specimen (aluminum coupon) length to separate reflected wavepackets. This allowed the reflections to be separately identified during signal processing. Boundary clamps were placed with their near edges 127.0 mm (5 $in.$) and 203.2 mm (8 $in.$) from center of the sensor as shown in Fig. 4-3. Each clamp was made of two 6.35 mm thick by 25.4 mm wide by 50.8 mm long ($\frac{1}{4}in.$ by 1 $in.$ by 2 $in.$) pieces of steel with 6.35 mm ($\frac{1}{4}$ $in.$) bolt holes at each end. Sonotech shear gel, an ultrasonic shear couplant, was applied between the aluminum coupon and boundary clamps to effectively produce an 'edge' boundary to the Lamb wave. The shear gel has an operating temperature range from $4°C$ to

$32°C$ ($40°F$ to $90°F$) and is water-soluble. Bolts were placed through the boundary clamp holes and were tightened to 0.11 $N \cdot m$ (100 $lbs \cdot in$) to produce a pressure of $\sim$ 28 MPa (4000 psi) between the clamps and coupon. The completely assembled 'SHM system' that was designed for use in all the tests is described in Section 3.3, and shown in Fig. 4-3, apart from the USB cable.

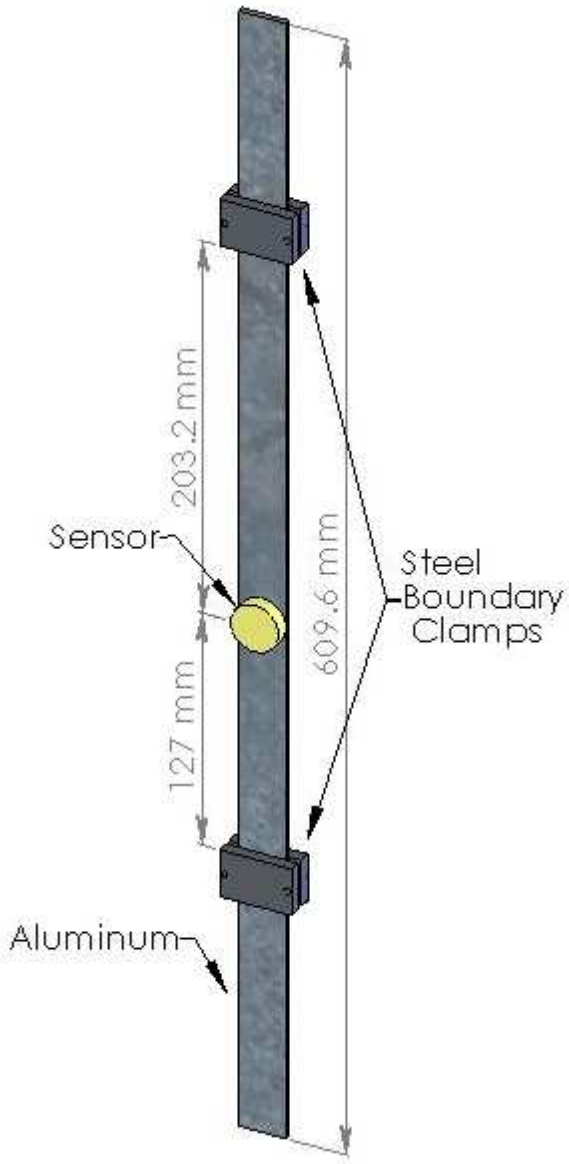

Figure 4-3: 'SHM system' used in all tests: asymmetrically-mounted node, aluminum coupon (structure), and boundary clamps.

4.2 Data-Acquisition System

Laptop PCs running Windows XP were used to run the M.E.T.I.-System software that was developed specifically for this work by MDC. The software is a LabVIEW based program that allows control (adjusting parameters, discussed below) of the SHM node. A screenshot of the software is shown in Fig. 4-4. Connecting the sensor node to the PC via a USB cable and running the software allows communication between the node and program. The LabVIEW program sends the actuating signal and acquires the sensor data (voltage vs. time), writing both to a specified comma-delimited file. This file is imported to MATLAB where post-processing of the data can occur.

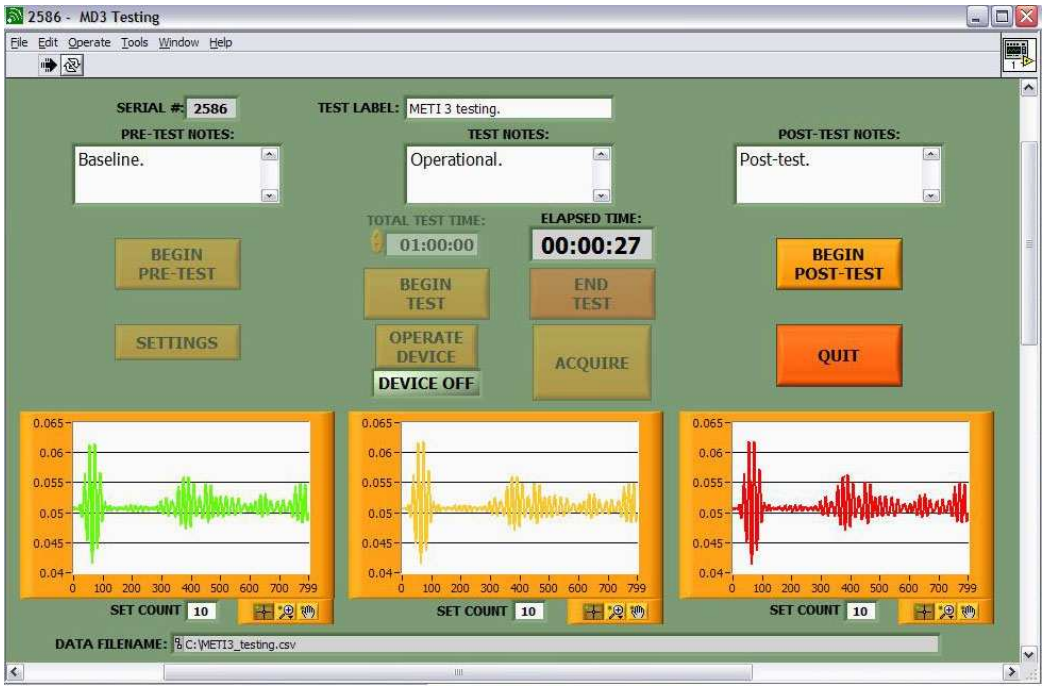

Figure 4-4: Screenshot of M.E.T.I.-System software with sample signals.

The excitation pulse sent to the node actuator is a five-sine wave signal in a Hanning window. This excitation pulse has a driving frequency of 60 kHz and an amplitude of 5.8 volts peak-to-peak (discussed in Chapter 5). The sensor acquires data at a sampling rate of 1000 kHz for 0.8 ms (800 data points). 16 data sets are taken in rapid succession and averaged on the microprocessor in the node. The averaged

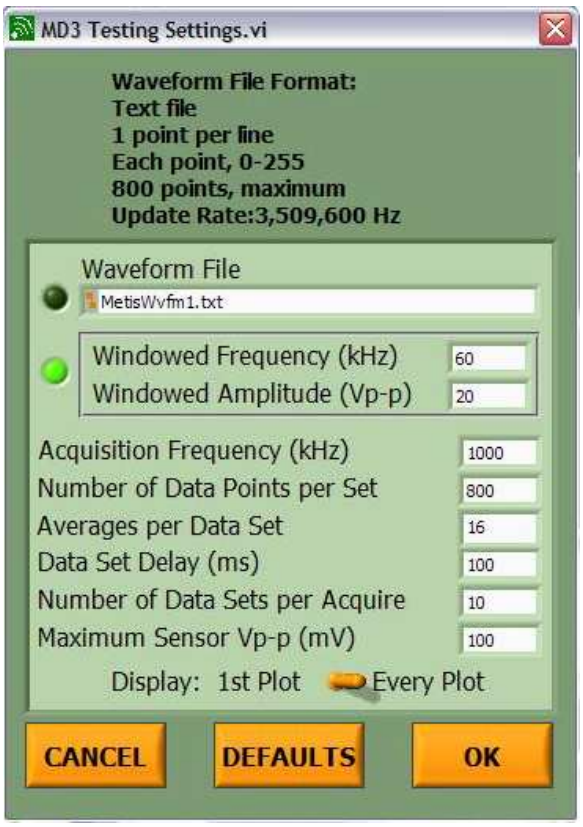

Figure 4-5: M.E.T.I.-System software settings.

data set is sent to the PC and displayed on the M.E.T.I.-System software, as shown in Fig. 4-4. Ten consecutive averaged sets, spaced 100 ms apart, were recorded for each sensor assessment point. These settings are selected before running a test using the controls shown in Fig. 4-5. Data sets were acquired at the start of each test (the baseline signal), at specified points throughout the defined test (operational signal), and after the test was complete and ambient conditions were reestablished (post-test signal). The experimental signals presented in Chapter 5 and Appendix B are one of the ten averaged data sets zeroed to their respective mean, and are considered representative by visual comparison to the other nine data sets. The additional data sets provide a robust signal in case a communication error occurs while transferring the data from the node to the PC. The sensor signals are also inverted to make the comparison between the excitation pulse and the measured sensor signal clear.

One topic that must be addressed when tailoring the existing standards is defining what 'device operating' means to SHM systems. General avionic equipment is usually

operating when power is applied (*e.g.,* cockpit gauges). SHM systems, particularly active systems such as used here, do not typically have a clear operating condition. SHM-specific standards will need to clearly define operating as the system powered, or the system operating (here, operating is sending Lamb-waves to the structure). For the tests conducted in this research, the 'device operating' condition was chosen to be the SHM system powered and excitation pulses being sent to the actuator, hereafter referred to as 'equipment operating'. However, no data is recorded during 'equipment operating' except at the specified pre-test, operational test, and post-test points. The 'device off' condition is defined as the node normally powered without any excitation signals sent to the actuator, hereafter referred to as 'equipment off'. Thus, device off is defined here (as equipment off) to mean that the node is powered but not sending/receiving ultrasonic waves.

4.3 Testing Procedures

The testing procedure for each environment listed in Table 3.3 is developed in the following sections. These procedures have been formed from existing avionic standards, as previously mentioned, and adapted to test SHM systems. Further refinement of specific procedures are necessary. Although not required in the avionic standards, functional testing during the test cycles should be addressed if a SHM system were envisioned for operation during flight or at other times when such conditions might be experienced. The procedures presented in this section were used to evaluate the performance of the surface mounted Lamb-wave type sensors. Following the explanation of the adapted testing procedure for each environment are the experimental procedures used to conduct the test. Illustrated on each test profile is the system's operating condition. For all tests, 'device operating' refers to the system powered and the activation signal continuously producing Lamb-waves (equipment operating). 'Device off' refers to the system normally powered but no activation signal being sent to the node (equipment off). Unless specified, the nodes were powered the duration of each test.

4.3.1 High-temperature

The purpose of the high-temperature test is to ensure that the equipment can survive the elevated temperatures an aircraft may experience. After the test, the SHM system should be inspected for temporary or permanent performance degradation. Some typical problems to observe include materials changing dimension, components overheating, high pressures created in sealed voids, and cracking of materials. The system should be operated the duration of the test. For the test, the system must be ramped from ambient conditions to the peak operational temperature. The ramp rate must not exceed $2°C$ per minute or it is defined as a thermal shock. Once the temperature is stabilized, the SHM system must undergo a 2 hour functional test at the operating high temperature. The temperature is then to ramp back to ambient, not exceeding the ramp rate, and the performance of the system is to be tested again. The system should be powered and operating during the entire test. The temperature profile for this procedure is shown in Fig. 4-6 to illustrate the test. The extreme operational high temperature is defined as $85°C$. This temperature

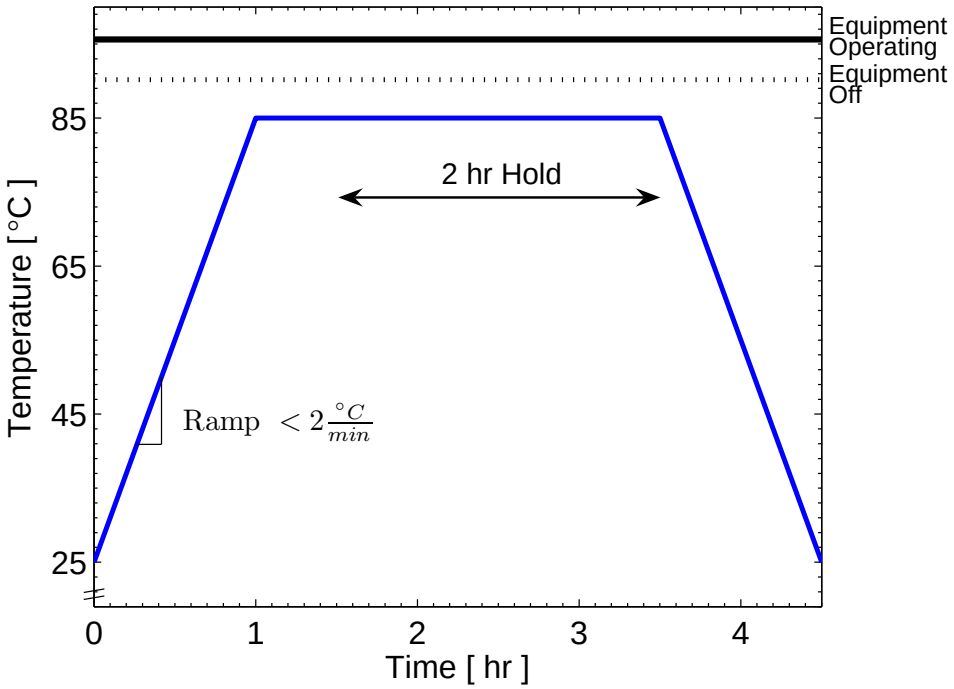

Figure 4-6: Nominal high-temperature test profile.

reflects data from military documents specifying that normally operated vehicles will not encounter temperatures greater than the high operational temperature [18]. This temperature is also an upper limit to which the test standard is valid.

The high-temperature test was conducted in an Applied Test Systems (ATS) 3610 oven/cooling chamber. The oven had been previously modified to accommodate tensile testing on a MTS tensile-compression machine. A 3-inch diameter hole was cut through the top and bottom of the oven. Plugs were machined from carbon to fit in these holes and were modified to accommodate our test specimen. The specimen was installed vertically with the lower boundary clamp resting in the lower endcap, as shown in Fig. 4-7. The temperature was controlled by an Omega CNi32 proportional-

Figure 4-7: ATS oven/cooling chamber with test specimen installed.

integral-derivative (PID) controller. The PID constants were set using the automatic tune cycle. Setpoints were programmed in the controller to produce a ramp rate of $2°C$ per minute. A 15 minute stabilization time was programmed before the 2 hour hold. After the hold, the oven heaters, controller, and circulation fan were turned off, and the temperature was allowed to return to ambient overnight before the post-test was conducted. An experimentally achieved test profile is shown in Fig. 4-8 for node 0041. Baseline signals were taken before each test. Operational signals were recorded along the ramp and through the hold. After allowing the nodes to gradually return to ambient conditions, the post-test signals were collected after 16 hours. The temperature profiles for all three samples are included in Appendix A, Figures A-1, A-2, and A-3. While testing node 0036, shown in Fig. A-2, the communication between the computer and node was lost after 14 minutes. The chamber was returned to ambient conditions before restarting the software and resuming the test. No temperature data was recorded after the 2 hour hold on nodes 0021 and 0036. The experimental ramp rates shown on the figures were calculated by taking an average over the entire ramp.

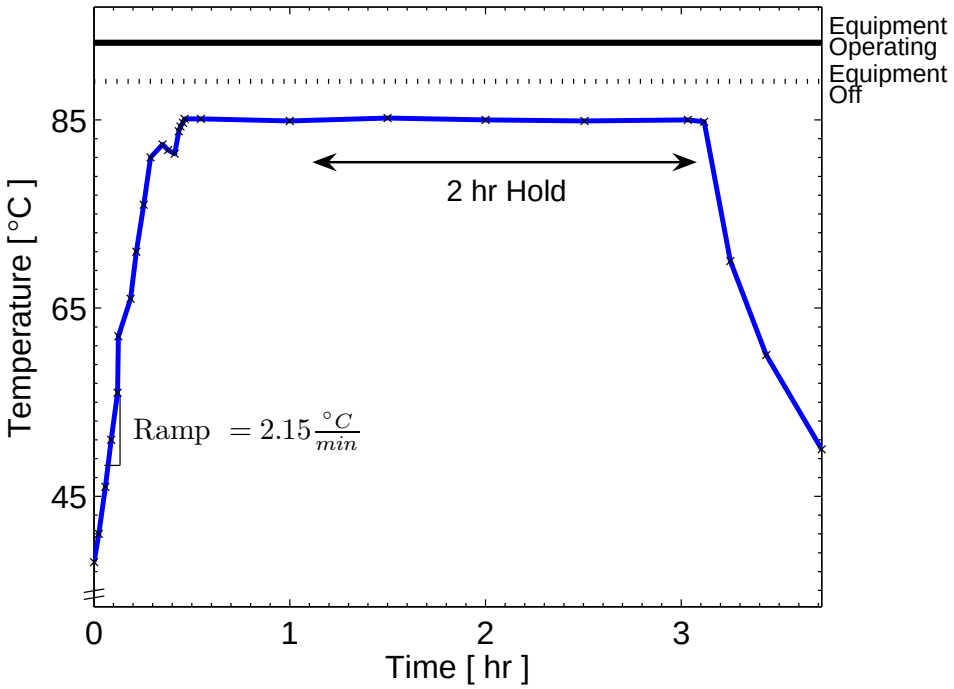

Figure 4-8: Experimental high-temperature test profile for node 0041.

The temperatures recorded had an accuracy of $\pm 0.1°C$ being measured by a J-type thermal couple. The thermal couple was attached to the Omega controller. The temperature reading was verified to be within $1°C$ accuracy using a glass thermometer. An over-temperature power cut-off device was placed in-line with the power to the controller and heater for safety.

4.3.2 Low-temperature

The low-temperature test examines the performance of the SHM system at reduced temperatures. The testing procedure follows the method discussed in the high-temperature test. The system should be assessed for changes in electrical components, stiffening of materials, cracking, debonding, and condensation of liquids. The extreme cold operating temperature is defined as -55°C. The nominal test profile is shown in Fig. 4-9.

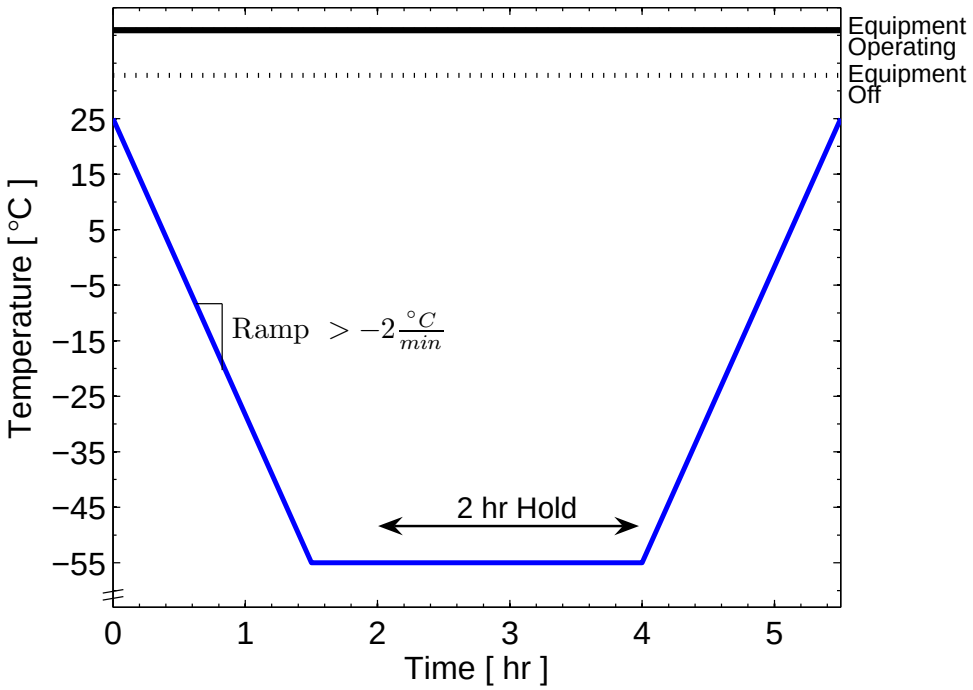

Figure 4-9: Nominal low-temperature test profile.

The ATS oven used for the high-temperature testing was also used for the low-temperature tests. The chamber had been previously modified to accept liquid nitro-

gen. A $\frac{1}{2}$ inch outer diameter metal tube had been installed through the oven wall into the heating chamber. A solenoid valve was installed and a liquid nitrogen supply was attached. An Omega CN2042 PID controller was used to achieve the low-temperature test profile. Figure 4-10 shows the test setup for the low-temperature and thermal-shock tests. The Omega controller had primary and secondary output controls. The heating elements were connected to the primary output while the cooling solenoid

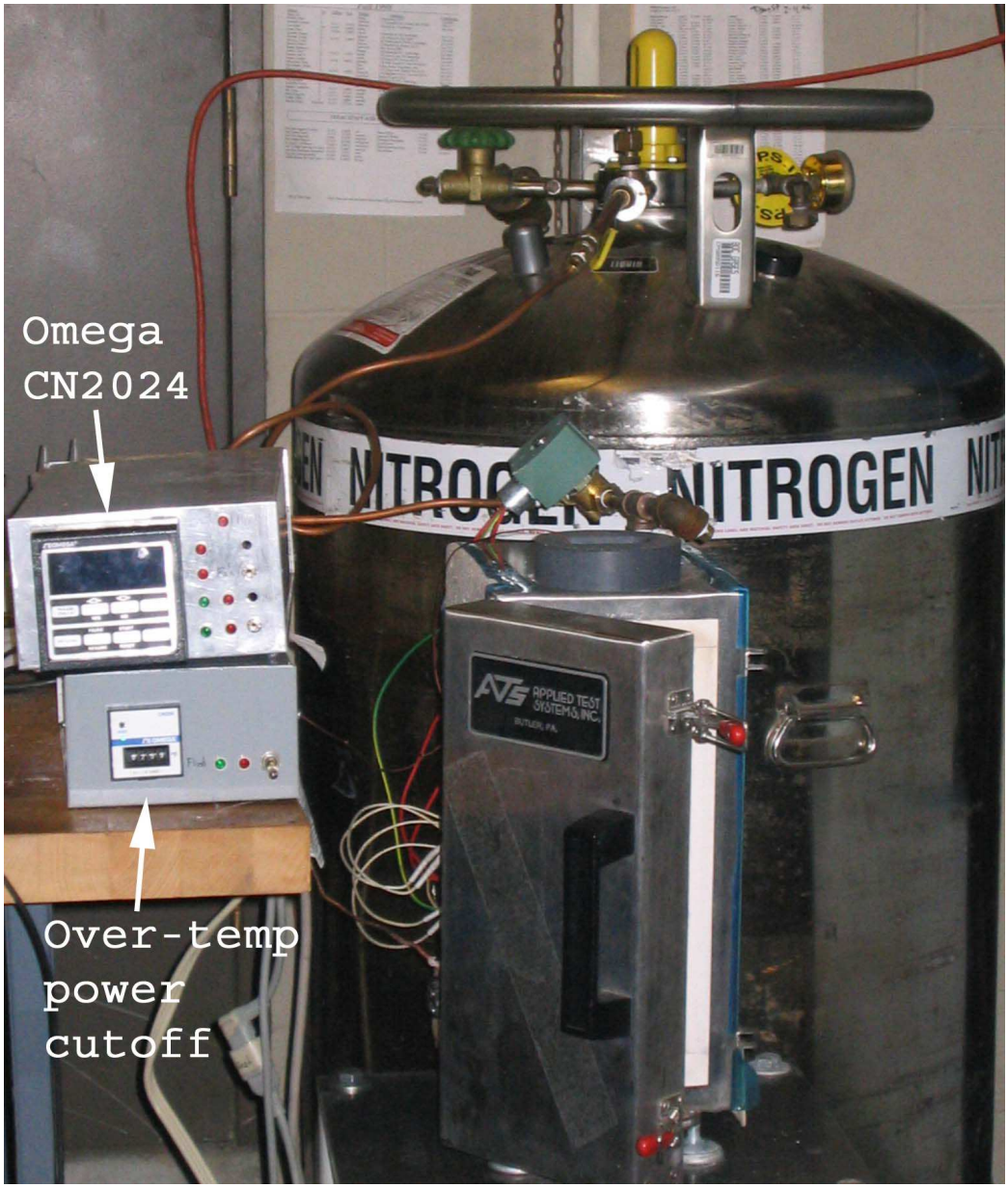

Figure 4-10: ATS chamber with Omega CN2024 controller, over-temperature power cut-off device, and liquid-nitrogen tank shown.

was attached to the secondary output. The primary and secondary PID constants were manually tuned. The proportional band (gain) was set at 5% and the derivative time (rate) was set at 0.04 minutes for both outputs. The integral time (reset) for the primary ouput was set at 4.5 resets per minute while the integral time for the secondary output was set at 4.07 resets per minute. The test profile was programmed into the controller, allowing 15 minute stabilization times. An experimental temperature profile for one low-temperature test is given in Fig. 4-11. The profiles for the three low-temperature tests are included in Appendix A, Figures A-4, A-5, and A-6. The controller had difficulty stabilizing the temperature. 50 minutes into the first test (node 0029) the controller was switched to manual control. The PID was used to control the ramps, but the temperature stabilization and hold was accomplished manually for all the tests. No temperature data was recorded after the 2 hour hold for node 0049.

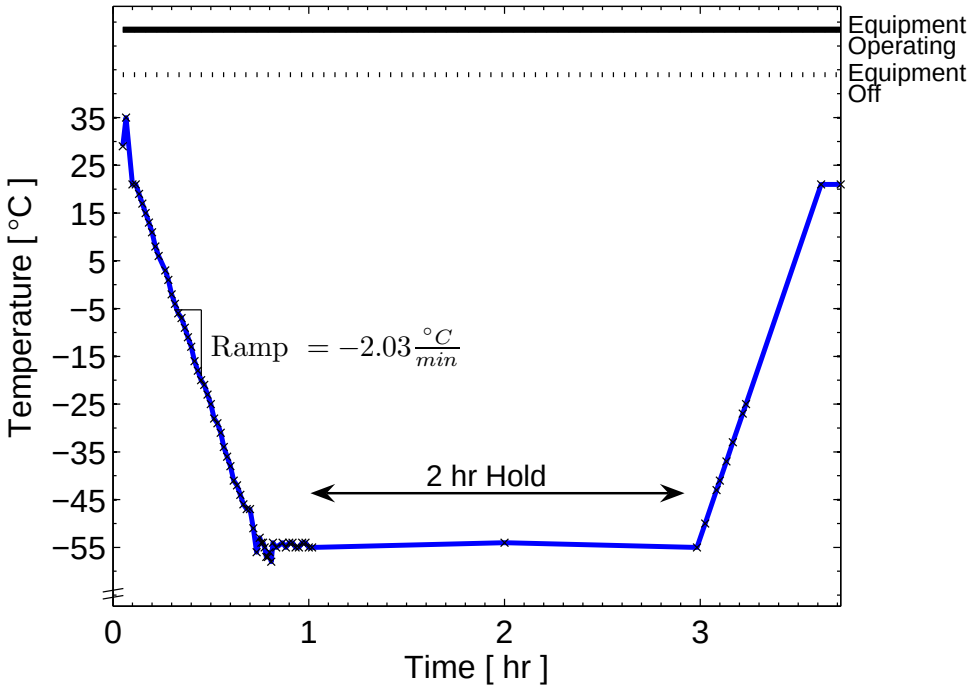

Figure 4-11: Experimental low-temperature test profile for node 0068.

4.3.3 Thermal Shock

For the thermal shock tests, the rate of temperature change is specified in addition to the endpoints. This is to simulate aircraft taking off from a hot desert climate and climbing to a high altitude cruise. With the system operating, the temperature is ramped from ambient conditions to the low operational temperature ($-55°C$) at a rate greater than $10°C$ per minute. This rate is used for any temperature changes. The temperature is stabilized before being ramped, at the specified ramp rate, to the high operational temperature ($85°C$). The temperature is stabilized and then the system is held in a non-operating state for 2 minutes. After the system is turned back on (interpreted here as equipment operating), ramp back to the low operational temperature. The system is stabilized and then held at the operational cold temperature for 60 minutes. After this hold, the system is placed in a non-operating state and held for an additional 30 minutes. Re-operating the system, the temperature is ramped to ambient conditions and allowed to stabilize. The nominal temperature profile for this procedure is shown in Fig. 4-12 illustrating one cycle. A minimum of two cycles must be completed for a valid durability test. After completion of the test, the system should undergo a functional test.

The ATS oven with the Omega CN2042 controller was used for the thermal shock tests. The same PID constants used for the low-temperature tests were used. One test cycle was programmed into the controller. The stabilization times were set to 20 minutes. Liquid nitrogen and the chamber's heating elements varied the oven's temperatures. An experimentally-achieved cycle is shown in Fig. 4-13. The profiles for the three thermal shock tests (nodes 0034, 0046, and 0061) are shown in Appendix A as Figures A-7, A-8, and A-10. Similar to the low-temperature tests, the controller had difficulties stabilizing the temperatures. Manual temperature stabilization control was taken over after the first heat cycle of node 0034. Node 0061 experienced additional cycles of testing. Half way through the second cycle of testing, the liquid nitrogen ran out. This partial test cycle is given in Fig. A-9. The liquid nitrogen tank was replaced and node 0061 was exposed to another 2 full cycles, shown in Fig. A-10.

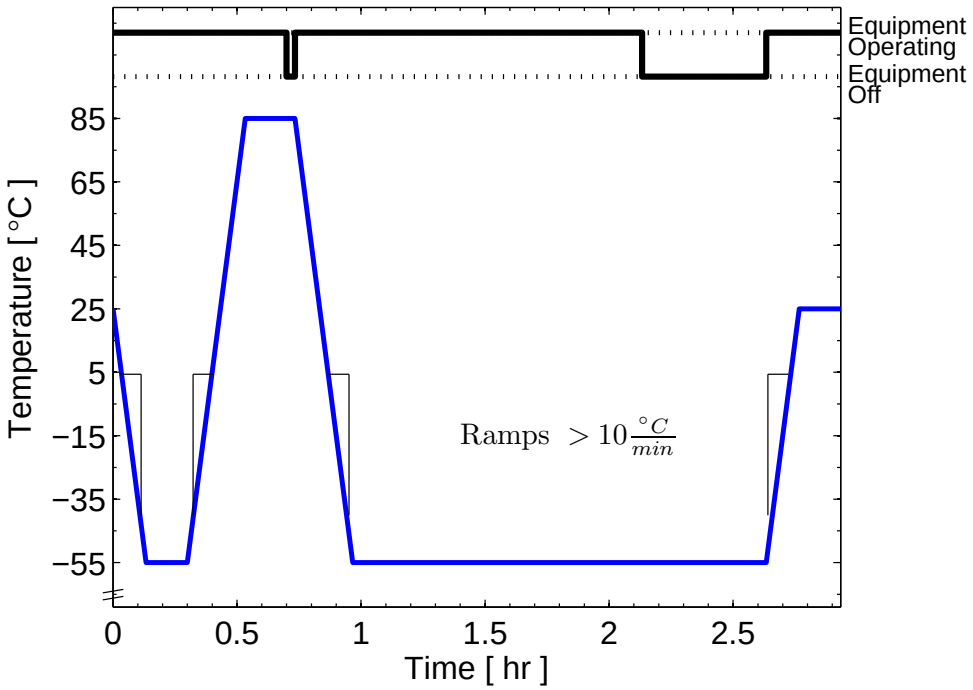

Figure 4-12: Nominal thermal shock test profile (1 of 2 required cycles).

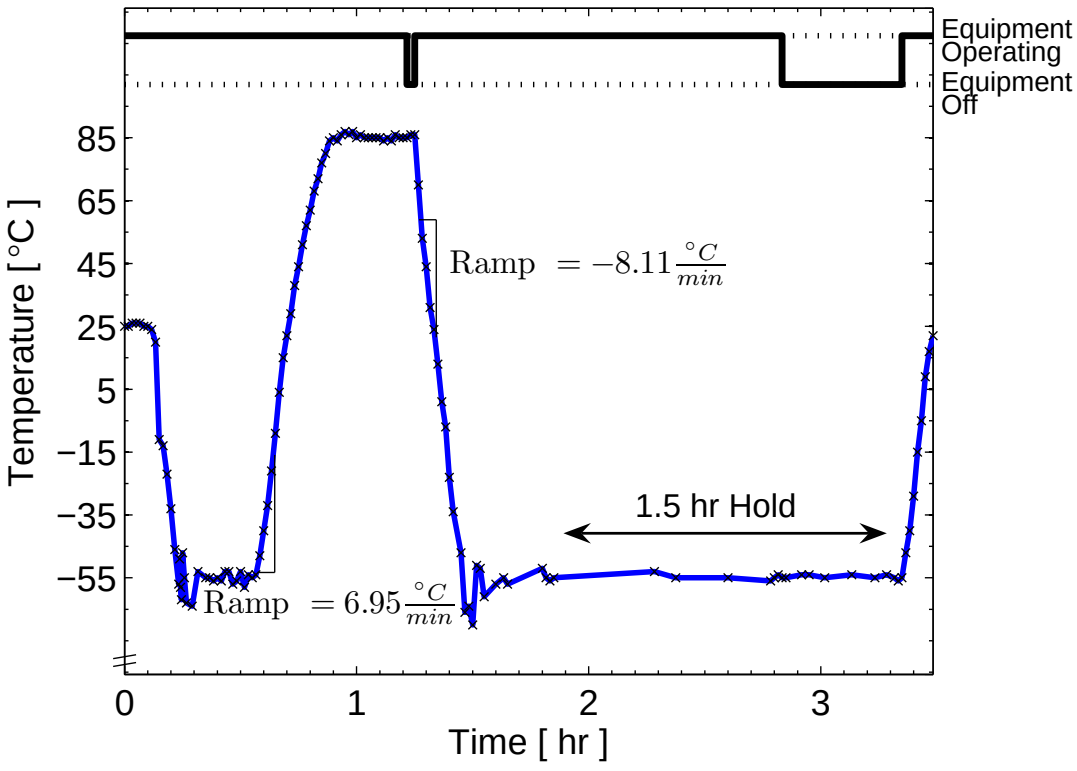

Figure 4-13: Experimental thermal shock test cycle (1 of 2 cycles) for node 0061.

4.3.4 Humidity

The humidity test determines the ability of a system to withstand natural or induced humid atmospheres [15]. The purpose of the test is to explore corrosion or other changes in equipment characteristics. For the test, the system is to be stabilized in a test chamber at $30°C$ and 85% relative humidity (RH). Over the next 2 hours, the temperature and humidity should be raised to $65°C$ and 95%RH, where it will be held for 6 hours. Over the next 16 hours, the chamber is to be reduced to $38°C$ with a RH of 85% or higher. This completes one cycle, and must be repeated ten times. One cycle of the nominal humidity test is illustrated in Fig. 4-14. The RH of the chamber should be held as close to 95% throughout the cycle, never going under $85\%RH$. Within 1 hour of completing all cycles, the system's performance should be evaluated. If the equipment is able to operate in the chamber, it should be operated the duration of the test with periodic performance checks. Systems requiring removal from the test chamber to conduct spot checks are allowed at the end of each cycle, where the spot-check is not to exceed 15 minutes.

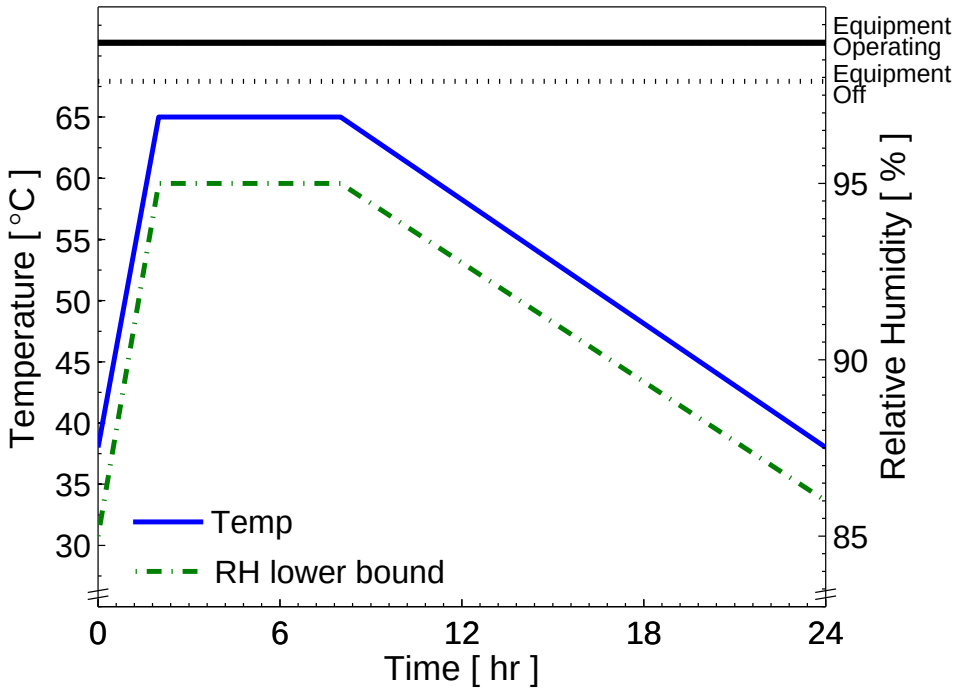

Figure 4-14: Nominal humidity test profile (1 of 10 cycles required).

A Blue M HR-361C high temperature/humidity chamber was used to conduct the humidity tests. Three nodes were placed on the middle shelf of the chamber and tested at the same time. The chamber was controlled by manually setting the desired dry-bulb and wet-bulb setpoints. The wet-bulb and dry-bulb controllers compared these setpoints to the current wet- and dry-bulb temperatures measured in the chamber. The chamber's controllers adjusted the power to the wet-bulb heater and dry-bulb heater to achieve the desired setpoints. An Omega HX93A RH/Temperature transmitter was installed in the test chamber to provide secondary measurements. The HX93A sensor was located on the wall of the chamber at the height of the nodes, with it's digital display and two $4-20\ mA$ outputs mounted outside the chamber. The digital display showed the temperature in degrees Fahrenheit and the humidity in percent relative humidity. Two precision resistors, with 265.9Ω resistance, were placed across the outputs of the transmitter to allow voltage measurement. The voltage was connected to a National Instruments DAQPad 6070E. The DAQPad 6070E connected to the laptop PC via a FireWire (IEEE 1394). An example continuous acquire and graph VI from LabVIEW was modified to output the scaled temperature and humidity outputs to a data file. The equations given in the HX93A User's Guide to scale the temperature and RH were:

$$^{\circ}C = (Measured\ mA - 4\text{mA}) \div 0.17\tfrac{mA}{^{\circ}C} - 20^{\circ}C$$

$$\%RH = (Measured\ mA - 4\text{mA}) \div 0.16\tfrac{mA}{\%RH}$$

Using Ohm's law with the value of the resistor and simplifying, the equations used in LabVIEW were:

$$^{\circ}C = 22.33\tfrac{^{\circ}C}{V}\ V_{Temp} - 46.75^{\circ}C$$

$$\%RH = 23.51\tfrac{\%RH}{V}\ V_{RH} - 25\%RH$$

The constant following the temperature was increased from $43.75^{\circ}C$ to account for a $3^{\circ}C$ calibration offset. An experimental temperature and relative humidity cycle is shown in Fig. 4-15 and the entire test (10 cycles) is shown in Fig. 4-16. The profiles

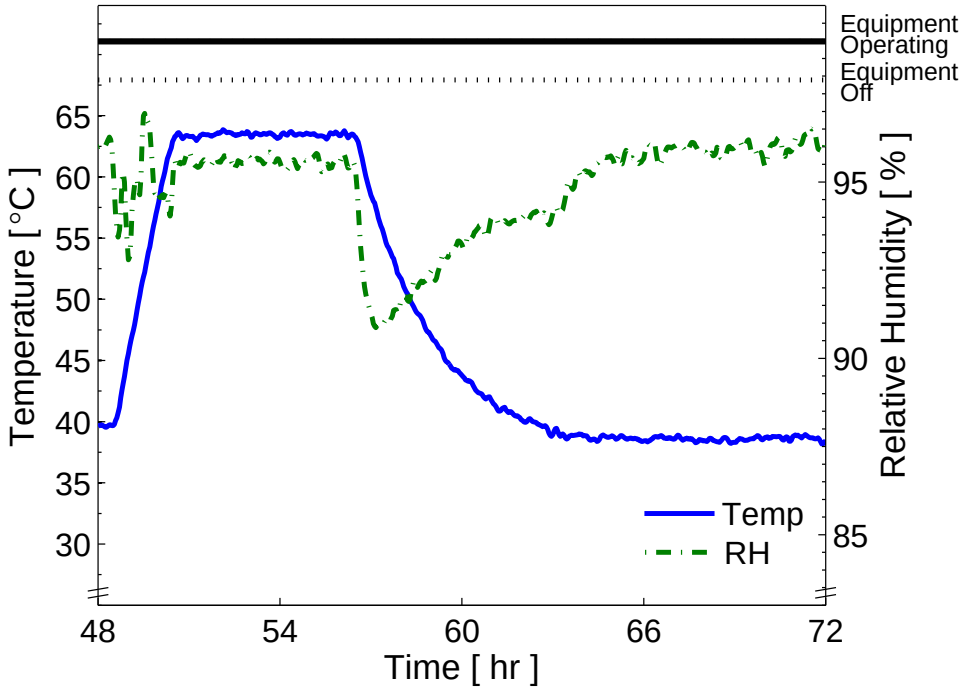

Figure 4-15: Experimental humidity single cycle profile for nodes 0016, 0021, and 0060.

for each of the 10 cycles are shown in Appendix A, figures A-12 through A-21. The performance of the nodes were tested during the up-ramp, at the beginning of the 6 hour hold, and at the end of the 6 hour hold before the temperature was decreased. To achieve the test profile for the humidity test, the setpoints were adjusted manually. The initial settings were $38°C$ dry-bulb temperature and $35.5°C$ wet-bulb temperature. This resulted in a relative humidity of $95\%RH$. These setpoints were increased $2.5°C$ every 10 minutes for 2 hours reaching a final setpoint of $65.0°C$ dry-bulb and $60.6°C$ wet-bulb. After the 6 hour hold the setpoints were lowered back to $38.0°C$ and $35.5°C$. The chamber slowly circulated in ambient air and lowered the temperature. These setpoints varied slightly day-to-day depending on the ambient conditions in the laboratory. The humidity chamber had an intake and exhaust port that allowed circulation of ambient air. The intake port was set to position 1, which was nearly closed, and the exhaust port damper was set to 100%. These settings minimized the ambient air circulation through the chamber, but still allowed the temperature in the chamber to fall to $38.0°C$ after the 6 hour hold. Filtered, demineralized spring water

was used in the humidity chamber.

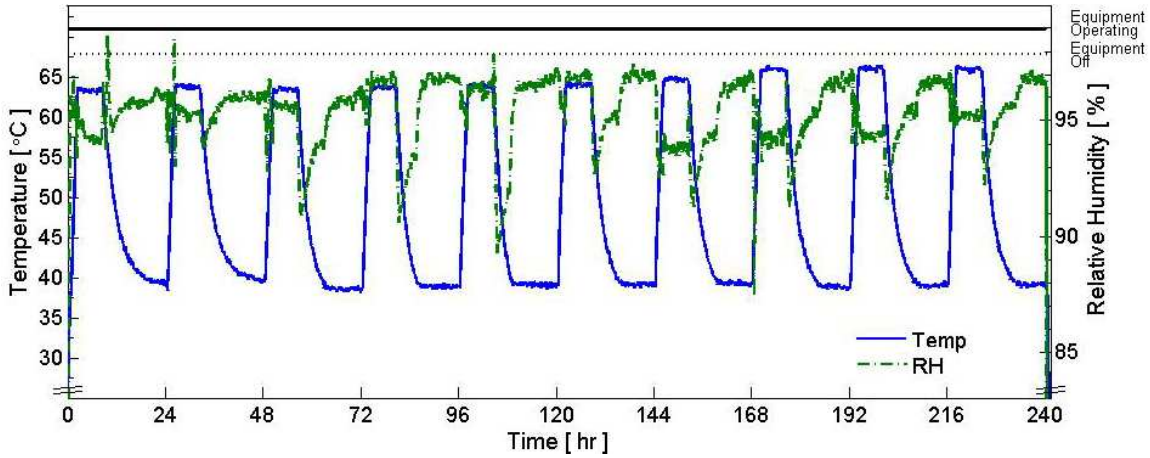

Figure 4-16: Experimental humidity test profile for nodes 0016, 0021, and 0060.

4.3.5 Fluid Susceptibility

The fluid susceptibility test determines if the system is compatible with exposure of common fluids used with aircraft. Such fluids include fuels, hydraulic fluids, lubricating oils, solvents and cleaning fluids, de-icing fluids, insecticides, disinfectants, coolant dielectric fluid, and fire extinguishants. The test should include all fluids which may contaminate the SHM system throughout its lifetime, including any fluid not mentioned. The test has two procedures: a spray test and an immersion test. All electrical connections should be attached, but power is only required during operation and assessment of the system.

For the spray test, the system should be sprayed one or more times a day to maintain a wetted condition. After a minimum of 24 hours of wetting, the system should be powered and operated for 10 minutes, then placed at a constant temperature of $65°C$ for 160 hours, unpowered. Afterward, the system should be returned to ambient conditions and then powered and operated for 2 hours. The system's performance is tested after the 2 hours. Fluids may be tested individually or mixed (if the fluids bases are the same).

For the immersion test, the system (including electrical connections) should be immersed in the fluid for 24 hours, after which, the system is powered and operated

for 10 minutes while still immersed. The system is then removed from the fluid and placed at $65°C$ for 160 hours, unpowered. Upon completion, the system is returned to ambient conditions then powered and operated for 2 hours before assessing the performance. The nominal test profile for both procedures is illustrated in Fig. 4-17. If the system passes the immersion test, the spray test is not necessary. Determination of the appropriate test procedure (spray or immersion) should be chosen dependent on the intended application of the system.

The immersion test was selected for the SHM system. The fluids were broken into two groups, water-based and oil-based. The fluids tested in the water-based group include: isopropyl alcohol, denatured alcohol, and Preston extended life antifreeze/coolant (ethylene glycol). The fluids tested in the oil-based group include: JetA fuel, AvGas, Mobil HyJet IV-A^{plus}, Mobil Aero HF, Mobil Aero HFA, Mobil Aero HFS, Exxon 20W-50 aviation oil, and Exxon Elite 20W-50 aviation oil. A basin was made of a 660 mm (26 $in.$) length of 72 mm (3 $in.$) Schedule 40 PVC pipe. An end-cap was glued on using PVC primer and cement. Three test specimens were

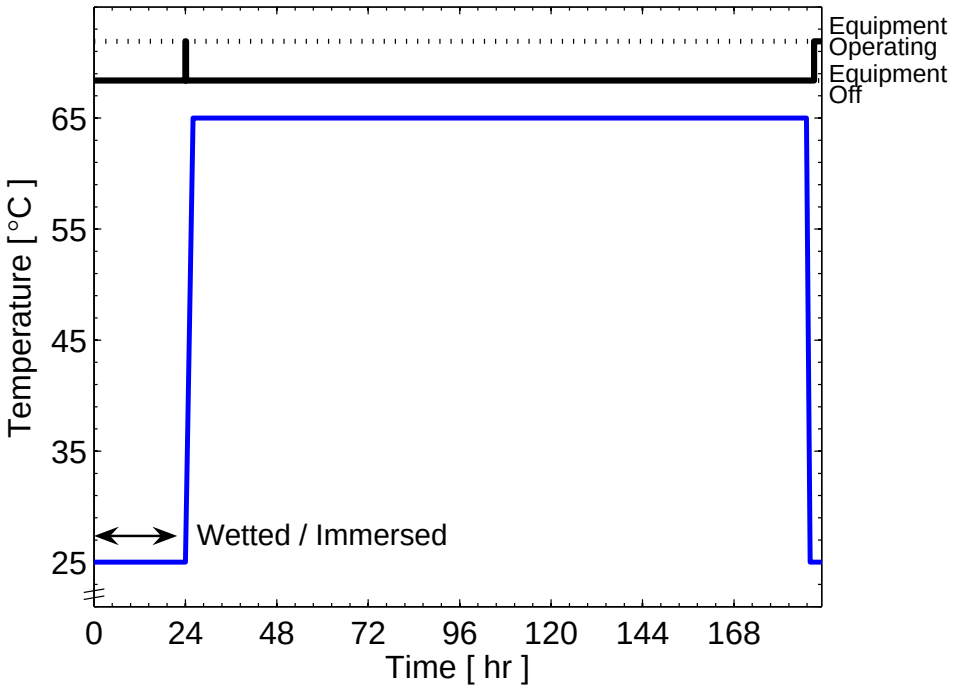

Figure 4-17: Nominal fluid susceptibility test profile.

inserted, with USB cables connected, in the tube. The tube was vertically held with a beaker stand and clamp, as shown in Fig. 4-18. Glass marbles were placed in the tube to minimize the required fluid volume. The marbles filled the PVC tube to the bottom of the nodes. The mixed oil-based fluids were poured into the tube and allowed to soak for 24 hours. After the soak, the three nodes were powered and operated for 10 minutes. The specimens were then powered-off and placed in a Blue M post-cure oven. The temperature in the oven was held at $65.0°C$. The PVC pipe was then cleaned out using acetone before repeating the above process with the mixture of water-based fluids. Each group remained in the oven for 160 hours before being removed. After ambient conditions were reestablished, the nodes were powered and operated for 2 hours. Performance of each node was then assessed. The experimental test profiles are given in Appendix A, Figures A-22 and A-23.

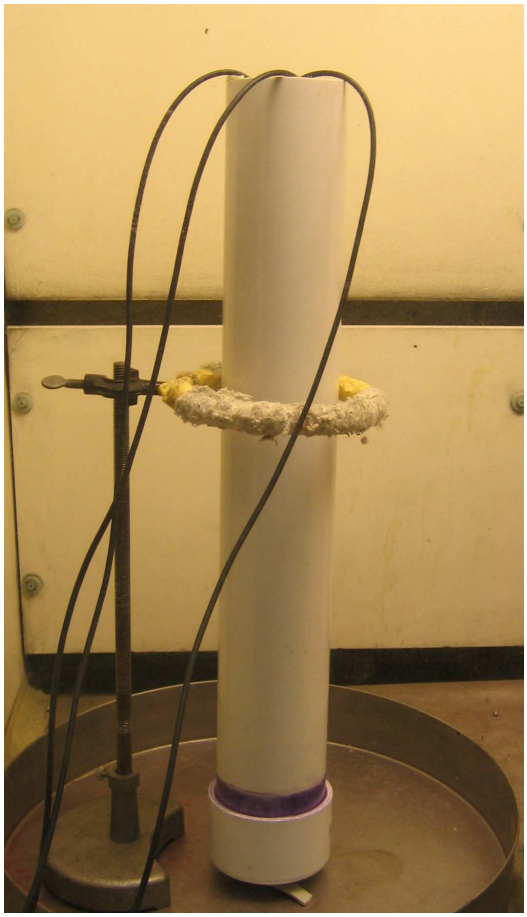

Figure 4-18: Fluid susceptibility test basin in fume hood with USB cables connected to nodes.

4.3.6 Altitude (Pressure)

The altitude test will determine if the SHM system can withstand and/or function in an extreme altitude environment. The test is broken into three categories: low-pressure, rapid decompression, and overpressure. The system should be inspected for leakage of gases or fluids from enclosures, deformation, rupture, explosion of sealed containers, overheating of devices due to reduced heat transfer, and erratic operation. The extreme altitudes are defined as $-4,572\ m$ $(-15,000\ ft)$ and $21,336\ m$ $(70,000\ ft)$ which corresponds to 170 kPa (25 $psia$) and 4.4 kPa (0.64 $psia$), respectively.

During the low-pressure test, the system is to be ramped from ambient conditions to the minimum operating pressure (corresponding to maximum operating altitude) of the vehicle. The ramp rate is not specified, but the pressure change should not be instantaneous. The equipment is allowed to stabilize and then this pressure (altitude) is held for a minimum of 2 hours. During the hold, the performance of the system should be assessed. After the hold, the pressure should be returned to ambient conditions. The system should be assessed for degradation. The nominal test profile for the low-pressure test is shown in Fig. 4-19.

The rapid decompression test is to simulate a damage event to an aircraft. Begin the test by operating the SHM system at ambient conditions. Gradually lower the pressure to 75.2 kPa (11 $psia$), equivalent to an altitude of $2,438\ m$ $(8,000\ ft)$. Allow the system to stabilize. Reduce the pressure to the the equivalent maximum operating altitude of the vehicle. The extreme case calls for virtually instantaneous decompression, however, the decompression must take no longer than 15 seconds. Operate the system for a minimum of 10 minutes at the operating high altitude, conducting functional tests of the system. Return the pressure to ambient conditions. After the equipment has stabilized at the ambient conditions, test the system for degradation. The nominal test profile is illustrated in Fig. 4-20.

The overpressure test is conducted with the system not powered. From ambient conditions, ramp the pressure to 170 kPa (25 $psia$), equivalent to $-4,572\ m$

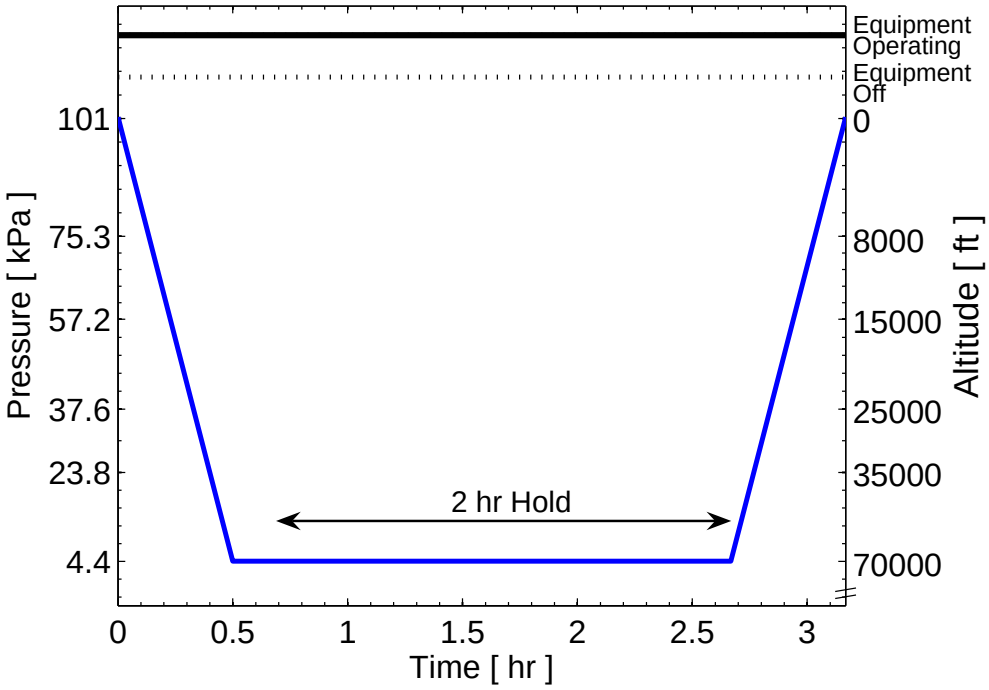

Figure 4-19: Nominal altitude test profile.

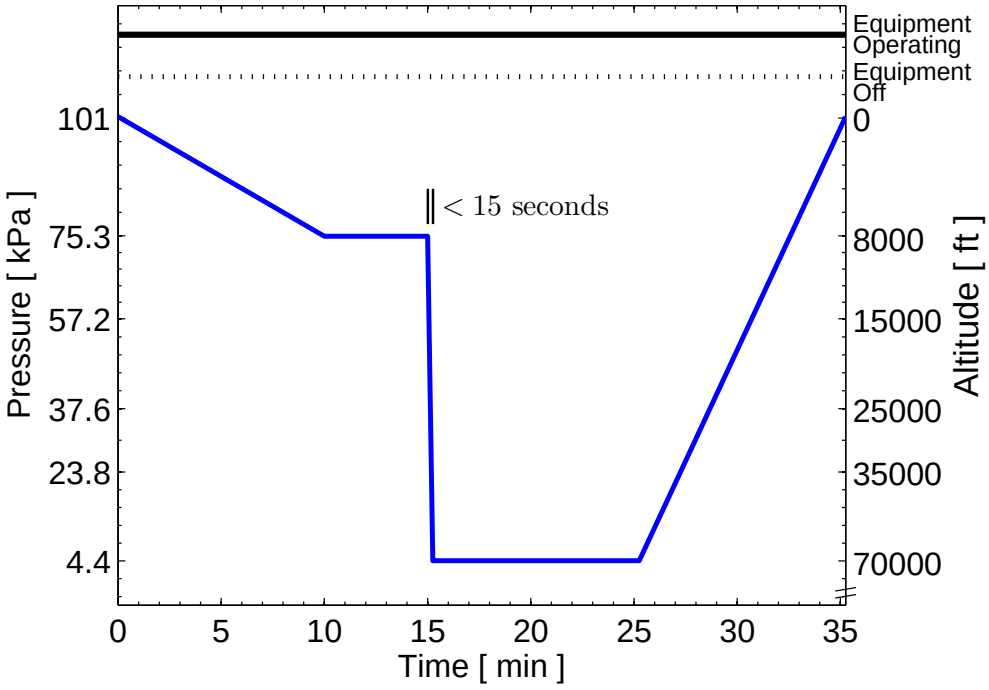

Figure 4-20: Nominal decompression test profile.

$(-15,000\ ft)$ altitude. Hold for a minimum of 10 minutes, then return to ambient conditions. Assess the performance of the SHM system. The nominal overpressure test profile is illustrated in Fig. 4-21.

To conduct the low-pressure and rapid decompression tests, a vacuum chamber was constructed from a 25 inch long $1\frac{1}{4}$ inch diameter Schedule 40 PVC pipe. Both ends of the PVC pipe were reduced to $\frac{3}{8}$ inch compression fittings, and vacuum tubing was attached. The reducers were threaded to allow installation and removal of the test specimen. From one end of the pipe, the vacuum tube was attached to a Heise absolute pressure gauge. The dial gauge had a resolution of $\pm 0.1\ psia$. From the other end of the pipe, the vacuum tube was attached to a tee. Off the tee were two valves. One valve opened or closed the connection to the vacuum pump. The other valve served as a bleed valve to the atmosphere which was used to manually control the test pressure. A $\frac{7}{16}$ inch hole was drilled through the PVC tube to allow connection of the USB cable with the node. Vacuum tape was used to seal the hole after installing the cable. A 4 foot length of 3 inch PVC pipe was sealed and connected to the system

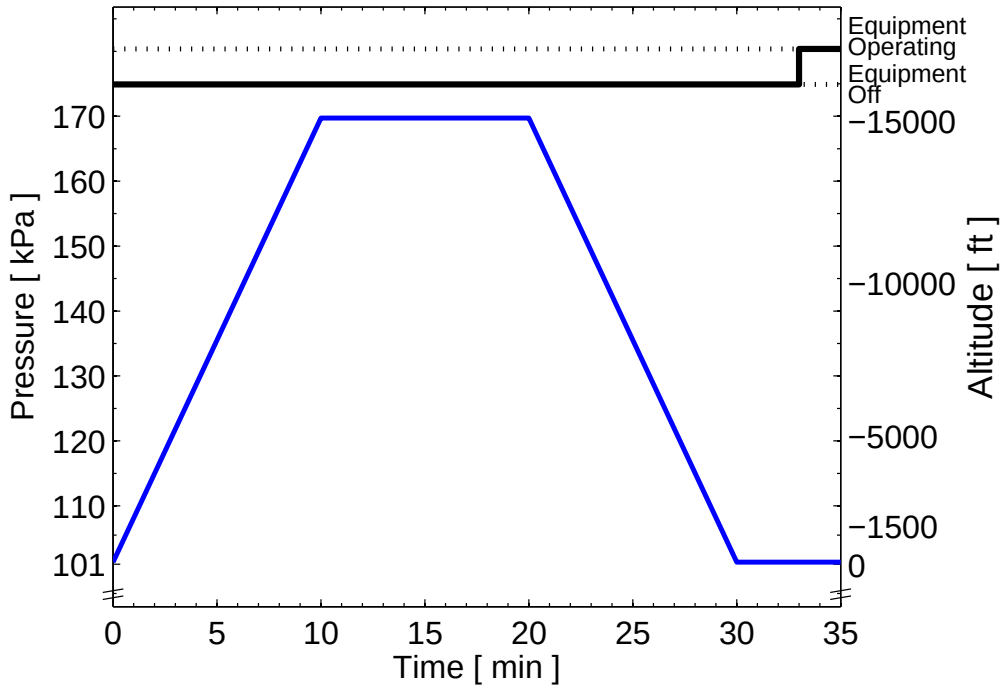

Figure 4-21: Nominal overpressure test profile.

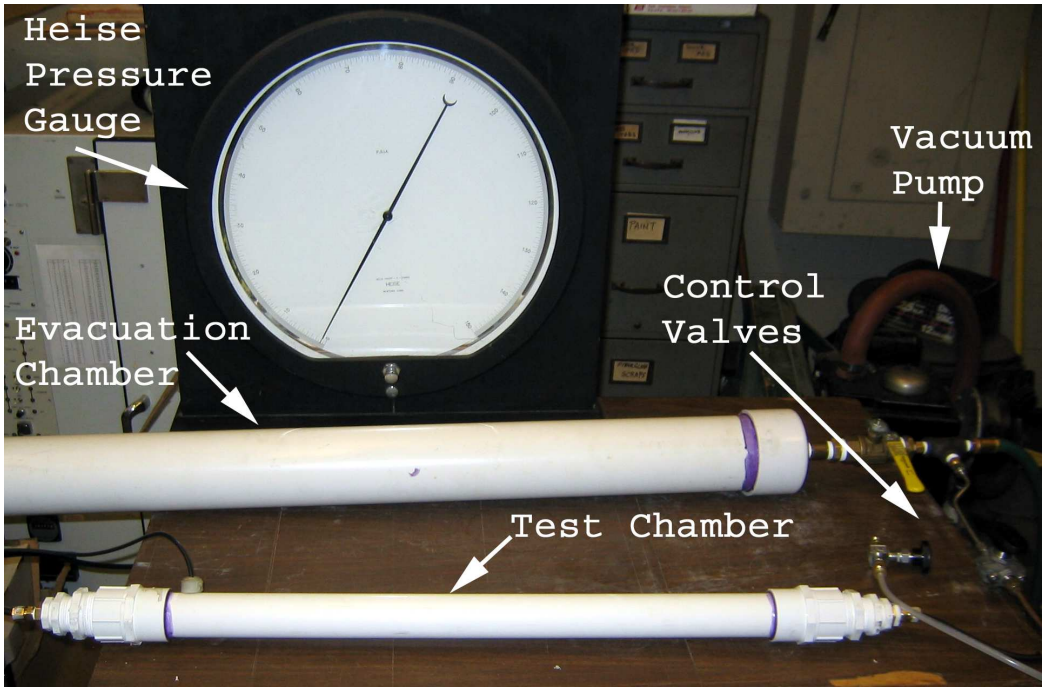

Figure 4-22: Low-pressure and rapid decompression test setup.

to serve as an evacuation chamber. However, the evacuation chamber was not used during testing because of the fast response of the vacuum pump.

The test specimens were installed one at a time and the test was conducted. The individual pressure profiles for each node are included in Appendix A, figures A-24 through A-29. For the rapid decompression tests, the pressure change from 75.3 kPa to 4.4 kPa occurred in 7 seconds.

The overpressure test was conducted in an autoclave. The Heise pressure gauge was used to monitor the pressure. Three test specimens were placed on a flat self and the autoclave was sealed. The pressure was raised in the autoclave chamber to 170 kPa (25 $psia$). Due to the leak rate of the autoclave at this pressure, the pressure oscillated between 169 kPa and 176 kPa (24.5 $psia$ and 25.5 $psia$). This oscillation appeared to be constant and was recorded over three periods as shown in Fig. 4-23. After the 10 minute hold at pressure, ambient conditions were returned and the node's performance were assessed.

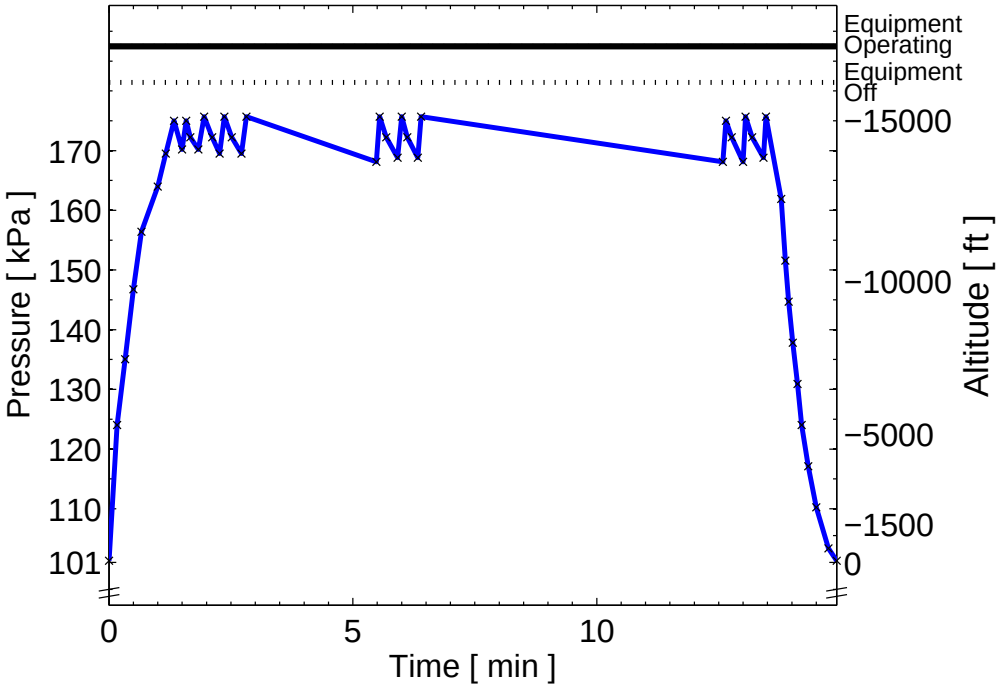

Figure 4-23: Experimental overpressure test profile for nodes 0011, 2586, and 2601.

4.3.7 Static Strain

The purpose of the static-strain test is to simulate normal strain levels experienced during operation of the aircraft. The coupon was installed in a $100k\ lbf$ MTS tensile-compression testing machine with an Instron controller, Fig. 4-24. The specimen was loaded in the machine and gripped past the boundary clamps. An axial displacement was then applied and the resulting tensile load was recorded. The displacement was increased to produce steps of 2.2 kN axial load until a stress (275 MPa) near yield ($\sim$ 330 MPa) was reached. The displacement was held constant while the SHM system underwent functional tests. The displacement was then stepped back down (increments = 4.4 kN) until the specimen was unloaded, with functional tests being preformed at each step. The experimental load-time curve illustrating this process is shown in Fig. 4-25. After the test, the bond between the sensor and aluminum was visually inspected for delamination/degradation.

Figure 4-24: MTS testing machine with Instron controller. Test specimen is loaded in the test machine's hydraulic grips.

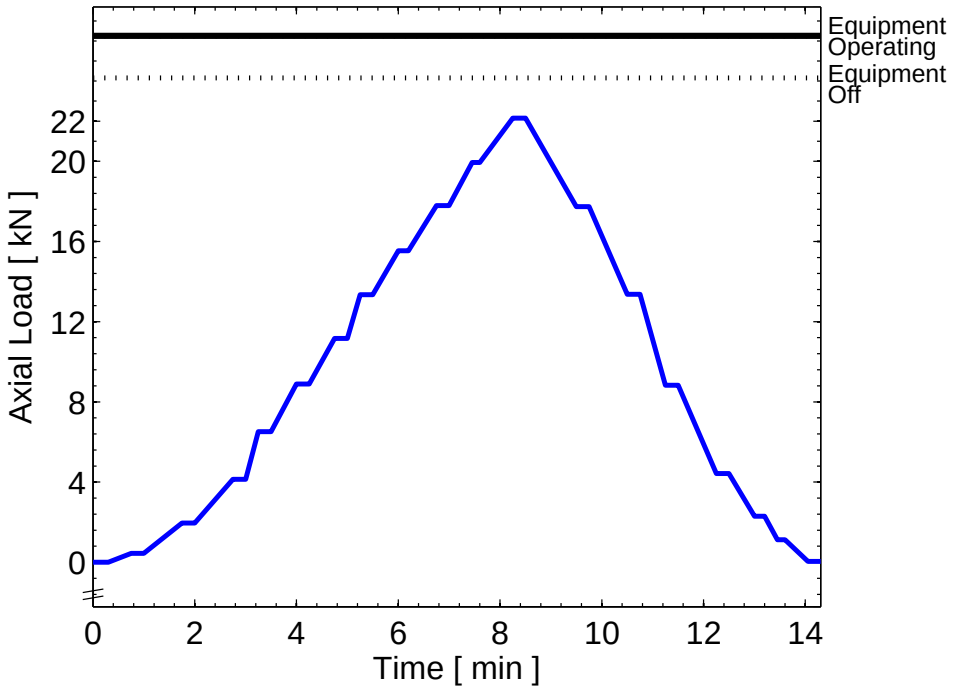

Figure 4-25: Experimental static-strain loading profile of node 0017.

Chapter 5

Results and Discussion

Experimental results for the environmental testing of Lamb-wave based SHM nodes are presented in this chapter. The format of the data files and the code used to process the files is first described. Example signals are then explained before presenting the results of the nine environmental tests conducted during this work. A table summarizing the test results is presented at the end of the chapter. Detailed test data for each node is included in Appendix B.

The M.E.T.I.-System software described in Section 4.2 generates a comma-separated value (CSV) file that contains node settings and the test data. An abridged data file from a high-temperature test is shown in Fig. 5-1. The first two columns of the file contain the settings used during the test, as input by the user to the software at the start of the data acquisition. The remaining columns, in sets of two, contain the acquired test data (voltages). The first of the two columns contains the pulse voltage data and the second column contains the sensed voltage data. The first two rows for each new column contain the test type (pre-test, operational test, or post-test), testing notes entered by the user, and the start time of the acquisition. The remaining rows contain the raw voltage data sent from the node. Two new columns are added to the file each time test data is sampled.

The voltage for each signal is sampled at 1 MHz, the set acquisition frequency. 16 voltage sets, each 800 points long (800 μs of data), are taken in rapid succession and are averaged on the node's microprocessor before being transmitted to the software.

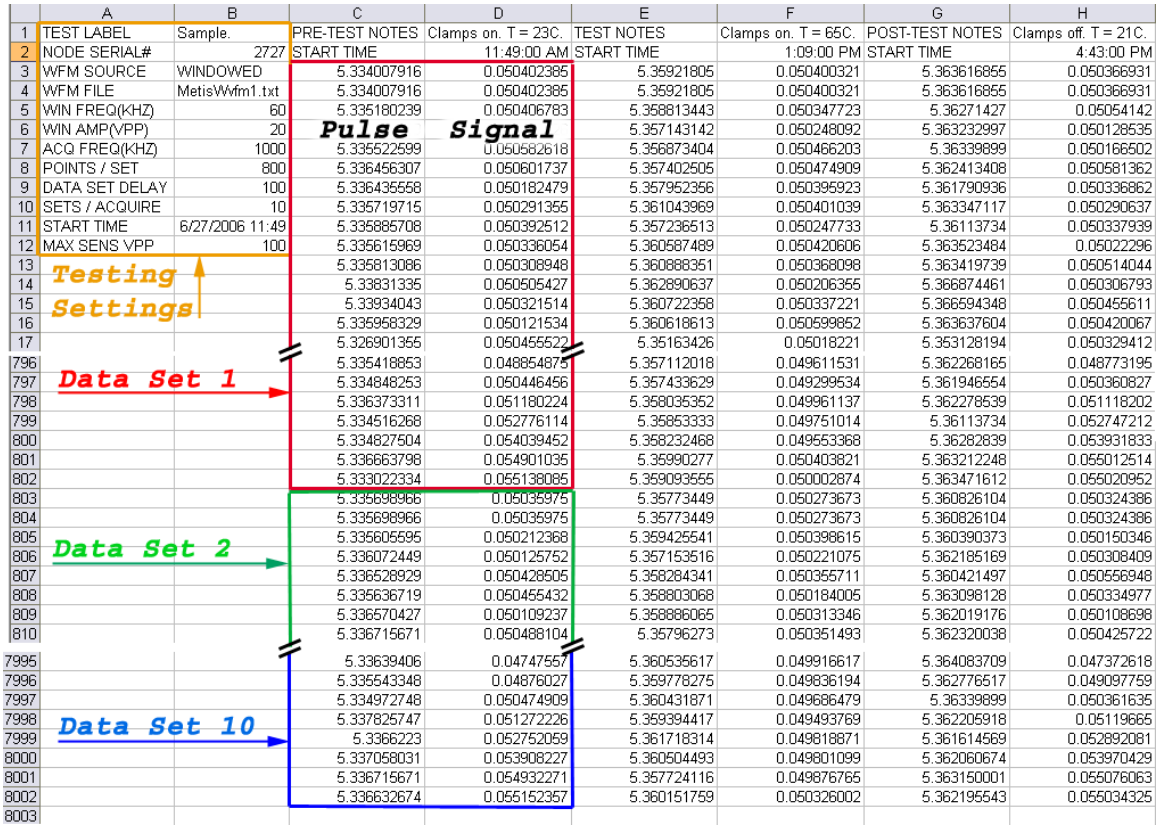

	A	B	C	D	E	F	G	H
1	TEST LABEL	Sample.	PRE-TEST NOTES	Clamps on. T = 23C.	TEST NOTES	Clamps on. T = 65C.	POST-TEST NOTES	Clamps off. T = 21C.
2	NODE SERIAL#	2727	START TIME	11:49:00 AM	START TIME	1:09:00 PM	START TIME	4:43:00 PM
3	WFM SOURCE	WINDOWED	5.334007916	0.050402385	5.35921805	0.050400321	5.363616855	0.050366931
4	WFM FILE	MetisWvfm1.txt	5.334007916	0.050402385	5.35921805	0.050400321	5.363616855	0.050366931
5	WIN FREQ(KHZ)	60	5.335180239	0.050406783	5.358813443	0.050347723	5.36271427	0.05054142
6	WIN AMP(VPP)	20	5.335522599	0.050582618	5.357143142	0.050248092	5.363232997	0.050128535
7	ACQ FREQ(KHZ)	1000	5.336456307	0.050601737	5.356873404	0.050466203	5.36339899	0.050166502
8	POINTS / SET	800	5.336435558	0.050182479	5.357402505	0.050474909	5.362413408	0.050581362
9	DATA SET DELAY	100	5.335719715	0.050291355	5.357952356	0.050395923	5.361790936	0.050336862
10	SETS / ACQUIRE	10	5.335885708	0.050392512	5.361043969	0.050401039	5.363347117	0.050290637
11	START TIME	6/27/2006 11:49	5.335615969	0.050336054	5.357236513	0.050247733	5.36113734	0.050337939
12	MAX SENS VPP	100	5.335813086	0.050308948	5.360587489	0.050420606	5.363523484	0.05022296
13			5.33831335	0.050505427	5.360888351	0.050368098	5.363419739	0.050514044
14			5.33934043	0.050321514	5.362890637	0.050206355	5.366874461	0.050306793
15			5.335958329	0.050121534	5.360722358	0.050337221	5.366594348	0.050455611
16			5.326901355	0.050455522	5.360618613	0.050599852	5.363637604	0.050420067
17			5.335418853	0.048854875	5.35163426	0.05018221	5.353128194	0.050329412
796			5.334848253	0.050446456	5.357112018	0.049611531	5.362268165	0.048773195
797			5.336373311	0.051180224	5.357433629	0.049299534	5.361946554	0.050360827
798			5.334516268	0.052776114	5.358035352	0.049961137	5.362278539	0.051118202
799			5.334827504	0.054039452	5.35853333	0.049751014	5.36113734	0.052747212
800			5.336663798	0.054901035	5.358232468	0.049553368	5.36282839	0.053931833
801			5.333022334	0.055138085	5.35990277	0.050403821	5.363212248	0.055012514
802			5.335698966	0.05035975	5.359093555	0.050002874	5.363471612	0.055020952
803			5.335698966	0.05035975	5.35773449	0.050273673	5.360826104	0.050324386
804			5.335605595	0.050212368	5.35773449	0.050273673	5.360826104	0.050324386
805			5.336072449	0.050125752	5.359425541	0.050398615	5.360390373	0.050150346
806			5.336528929	0.050428505	5.357153516	0.050221075	5.362185169	0.050308409
807			5.335636719	0.050455432	5.358284341	0.050355711	5.360421497	0.050556948
808			5.336570427	0.050109237	5.358803068	0.050184005	5.363098128	0.050334977
809			5.336715671	0.050488104	5.358886065	0.050313346	5.362019176	0.050108698
810			5.33639406	0.04747557	5.35796273	0.050351493	5.362320038	0.050425722
7995			5.335543348	0.04876027	5.360535617	0.049916617	5.364083709	0.047372618
7996			5.334972748	0.050474909	5.359778275	0.049836194	5.362776517	0.049097759
7997			5.337825747	0.051272226	5.360431871	0.049686479	5.36339899	0.050361635
7998			5.3366223	0.052752059	5.359394417	0.049493769	5.362205918	0.05119665
7999			5.337058031	0.053908227	5.361718314	0.049818871	5.361614569	0.052892081
8000			5.336715671	0.054932271	5.360504493	0.049801099	5.362060674	0.053970429
8001			5.336632674	0.055152357	5.357724116	0.049876765	5.363150001	0.055076063
8002					5.360151759	0.050326002	5.362195543	0.055034325
8003								

Figure 5-1: Sample CSV data file created from the M.E.T.I.-System software. This file has been abridged (some columns removed and titles changed) from a high-temperature test. The CSV file was opened in Excel. Illustrations have been overlaid on the file image to highlight the testing settings and one data acquisition.

The node pauses for 100 *ms* before sampling the next data set. This process is repeated until 10 data sets are transmitted to the software. The software writes the data to the specified CSV file, stacking the 10 data sets (resulting in two columns with 8002 rows). The 10 stacked data sets for the pre-test pulse signal and sensed signal are shown in Fig. 5-1, columns C and D (partial data sets shown).

A MATLAB code (see Appendix F) was developed to analyze the experimental test files. The code reads the specified CSV file and creates a matrix populated with the contents of the CSV file. The user then specifies the three columns containing the baseline, operational, and post-test signals. The user can also specify a specific data set to analyze or choose to average the 10 data sets. The code then creates two new matrices, one containing the pulse data for the three tests (baseline, operational, and post-test) and one containing the sensed data for the three tests. The

six signals (3 pulse signals and 3 sensed signals) are then zeroed to their respective mean. A Hilbert transform is then used to create signal envelopes that capture the wavepackets. These envelopes contained high-frequency components which are eliminated using a 20-point forward and reverse (zero-phased) averaging filter. The peak voltage along with its location for each signal is then determined. A threshold is applied to eliminate the weak signal noise [25]. The threshold value was set to 18% of the sensed signal envelope's peak voltage. This value seperates the wavepackets from the low-voltage noise. Envelope values below the threshold are set to zero. The peaks of each wavepacket are then found by looking for changes in sign of the filtered envelope's slope. The sensed signal wavepackets' peak voltages and respective time-of-flight are captured. Once all signal processing is complete, all test times are shifted to have the peak of the pulse signal occur at time zero. The code then plots the pulse, baseline, operational, and post-test signals. On each of the four plots, the envelope is shown as a dotted ($\cdots$) line and the peak wavepacket voltages are displayed as upsidedown triangles ($\bigtriangledown$). An example of these plots is shown in Fig. 5-2, the humidity test signals for node 0060. The code also produces a plot with three calculated envelopes (baseline, operational, post-test), an example shown in Fig. 5-3 for the humidity test of node 0060. The top half of the envelope is shown since the envelopes are symmetric about zero voltage. The code then computes and outputs the TOF and voltage metric data. The MATLAB code used to analyze the experimental test data is discussed in detail and presented in Appendix F.

An example pulse and sensed signal are shown in Fig. 5-4. The two signals are the excitation pulse sent to the actuator and the baseline sensed signal for the humidity test for node 0060. These signals display the entire 800 points collected. For this work, no usable wavepackets were discovered after 500 μs. Therefore, for all results included in this work, the signals are only displayed to 500 μs. The pulse signals exhibited very small variations from test to test. The pulses from the baseline, operational, and post-test signal for the humidity test are overlapped in Fig. 5-4a. As can be seen, there is no visible change in the three sent pulses, with the peak voltage occurring at the same time in each. Therefore, the baseline pulse was used for each test to set

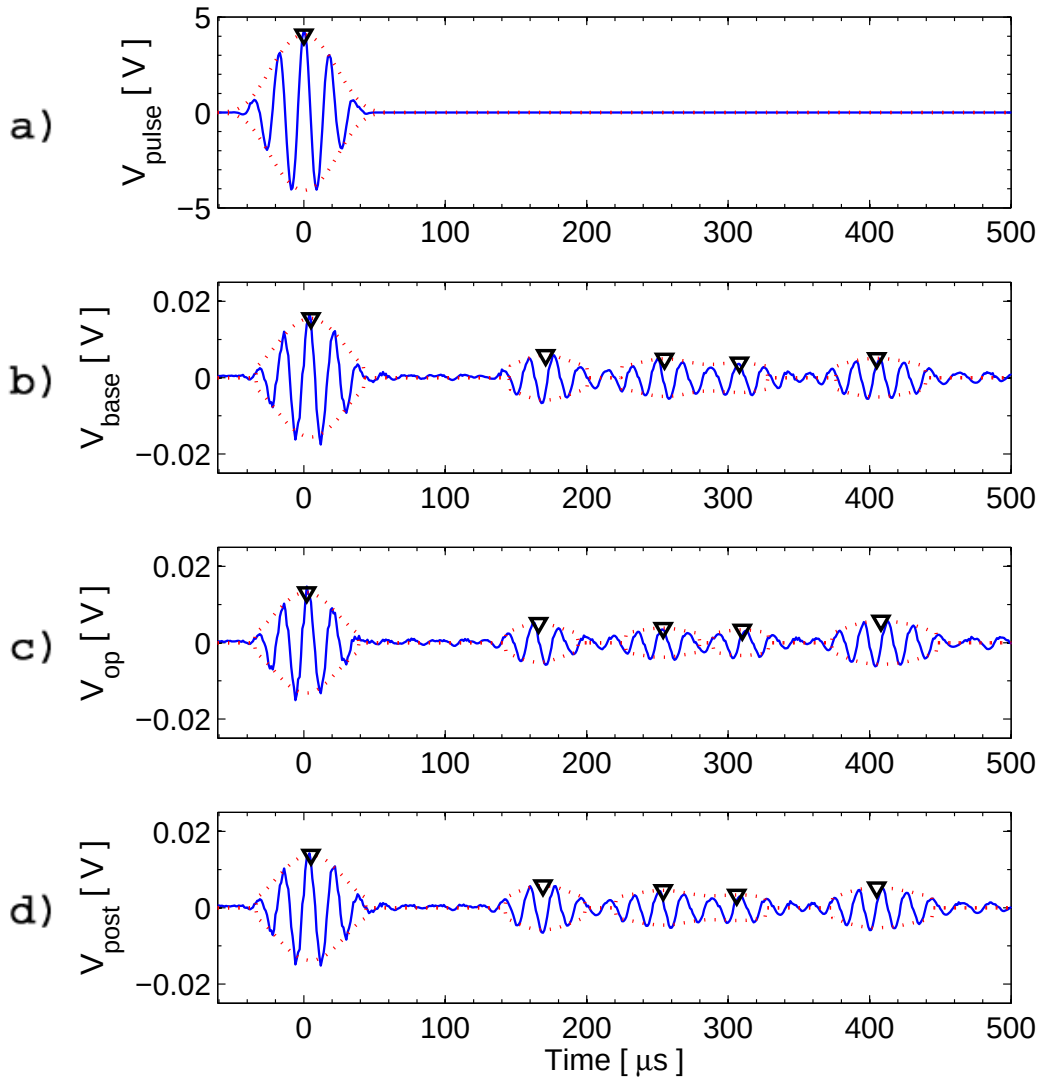

Figure 5-2: Example test signal plots. a) Excitation pulse, b) baseline signal, c) operational signal, d) post-test signal. Envelopes shown as dotted ($\cdots$) lines and peak voltages shown as triangles ($\bigtriangledown$).

the zero time. Circled on the sensed signal plot, Fig. 5-4b, is the initial wavepacket received directly from the actuator (labeled 1) and the antisymmetric (A_0) mode reflection from the near boundary clamp (labeled 2). These wavepackets are used for analyzing the delta metrics of the operational and post-test signal deviations from the baseline. The wavepackets occurring after the near-boundary clamp reflection,

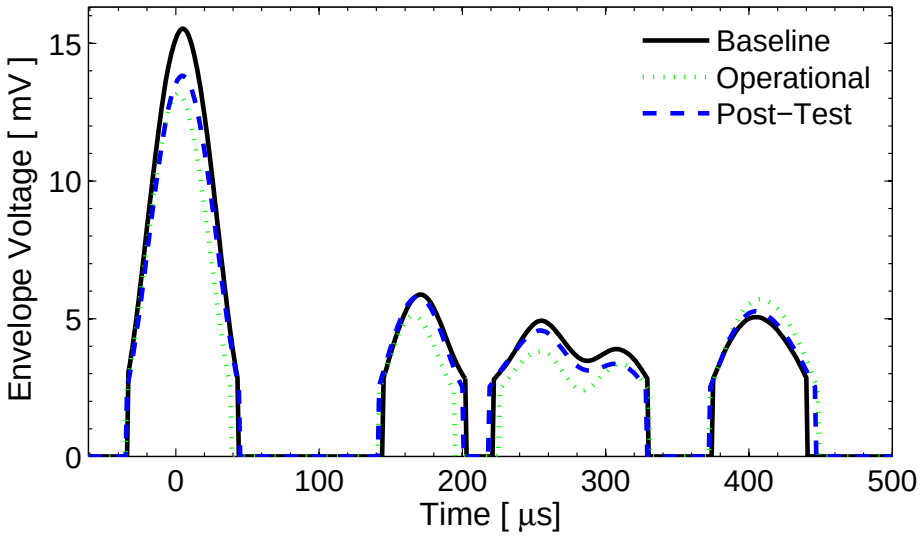

Figure 5-3: Example plot showing sensed baseline, operational, and post-test envelopes.

wavepacket 2, contain relevant information about the structure, however, due to the complexities of multiple Lamb-wave modes interacting, the data is not assessed in this work. The first two wavepackets are used with the delta metrics to determine the TOF difference and the peak voltage change between the baseline signal and the operational and post-test signals to assess node performance. The percentage variance ($\pm$) listed in the metric result tables (*e.g.,* Table 5.1) and in the sections that follow is the standard deviation over the 3 samples.

5.1 High-temperature Test Results

The high-temperature test was conducted as described in Section 4.3.1 with nodes 0026, 0036, and 0041. The recorded data from these tests are shown in Appendix B, Figures B-1, B-3, and B-5. The excitation pulse frequency for the high-temperature tests was 65 kHz, different than the standard frequency of 60 kHz. There was also no on-node averaging of the test signals and data was sampled for 1.0ms (1000 points). The reason for the testing differences was that the high-temperature and static-strain tests were the first of the environmental tests to be conducted. After analyzing the

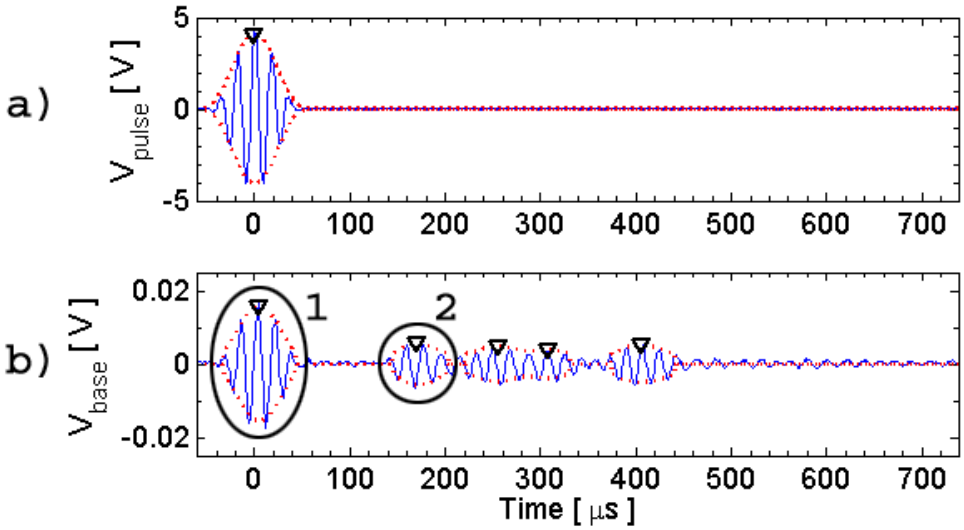

Figure 5-4: Example pulse and sensed signal. a) Baseline, operational, and post-test excitation pulses overlapped. b) Baseline sensed signal with direct wavepacket (1) and near boundary reflection wavepacket (2) circled.

data from these tests, the testing settings were refined to 60 kHz actuating frequency and 16 data set on-node averaging.

The wavepacket envelopes for the high-temperature baseline, operational, and post-test signals of node 0026 are shown in Fig. 5-5. As can be seen, the envelopes of the first wavepacket are only slightly affected by the high-temperature test. A trend was noted that the wavepackets from the reflections of the operational signals were below the threshold. Because of this, only one of the three nodes tested had a detected second wavepacket for the operational signal. For all three tests, the post-test signal had a decrease in peak voltage of both wavepackets. Node 0036 had irregular results in that only the first wavepackets from the baseline and operational tests were detected. Also, node 0036 was the only node of this work to have a large increase (77%) in a signal compared to the baseline. These irregularites could be due to many effects including poor bonding or a defective node. The post-test envelope of node 0036 shows multiple wavepackets, but this is due to the small peak voltage in the first wavepacket resulting in a low threshold cutoff value.

The first and second baseline wavepackets had averaged times-of-flight of 2.3 $\mu s \pm$ 1 μs and 172.5 $\mu s \pm 1$ μs, respectively, and averaged peak voltages of 11.4 $mV \pm 15$ μV

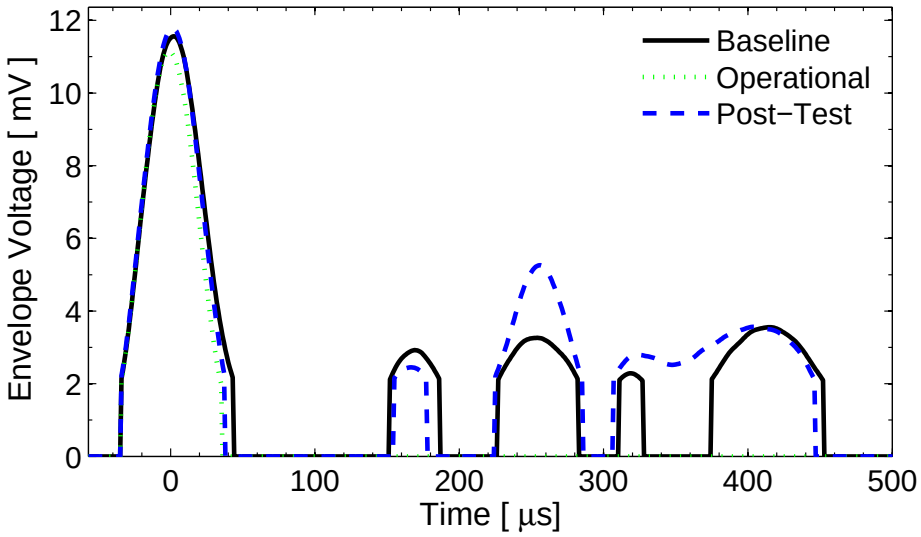

Figure 5-5: High-temperature test envelopes for node 0026. Operational signal at $85°C$ (time=3 hrs).

and 3.2 $mV \pm 15\ \mu V$, respectively. Calculating the TOF metric between the baseline wavepackets and the post-test wavepackets gives an average change of $22.2\% \pm 63.1\%$ between the first wavepacket and $-2.0\% \pm 1.3\%$ for the second wavepacket. Calculating the voltage metric gives an average change of $-30.6\% \pm 29.0\%$ for the first wavepacket and $-28.2\% \pm 17.0\%$ for the second wavepacket. The metric values have been averaged over the three high-temperature tests. The node specific metrics are listed in Appendix B, Tables B.1, B.2, and B.3. The three nodes tested survived the high-temperature test. There were no visual changes to the node or the adhesive. It was noted during each test that the shear couplant became viscous at the elevated temperatures and flowed from the boundary clamps. This likely partially explains the change in the voltage metric between the baseline and post-test.

5.2 Low-temperature Test Results

The low-temperature tests were conducted following the procedures described in Section 4.3.2 for nodes 0029, 0049, and 0068. The recorded test signals from these tests are shown in Appendix B, Figures B-7, B-9, and B-11. The wavepacket envelopes

for the low-temperature test of node 0029 are shown in Fig. 5-6. As can be seen in the figure, slight voltage changes of the two wavepackets were experienced between the baseline and post-test signals. The operational voltage had much more degradation, however, the wavepackets maintained their general shape and times-of-flight. The operational test data for nodes 0049 and 0068 were lost due to a somewhat reoccurring problem with the software. The communication between the PC and the node would be intermittently lost causing the software to crash and the software-stored data to be lost. It was noted during each of the low-temperature tests that condensation formed on the cold aluminum samples and as the temperature was returned to ambient, some of the water-soluble shear gel would dissolve. Overall, the low-temperature had a temporary degradation effect on the system that was largely recovered when ambient conditions were reestablished.

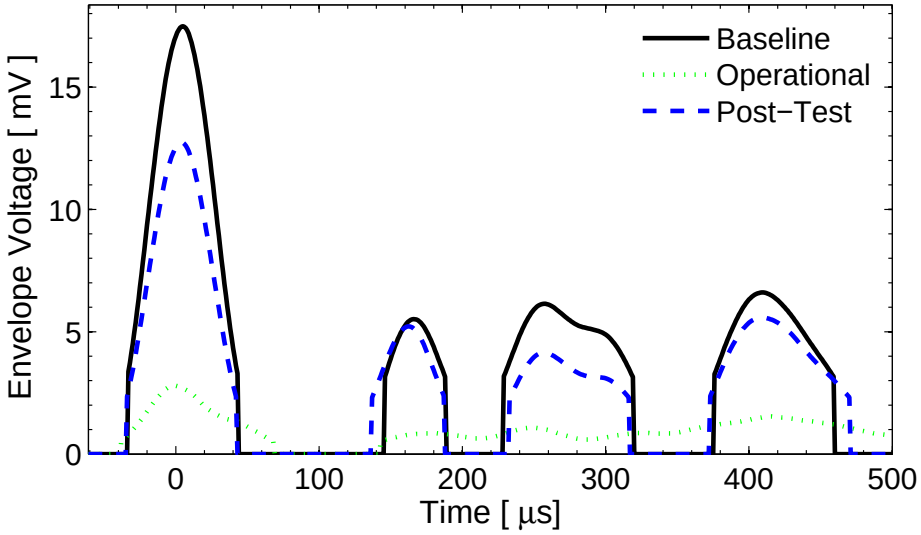

Figure 5-6: Low-temperature test envelopes for node 0029. Operational signal at $-55°C$ (time=1 hrs).

The first and second baseline wavepackets had averaged times-of-flight of 4.7 $\mu s \pm$ 1 μs and 168.0 $\mu s \pm 1$ μs, respectively, and averaged peak voltages of 17.8 $mV \pm 15$ μV and 5.6 $mV \pm 15$ μV, respectively. Calculating the TOF metric between the baseline wavepackets and the post-test wavepackets gives an average change of $-15.0\% \pm$ 13.2% between the first wavepacket and $-1.0\% \pm 1.4\%$ for the second wavepacket.

Calculating the voltage metric gives an average change of $-8.1\% \pm 17.0\%$ for the first wavepacket and $2.7\% \pm 19.0\%$ for the second wavepacket. The metric values have been averaged over the three low-temperature tests. The node specific metrics are listed in Appendix B, Tables B.4, B.5, and B.6.

5.3 Thermal Shock Test Results

The thermal shock test followed the testing procedures described in Section 4.3.3 for nodes 0034, 0046, and 0061. The recorded test signals from these tests are shown in Appendix B, Figures B-13, B-15, and B-17. A decrease in the wavepacket voltages was noted on two of the three tests. The third test, node 0061, had a slight increase in voltage in all wavepackets. As with the low-temperature test, condensation formed while the aluminum was cold and caused the shear gel to dissolve. Also, during the high-temperature cycles, the shear gel became viscous and flowed from the boundary clamps. However, upon post-test inspection, no damage to the nodes was noted and some shear gel remained between the boundary clamps and aluminum samples. The thermal shock test envelopes for node 0046 are shown in Fig. 5-7

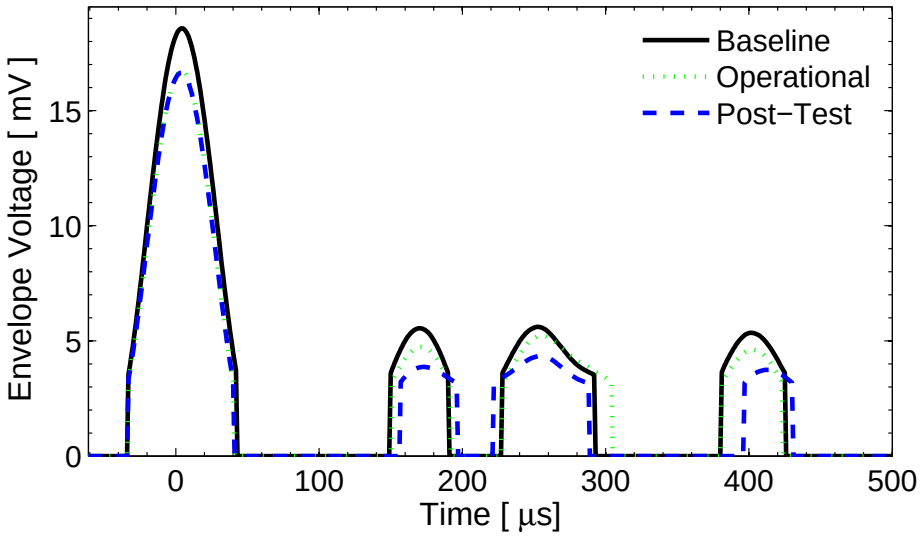

Figure 5-7: Thermal shock test envelopes for node 0046. Operational signal at $24°C$ (time=3.7 hrs).

The first and second baseline wavepackets had averaged times-of-flight of 5.0 $\mu s \pm$ 1 μs and 173.3 $\mu s \pm 1$ μs, respectively, and averaged peak voltages of 18.5 $mV \pm 15$ μV and 6.3 $mV \pm 15$ μV, respectively. Calculating the TOF metric between the baseline wavepackets and the post-test wavepackets gives an average change of $-1.2\% \pm 26.8\%$ between the first wavepacket and $0.6\% \pm 1.5\%$ for the second wavepacket. Calculating the voltage metric gives an average change of $-9.9\% \pm 12.8\%$ for the first wavepacket and $-14.8\% \pm 26.7\%$ for the second wavepacket. The metric values have been averaged over the three thermal shock tests. The node specific metrics are listed in Appendix B, Tables B.7, B.8, and B.9.

5.4 Humidity Test Results

The humidity test followed the testing procedures described in Section 4.3.4 for nodes 0016, 0021, and 0060. The recorded test signals from these tests are shown in Appendix B, Figures B-19, B-21, and B-23. Node 0016 experienced the greatest degradation in signal voltage ($\sim -80\%$) in the post-test. This degradation was not significant until the second half (after 120 hours) of the test. Comparing the operational signal taken half-way (120.5 hours) through the test to the baseline signal shows insignificant changes. The metric changes for the other nodes tested (0021 and 0060) showed much smaller degradation. It is possible that moisture on the USB connection of node 0016 caused connectivity problems resulting in the large voltage degradation. As with the previously described temperature tests, the moisture and elevated temperatures experienced during this test caused the shear gel to flow from the boundary clamps. The humidity test envelopes for node 0021 are shown in Fig. 5-8.

The first and second baseline wavepackets had averaged times-of-flight of 4.7 $\mu s \pm$ 1 μs and 169.7 $\mu s \pm 1$ μs, respectively, and averaged peak voltages of 14.1 $mV \pm 15$ μV and 4.9 $mV \pm 15$ μV, respectively. Calculating the TOF metric between the baseline wavepackets and the post-test wavepackets gives an average change of $-15.0\% \pm$ 13.2% between the first wavepacket and $-0.8\% \pm 0.3\%$ for the second wavepacket. Calculating the voltage metric gives an average change of $-36.7\% \pm 39.0\%$ for the

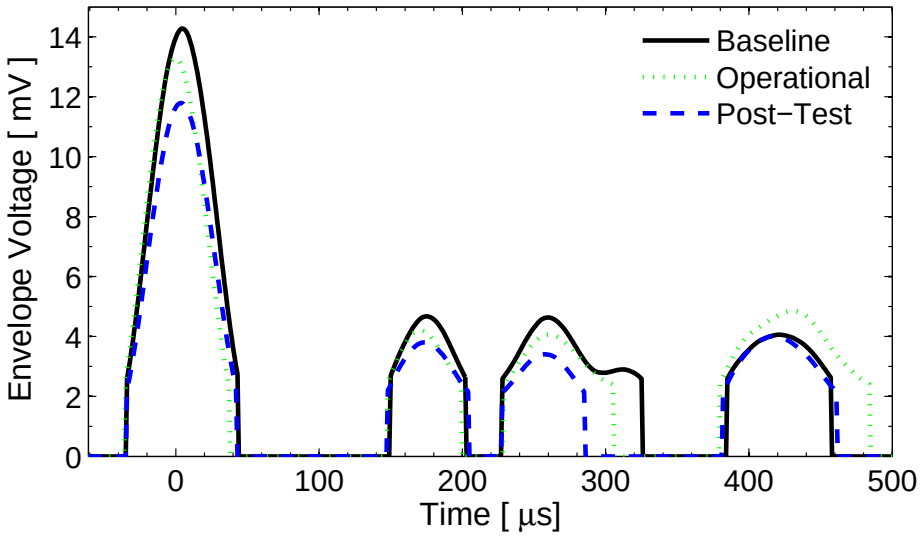

Figure 5-8: Humidity test envelopes for node 0021. Operational signal at $65°C$ and 94.8%RH (time=200.5 hrs).

first wavepacket and $-33.4\% \pm 41.6\%$ for the second wavepacket. The metric values have been averaged over the three humidity tests. The node specific metrics are listed in Appendix B, Tables B.10, B.11, and B.12.

5.5 Oil-based Fluids Susceptibility Test Results

The oil-base fluids susceptibility test followed the testing procedures described in Section 4.3.5 for nodes 0010, 0015, and 0052. The recorded test signals from these tests are shown in Appendix B, Figures B-25, B-27, and B-29. This test was conducted *without* boundary clamps. This creates a delay in the time of the reflected wavepackets, relative to tests *with* boundary clamps, as the boundaries are further. The three nodes tested showed a common trend of a significantly degraded voltage on the operational wavepackets. The operational signals were taken directly following the 160 hour hold at $65°C$. It was noted on all nodes that when ambient conditions were reestablished, the wavepacket voltages returned to near baseline levels. Node 0015 showed a significant increase (26%) in first wavepacket post-test voltage compared to the baseline. Node 0052 also showed a slight ($\sim$ 10%) increase in both post-test

wavepacket voltages. The third node (0010) showed a slight decrease in wavepacket voltages. No visual changes of the nodes were noted and no connectivity issues were found throughout the test, including while the nodes were immersed. The test envelopes for node 0052 are shown in Fig. 5-9.

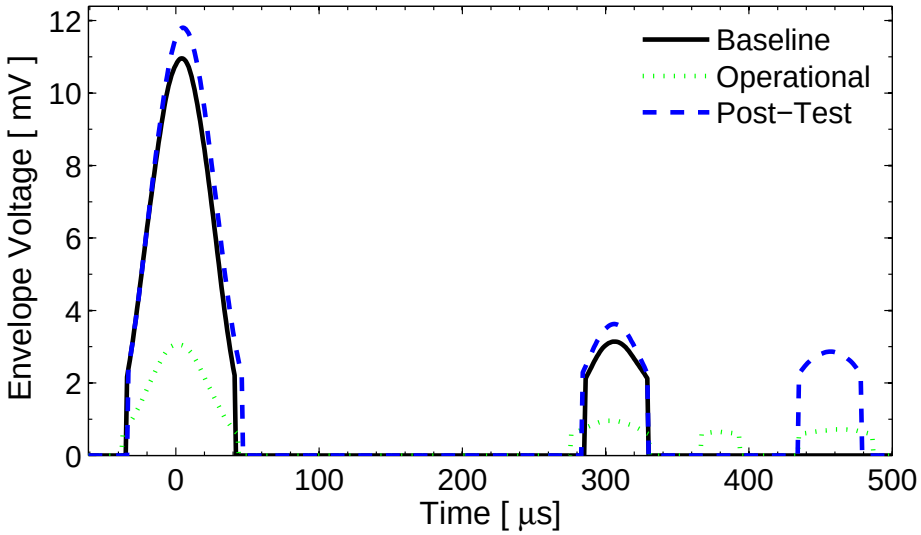

Figure 5-9: Oil-based fluids susceptibility test envelopes for node 0052. Operational signal at $22°C$ (time=214 hrs).

The first and second baseline wavepackets had averaged times-of-flight of 4.0 $\mu s \pm$ 1 μs and 306.0 $\mu s \pm 1$ μs, respectively, and averaged peak voltages of 14.2 $mV \pm 15$ μV and 5.5 $mV \pm 15$ μV, respectively. Calculating the TOF metric between the baseline wavepackets and the post-test wavepackets gives an average change of $19.4\% \pm 17.3\%$ between the first wavepacket and $-0.2\% \pm 0.3\%$ for the second wavepacket. Calculating the voltage metric gives an average change of $9.3\% \pm 16.0\%$ for the first wavepacket and $-1.8\% \pm 16.1\%$ for the second wavepacket. The metric values have been averaged over the three oil-based fluids susceptibility tests. The node specific metrics are listed in Appendix B, Tables B.13, B.14, and B.15.

5.6 Water-based Fluids Susceptibility Test Results

The water-base fluids susceptibility test followed the testing procedures described in Section 4.3.5 for nodes 0012, 0203, and 2598. The recorded test signals from these tests are shown in Appendix B, Figures B-31, B-33, and B-35. As with the oil-based fluids test, this test was conducted *without* boundary clamps. The results for the three nodes were consistent and resulted in small metric variances. All showed a significant post-test voltage degradation. Similar to the oil-based fluids test, the operational signals were taken directly following the 160 hour hold at $65°C$. As ambient conditions were reestablished the signal voltage recovered somewhat. One possible source for the degradation is that one (or more) of the water-based fluids was able to permeate the node itself, the bondline, or affect the USB connection. The test envelopes for node 2598 are shown in Fig. 5-10.

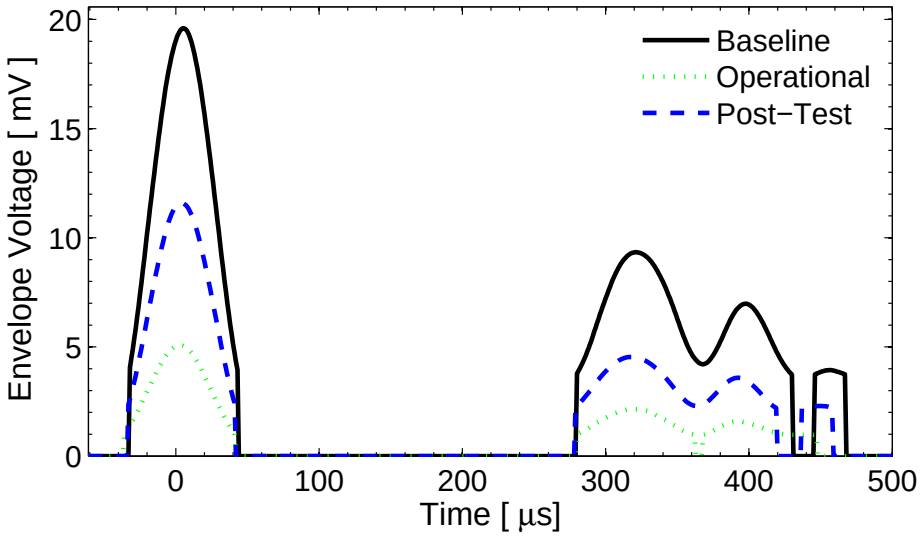

Figure 5-10: Water-based fluids susceptibility test envelopes for node 2598. Operational signal at $22°C$ (time=214 hrs).

The first and second baseline wavepackets had averaged times-of-flight of 6.0 $\mu s \pm$ 1 μs and 323.7 $\mu s \pm 1$ μs, respectively, and averaged peak voltages of 20.4 $mV \pm 15$ μV and 9.9 $mV \pm 15$ μV, respectively. Calculating the TOF metric between the baseline wavepackets and the post-test wavepackets gives an average change of $-11.4\% \pm$ 10.3% between the first wavepacket and $-2.6\% \pm 3.2\%$ for the second wavepacket.

Calculating the voltage metric gives an average change of $-44.0\% \pm 5.0\%$ for the first wavepacket and $-52.1\% \pm 0.6\%$ for the second wavepacket. The metric values have been averaged over the three water-based fluids susceptibility tests. The node specific metrics are listed in Appendix B, Tables B.16, B.17, and B.18.

5.7 Altitude (Low-pressure) Test Results

The altitude test followed the testing procedures described in Section 4.3.6 for nodes 2555, 2557, and 2595. The recorded test signals from these tests are shown in Appendix B, Figures B-37, B-39, and B-41. The altitude tests were conducted *without* boundary clamps due to test chamber geometry. All three nodes tested had a slight decrease in wavepacket voltages in both the operational and post-test signals. The nodes did not seem to be affected by the altitude test. No visual changes (*e.g.*, ruptures) were noted. The test envelopes for node 2595 are shown in Fig. 5-11.

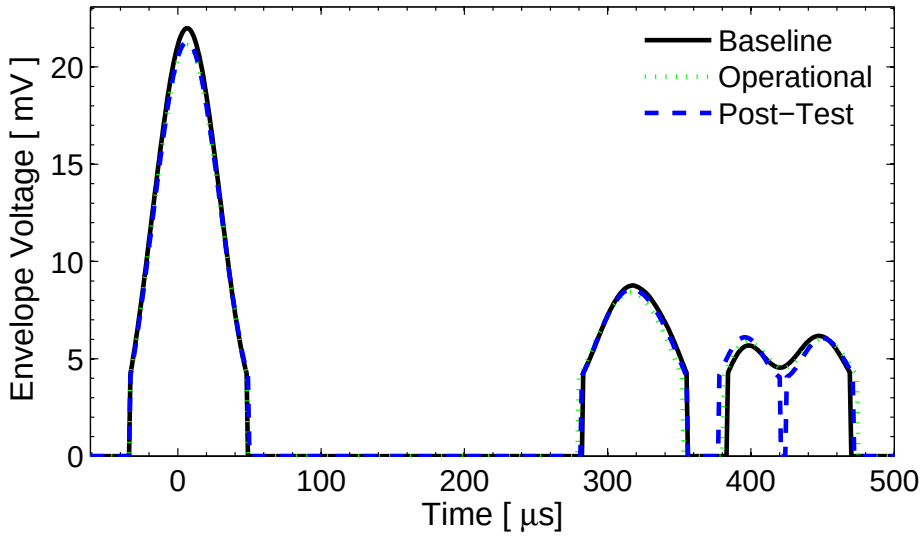

Figure 5-11: Altitude (low-pressure) test envelopes for node 2595. Operational signal at $21°C$ and 4.4 kPa (time=0.25 hrs).

The first and second baseline wavepackets had averaged times-of-flight of 6.7 $\mu s \pm$ 1 μs and 337.7 $\mu s \pm 1$ μs, respectively, and averaged peak voltages of 20.7 $mV \pm 15$ μV and 7.9 $mV \pm 15$ μV, respectively. Calculating the TOF metric between the baseline

wavepackets and the post-test wavepackets gives an average change of $-5.6\% \pm 9.6\%$ between the first wavepacket and $-0.2\% \pm 0.3\%$ for the second wavepacket. Calculating the voltage metric gives an average change of $-5.9\% \pm 2.7\%$ for the first wavepacket and $-9.7\% \pm 7.1\%$ for the second wavepacket. The metric values have been averaged over the three altitude tests. The node specific metrics are listed in Appendix B, Tables B.19, B.20, and B.21.

5.8 Decompression Test Results

The decompression test followed the testing procedures described in Section 4.3.6 for nodes 0204, 2575, and 2578. The recorded test signals from these tests are shown in Appendix B, Figures B-43, B-45, and B-47. The decompression test was conducted *without* boundary clamps due to the test chamber geometry. The pulse signal of node 2578 was irregular, as were the sensed signals (noticeable in the first wavepacket). The pulse signal did not completely follow the Hanning window. Specifically, the third sine wave in the pulse had an amplitude smaller than normal. The first wavepacket of the sensed signals had erratic noise within the signal. This noise was not sensed in the reflected wavepackets. No other nodes tested during this work had this issue. The envelopes from node 2578 showed slightly larger degradation than the metric results from nodes 0204 and 2575. All the nodes from this test showed a decrease in post-test wavepacket voltages. No visual changes (*e.g.,* ruptures) were observed after the tests. The decompression test envelopes of node 2578 are shown in Fig. 5-12.

The first and second baseline wavepackets had averaged times-of-flight of 7.3 $\mu s \pm$ 1 μs and 323.3 $\mu s \pm 1$ μs, respectively, and averaged peak voltages of 19.2 $mV \pm 15$ μV and 9.1 $mV \pm 15$ μV, respectively. Calculating the TOF metric between the baseline wavepackets and the post-test wavepackets gives an average change of $-20.7\% \pm$ 23.0% between the first wavepacket and $-1.4\% \pm 1.1\%$ for the second wavepacket. Calculating the voltage metric gives an average change of $-10.3\% \pm 8.4\%$ for the first wavepacket and $-11.4\% \pm 13.3\%$ for the second wavepacket. The metric values have been averaged over the three decompression tests. The node specific metrics are listed

in Appendix B, Tables B.22, B.23, and B.24.

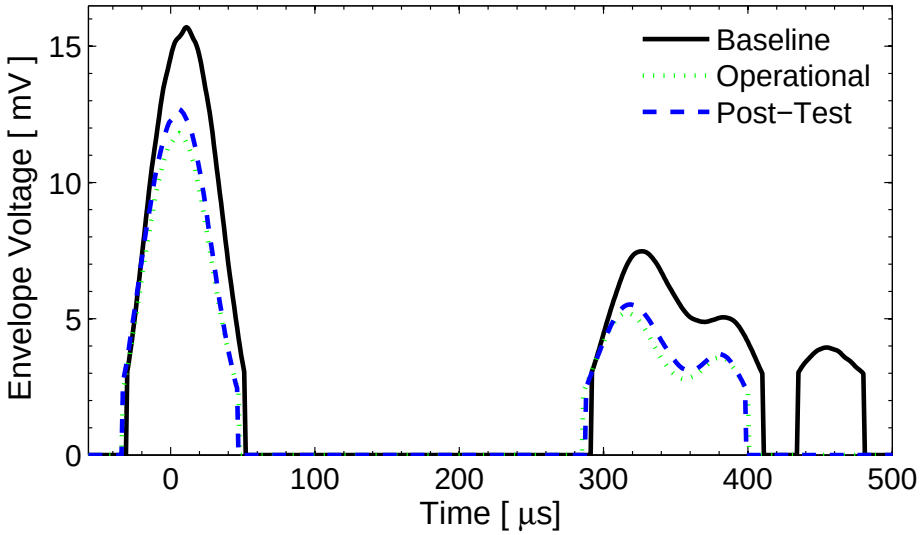

Figure 5-12: Decompression test envelopes for node 2578. Operational signal at 21°C and 4.4 kPa (time=20 min).

5.9 Overpressure Test Results

The overpressure test followed the testing procedures described in Section 4.3.6 for nodes 0011, 2586, and 2601. The recorded test signals from these tests are shown in Appendix B, Figures B-49, B-51, and B-53. The overpressure tests were conducted *without* boundary clamps. The metrics from this test show the least change of all tests for this work, similar to the results for the low-pressure test in Section 4.3.6. This was also one of the shortest duration tests. The nodes were only powered and operated to collect the baseline and post-test signals. No operational data was collected per test definitions. One of the nodes tested (2586) showed a slight increase in both wavepacket voltages while the other nodes showed insignificant changes. The overpressure test envelopes for node 2601 are shown in Fig. 5-13.

The first and second baseline wavepackets had averaged times-of-flight of 5.3 $\mu s \pm$ 1 μs and 324.0 $\mu s \pm 1$ μs, respectively, and averaged peak voltages of 19.6 $mV \pm$ 15 μV and 10.0 $mV \pm 15$ μV, respectively. Calculating the TOF metric between

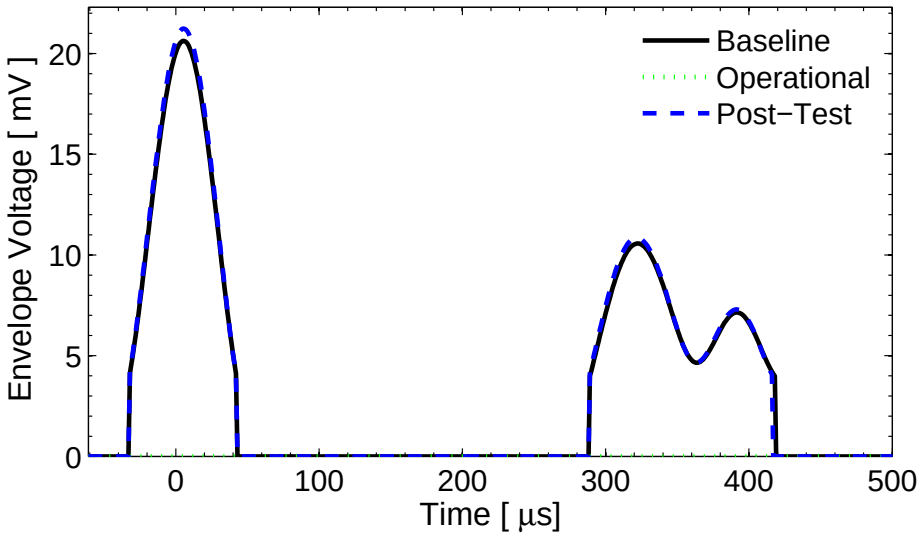

Figure 5-13: Overpressure test envelopes for node 2601. No operational signal per test definition.

the baseline wavepackets and the post-test wavepackets gives an average change of 0.0%±0.0% between the first wavepacket and −0.1%±0.2% for the second wavepacket. Calculating the voltage metric gives an average change of 3.4% ± 5.0% for the first wavepacket and 3.9% ± 6.5% for the second wavepacket. The metric values have been averaged over the three overpressure tests. The node specific metrics are listed in Appendix B, Tables B.25, B.26, and B.27.

5.10 Static-strain Test Results

The static-strain test followed the testing procedures described in Section 4.3.7 for node 0017. The recorded test signals from this test are shown in Appendix B, Fig. B-55. As with the high-temperature tests, the excitation pulse frequency for the static-strain test was 65 kHz, different than the standard frequency of 60 kHz. There was also no on-node averaging of the test signals and data was sampled for 1.0ms (1000 points). The operational signal was taken at 13.3 kN axial load (46% of σ_y). No node damage was observed after testing. The wavepacket envelopes for the static-strain test are shown in Fig. 5-14.

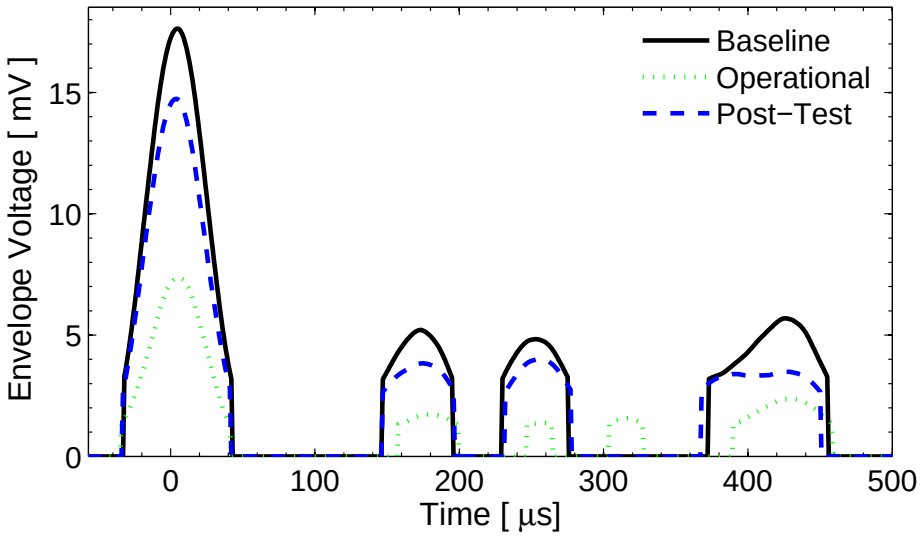

Figure 5-14: Static-strain test envelopes for node 0017. Operational signal at 46% of σ_y.

The first and second baseline wavepackets had times-of-flight of 5.0 $\mu s \pm 1$ μs and 173.0 $\mu s \pm 1$ μs, respectively, and peak voltages of 17.6 $mV \pm 15$ μV and 5.2 $mV \pm 15$ μV, respectively. Calculating the TOF metric between the baseline wavepackets and the post-test wavepackets gives a of -20.0% between the first wavepacket and 1.2% for the second wavepacket. Calculating the voltage metric gives an average change of -16.4% for the first wavepacket and -26.4% for the second wavepacket. The metric values are reported for the one static-strain test. The node specific metrics are listed in Appendix B, Table B.28.

5.11 Test Result Summary and Discussion

The delta metric results for each environmental test are summarized in Table 5.1. The values in this table are the averaged percent change from the baseline to post-test envelopes with the standard deviation (shown as $\pm$). The average and standard deviation were computed from the three tests in each environment, except in the static-strain test (only one node tested). The $\triangle$TOF metrics show large changes in the first wavepacket compared to the $\triangle$TOF of the second wavepacket. This is

because the first wavepacket occurs within the first 11 μs and the sampling rate is once every 1 μs. Overall, no large changes were found in the TOF of either wavepacket for all the tests, although the second wavepacket decreased slightly (*i.e.,* the wavepacket accelerated) on average. Typically, the TOF decreased from the baseline signal to the post-test signal for the second wavepacket. However, this change was also quite small. In most cases the variance in the $\triangle$TOF was as large as, or larger than, the average $\triangle$. The $\triangle$TOF metric does not appear to give useful information in regards to the system's performance. Therefore, system performance assessments are not based on the TOF data. For most tests, the voltage decreased between the baseline and post-test signals. Most of these changes are close to the manufacturer's stated variance of $\pm 5\%$ while the node is normally operated at ambient conditions [26]. The difference may be accounted for in the standard deviations. The three tests that had a significant effect on the nodes' signal voltage were the high-temperature, humidity, and water-based fluids susceptibility environments and are discussed below.

The voltage metric ($\triangle V$) was very useful in assessing the system's performance. The first wavepacket allows the performance of the node to be assessed with minimal interaction from the structure. This wavepacket is a direct-path signal with the Lamb-waves traveling only below the node between the inner and outer piezoelectric elements. The adhesive bond between the node and the aluminum coupon is a primary factor influencing this metric, along with the node itself. The second wavepacket is also susceptible to influences from the adhesive and node, but is also affected by any changes to the boundary conditions (*i.e.* the shear gel dissolving and/or flowing from the boundary clamps). However, no common $\triangle V$ trends (increase or decrease in voltage) exist within a test type, nor between test types, even including the situation where the shear gel flows out. This suggests that the shear gel may have a negligible effect on the boundary conditions. Throughout all the environments, there were no trends of the first wavepacket $\triangle V$ degrading significantly more than the second wavepacket or vice versa.

The post-test signals degraded from the baseline in 21 of the 28 tests for the first wavepacket and in 22 of the 28 tests for the second wavepacket. In the other cases

the $\triangle V$ increase was small and likely associated with the standard deviation of the signals. The operational test signals degraded from the baseline in 21 of the 22[1] tests with recorded operational data for the first wavepacket and in 20 of the 21 tests with data for the second wavepacket.

Only the fluids susceptibility and low-temperature tests showed consistent voltage recovery between the operational signal and the post-test signal. The oil-based fluids tests showed an average 65% voltage recovery and the water-based fluids tests had an average 20% voltage recovery. For the three low-temperature tests, the operational data was only saved on one of the tests. In this single test, a 60% voltage recovery was noted between the operational and post-test signals.

The decompression tests showed slightly greater degradation (-10% and -11% for the first and second wavepacket $\triangle V$s, respectively) than the altitude (low-pressure) tests (both experience the same extreme pressure) and the overpressure tests. This suggests that the nodes may be affected by the rate of pressure change. However, the variance in the voltage metric may also account for the slight increase in degradation between the two tests.

Another factor that may influence the voltage metric is fatigue of the SHM system, including especially the piezoelectric actuator material. The number of cycles the nodes endure during each durability test is significant ranging from the millions to billions of cycles. Table 5.2 lists an estimated number of excitation cycles experienced by the nodes during each test. The operational time listed in the table is an averaged number including the time the nodes are operated before, during, and after the tests. During the device operating condition (described in Section 4.3), one pulse is sent every 800 μs. Each pulse lasts 83 μs and contains 5 complete sine waves (at the driving frequency, 60 kHz) as shown earlier in Fig. 5-2a. This equates to a fatigue cycle frequency of 6.25 kHz. The number of fatigue cycles is calculated by multiplying this fatigue cycle frequency with the operational time. The high-temperature and static-strain tests sent pulses every 1000 μs with a driving frequency of 65 kHz resulting in

[1]Excluding the operational signal collected for the first wavepacket from the high-temperature test for node 0036 that had an anomalous 77% increase.

a fatigue cycle frequency of 5 kHz.

Table 5.1: Summary of averaged metrics (post-test compared to baseline) for all testing.

Environment	△ **TOF Metric*** [%]		△ **Voltage Metric*** [%]	
	1^{st} wavepacket	2^{nd}wavepacket	1^{st}wavepacket	2^{nd}wavepacket
High-temperature	22.2 ±63.1	-2.0±1.3	-30.6±29.0	-28.2±17.0
Low-temperature	-15.0±13.2	-1.0±1.4	-8.1 ±17.0	2.7 ±19.0
Thermal shock	-1.2 ±26.8	0.6 ±1.5	-9.9 ±12.8	-14.8±26.7
Humidity	-15.0±13.2	-0.8±0.3	-36.7±39.0	-33.4±41.6
Oil-based Fluids	19.4 ±17.3	-0.2±0.3	9.3 ±16.0	-1.8 ±16.1
Water-based Fluids	-11.4±10.3	-2.6±3.2	-44.0±5.0	-52.1±0.6
Altitude	-5.6 ±9.6	-0.2±0.3	-5.9 ±2.7	-9.7 ±7.1
Decompression	-20.7±23.0	-1.4±1.1	-10.3±8.4	-11.4±13.3
Overpressure	0.0 ±0.0	-0.1±0.2	3.4 ±5.0	3.9 ±6.5
Static-strain†	-20.0	1.2	-16.4	-26.4

*Percentage values listed as mean ± standard deviation ($\bar{x} \pm \sigma$).

† Only one node tested.

Table 5.2: Estimated number of excitation fatigue cycles of nodes for each test.

Environment	**Operation Time [hrs]**	**Fatigue Cycles, N**	**log(N)**
High-temperature	3.5	63,000,000	7.80
Low-temperature	3.5	78,750,000	7.90
Thermal shock	6.0	135,000,000	8.13
Humidity	240	5,400,000,000	9.73
Oil-based Fluids	2.2	49,500,000	7.70
Water-based Fluids	2.2	49,500,000	7.70
Altitude	2.5	56,250,000	7.75
Decompression	0.5	11,250,000	7.05
Overpressure	0.3	6,750,000	6.83
Static-strain	0.25	4,500,000	6.65

Chapter 6

Conclusions and Recommendations

The benefits of SHM include significant cost savings and safer aircraft. It is critical that testing and certification standards for SHM systems are formed so that such benefits can be realized. It is recommended that current testing and certification standards for avionic equipment be used as a foundation for SHM standards, following the path taken in this work. SHM standards should be formed for the most complex/extensive SHM systems, where systems of lesser complexity can use portions of the standard that are pertinent. The environmental operating envelopes of traditional aircraft have been well defined for existing vehicles. It is critical to define testing standards which are valid to the extremes of these envelopes and beyond for next generation transports.

6.1 Conclusions

The following summarizes the results from the durability tests conducted during this work and the contributions made toward developing standards specific for SHM and smart structure systems:

1. A framework for developing SHM durability standards for aerospace vehicles has been offered. The framework brings together existing structural and environmental standards as a foundation. The framework also captures issues that are unique to SHM systems. The present work addressed three areas of

SHM durability via test definition and experimental tests: the intersection of structural design standards and SHM durability standards, the intersection of environmental test standards and SHM durability standards, and the issues unique to SHM systems. Coupling between the environmental and structural standards was not addressed.

2. The SHM 'system' tested was selected at the beginning of this work to be the node, the adhesive that bonds the node to the structure, the aluminum coupon (structure) between the boundary clamps, the boundary clamps, and the shear gel between the boundary clamps and coupon. This was chosen to allow the structure to be installed in testing fixtures without affecting the system. An issue was found throughout some of the testing environments that the shear gel dissolved or lost viscosity and flowed from beneath the boundary clamps, thus, possibly changing the pre-defined system. It is crucial to carefully define the SHM system and recognize that for most SHM systems, as in this work, the structure being monitored for health is part of the system.

3. The boundary clamps were effective in producing reflections of the Lamb waves. The TOF of the first reflected wavepacket doubles when no boundary clamps are used. The distance the waves travel also doubles when the boundary clamps are removed, which implies that the boundary clamps successfully reflected the Lamb waves. However, the analytical TOF did not match the experimental results. The first reflected wavepacket's theoretical TOF was calculated to be $\sim 110\ \mu s$ and the experimental TOF was $\sim 170\ \mu s$.

4. An initial test matrix was formed to conduct durability tests on the Lamb wave-based SHM system focused on in this work. Environments were selected that were likely to significantly affect the system. These environments include high-temperature, low-temperature, thermal shock, high humidity, fluids susceptibility (oil- and water-based), altitude (low-pressure), rapid decompression, over pressurization, and mechanical strain. The current standards used to populate the test matrix typically have operational categories corresponding to the

maximum expected environmental or structural loading to be regularly experienced by the component under test.

5. Criteria to assess the performance of SHM systems were developed based on deltas/changes in measurable system quantities: the first metric is the time-of-flight (TOF) of the first two sensed wavepackets, and the second metric is the maximum voltage of the sensed wavepackets. Both metrics compare signals to a baseline value. It was found that the $\triangle$TOF metric did not yield useful information in assessing the performance of the SHM system because changes were below the measurement threshold, therefore, system performance assessments are not based on the TOF data. However, the $\triangle$V metric was very useful in providing relevant information on the performance of the system.

6. Of the 28 Lamb-wave nodes exposed to various environmental and structural conditions, all survived and were functioning upon completion of the tests. The three tests that had the largest influence on the system were the high-temperature, humidity, and water-base fluids susceptibility tests. The following are the key findings from the experimental results:

    - An overall trend of signal voltage degradation (both wavepackets averaged) was noted in 77% of the tests. Across all tests, the average signal degradation ($\triangle V$) was -16%. The high-temperature, humidity, and water-based fluids susceptibility tests had the greatest influence on the sensors, with an average voltage degradation of -38%.

    - The decompression tests showed slightly greater degradation than the altitude tests suggesting that the nodes may be affected by the rate of pressure change.

    - In most tests there was a voltage recovery between the operational and post-test signals once ambient conditions had been reestablished. The fluid susceptibility and low-temperature tests consistently showed significant (48%) signal voltage recovery between the operational signals and the

post-test signals.

6.2 Recommendations

Based on the findings and results from this work, the following are recommendations for future work that will contribute to SHM implementation:

1. One of the most important considerations when forming SHM specific standards is a clear and precise definition of the 'system.' Because the structure being monitored becomes an integral component of the SHM system, it will be important to decipher between degradation of the sensors (or smart components) versus the structure. For the 'system' considered during this work, studies investigating the effects of the shear gel and the clamping pressure of the boundary clamps would be of interest.

2. Further work should continue to define required tests within the framework to develop SHM durability standards. This work took the first step in defining a durability test matrix by investigating and identifying several existing standards relevant to SHM systems, but additional environments considered were not included (see Tables 3.1 and 3.2). As specific SHM systems are developed, unique requirements will need to be identified and added to the standards. Additional testing requirements need to be described in the areas considered here and for coupled structural-environmental conditions. The framework provided here and the existing avionic standards provide a good path to fully defining environmental conditions to test. Additional structural standards will need to be explored and tailored to test the durability of SHM systems.

3. The effects of combined loading on SHM systems needs additional consideration. The work in this research has focused on single, not combined, aspects of environmental and structural loading. Combined loading of such tests are typically coupled (not simple superposition) and therefore combined tests are

necessary to fully assess durability. The combined loading tests should be designed to simulate typical flight cycles. Such cycles could be broken into various stages, such as during taxiing, takeoff, cruise, and landing. As an example, such tests would combine pressure, temperature, and vibration conditions to form the SHM system test.

4. The nodes used for this test operated for long time durations and accumulated large numbers of actuation cycles (4.5 million to 5.4 billion cycles). One issue that may account for the voltage degradation is the ultrasonic fatigue of the actuator from normal operation. A suggested test would be to investigate the voltage degradation as a function of the number of actuation cycles at ambient conditions.

5. Expanding the fluids used in the fluids susceptibility tests should be considered. Not all fluid classes listed in the standards were tested during this work. Depending on the application/location of the SHM system, it is possible that some fluid classes or test fluids can be eliminated from the test. However, it is important to have the standard encompass all possible fluids used in/on aircraft and allow specific applications to test only relevant fluids. The system tested here needs additional fluids tests.

6. Finite element modeling of the Lamb-wave propagation through the aluminum coupon will provide insight to the reflections occurring in the structure. This modeling can help assess the 1-dimensional problem assumed during this work. It may also give insight to the difference between the analytical and experimental wave velocities. A detailed FEA model will also be able to simulate the reflections from the boundary clamps and determine if a complete (100% of the wave energy) reflection occurs at the boundary clamp or if some of the wave energy is transmitted through the boundary clamp.

SHM standards for durability will require input from the SHM community, the government (*e.g.,* FAA), and the commercial and military aircraft manufacturers.

These groups will need to work together to define methods to assess operational capabilities and limitations for SHM systems so that their value can be realized in the high-payoff commercial aircraft sector.

References

[1] S.R. Hall. "The Effective Management and Use of Structural Health Data". In *Proceedings of the 2nd International Workshop on Structural Health Monitoring*, pages 265–275, Stanford, CA, 8–10 September 1999.

[2] AC21-16E. *Advisory Cricular No: 21–16E*. U.S. Department of Transportation, Federal Aviation Administration, December 2005.

[3] S.S. Kessler. *Piezoelectric–Based In–Situ Damage Detection of Composite Materials for Structural Health Monitoring Systems*. PhD dissertation, Massachusetts Institute of Technology, Dept. of Aeronautics and Astronautics, Cambridge, MA, January 2002.

[4] S.S. Kessler, S.M. Spearing, M.J. Atalla, C.E.S. Cesnik, and C. Soutis. "Structural Health Monitoring in Composite Materials using Frequency Response Methods". *Composites Part B*, v.33:87–95, January 2002.

[5] S.S. Kessler, S.M. Spearing, and C. Soutis. "Structural Health Monitoring in Composite Materials using Lamb Wave Methods". *Smart Materials and Structures*, v.11:269–278, April 2002.

[6] S.S. Kessler, S.M. Spearing, Y. Shi, and C.T. Dunn. "Packaging of Structural Health Monitoring Components". In *Proceedings of the SPIE's 11th International Symposium on Smart Structures and Materials*, pages 219–229, San Diego, CA, 14–18 March 2004.

[7] S.S. Kessler and D.J. Shim. "Validation of a Lamb Wave–Based Structural Health Monitoring for Aircraft Applications". In *Proceedings of the SPIE's 12th International Symposium on Smart Structures and Materials*, pages 293–301, San Diego, CA, 7–10 March 2005.

[8] Y. Bar-Cohen. "Emerging NDE Technologies and Challenges at the Beginning of the 3rd Millennium". In *Materials Evaluation*, volume v.58, 2000.

[9] F-K Chang. "Structural Health Monitoring: A Summary Report". In *Proceedings of the 2nd International Workshop on Structural Health Monitoring*, Stanford, CA, 8–10 September 1999.

[10] V. Giurgiutiu. "Tuned Lamb–Wave Excitation and Detection with Piezoelectric Wafer Active Sensors for Structural Health Monitoring". *Journal of Intelligent Material Systems and Structures*, v.16:291–306, 16 April 2005.

[11] S.S. Kessler. "Certifying a Structural Health Monitoring System: Characterizing Durability, Reliability and Longevity". In *Proceedings of the 1st International Forum on Integrated Systems Health Engineering and Management in Aerospace*, Napa, CA, 7–10 November 2005.

[12] J.T. Chambers, B.L. Wardle, and S.S. Kessler. "Durability Assessment of Lamb Wave-Based Structural Health monitoring Nodes". In *47th AIAA Structures, Structural Dynamics, and Materials Conference*, Newport, RI, 1–4 May 2006. AIAA 2006-2263.

[13] S.S. Kessler, K. Amaratunga, and B.L. Wardle. "An Assessment of Durability Requirements for Aircraft Structural Health Monitoring Sensors". In *Proceedings of the 5th International Workshop on Structural Health Monitoring*, Stanford, CA, 12–14 September 2005.

[14] V. Giurgiutiu, C. Jenkins, J. Kendall, and L. Yu. "In–Situ Imaging of Crack Growth with Piezoelectric Wafer Active Sensors". In *47th AIAA Structures, Structural Dynamics, and Materials Conference*, Newport, RI, 1–4 May 2006. AIAA 2006-2114.

[15] RTCA, Washington, D.C. *DO–160E, Environmental Conditions and Test Procedures for Airborne Equipment*, December 2004. RTCA Paper No. 111-04/SC135-645.

[16] *MIL-STD-810F, Department of Defense Test Method Standard for: Environmental Engineering Considerations and Laboratory Tests*, January 2000 (original), November 2000, August 2002, and May 2003 (change notices 1-3).

[17] *MIL-STD-461E, Department of Defense Interface Standard: Requirements for the Control of Electromagnetic Interference Characteristics of Subsystems and Equipment*, August 1999.

[18] *MIL-HDBK-310, Global Climatic Data for Developing Military Products*, June 1997.

[19] K.F. Graff. *Wave Motion in Elastic Solids*, pages 431–458. Dover, New York, 1991.

[20] Horacc Lamb. "On Waves in an Elastic Plate". In *Proceedings of the Royal Society of London. Series A, Containing Papers of a Mathematical and Physical Character*, volume 93, pages 114–128, 1 March 1917.

[21] J.L. Rose. *Ultrasonic Waves in Solid Media*. Cambridge University Press, November 1999.

[22] *MIL-HDBK-5J, Metallic Materials and Elements for Aerospace Vehicle Structures*, January 2003.

[23] AC29-2C. *Advisory Cricular No: 29–2C*. U.S. Department of Transportation, Federal Aviation Administration, February 2003.

[24] ALCOA, Inc. *SPD-10-036, Alloy 2024 Sheet and Plate*.

[25] C.Y. Wu and B.L. Wardle. "Improved Damage Detection Using Lamb-waves for Structural Health Monitoring Applications". To be submitted to Smart Materials and Structures, 2006.

[26] Metis Design Corporation. Personal communications with Dr. Seth Kessler, 2006.

[27] Vishay Intertechnology, Inc. *M-Bond AE-10 Adhesive*. World Wide Web, http://www.vishay.com/company/brands/measurements-group/guide/a110/acc/mbae10.htm, 2006.

Appendices

Appendix A

Experimental Testing Profiles

This appendix includes the experimentally achieved testing profiles for each test reported. Profile specifics are discussed in Chapter 4. The profile data was recorded at various intervals depending on the test and is marked on the profiles as x's, except for the humidity and static-strain profiles. For the humidity profiles, LabVIEW sampled the temperature and relative humidity every 2.5 minutes. For the static-strain profile, LabVIEW sampled the axial load at 1 hertz. No temperature data was recorded after the time shown in Figures A-1, A-2, and A-5.

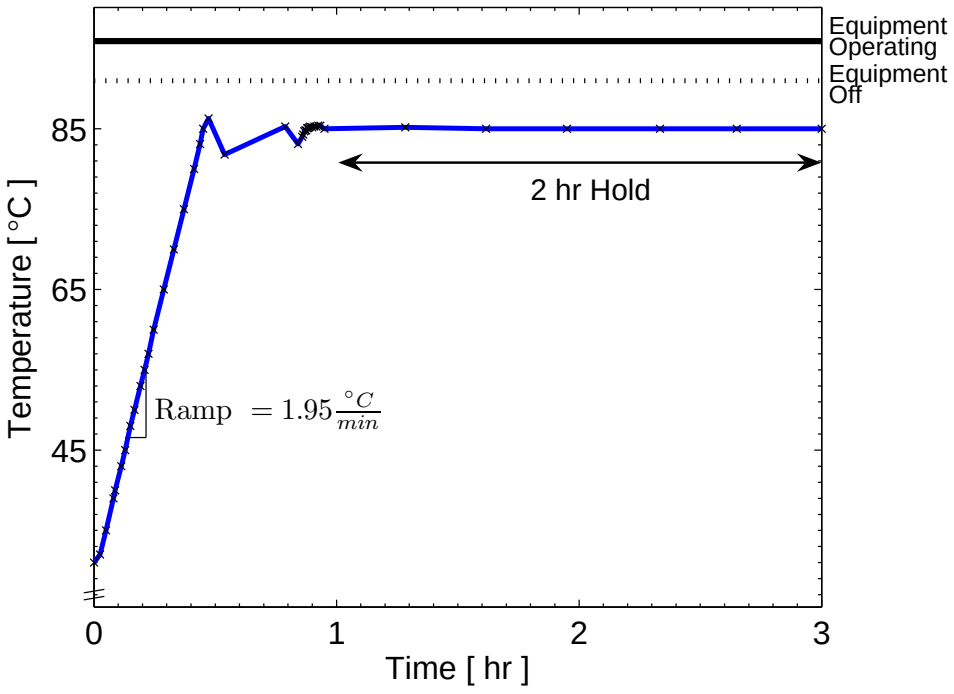

Figure A-1: Experimental high-temperature test profile for node 0026.

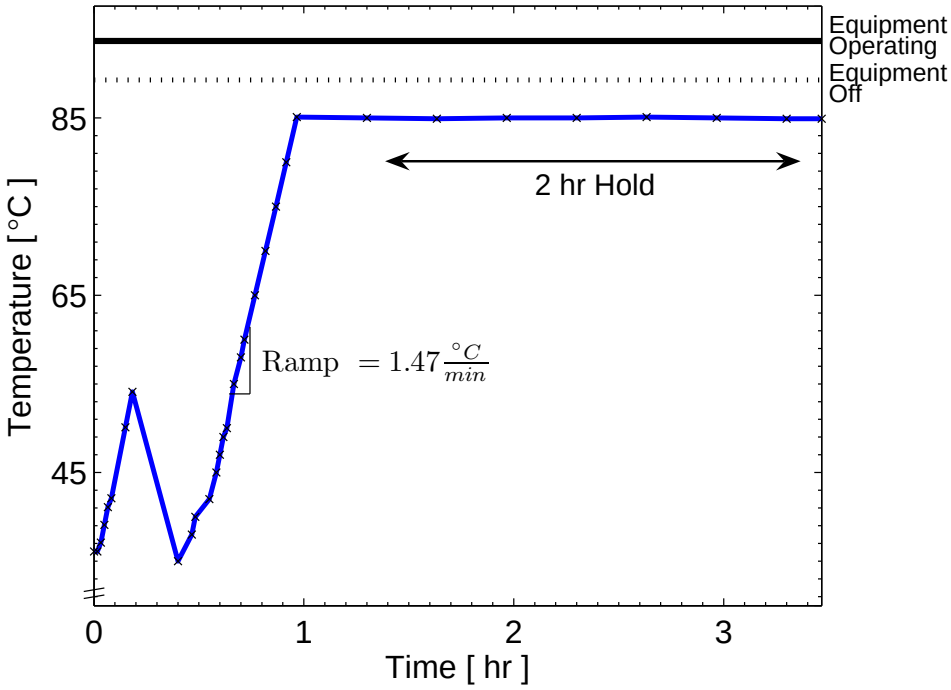

Figure A-2: Experimental high-temperature test profile for node 0036.

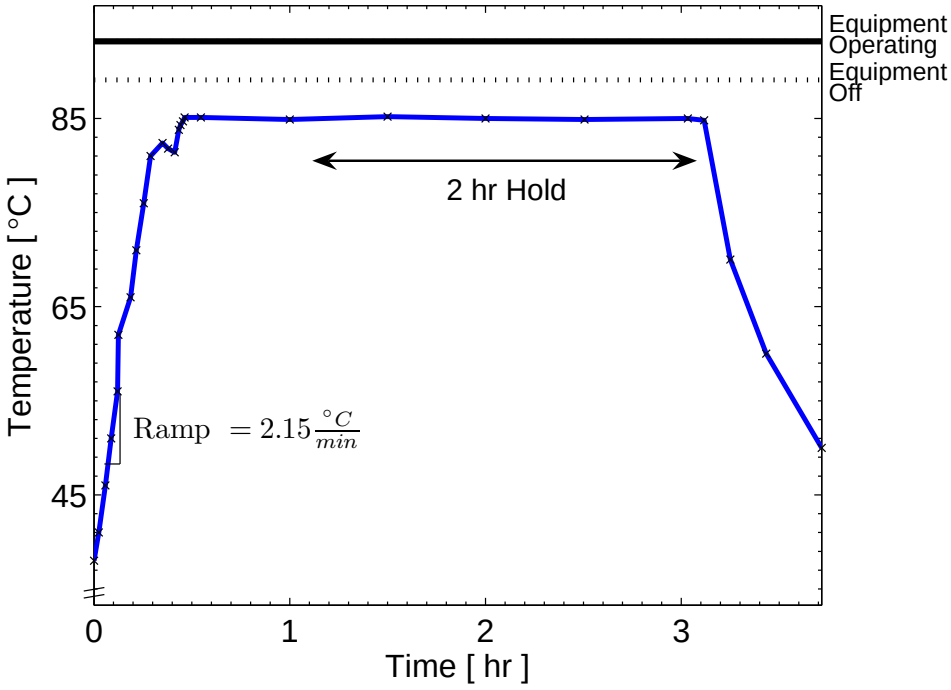

Figure A-3: Experimental high-temperature test profile for node 0041.

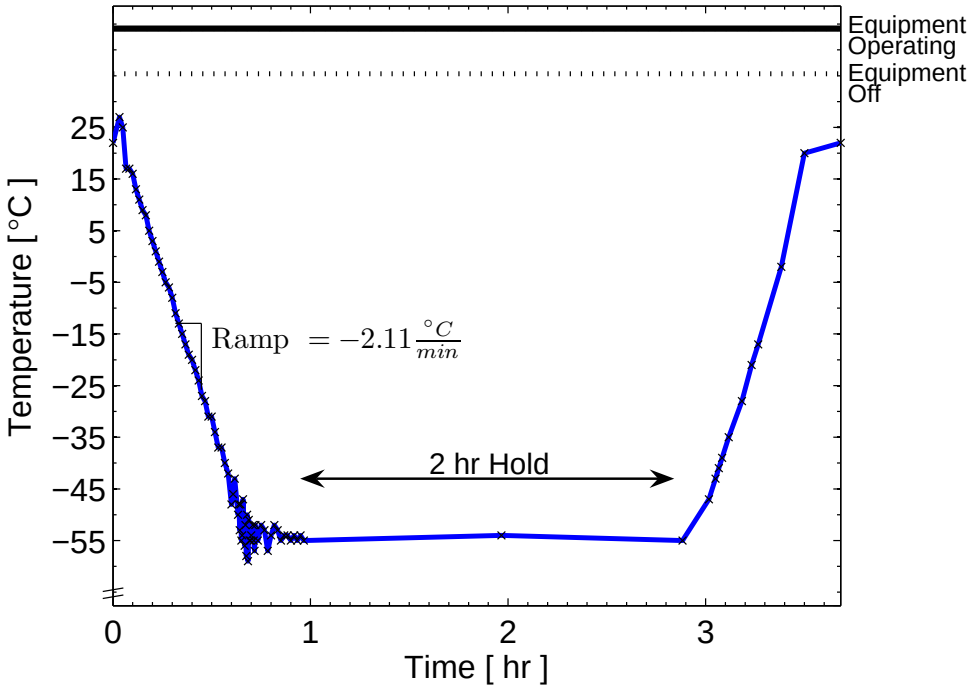

Figure A-4: Experimental low-temperature test profile for node 0029.

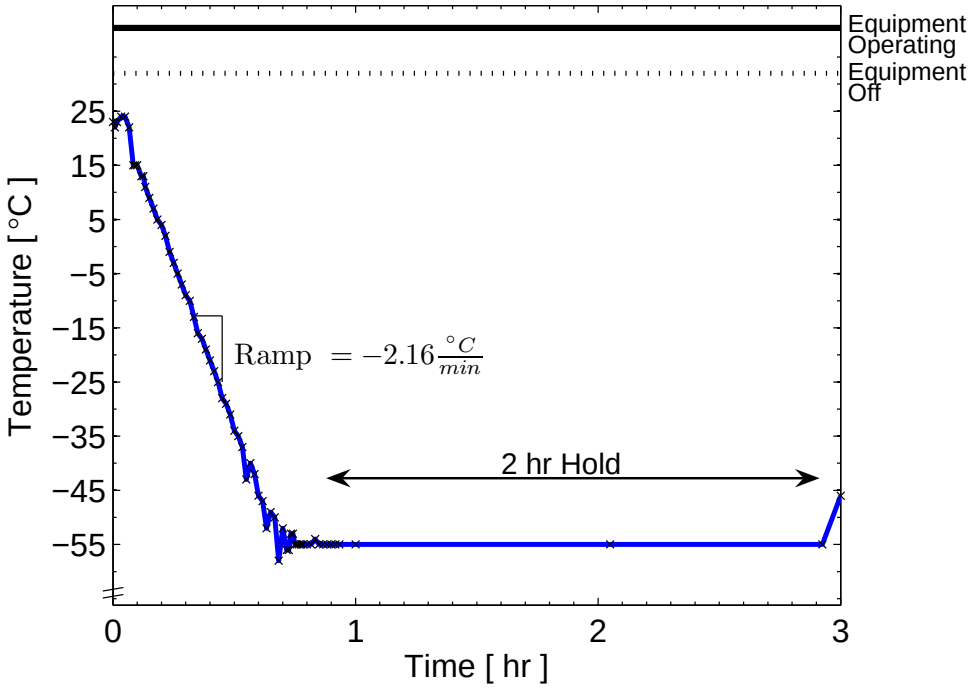

Figure A-5: Experimental low-temperature test profile for node 0049.

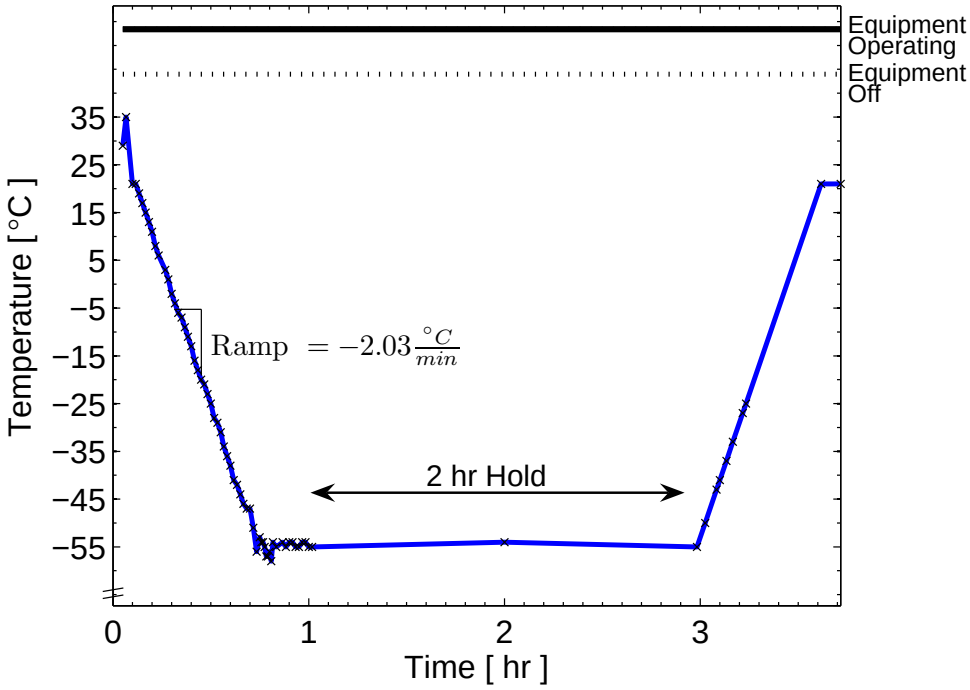

Figure A-6: Experimental low-temperature test profile for node 0068.

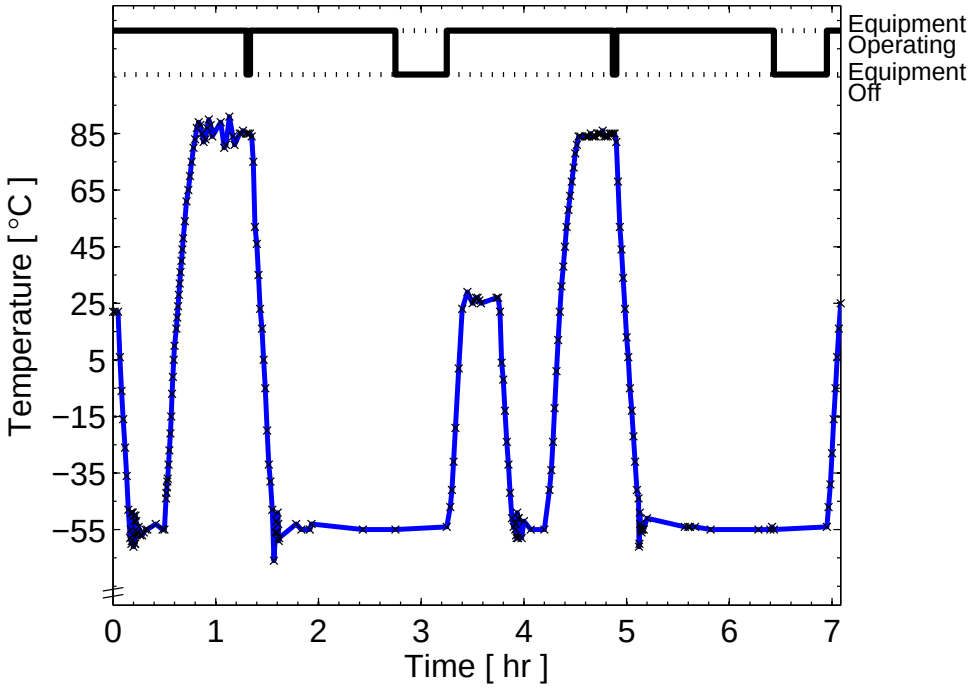

Figure A-7: Experimental thermal shock test profile for node 0034.

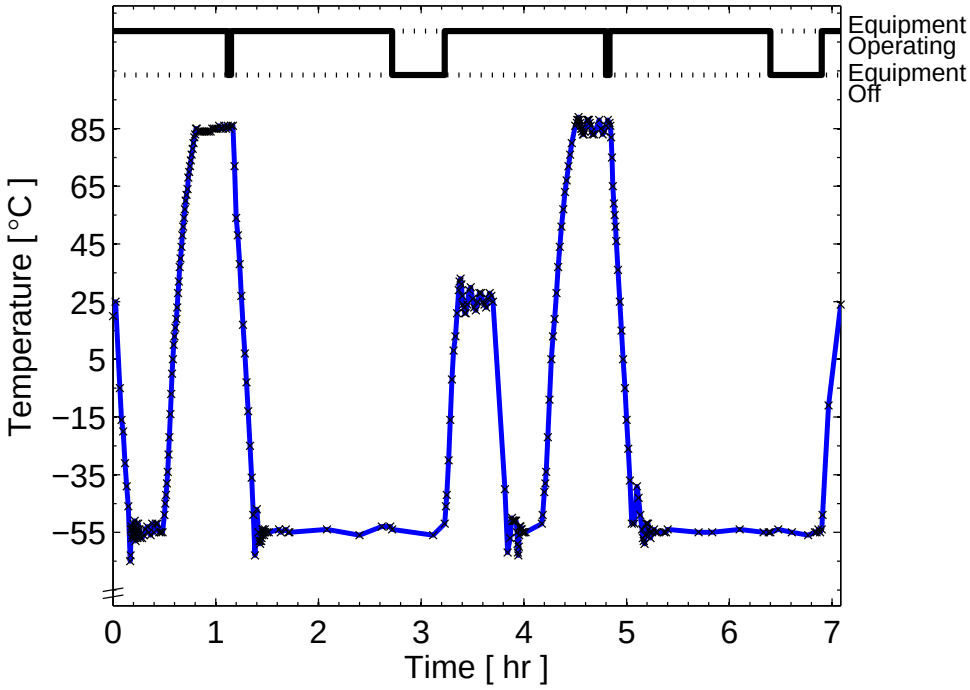

Figure A-8: Experimental thermal shock test profile for node 0046.

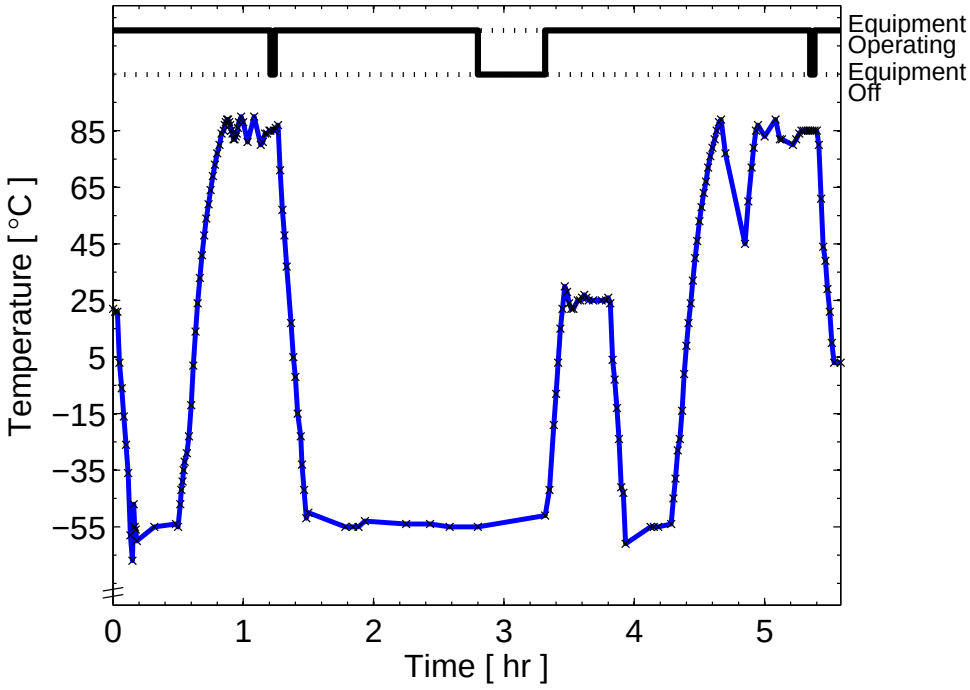

Figure A-9: Experimental thermal shock test profile for node 0061, incomplete.

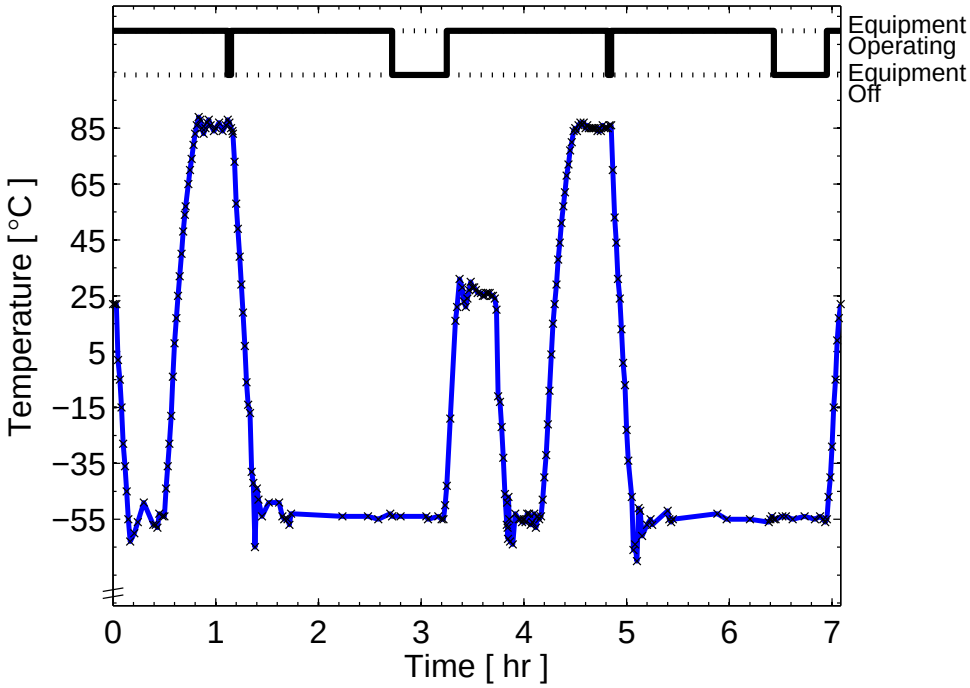

Figure A-10: Experimental thermal shock test profile for node 0061, ran after previous cycles shown in Fig. A-9.

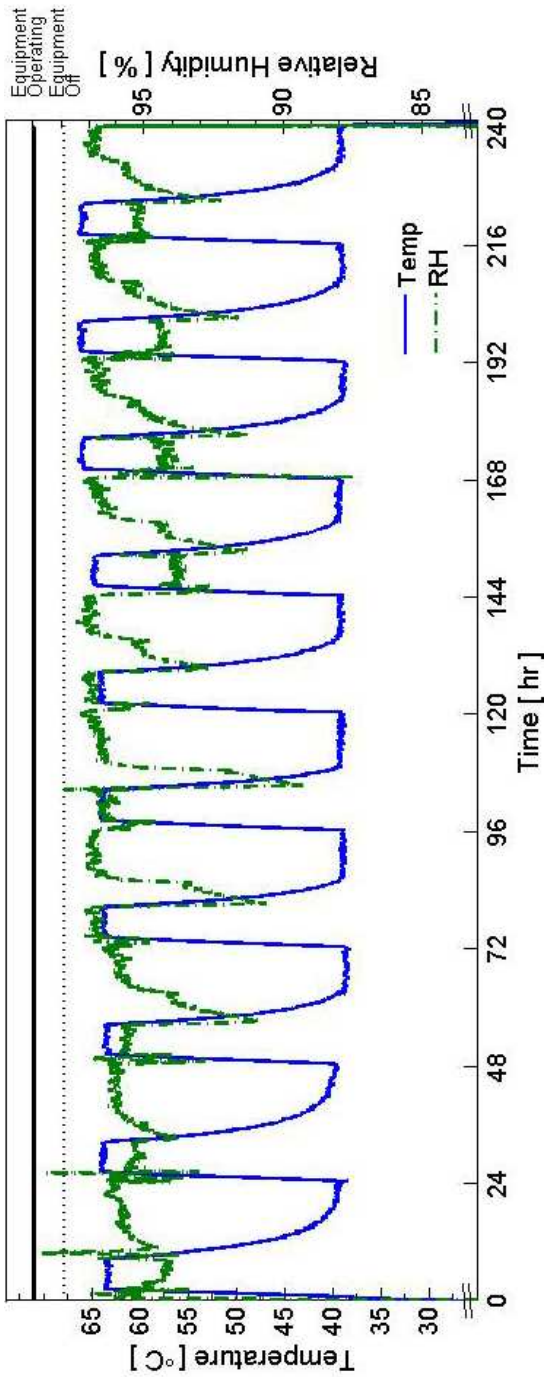

Figure A-11: Experimental humidity test profile for nodes 0016, 0021, and 0060.

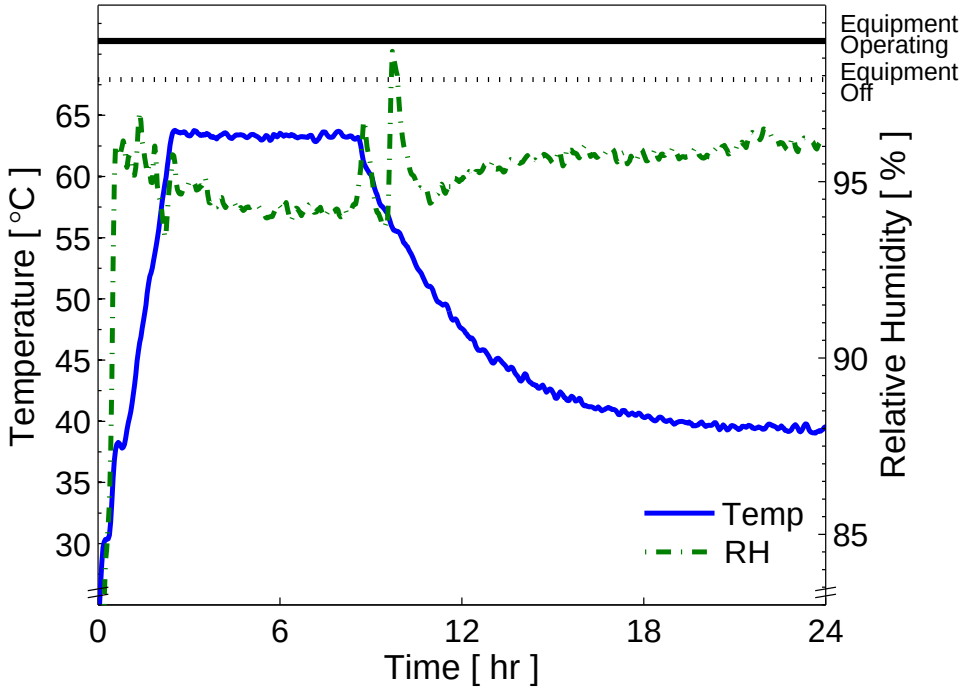

Figure A-12: Experimental humidity test profile, cycle 1, for nodes 0016, 0021, and 0060.

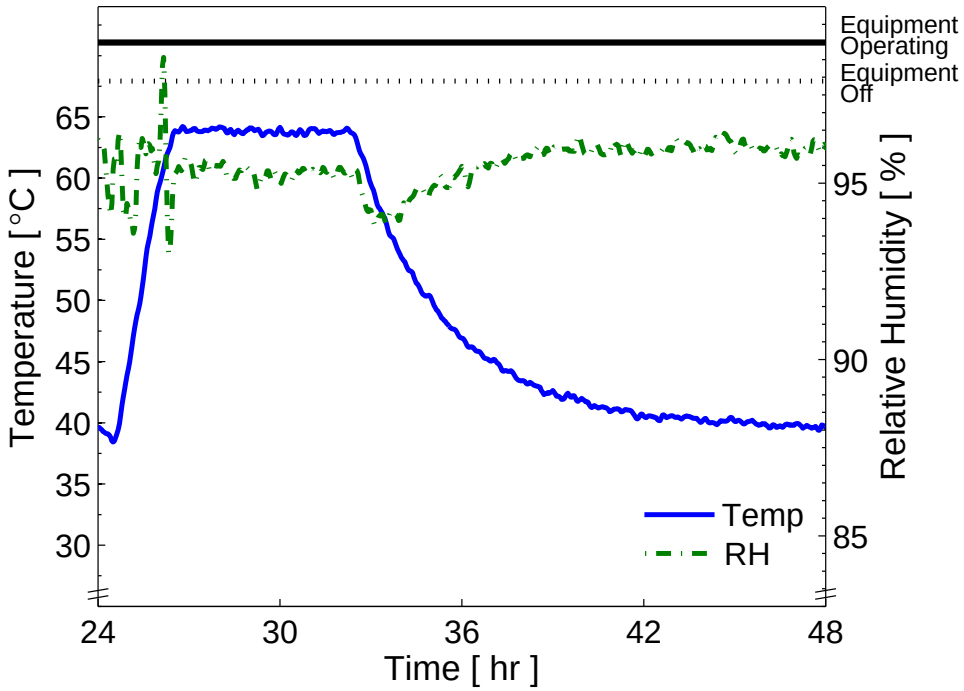

Figure A-13: Experimental humidity test profile, cycle 2, for nodes 0016, 0021, and 0060.

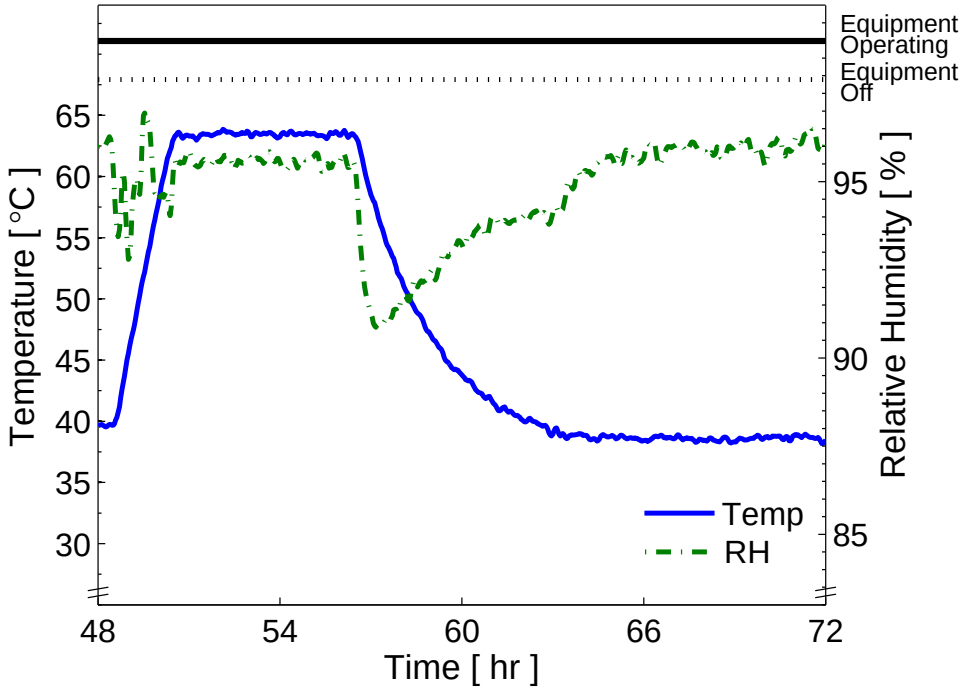

Figure A-14: Experimental humidity test profile, cycle 3, for nodes 0016, 0021, and 0060.

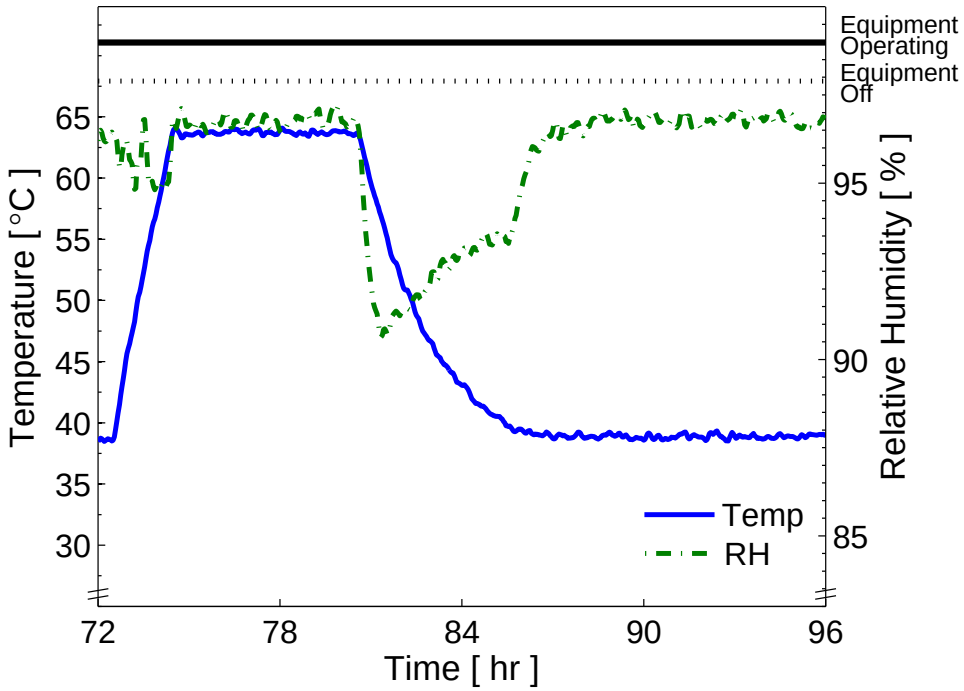

Figure A-15: Experimental humidity test profile, cycle 4, for nodes 0016, 0021, and 0060.

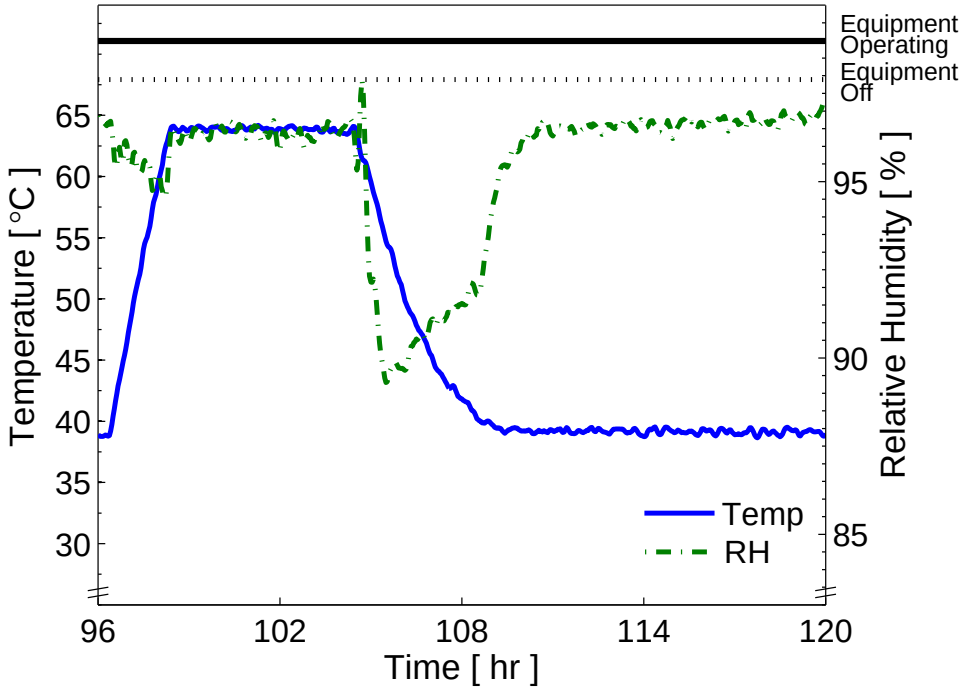

Figure A-16: Experimental humidity test profile, cycle 5, for nodes 0016, 0021, and 0060.

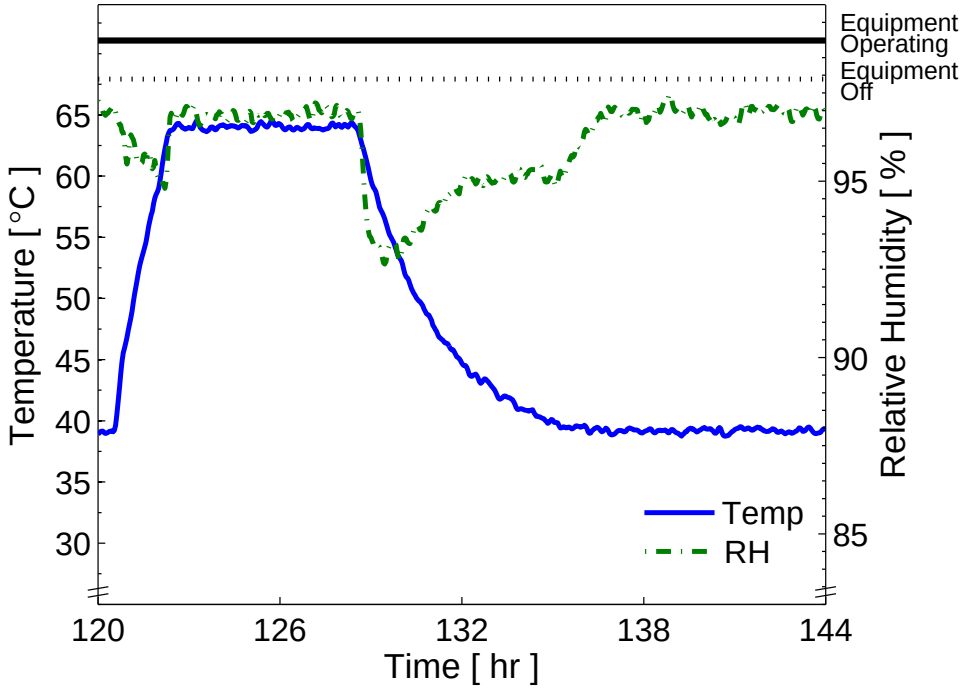

Figure A-17: Experimental humidity test profile, cycle 6, for nodes 0016, 0021, and 0060.

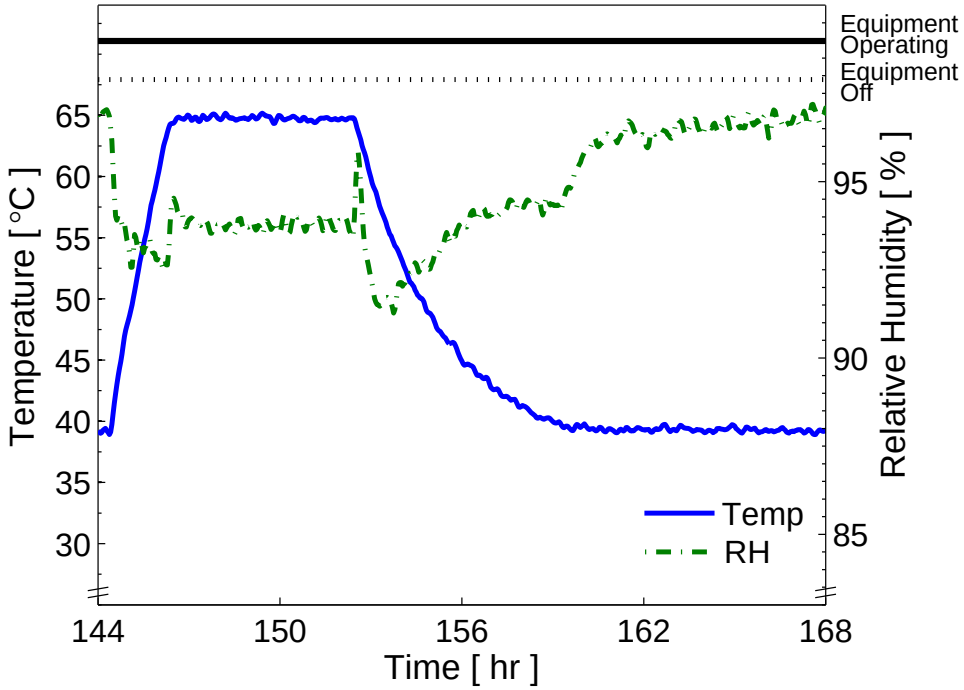

Figure A-18: Experimental humidity test profile, cycle 7, for nodes 0016, 0021, and 0060.

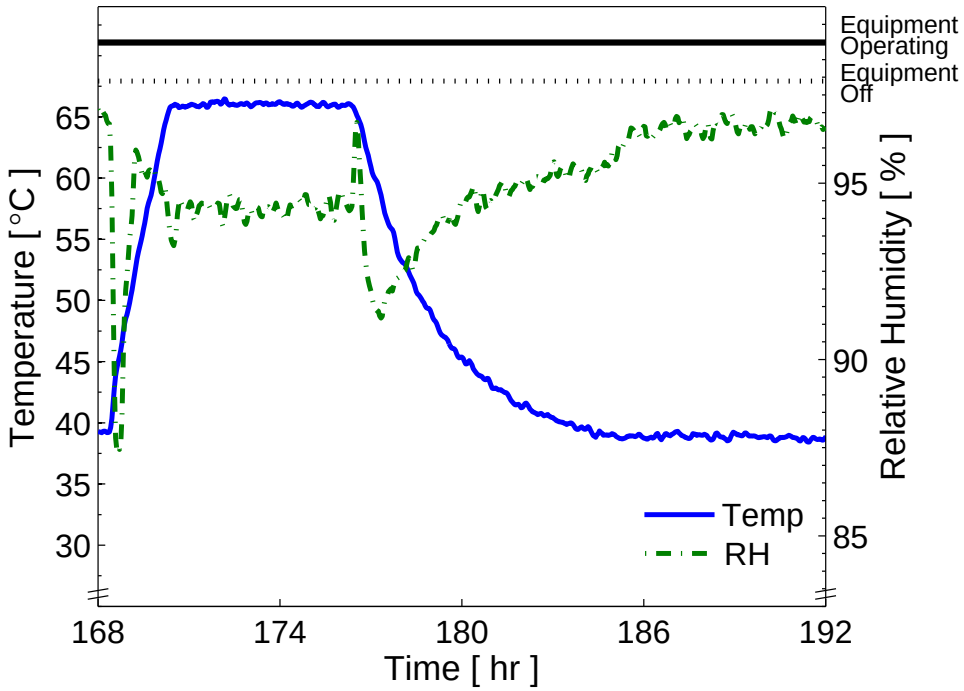

Figure A-19: Experimental humidity test profile, cycle 8, for nodes 0016, 0021, and 0060.

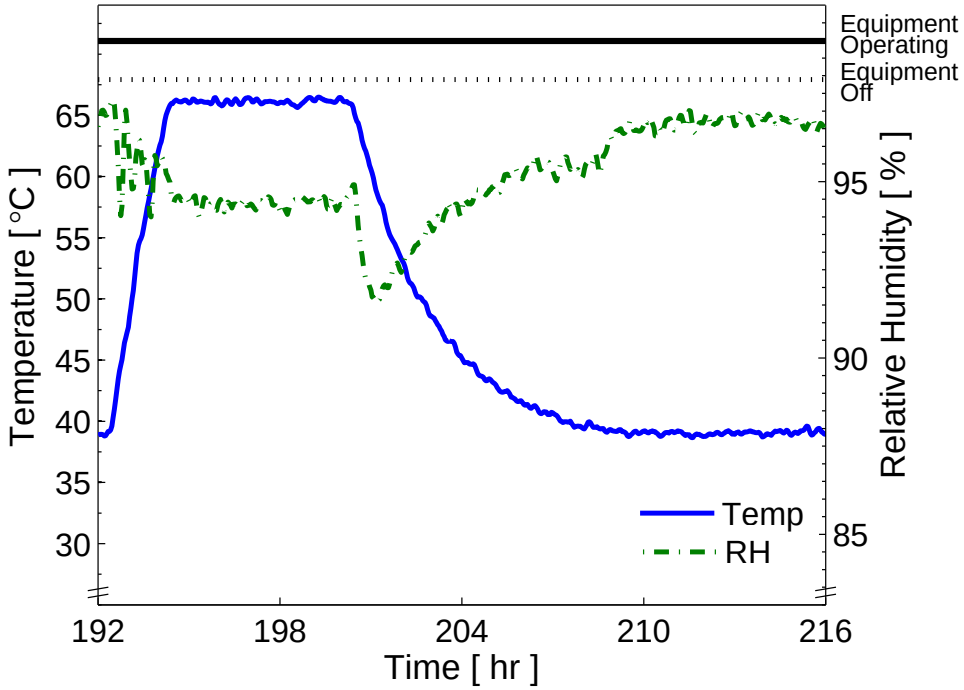

Figure A-20: Experimental humidity test profile, cycle 9, for nodes 0016, 0021, and 0060.

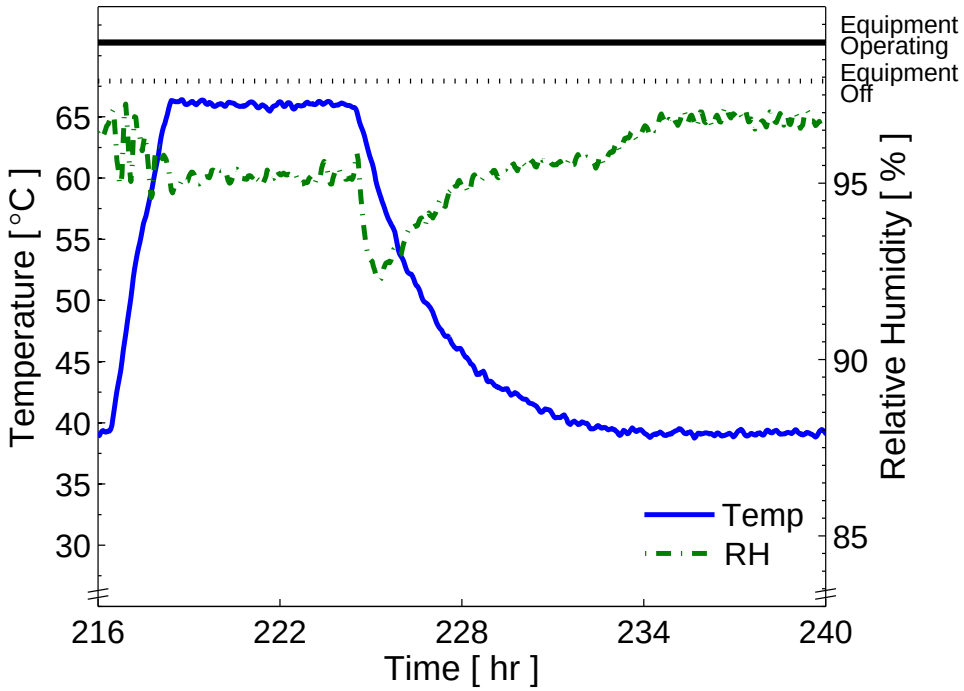

Figure A-21: Experimental humidity test profile, cycle 10, for nodes 0016, 0021, and 0060.

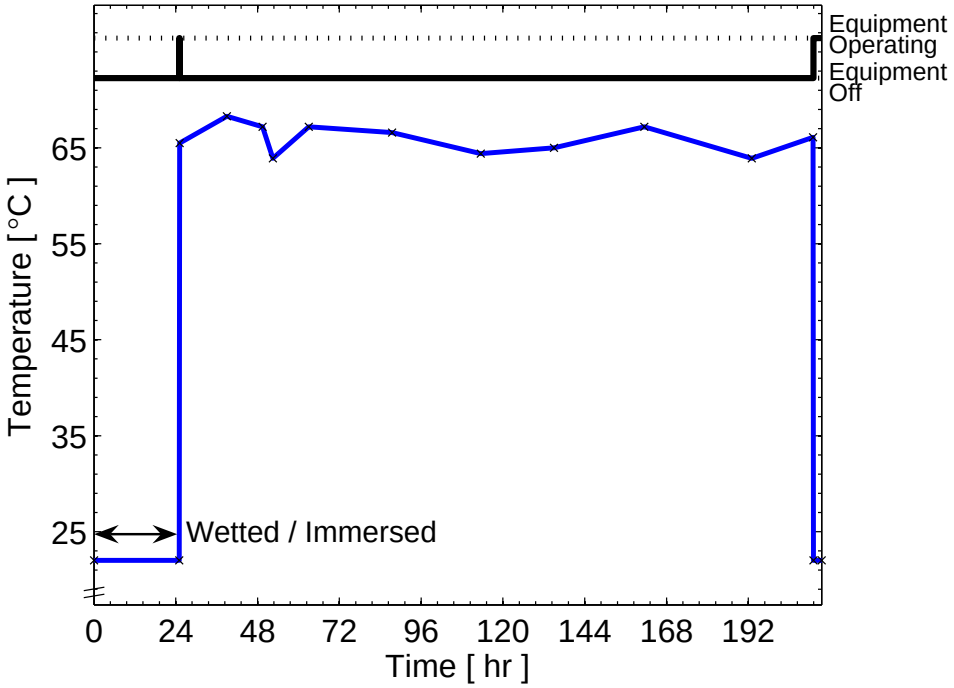

Figure A-22: Experimental oil-based fluid susceptibility test profile for nodes 0010, 0015, and 0052.

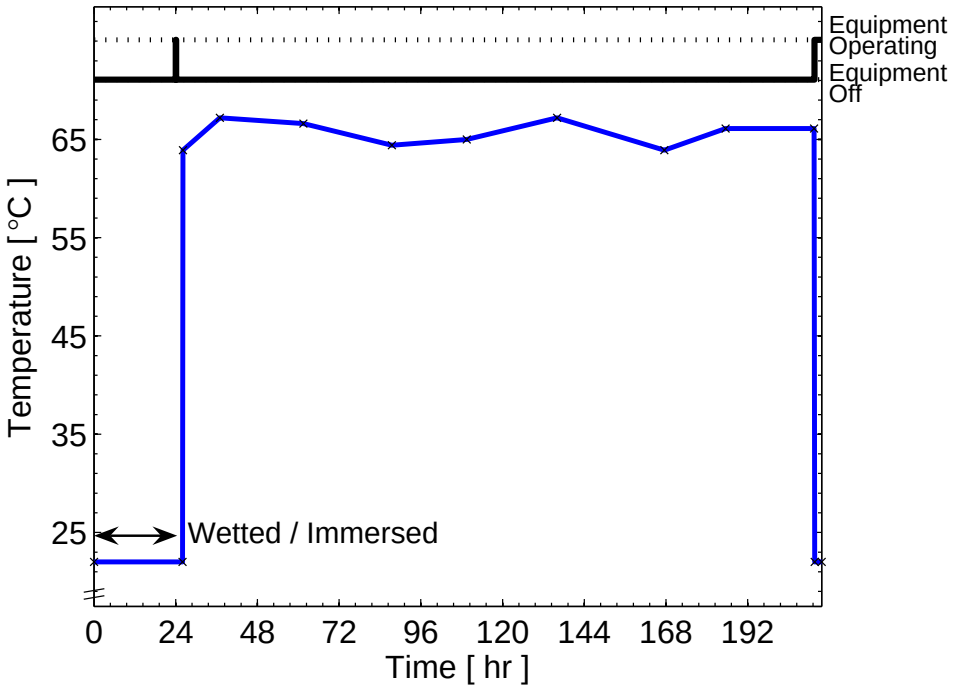

Figure A-23: Experimental water-based fluid susceptibility test profile for nodes 0012, 0203, and 2598.

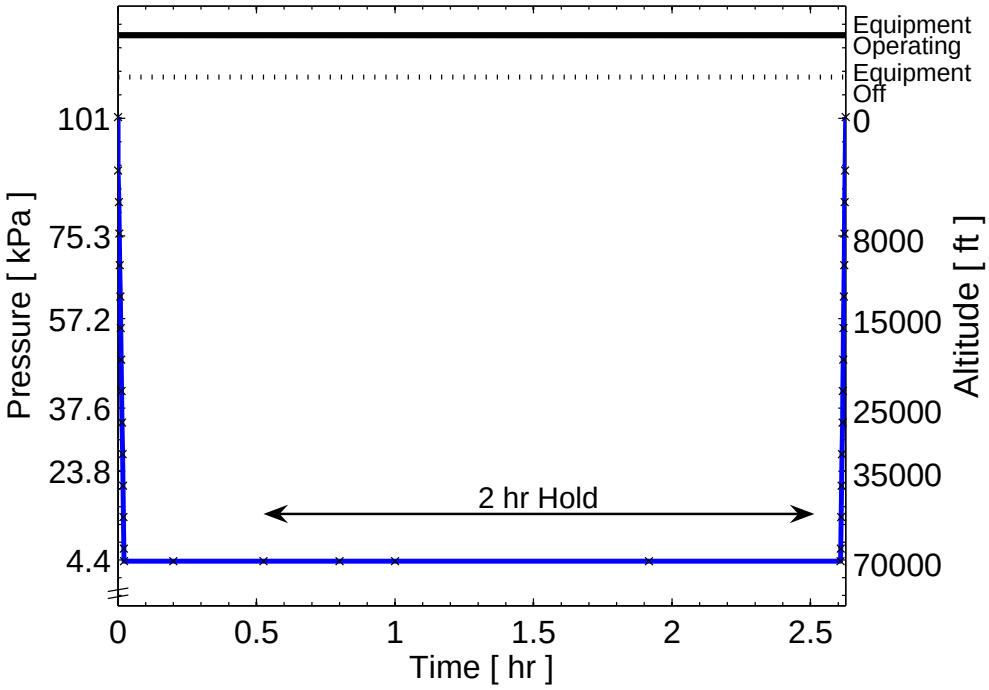

Figure A-24: Experimental altitude test profile for node 2555.

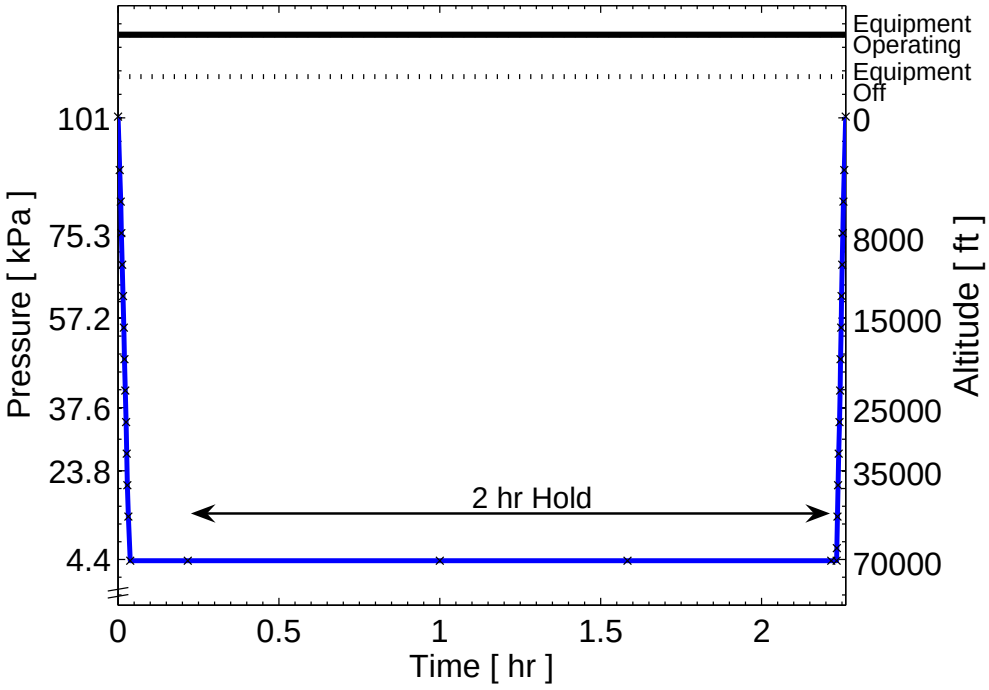

Figure A-25: Experimental altitude test profile for node 2557.

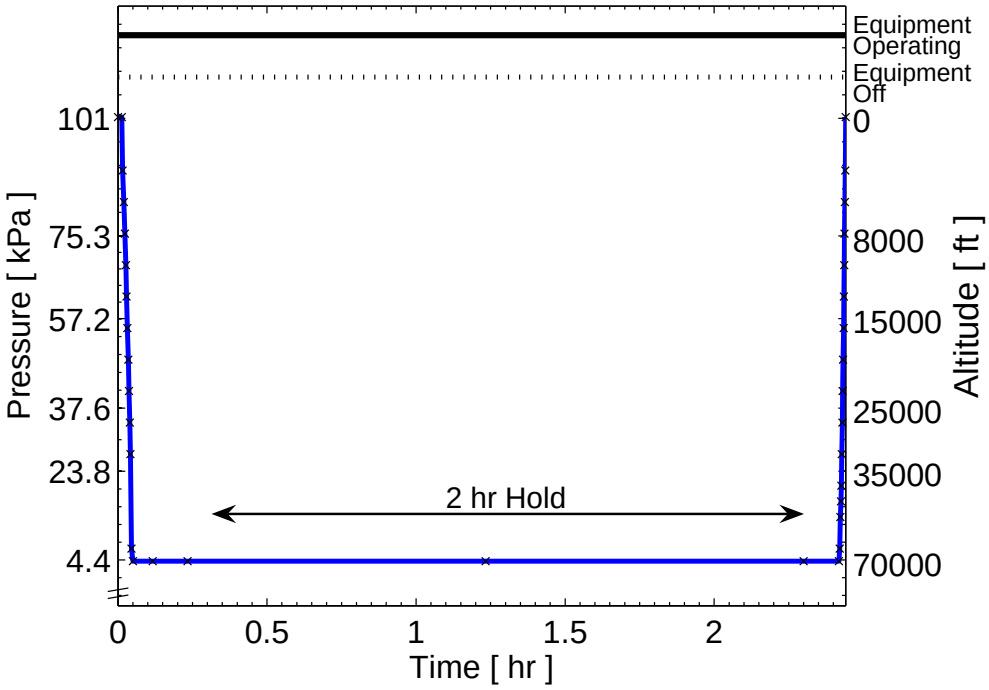

Figure A-26: Experimental altitude test profile for node 2595.

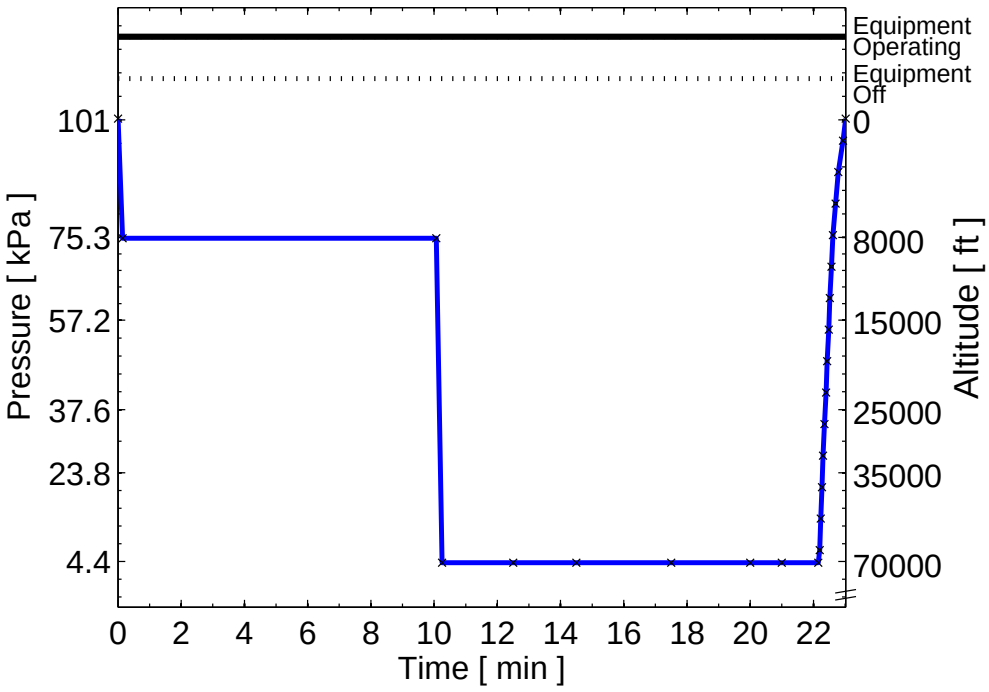

Figure A-27: Experimental decompression test profile for node 0204.

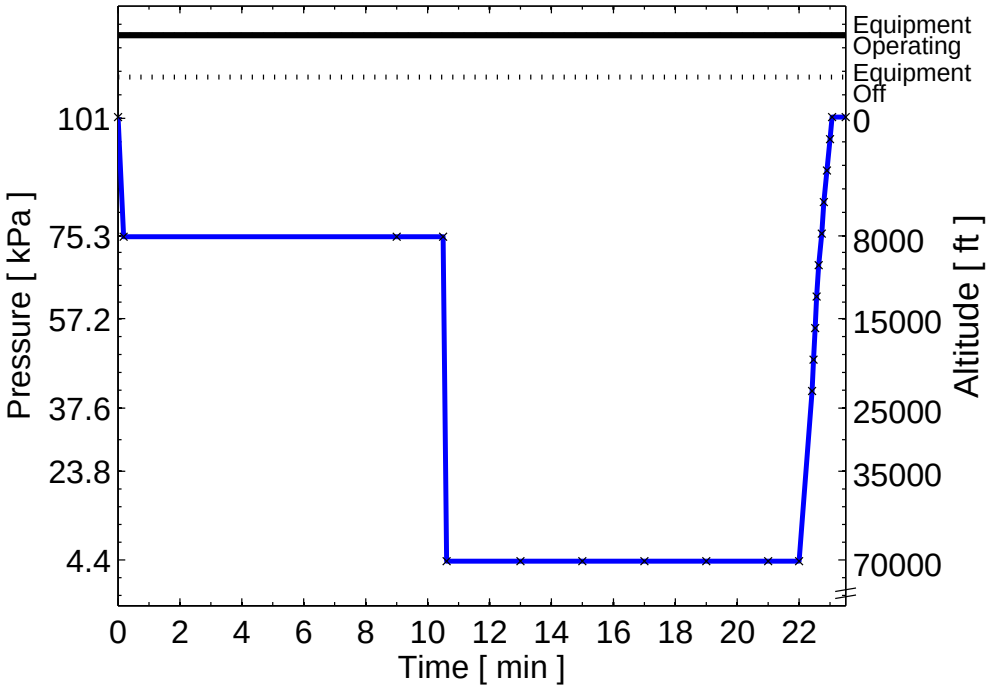

Figure A-28: Experimental decompression test profile for node 2575.

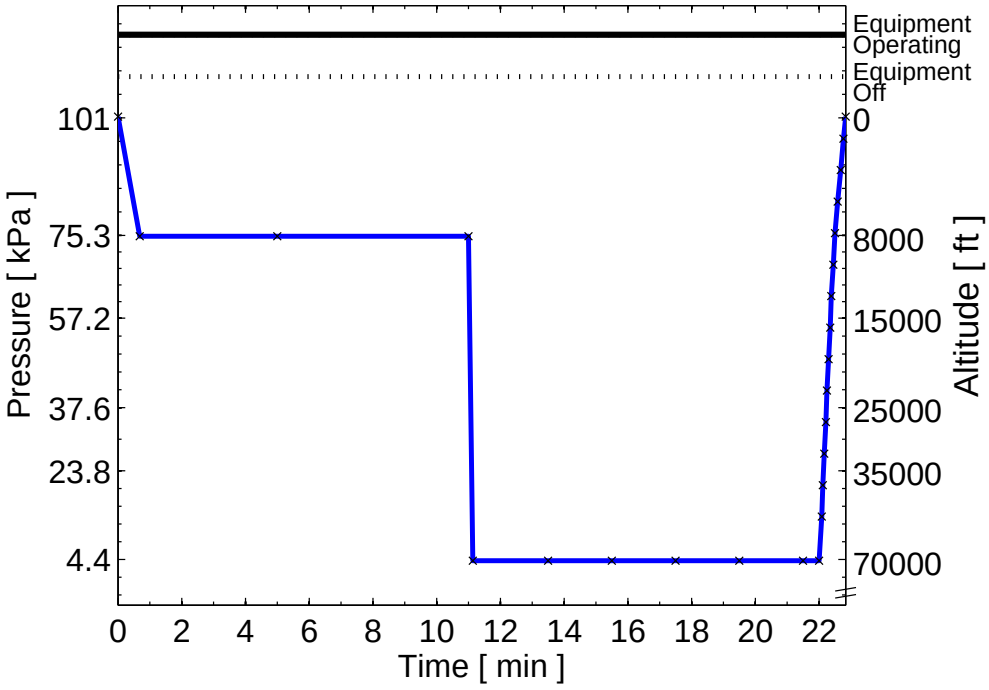

Figure A-29: Experimental decompression test profile for node 2578.

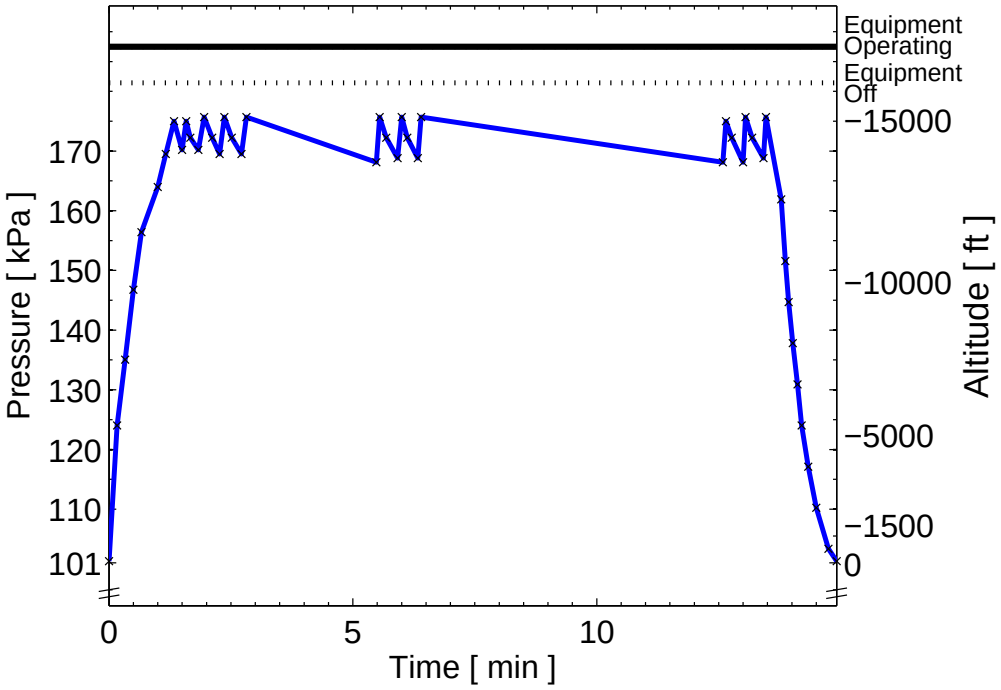

Figure A-30: Experimental overpressure test profile for nodes 0011, 2586, and 2601.

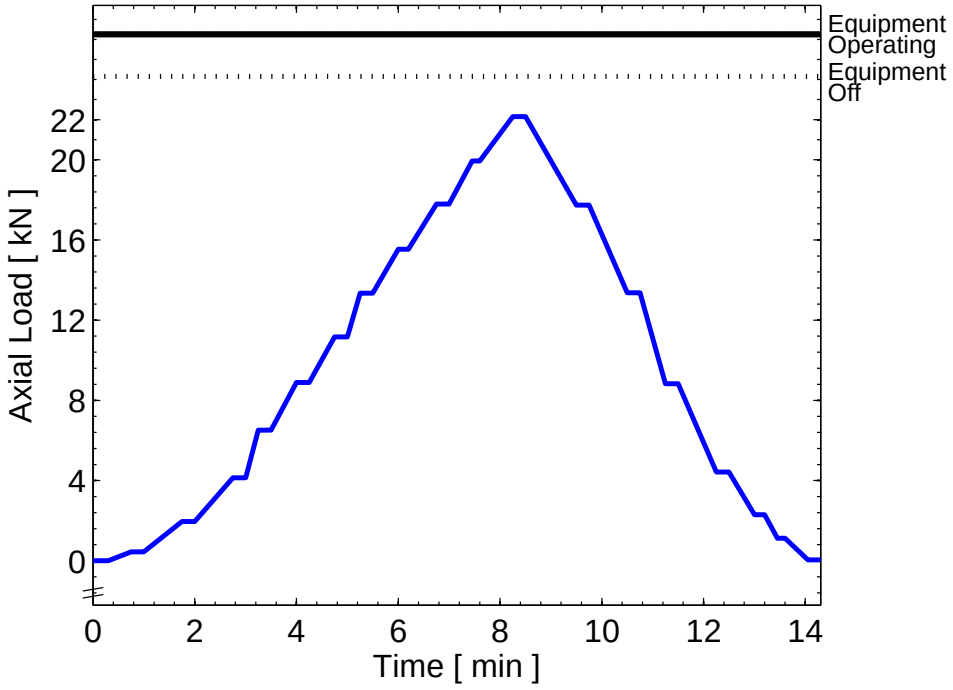

Figure A-31: Experimental static-strain test profile for node 0017.

Appendix B

Experimental Test Signals and Metrics

This appendix contains experimental signals collected for each node and the raw data used for metric analysis. For each node tested, two figures (test signals and envelopes) and a table of the node performance metrics are shown. The test signals shown are from the first of the ten data sets acquired, unless otherwise noted in the figure's caption. The excitation pulse shown is the signal sent to excite the node. This pulse was shown to have small variations over time, and therefore is taken to be the same for each of the three pulse-echo signals (baseline, operational, and post-test signals). The baseline signal is the acquired signal from the node at ambient conditions prior to any environmental change. The operational signal is the node's response part-way through a test as identified in the figure caption. The post-test signal is the response of the node after the test has been completed and ambient conditions have been reestablished.

The experimental signal data is plotted for each node with the signal envelopes shown as dots, $\cdots$, and the location of the maximum voltage of each wavepacket marked with a triangle, $\bigtriangledown$ (*e.g.,* Fig. B-1). The triangles' location gives the times used to calculate the TOF metrics. Each set of test signals is followed by signal envelopes and a table summarizing the metrics for the first two wavepackets of that test, both produced following the procedures detailed in Chapter 5. "x" in a table indicates that no wavepacket could be identified. "Data lost" indicates a somewhat recurring issue of the software on the computer losing communication with the node and crashing, causing a loss of buffered data. "No clamps" indicates that the test was conducted without the boundary clamps described in Section 4.1. The high-temperature and static-strain tests were excited with a driving frequency of 65 kHz and without any on-node averaging of the sensed signals. For these tests, the ten data sets collected were averaged in MATLAB before displaying the signals and analyzing the metrics. For all other tests, a driving frequency of 60 kHz and on-node averaging was used as described in Section 4.2. An irregularity in test signal was noticed on the post-test signal for the high-temperature test of node 0036, Fig. B-3d. The initial wavepacket had a low peak value which set the threshold extremely low allowing the signal noise to be picked up as wavepackets. Because of this, multiple peaks are shown

on the figure. The first TOF and voltage shown in Table B.2 is from the first (after the direct wavepacket) of these peaks. It is also noted that an anomaly occurred with the Hilbert transform when creating the envelopes for: post-test signal of node 0036 (Fig. B-4), baseline and post-test signals of node 0012 (Fig. B-32), post-test signal of node 0203 (Fig. B-34), all signals of node 2555 (Fig. B-38), baseline signal of 0204 (Fig. B-44), and all signals for node 2575 (Fig. B-46). In each of these cases the transform created a wavepacket envelope before the initial pulse (slightly visible to the left extreme of the figures). Inspecting the actual signal from these tests shows no such wavepackets.

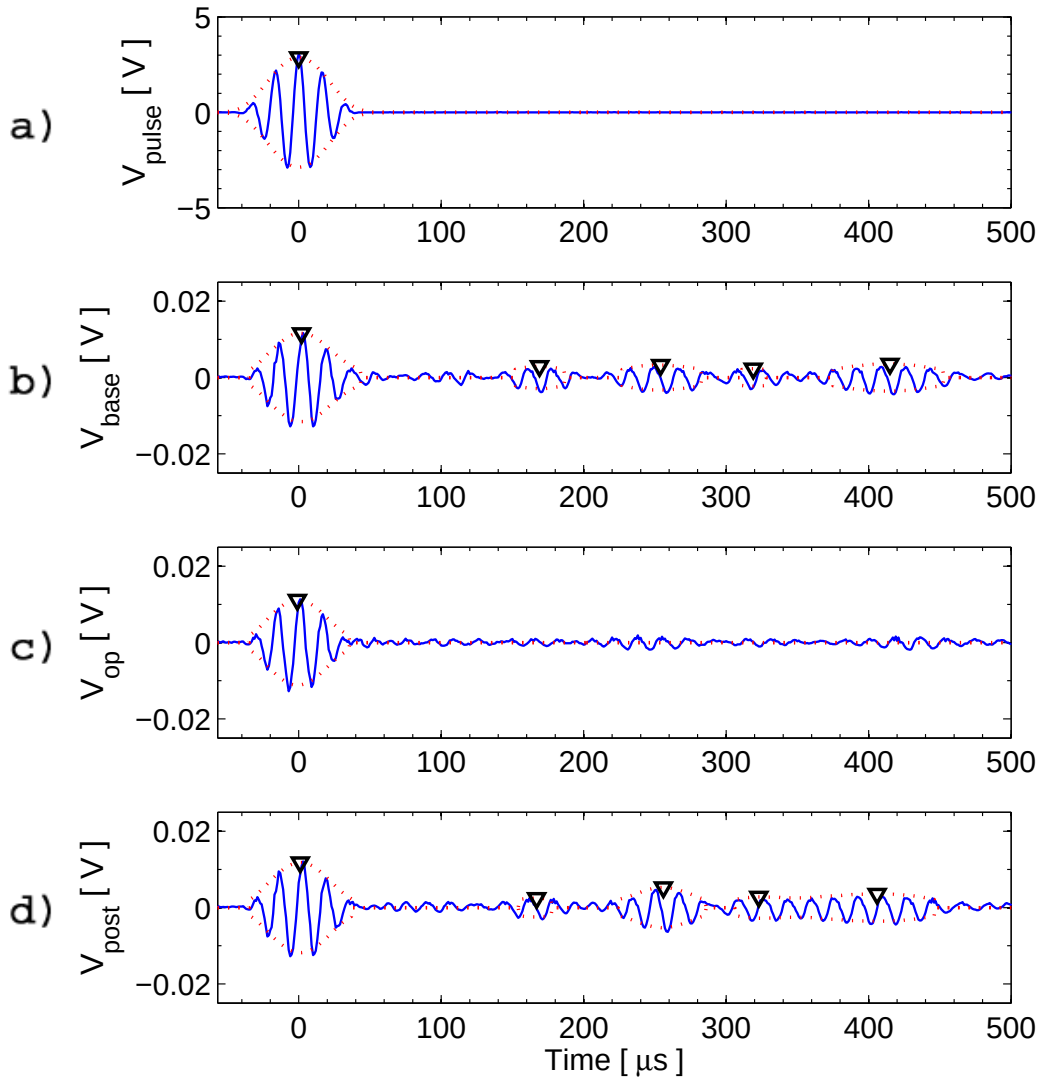

Figure B-1: High-temperature averaged test signals for node 0026. a) Excitation pulse (65 kHz), b) baseline signal at 22°C (time=0 hrs), c) operational signal at 85°C (time=3 hrs), d) post-test signal at 20°C (time=25 hrs).

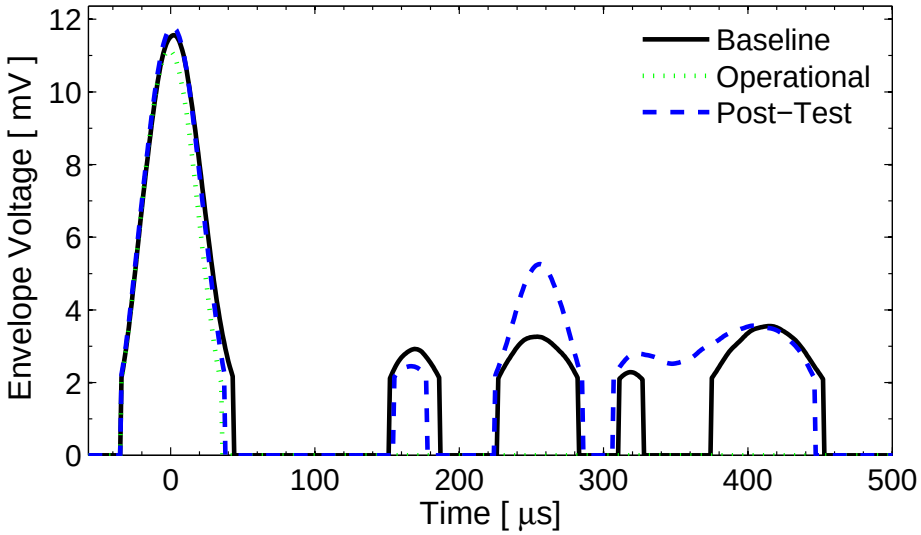

Figure B-2: High-temperature test signal envelopes for node 0026.

Table B.1: Metric values and differences (deltas) of node 0026 for the high-temperature test.

	1^{st} wavepacket			2^{nd} wavepacket		
	Base	Op	Post	Base	Op	Post
TOF [μs]	2	-1	1	169	x	167
ΔTOF [μs]	-	-3	-1	-	x	-2
ΔTOF [%]	-	-150.0	-50.0	-	x	-1.2
V [mV]	11.6	11.1	11.8	2.9	x	2.4
ΔV [mV]	-	-0.5	0.2	-	x	-0.5
ΔV [%]	-	-3.7	1.9	-	x	-16.2

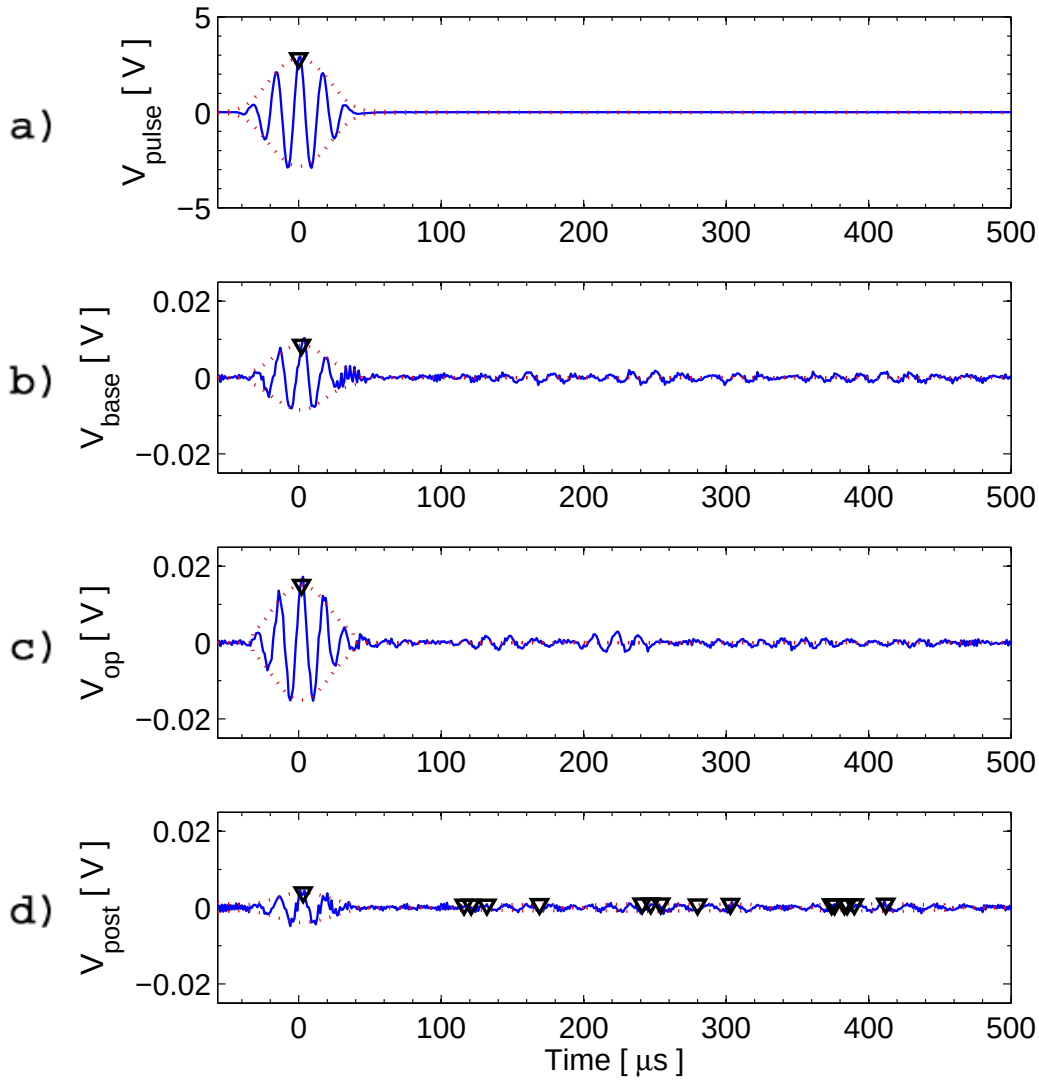

Figure B-3: High-temperature averaged test signals for node 0036. a) Excitation pulse (65 kHz), b) baseline signal at 42°C (time=0.5 hrs), c) operational signal at 85°C (time=2.6 hrs), d) post-test signal at 24°C (time=4.5 hrs).

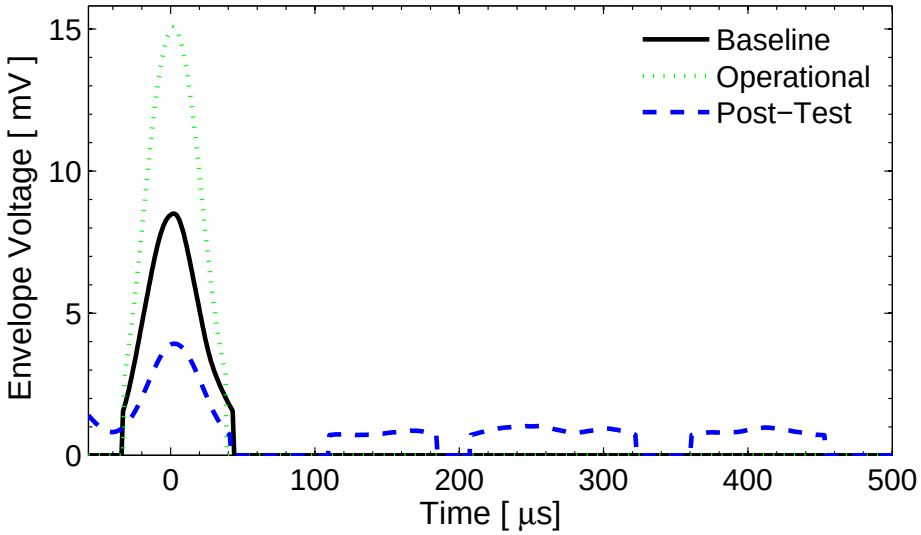

Figure B-4: High-temperature test signal envelopes for node 0036.

Table B.2: Metric values and differences (deltas) of node 0036 for the high-temperature test.

	1^{st} wavepacket			2^{nd} wavepacket		
	Base	Op	Post	Base	Op	Post
TOF [μs]	2	2	3	x	x	116
ΔTOF [μs]	-	0	1	-	x	x
ΔTOF [%]	-	0	50.0	-	x	x
V [mV]	8.5	15.0	3.9	x	x	0.7
ΔV [mV]	-	6.5	-4.6	-	x	x
ΔV [%]	-	77.0	-53.9	-	x	x

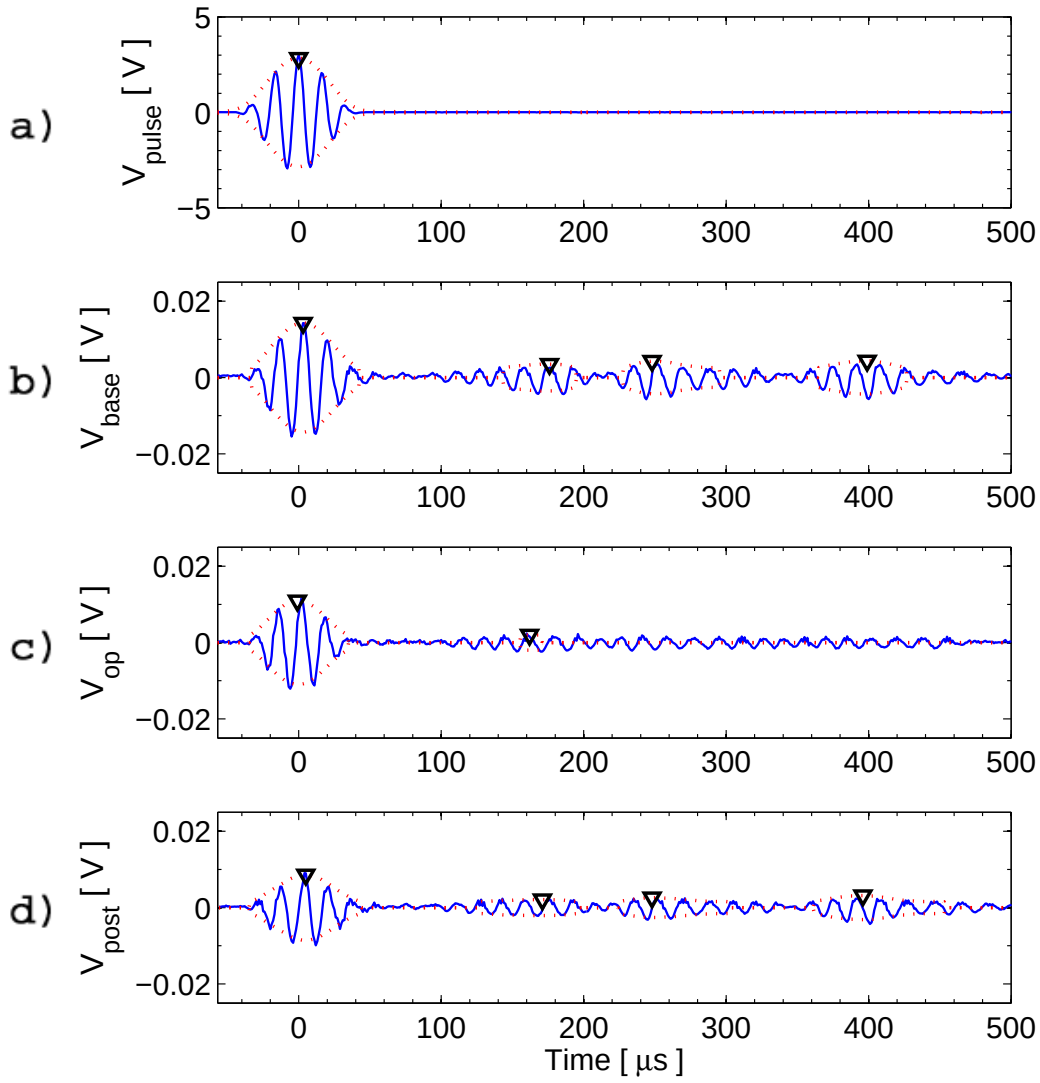

Figure B-5: High-temperature averaged test signals for node 0041. a) Excitation pulse (65 kHz), b) baseline signal at 36°C (time=0 hrs), c) operational signal at 85°C (time=3 hrs), d) post-test signal at 23°C (time=4.5 hrs).

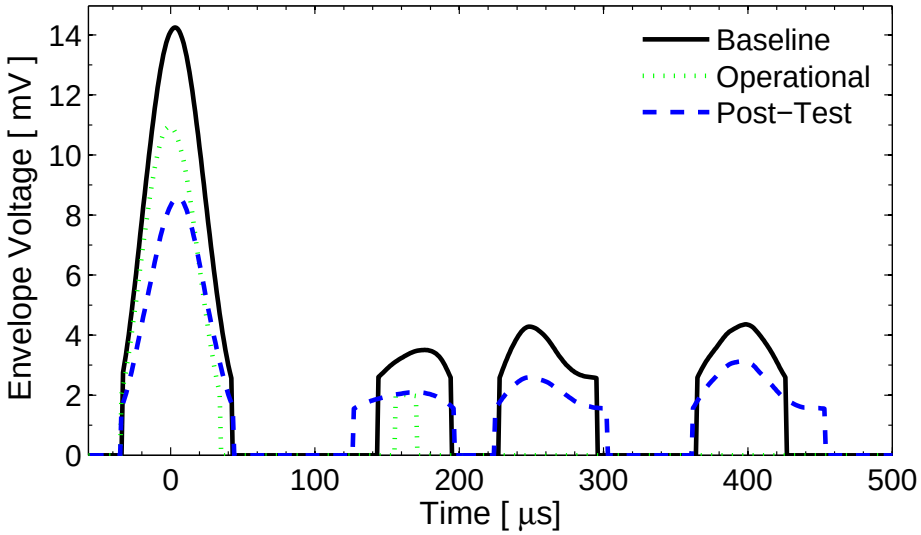

Figure B-6: High-temperature test signal envelopes for node 0041.

Table B.3: Metric values and differences (deltas) of node 0041 for the high-temperature test.

	1^{st} wavepacket			2^{nd} wavepacket		
	Base	Op	Post	Base	Op	Post
TOF [μs]	3	-1	5	176	162	171
ΔTOF [μs]	-	-4	2	-	-14	-5
ΔTOF [%]	-	-133.3	66.7	-	-7.9	-2.8
V [mV]	14.2	10.9	8.6	3.5	2.0	2.1
ΔV [mV]	-	-3.3	-5.6	-	-1.5	-1.4
ΔV [%]	-	-23.2	-39.7	-	-42.7	-40.2

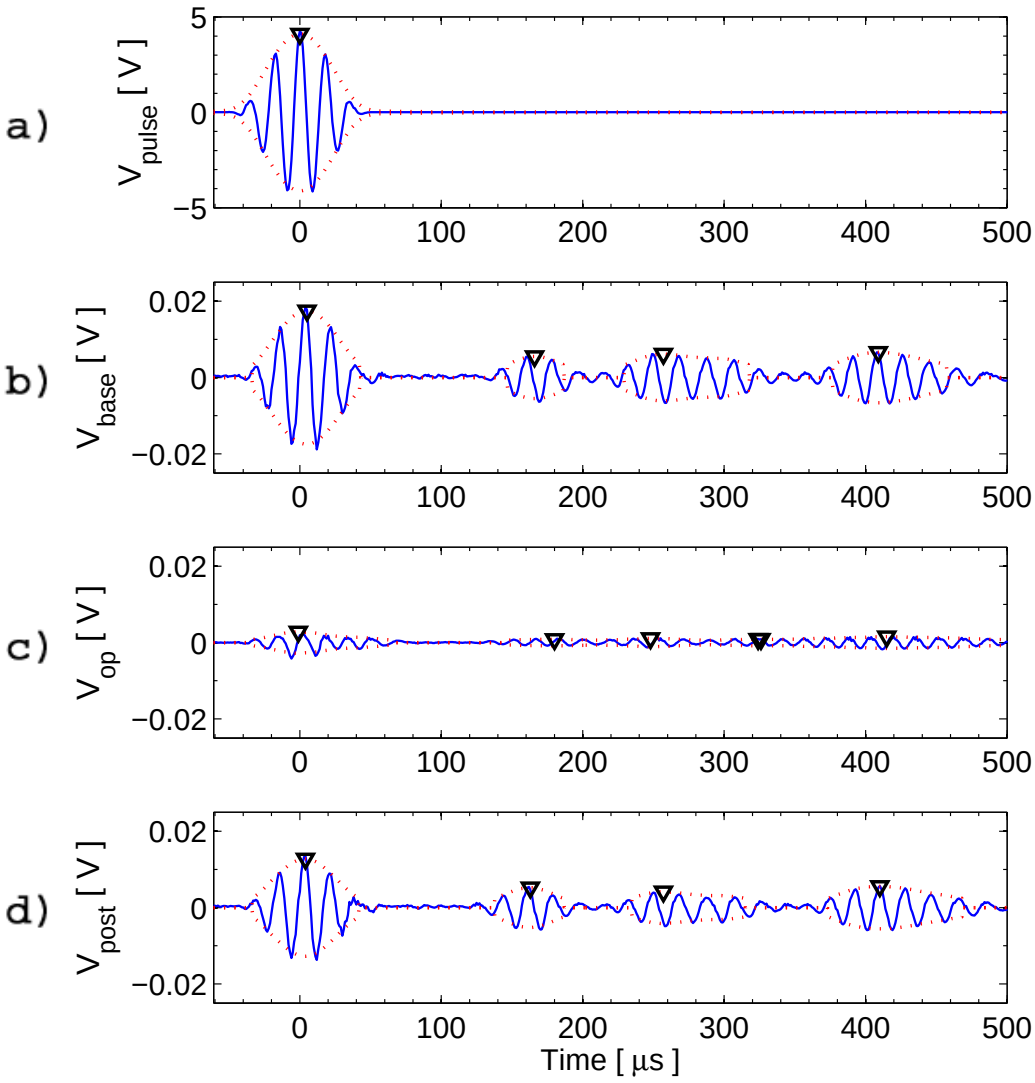

Figure B-7: Low-temperature test signals for node 0029, data set 10. a) Excitation pulse, b) baseline signal at 23°C (time=0 hrs), c) operational signal at -55°C (time=1 hrs), d) post-test signal at 22°C (time=3.7 hrs).

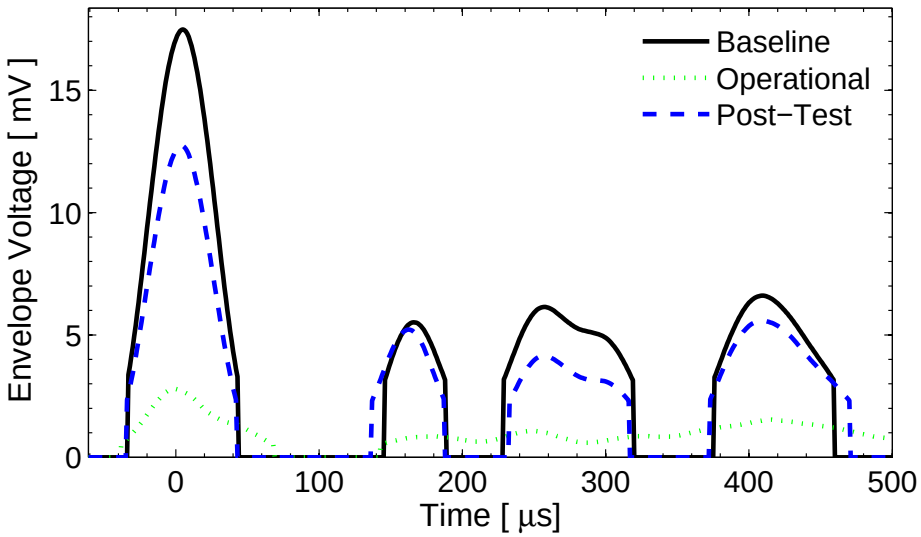

Figure B-8: Low-temperature test signal envelopes for node 0029.

Table B.4: Metric values and differences (deltas) of node 0029 for the low-temperature test.

	1^{st} wavepacket			2^{nd} wavepacket		
	Base	Op	Post	Base	Op	Post
TOF [μs]	5	-1	4	166	180	163
ΔTOF [μs]	-	-6	-1	-	14	-3
ΔTOF [%]	-	-120.0	-20.0	-	8.4	-1.8
V [mV]	17.5	2.8	12.7	5.5	0.9	5.2
ΔV [mV]	-	-14.7	-4.7	-	-4.7	-0.3
ΔV [%]	-	-84.0	-27.1	-	-84.5	-5.3

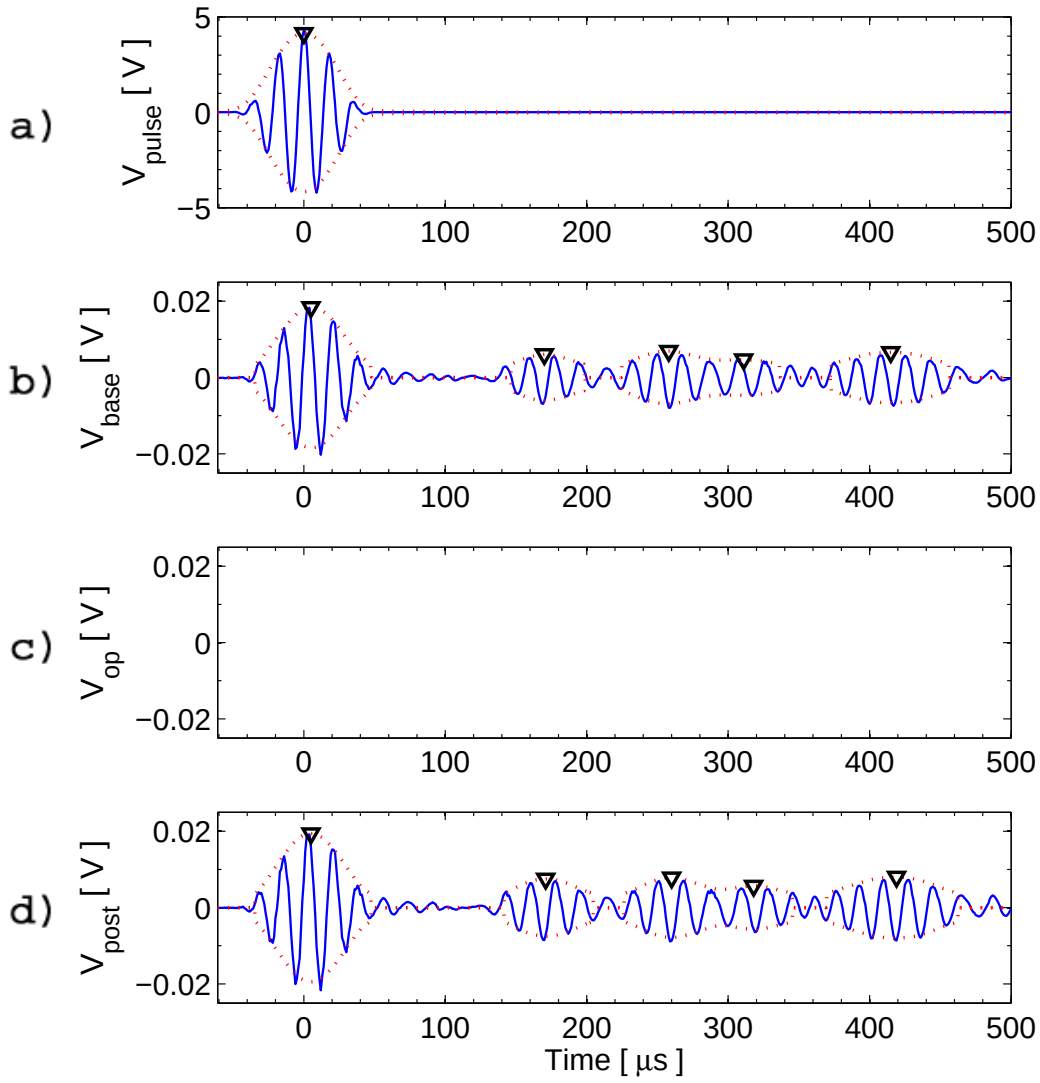

Figure B-9: Low-temperature test signals for node 0049, data set 10. a) Excitation pulse, b) baseline signal at 23°C (time=0), c) operational signal data lost, d) post-test signal at 21°C (time=4 hrs).

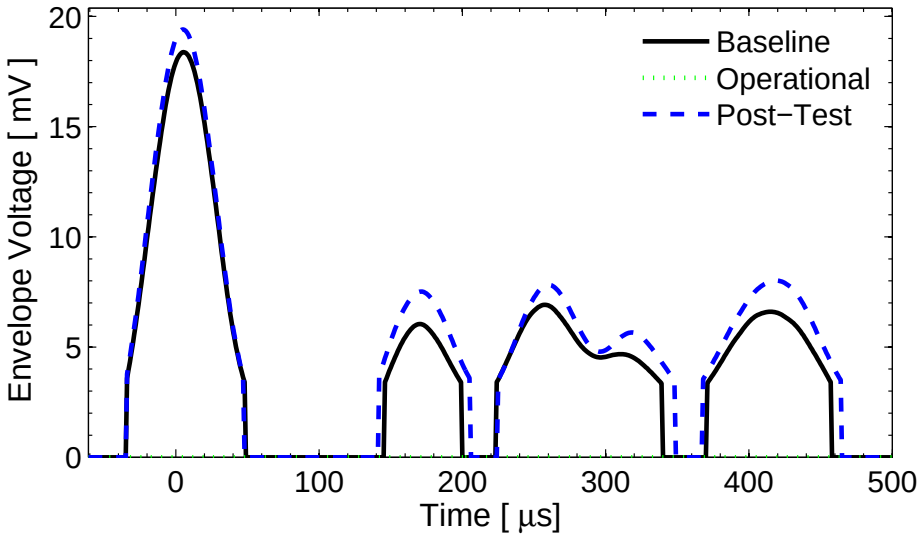

Figure B-10: Low-temperature test signal envelopes for node 0049.

Table B.5: Metric values and differences (deltas) of node 0049 for the low-temperature test.

	1^{st} wavepacket			2^{nd} wavepacket		
	Base	Op	Post	Base	Op	Post
TOF [μs]	5	-	5	170	-	171
ΔTOF [μs]	-	-	0	-	-	1
ΔTOF [%]	-	-	0	-	-	0.6
V [mV]	18.4	-	19.4	6.0	-	7.5
ΔV [mV]	-	-	1.0	-	-	1.5
ΔV [%]	-	-	5.6	-	-	24.4

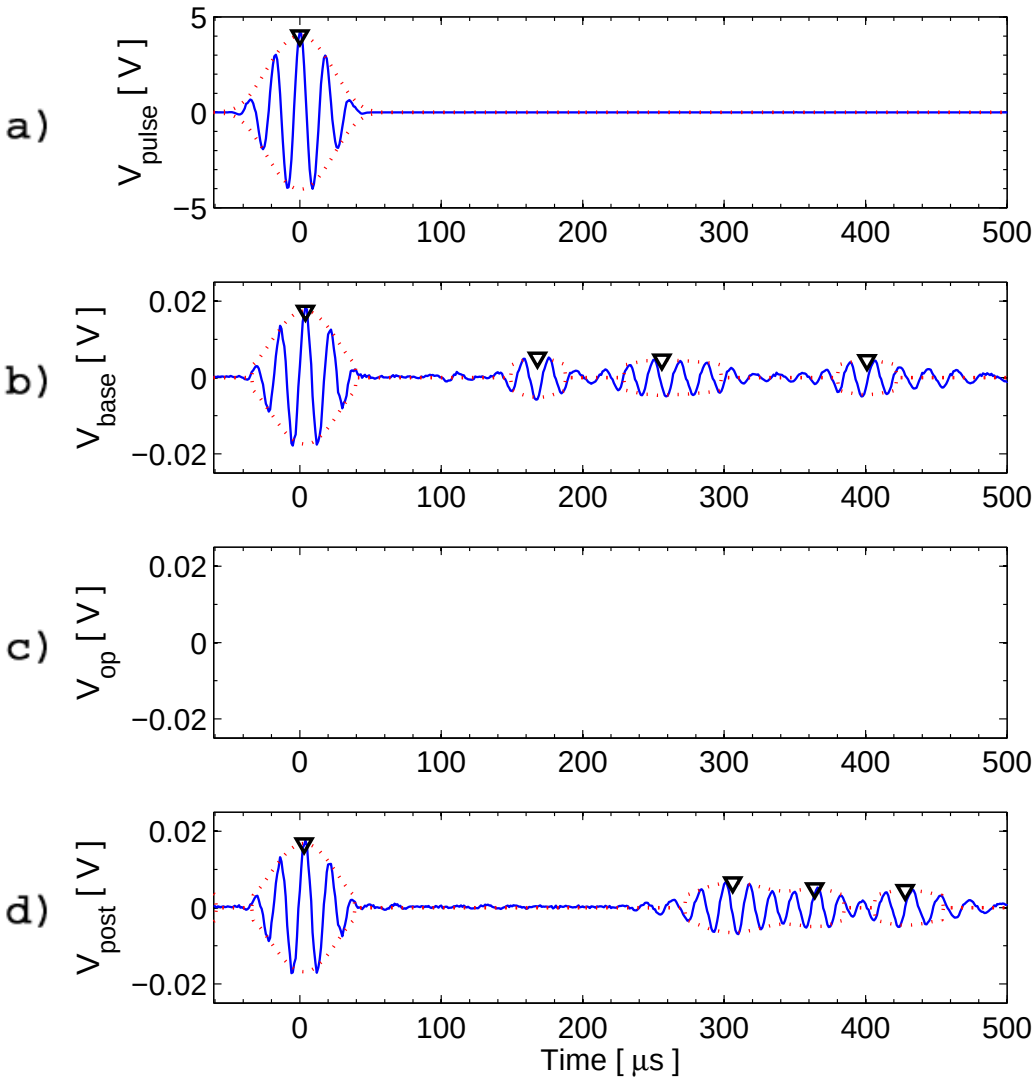

Figure B-11: Low-temperature test signals for node 0068, data set 9. a) Excitation pulse, b) baseline signal at $22°C$ (time=0 hrs), c) operational signal data lost, d) post-test signal at $22°C$ (time=20 hrs).

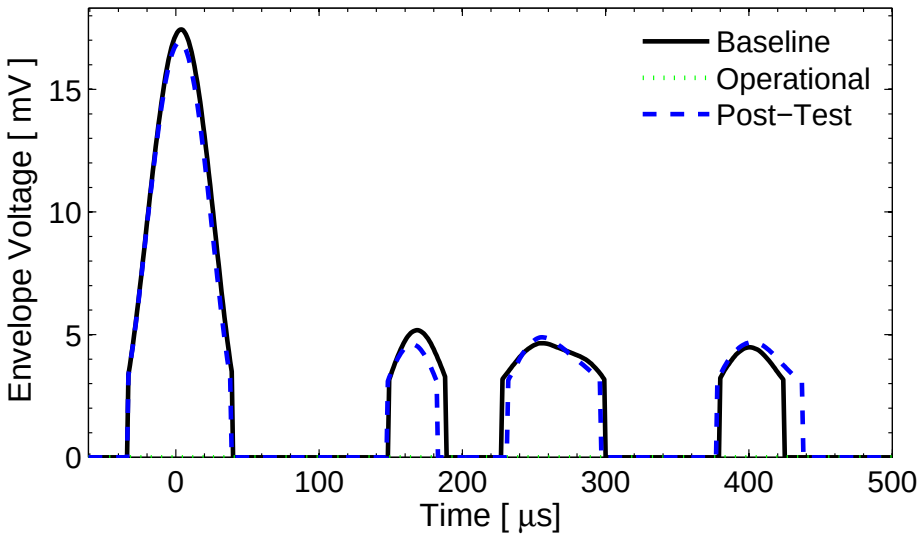

Figure B-12: Low-temperature test signal envelopes for node 0068.

Table B.6: Metric values and differences (deltas) of node 0068 for the low-temperature test.

	1^{st} wavepacket			2^{nd} wavepacket		
	Base	Op	Post	Base	Op	Post
TOF [μs]	4	-	3	168	-	165
ΔTOF [μs]	-	-	-1	-	-	-3
ΔTOF [%]	-	-	-25.0	-	-	-1.8
V [mV]	17.4	-	16.9	5.2	-	4.6
ΔV [mV]	-	-	-0.5	-	-	-0.6
ΔV [%]	-	-	-2.9	-	-	-11.0

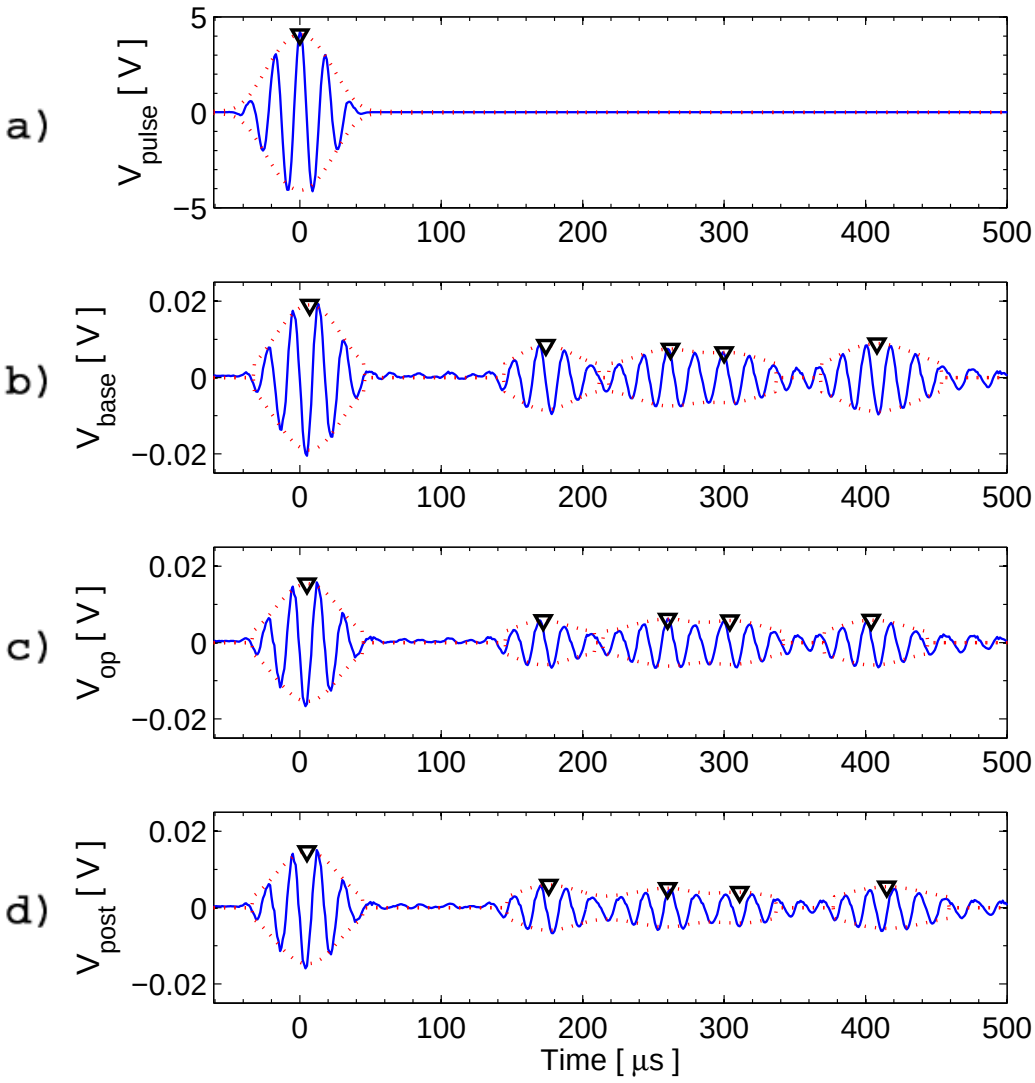

Figure B-13: Thermal shock test signals for node 0034, data set 8. a) Excitation pulse, b) baseline signal at $21°C$ (time=0 hrs), c) operational signal at $25°C$ (time=3.6 hrs), d) post-test signal at $21°C$ (time=21.6 hrs).

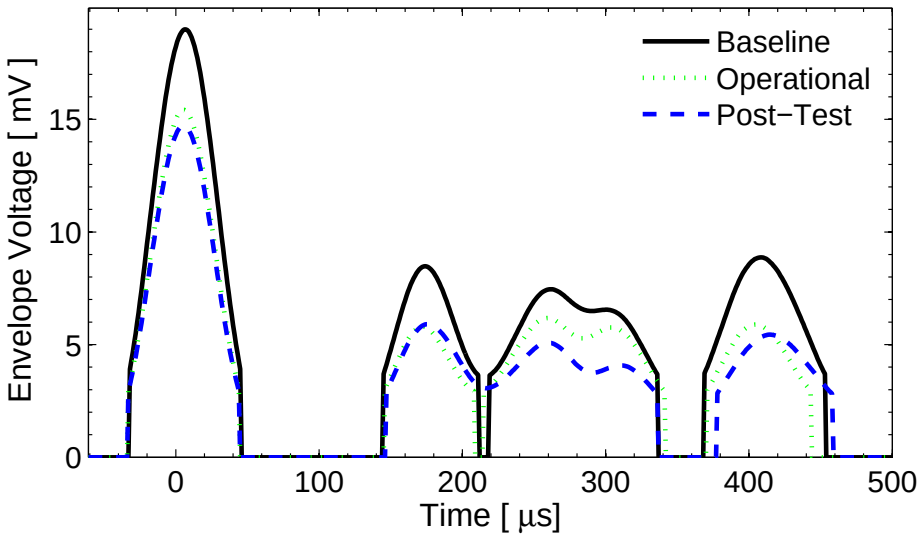

Figure B-14: Thermal shock test signal envelopes for node 0034.

Table B.7: Metric values and differences (deltas) of node 0034 for the thermal shock test.

	1^{st} wavepacket			2^{nd} wavepacket		
	Base	Op	Post	Base	Op	Post
TOF [μs]	7	5	5	174	172	176
ΔTOF [μs]	-	-2	-2	-	-2	2
ΔTOF [%]	-	-28.6	-28.6	-	-1.1	1.1
V [mV]	19.0	15.4	14.7	8.5	5.8	5.9
ΔV [mV]	-	-3.6	-4.3	-	-2.7	-2.6
ΔV [%]	-	-18.8	-22.5	-	-31.5	-30.3

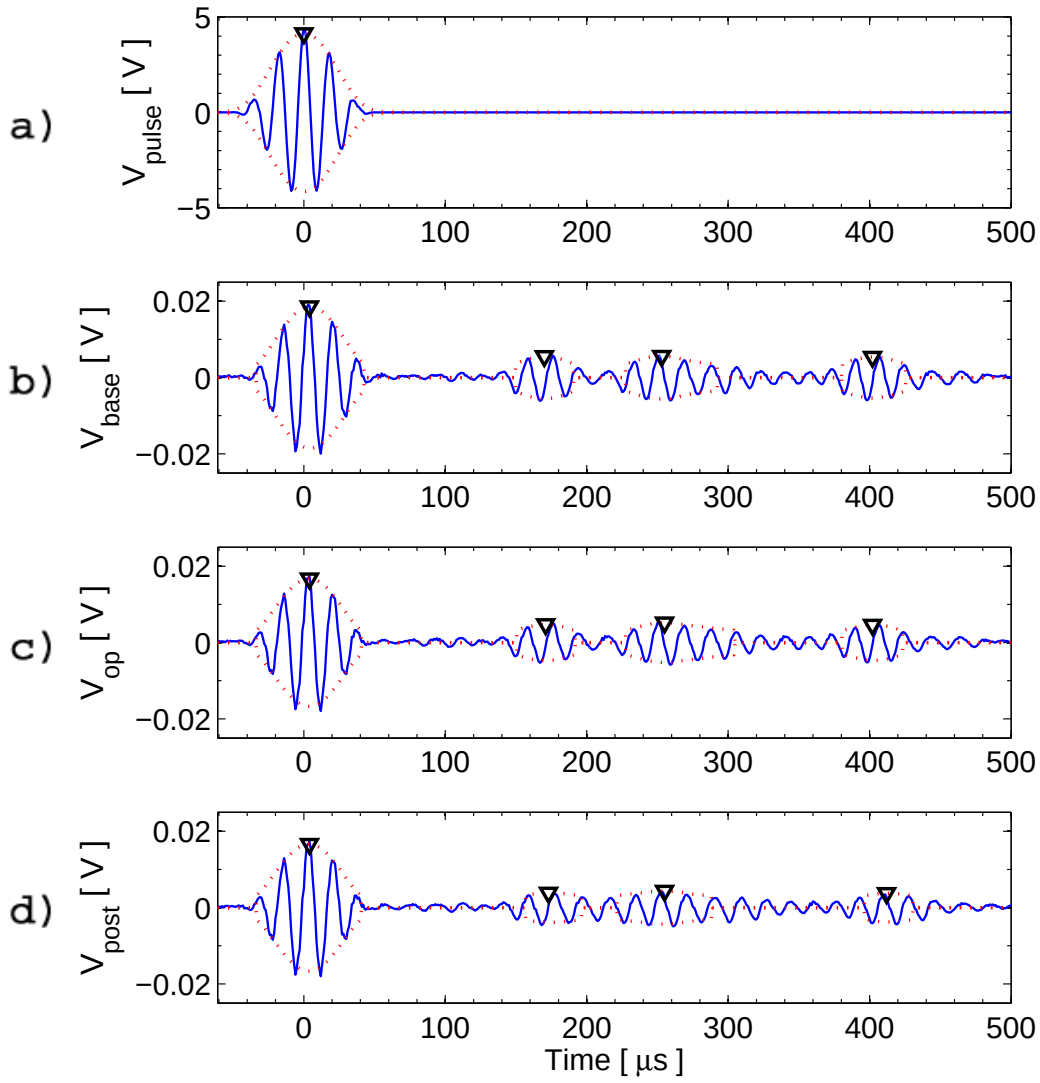

Figure B-15: Thermal shock test signals for node 0046, data set 2. a) Excitation pulse, b) baseline signal at $22°C$ (time=0 hrs), c) operational signal at $24°C$ (time=3.7 hrs), d) post-test signal at $22°C$ (time=24.7 hrs).

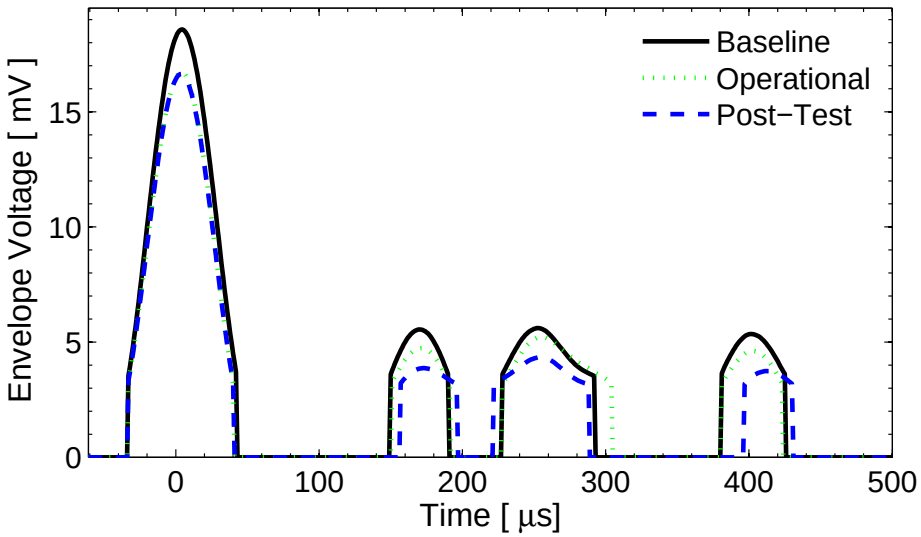

Figure B-16: Thermal shock test signal envelopes for node 0046.

Table B.8: Metric values and differences (deltas) of node 0046 for the thermal shock test.

	1^{st} wavepacket			2^{nd} wavepacket		
	Base	Op	Post	Base	Op	Post
TOF [μs]	4	4	4	170	171	173
ΔTOF [μs]	-	0	0	-	1	3
ΔTOF [%]	-	0	0	-	0.6	1.8
V [mV]	18.6	16.7	16.6	5.5	4.7	3.9
ΔV [mV]	-	-1.9	-2.0	-	-0.8	-1.6
ΔV [%]	-	-10.0	-10.4	-	-14.6	-30.2

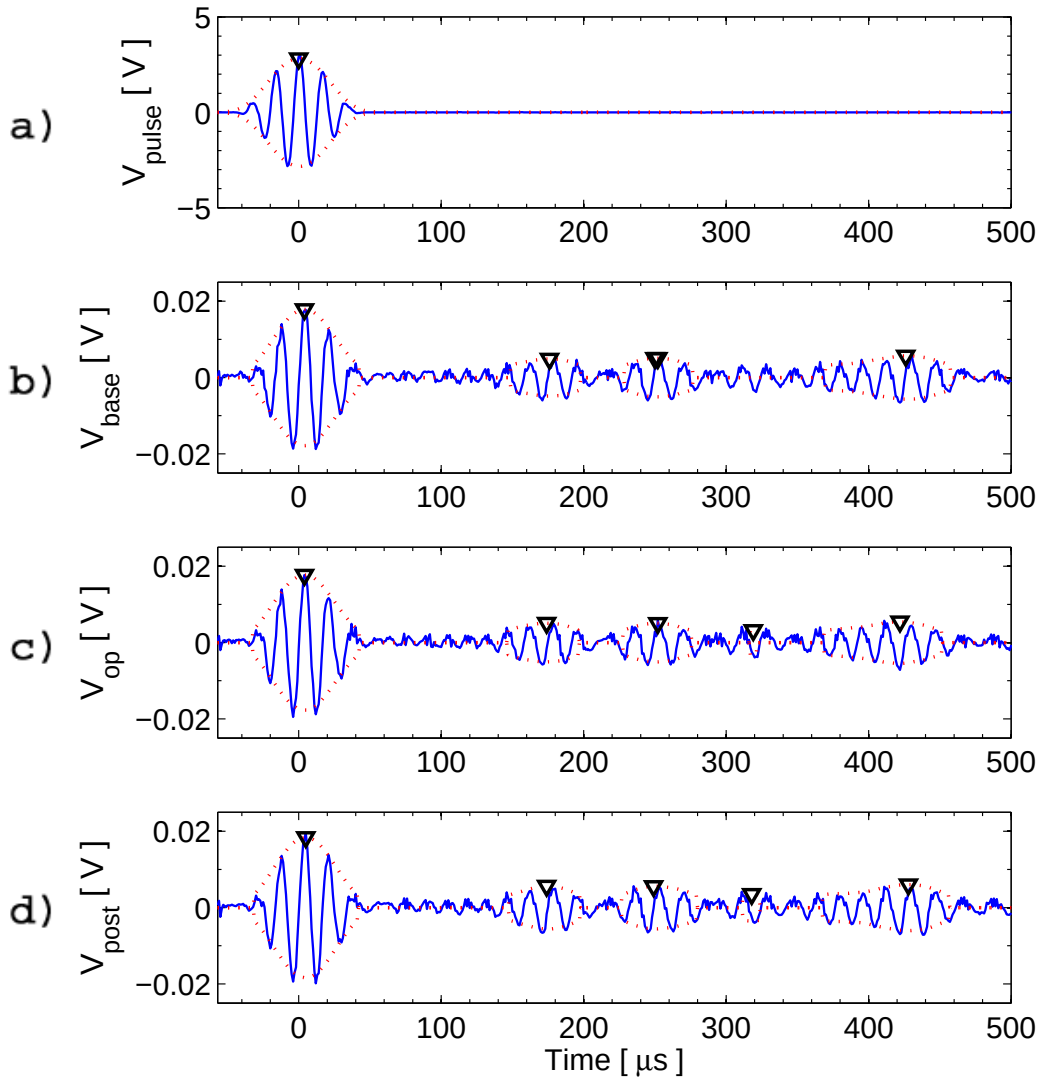

Figure B-17: Thermal shock test signals for node 0061. a) Excitation pulse, b) baseline signal at 22°C (time=0 hrs), c) operational signal at 26°C (time=3.7 hrs), d) post-test signal at 22°C (time=27.7 hrs).

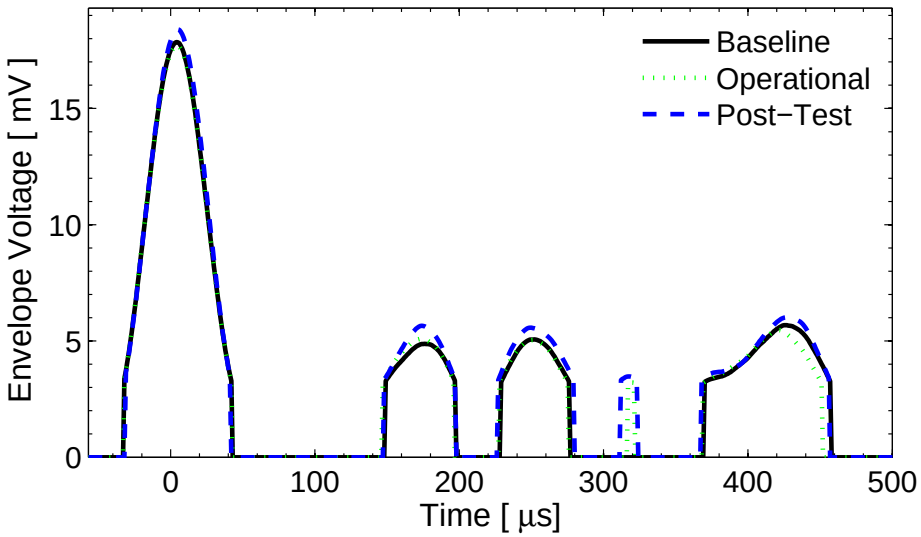

Figure B-18: Thermal shock test signal envelopes for node 0061.

Table B.9: Metric values and differences (deltas) of node 0061 for the thermal shock test.

	1^{st} wavepacket			2^{nd} wavepacket		
	Base	Op	Post	Base	Op	Post
TOF [μs]	4	4	5	176	174	174
ΔTOF [μs]	-	0	1	-	-2	-2
ΔTOF [%]	-	0	25.0	-	-1.1	-1.1
V [mV]	17.8	17.7	18.4	4.9	5.1	5.6
ΔV [mV]	-	-0.1	0.6	-	0.2	0.7
ΔV [%]	-	-0.8	3.1	-	4.4	16.0

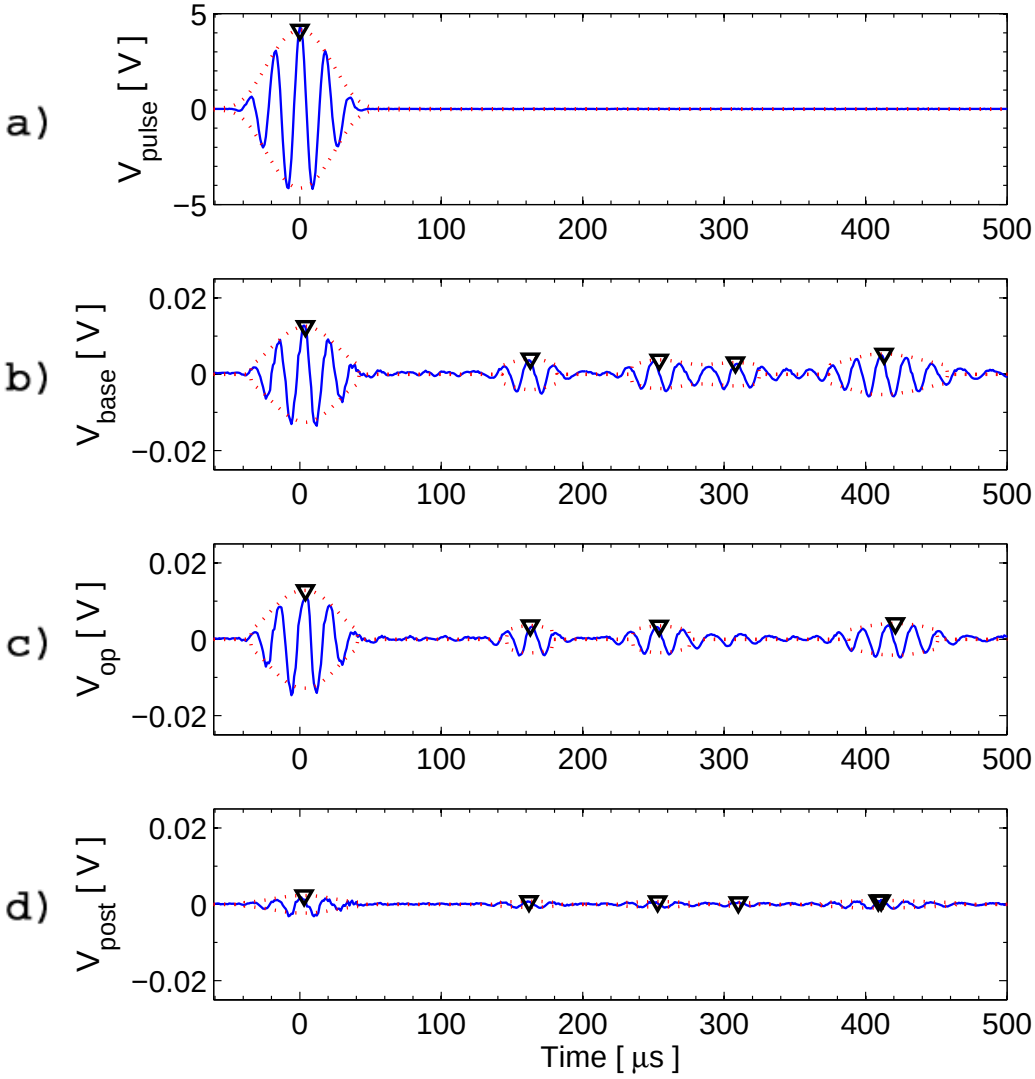

Figure B-19: Humidity test signals for node 0016, data set 3. a) Excitation pulse, b) baseline signal at 23°C and 59%RH (time=0 hrs), c) operational signal at 39.4°C and 97.1%RH (time=120.5 hrs), d) post-test signal at 26°C and 59.7%RH (time=241 hrs).

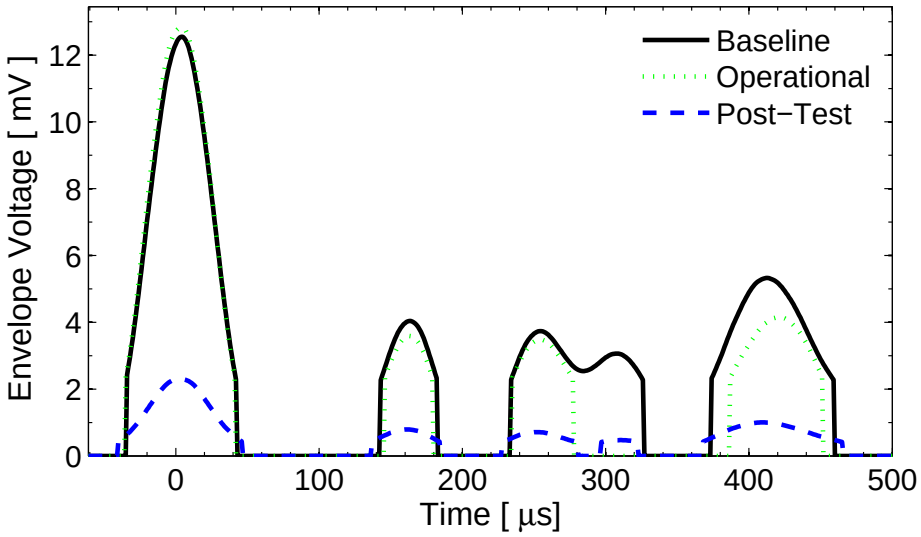

Figure B-20: Humidity test signal envelopes for node 0016.

Table B.10: Metric values and differences (deltas) of node 0016 for the humidity test.

	1^{st} wavepacket			2^{nd} wavepacket		
	Base	Op	Post	Base	Op	Post
TOF [μs]	4	4	3	163	163	162
ΔTOF [μs]	-	0	-1	-	0	-1
ΔTOF [%]	-	0	-25.0	-	0	-0.6
V [mV]	12.5	12.8	2.3	4.0	3.6	0.8
ΔV [mV]	-	0.3	-10.2	-	-0.4	-3.2
ΔV [%]	-	2.0	-81.6	-	-11.2	-80.4

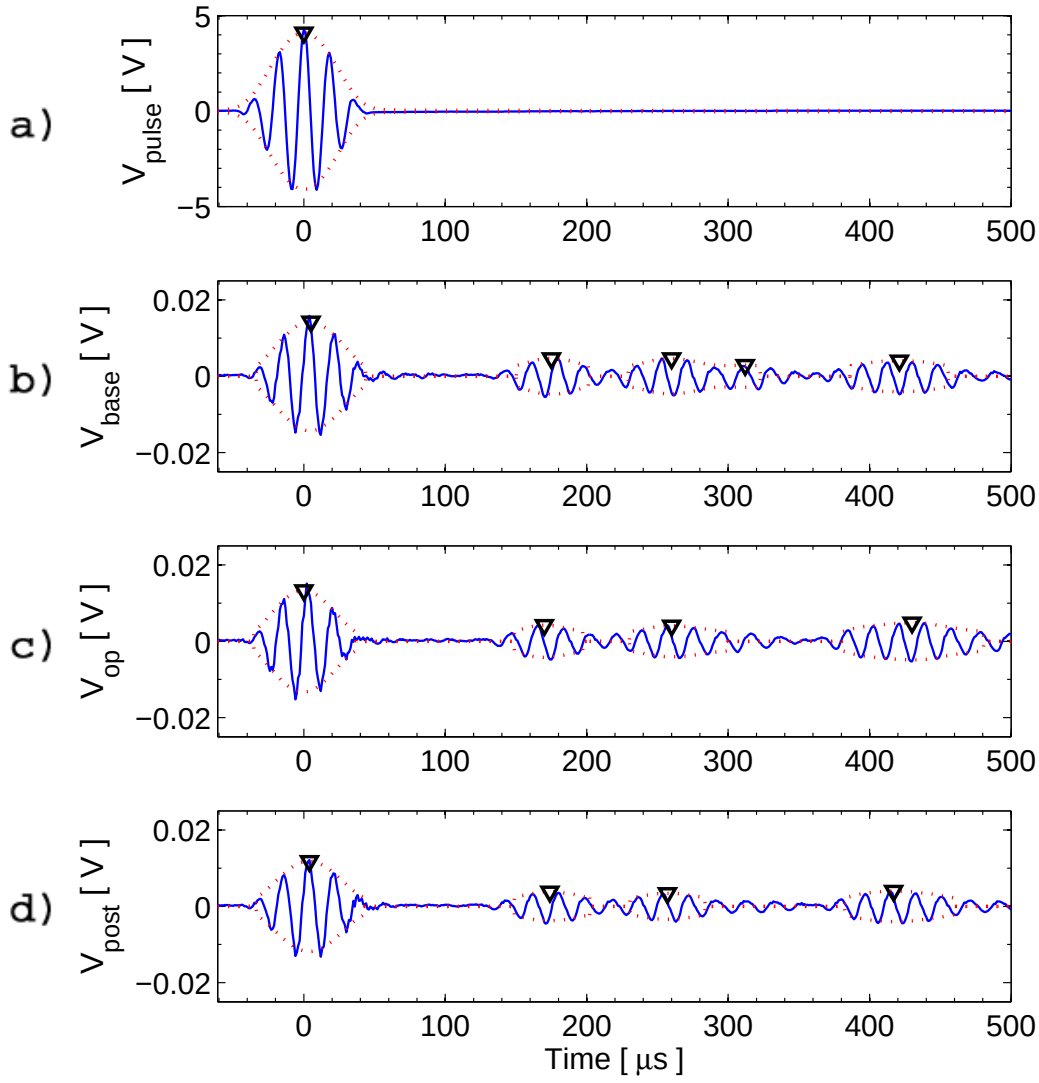

Figure B-21: Humidity test signals for node 0021, data set 5. a) Excitation pulse, b) baseline signal at 23°C and 59.0%RH (time=0 hrs), c) operational signal at 65°C and 94.8%RH (time=200.5 hrs), d) post-test signal at 26°C and 59.7%RH (time=241 hrs).

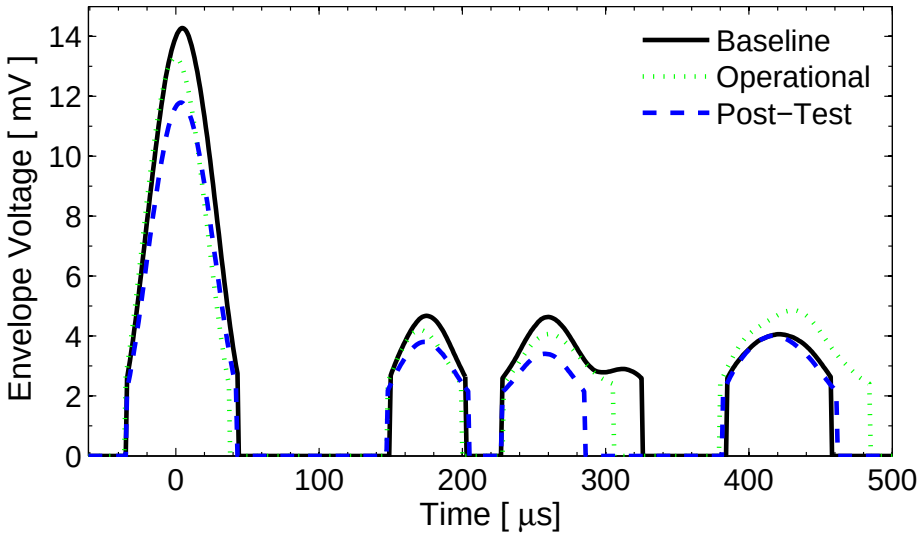

Figure B-22: Humidity test signal envelopes for node 0021.

Table B.11: Metric values and differences (deltas) of node 0021 for the humidity test.

	1^{st} wavepacket			2^{nd} wavepacket		
	Base	Op	Post	Base	Op	Post
TOF [μs]	5	0	4	175	170	174
ΔTOF [μs]	-	-5	-1	-	-5	-1
ΔTOF [%]	-	-100	-20.0	-	-2.9	-0.6
V [mV]	14.3	13.3	11.8	4.7	4.2	3.8
ΔV [mV]	-	-1.0	-2.5	-	-0.5	-0.9
ΔV [%]	-	-7.0	-17.4	-	-10.3	-18.6

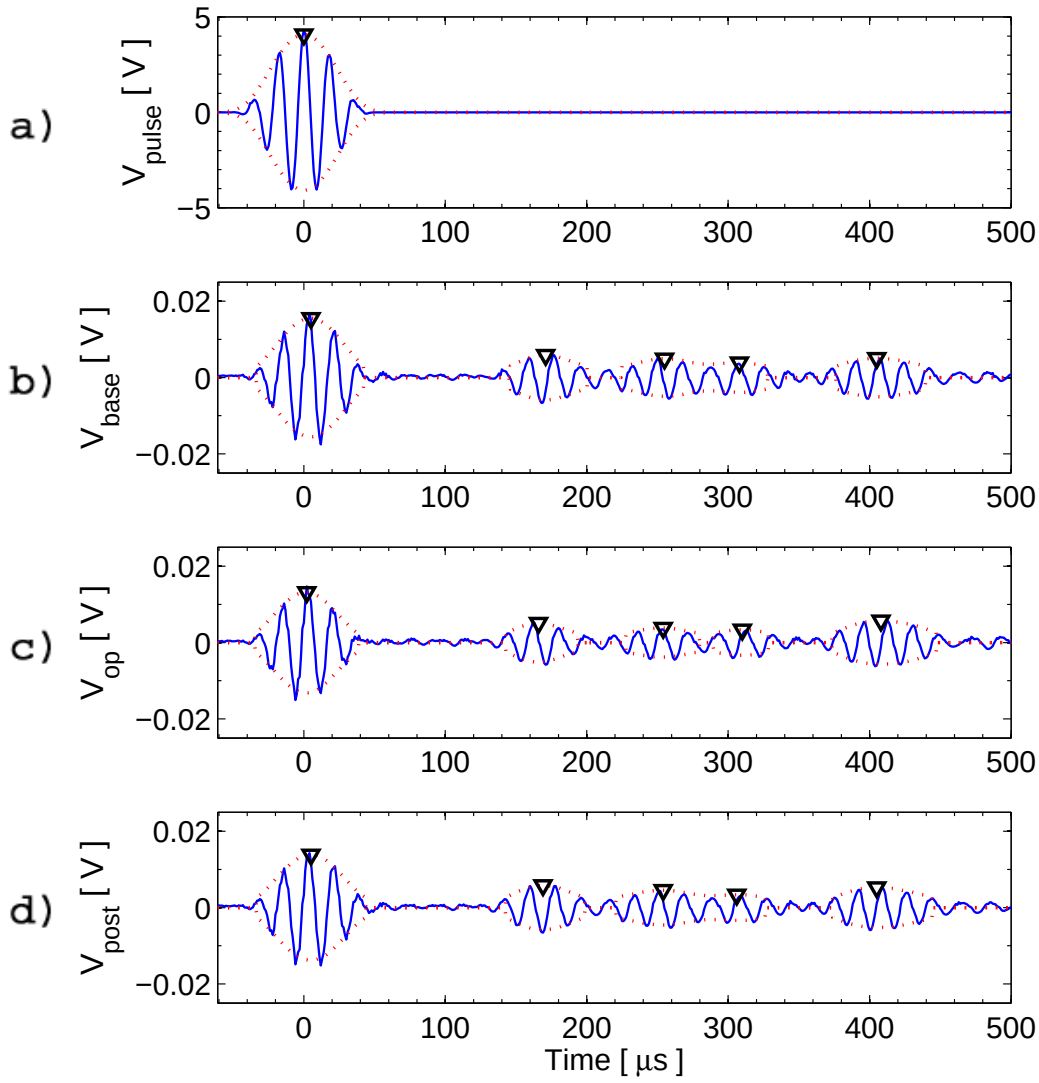

Figure B-23: Humidity test signals for node 0060. a) Excitation pulse, b) baseline signal at 23°C and 59.0%RH (time=0 hrs), c) operational signal at 65°C and 94.4%RH (time=152.5 hrs), d) post-test signal at 26°C and 59.7%RH (time=241 hrs).

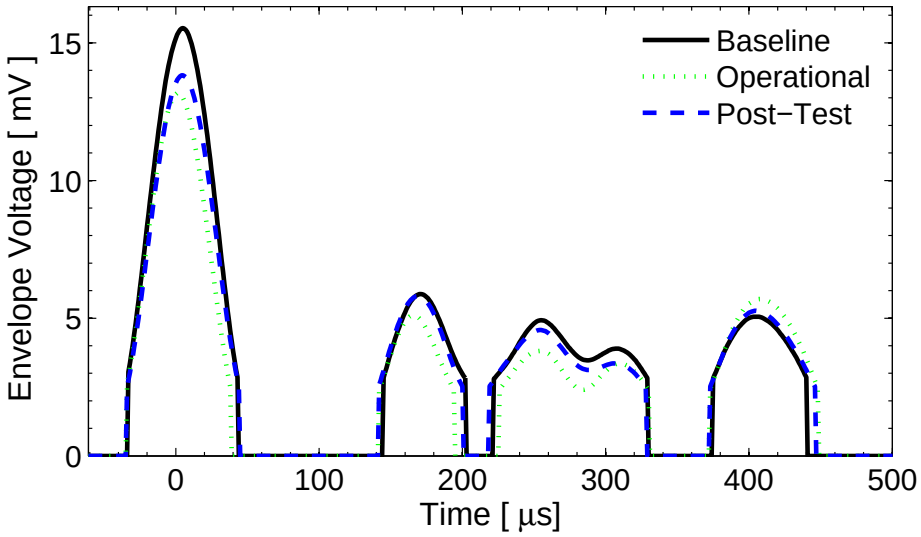

Figure B-24: Humidity test signal envelopes for node 0060.

Table B.12: Metric values and differences (deltas) of node 0060 for the humidity test.

	1^{st} wavepacket			2^{nd} wavepacket		
	Base	Op	Post	Base	Op	Post
TOF [μs]	5	2	5	171	166	169
ΔTOF [μs]	-	-3	0	-	-5	-2
ΔTOF [%]	-	-60.0	0	-	-2.9	-1.1
V [mV]	15.5	13.2	13.8	5.9	5.1	5.8
ΔV [mV]	-	-2.4	-1.7	-	-0.8	-0.1
ΔV [%]	-	-15.2	-11.0	-	-13.2	-1.3

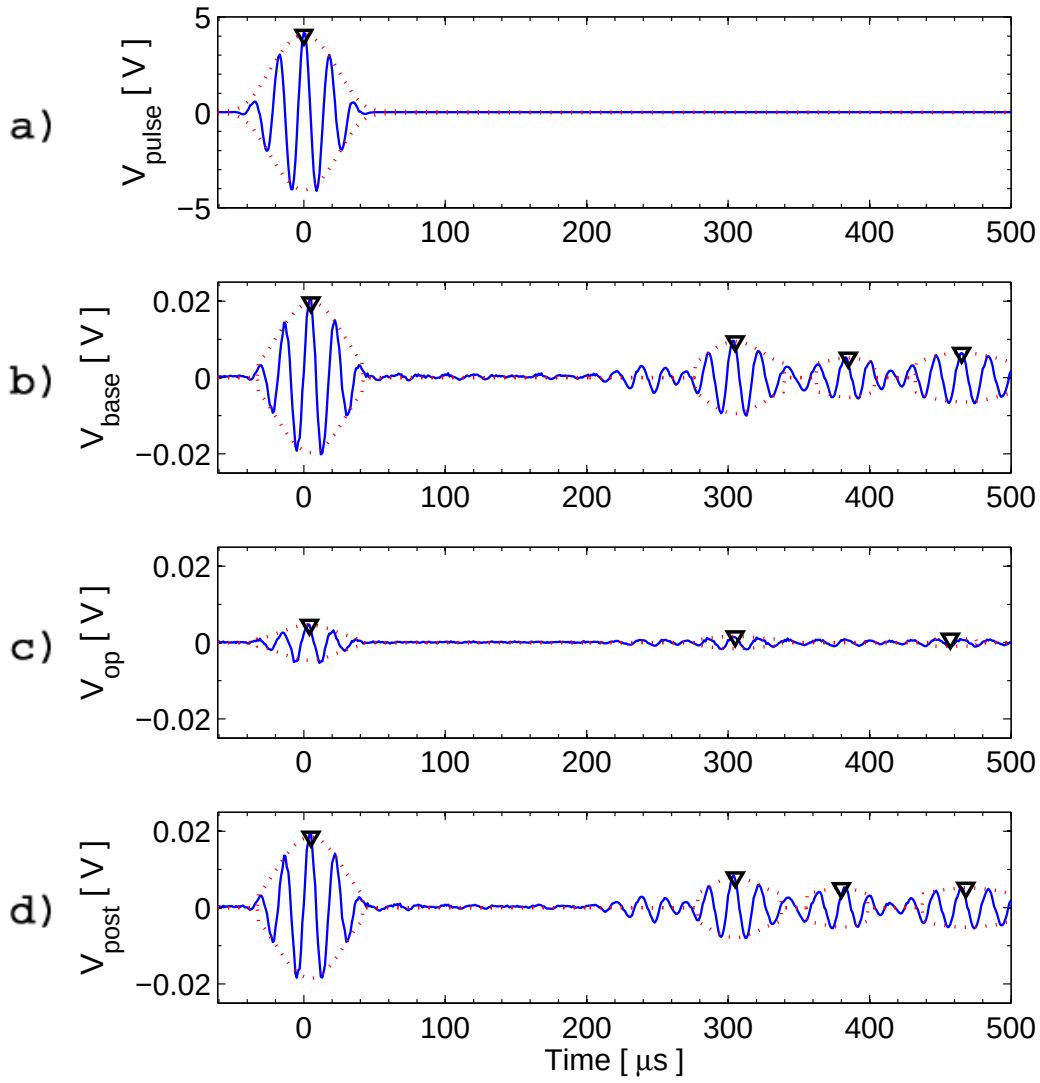

Figure B-25: Oil-based fluid susceptibility test signals for node 0010, no clamps. a) Excitation pulse, b) baseline signal at 22°C (time=0 hrs), c) operational signal at 22°C (time=214 hrs), d) post-test signal at 22°C (time=216 hrs).

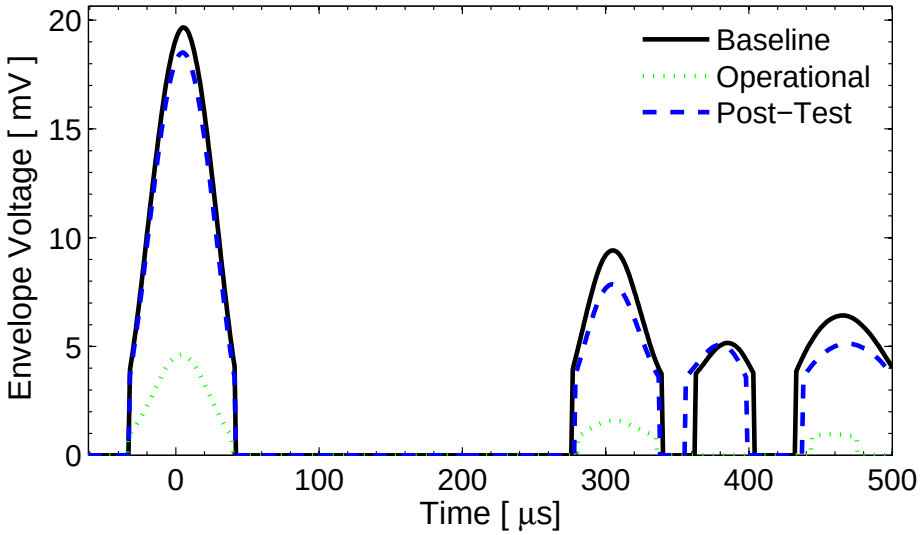

Figure B-26: Oil-based fluid susceptibility test signal envelopes for node 0010.

Table B.13: Metric values and differences (deltas) of node 0010 for the oil-based fluid susceptibility test.

	1^{st} wavepacket			2^{nd} wavepacket		
	Base	Op	Post	Base	Op	Post
TOF [μs]	5	4	5	305	305	305
ΔTOF [μs]	-	-1	0	-	0	0
ΔTOF [%]	-	-20.0	0	-	0	0
V [mV]	19.7	4.6	18.5	9.4	1.6	7.9
ΔV [mV]	-	-15.1	-1.2	-	-7.8	-1.5
ΔV [%]	-	-76.6	-5.8	-	-83.1	-16.5

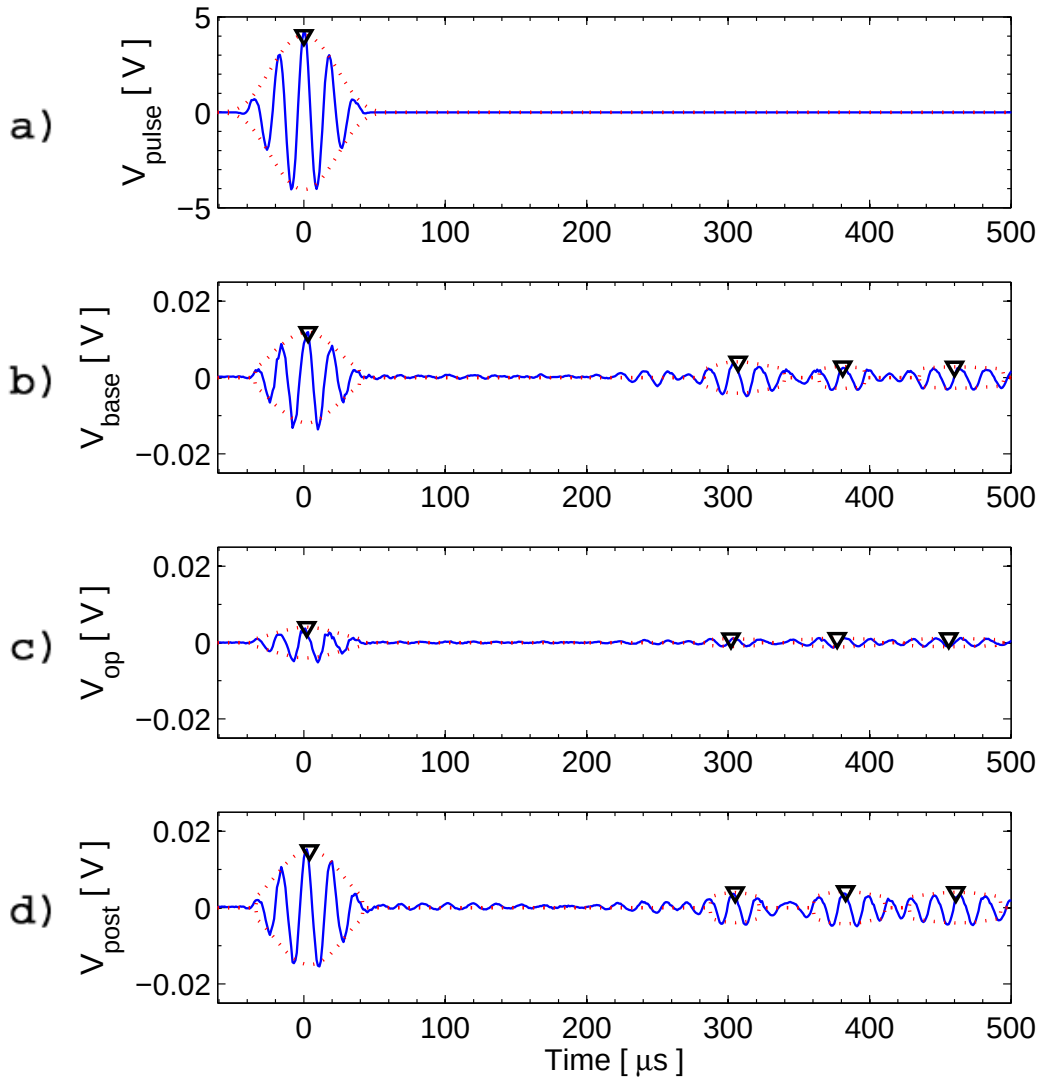

Figure B-27: Oil-based fluid susceptibility test signals for node 0015, no clamps. a) Excitation pulse, b) baseline signal at 22°C (time=0 hrs), c) operational signal at 22°C (time=214 hrs), d) post-test signal at 22°C (time=216 hrs).

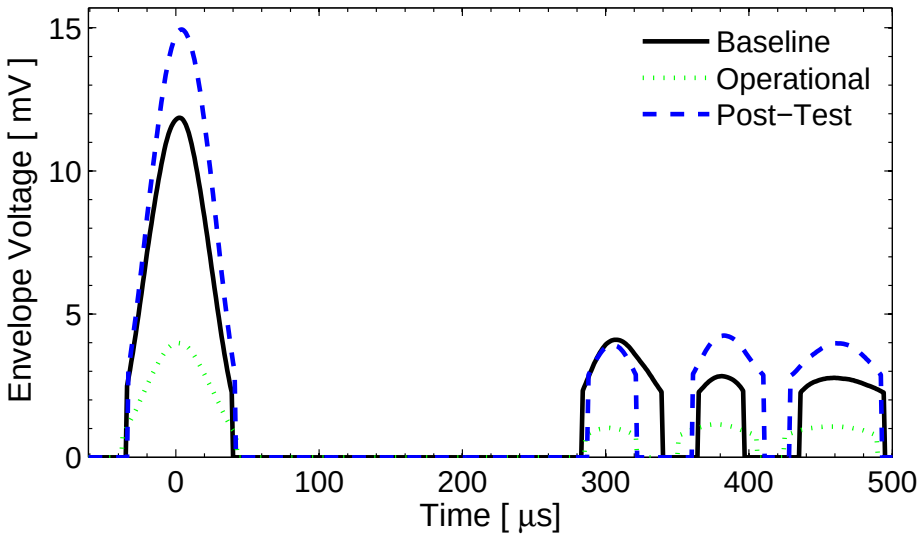

Figure B-28: Oil-based fluid susceptibility test signal envelopes for node 0015.

Table B.14: Metric values and differences (deltas) of node 0015 for the oil-based fluid susceptibility test.

	1^{st} wavepacket			2^{nd} wavepacket		
	Base	Op	Post	Base	Op	Post
TOF [μs]	3	2	4	307	302	305
ΔTOF [μs]	-	-1	1	-	-5	-2
ΔTOF [%]	-	-33.3	33.3	-	-1.6	-0.6
V [mV]	11.9	4.0	14.9	4.1	1.0	3.9
ΔV [mV]	-	-7.9	3.0	-	-3.1	-0.2
ΔV [%]	-	-66.4	26.0	-	-75.1	-4.4

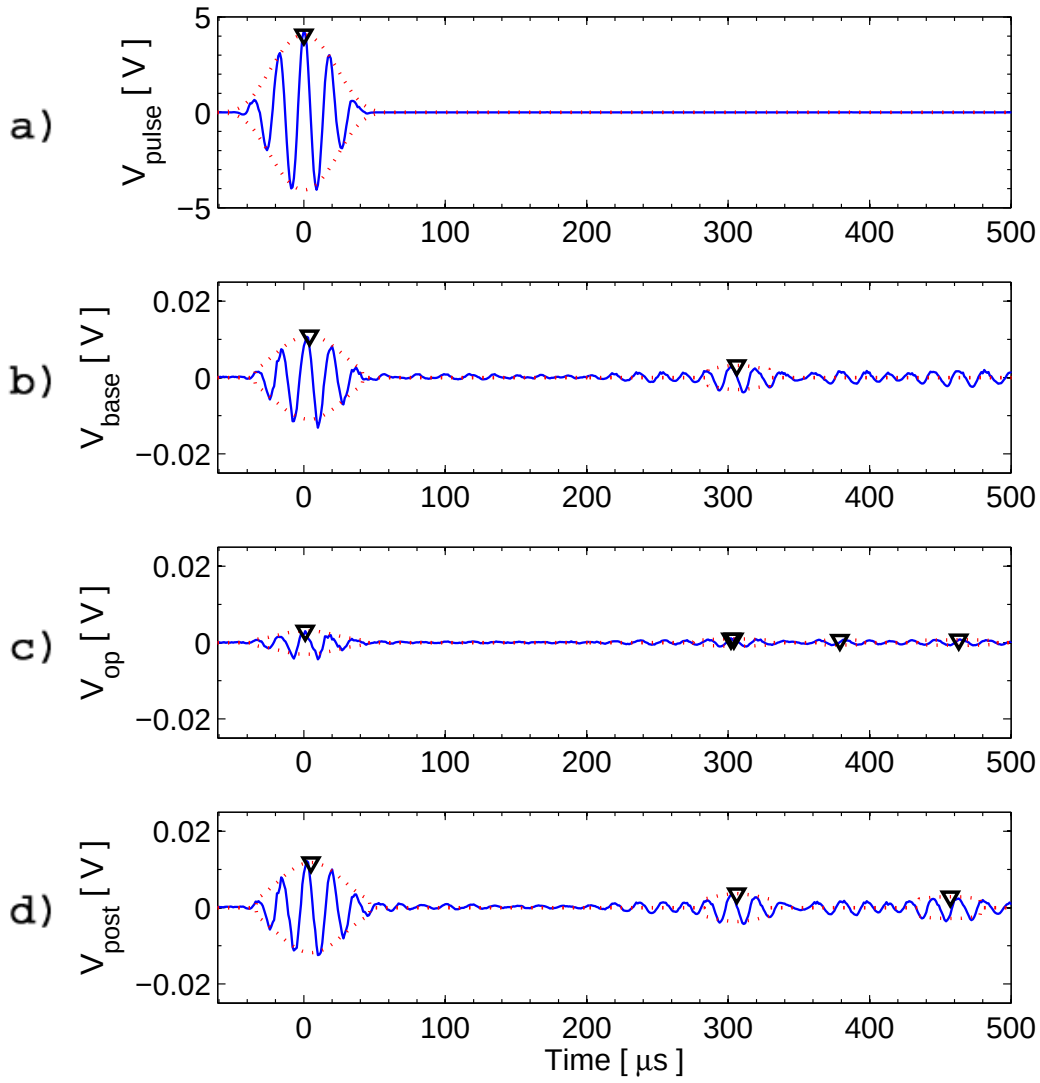

Figure B-29: Oil-based fluid susceptibility test signals for node 0052, no clamps. a) Excitation pulse, b) baseline signal at 22°C (time=0 hrs), c) operational signal at 22°C (time=214 hrs), d) post-test signal at 22°C (time=216 hrs).

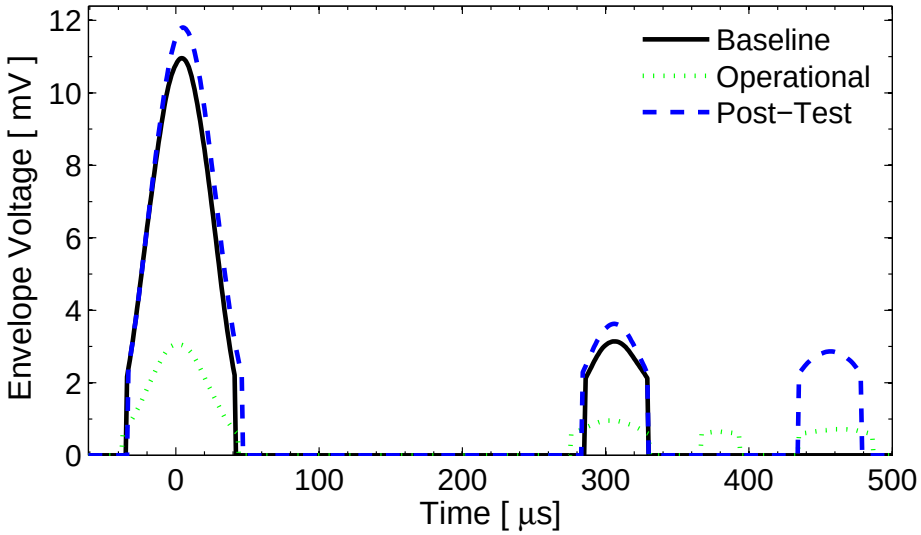

Figure B-30: Oil-based fluid susceptibility test signal envelopes for node 0052.

Table B.15: Metric values and differences (deltas) of node 0052 for the oil-based fluid susceptibility test.

	1^{st} wavepacket			2^{nd} wavepacket		
	Base	Op	Post	Base	Op	Post
TOF [μs]	4	1	5	306	302	306
ΔTOF [μs]	-	-3	1	-	-4	0
ΔTOF [%]	-	-75.0	25.0	-	-1.3	0
V [mV]	11.0	3.1	11.8	3.1	1.0	3.6
ΔV [mV]	-	-7.9	0.8	-	-2.1	0.5
ΔV [%]	-	-72.0	7.7	-	-69.6	15.4

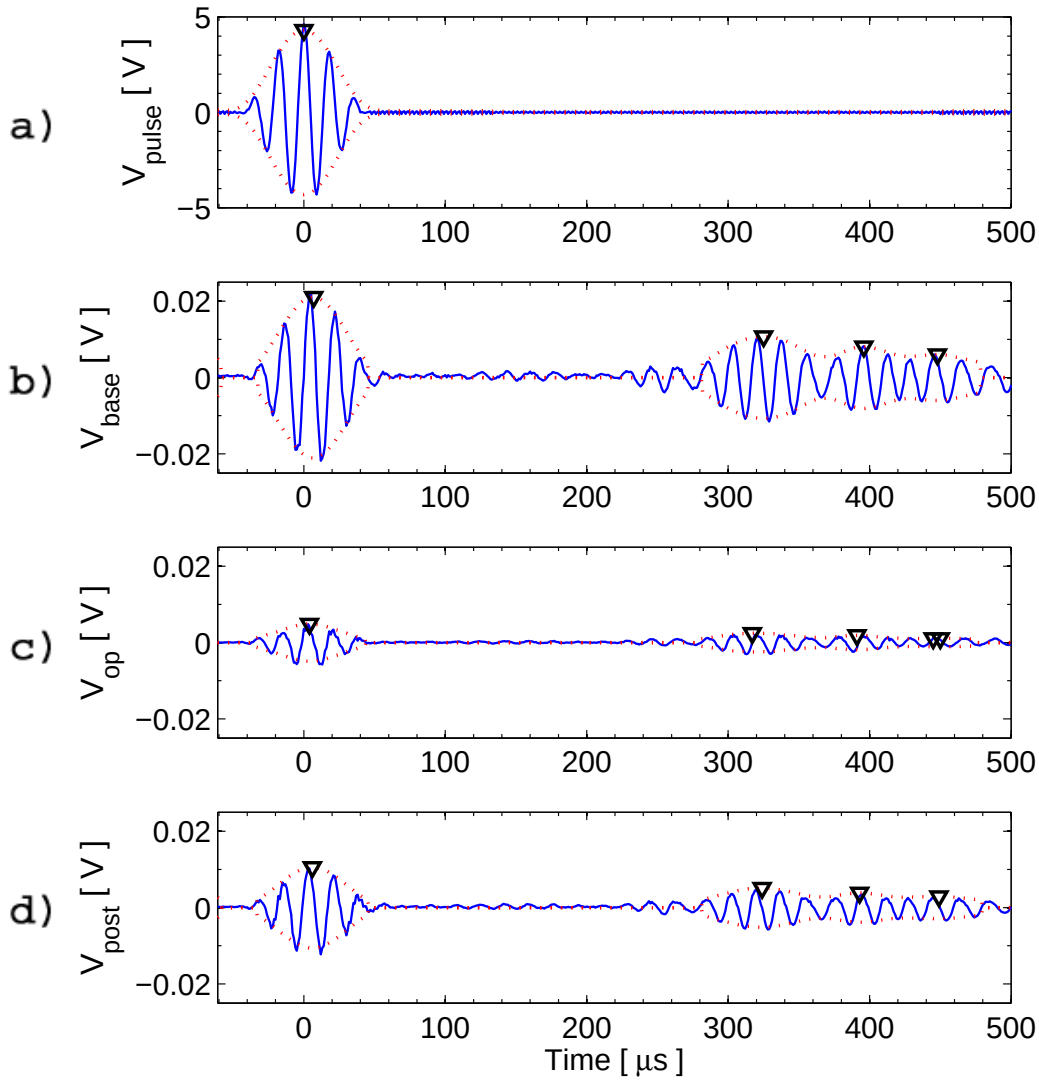

Figure B-31: Water-based fluid susceptibility test signals for node 0012, no clamps. a) Excitation pulse, b) baseline signal at 22°C (time=0 hrs), c) operational signal at 22°C (time=214 hrs), d) post-test signal at 22°C (time=216 hrs).

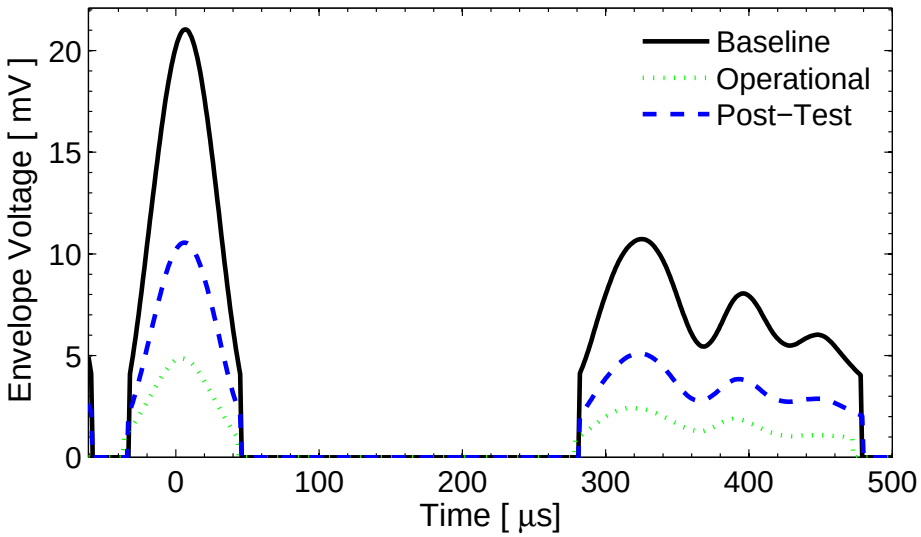

Figure B-32: Water-based fluid susceptibility test signal envelopes for node 0012.

Table B.16: Metric values and differences (deltas) of node 0012 for the water-based fluid susceptibility test.

	1^{st} wavepacket			2^{nd} wavepacket		
	Base	Op	Post	Base	Op	Post
TOF [μs]	7	4	6	325	317	324
ΔTOF [μs]	-	-3	-1	-	-8	-1
ΔTOF [%]	-	-42.9	-14.3	-	-2.5	-0.3
V [mV]	21.0	4.8	10.5	10.7	2.4	5.1
ΔV [mV]	-	-16.2	-10.5	-	-8.3	-5.6
ΔV [%]	-	-76.9	-49.8	-	-77.4	-52.5

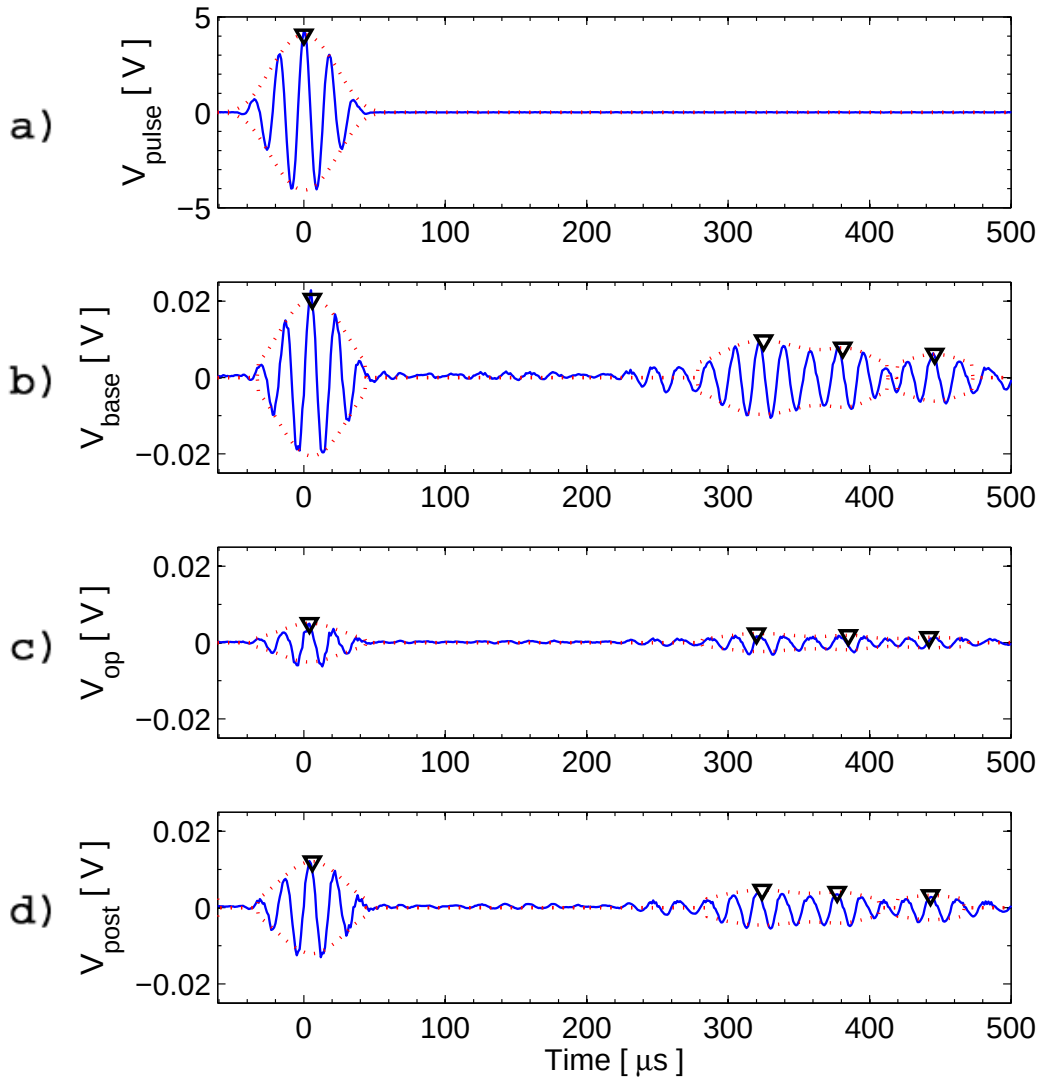

Figure B-33: Water-based fluid susceptibility test signals for node 0203, no clamps. a) Excitation pulse, b) baseline signal at $22°C$ (time=0 hrs), c) operational signal at $22°C$ (time=214 hrs), d) post-test signal at $22°C$ (time=216 hrs).

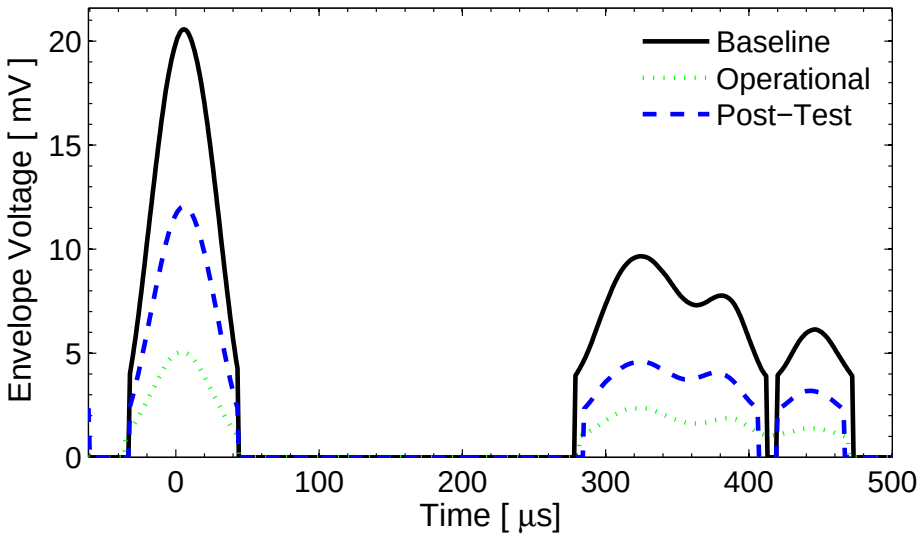

Figure B-34: Water-based fluid susceptibility test signal envelopes for node 0203.

Table B.17: Metric values and differences (deltas) of node 0203 for the water-based fluid susceptibility test.

	1^{st} wavepacket			2^{nd} wavepacket		
	Base	Op	Post	Base	Op	Post
TOF [μs]	6	4	6	325	320	324
ΔTOF [μs]	-	-2	0	-	-5	-1
ΔTOF [%]	-	-33.3	0	-	-1.5	-6.3
V [mV]	20.6	5.1	12.0	9.7	2.4	4.6
ΔV [mV]	-	-15.5	-8.5	-	-7.3	-5.1
ΔV [%]	-	-75.4	-41.4	-	-75.5	-52.5

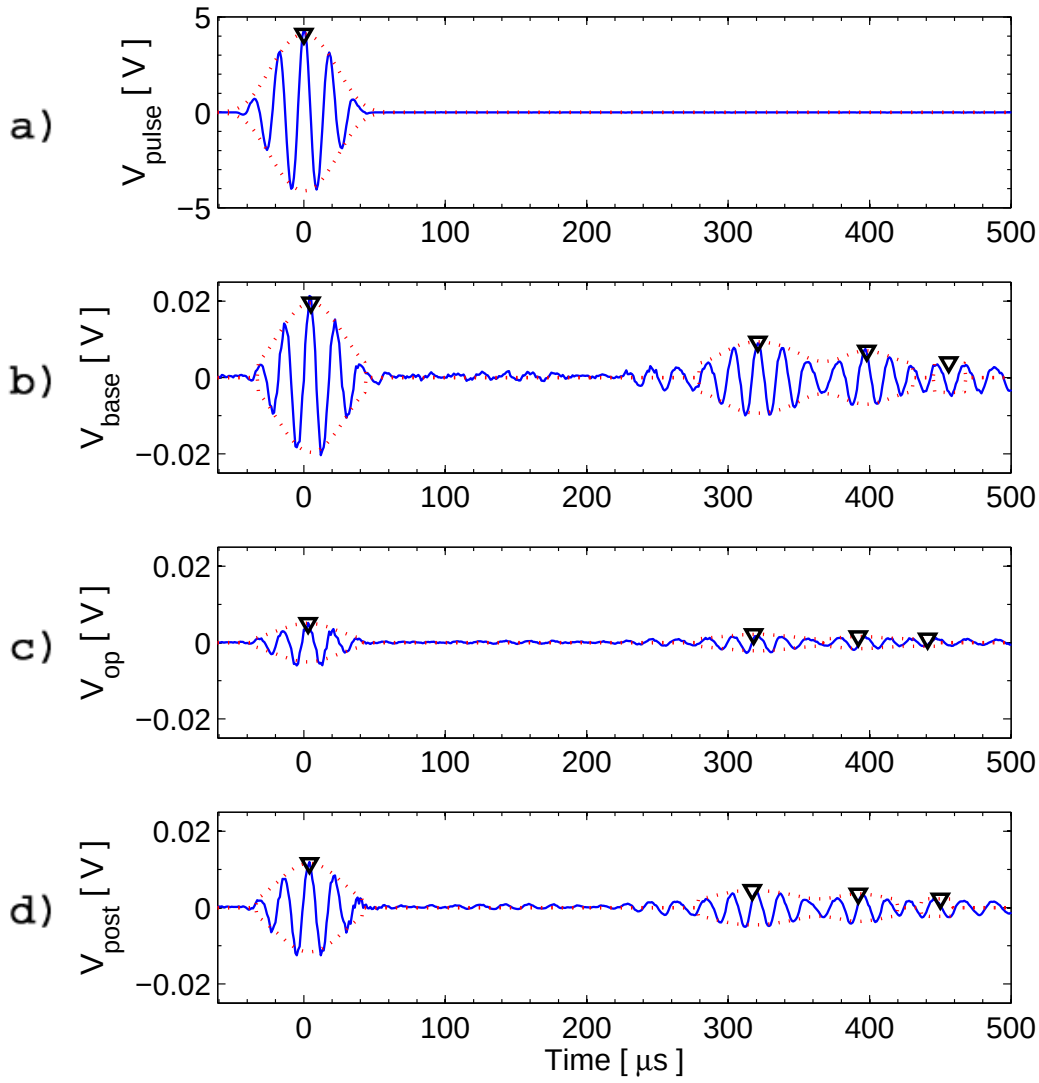

Figure B-35: Water-based fluid susceptibility test signals for node 2598, no clamps. a) Excitation pulse, b) baseline signal at $22°C$ (time=0 hrs), c) operational signal at $22°C$ (time=214 hrs), d) post-test signal at $22°C$ (time=216 hrs).

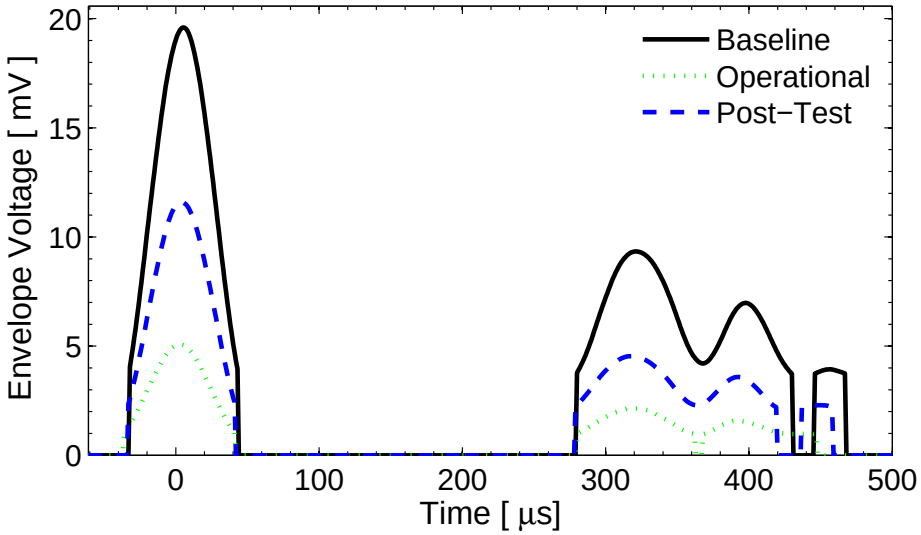

Figure B-36: Water-based fluid susceptibility test signal envelopes for node 2598.

Table B.18: Metric values and differences (deltas) of node 2598 for the water-based fluid susceptibility test.

	1^{st} wavepacket			2^{nd} wavepacket		
	Base	Op	Post	Base	Op	Post
TOF [μs]	5	3	4	321	318	317
ΔTOF [μs]	-	-2	-1	-	-3	-4
ΔTOF [%]	-	-40.0	-20.0	-	-0.9	-1.2
V [mV]	19.6	5.1	11.6	9.3	2.1	4.5
ΔV [mV]	-	-14.5	-8.0	-	-7.2	-4.8
ΔV [%]	-	-74.1	-40.8	-	-76.9	-51.4

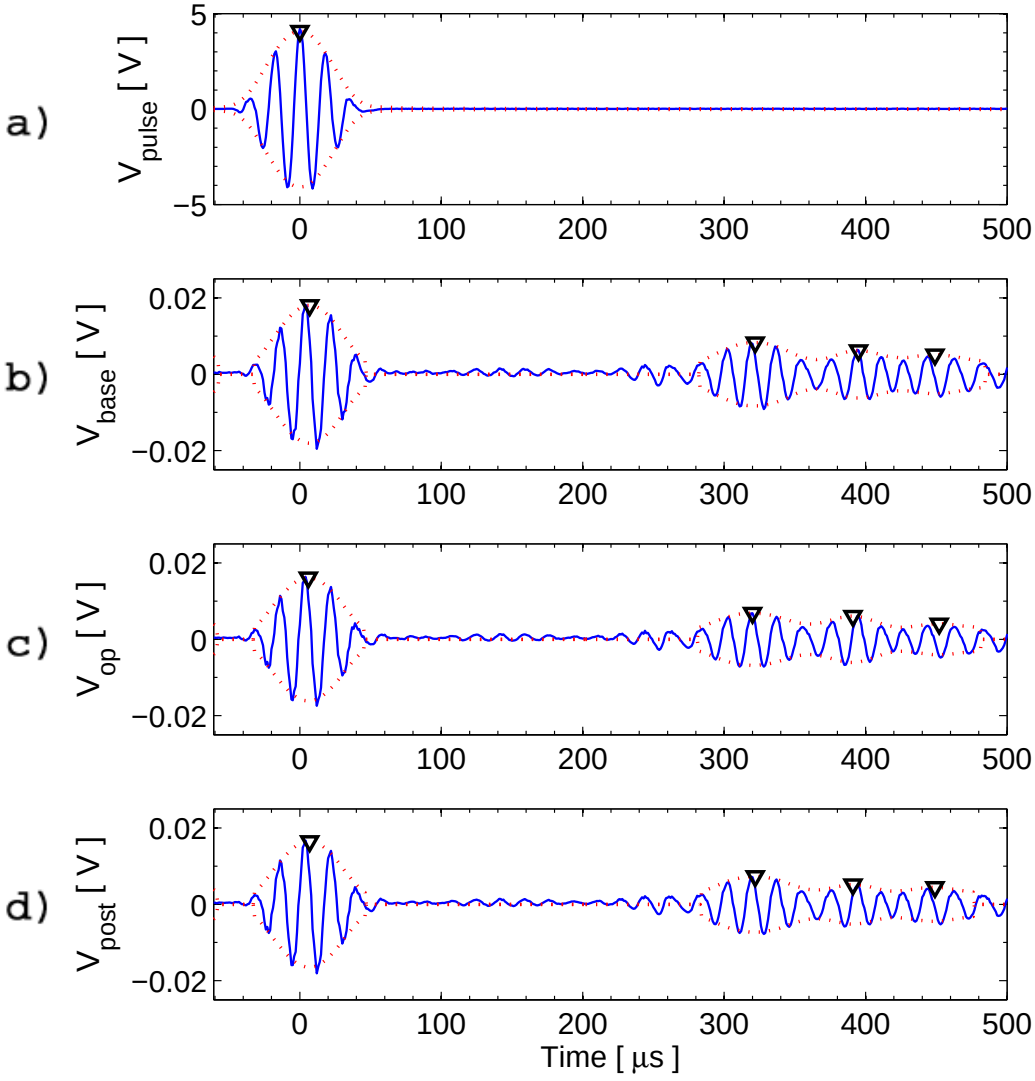

Figure B-37: Altitude test signals for node 2555, no clamps, data set 8. a) Excitation pulse, b) baseline signal at 21°C and 101.3 kPa (time=0 hrs), c) operational signal at 21°C and 4.4 kPa (time=2.5 hrs), d) post-test signal at 21°C and 101.3 kPa (time=2.7 hrs).

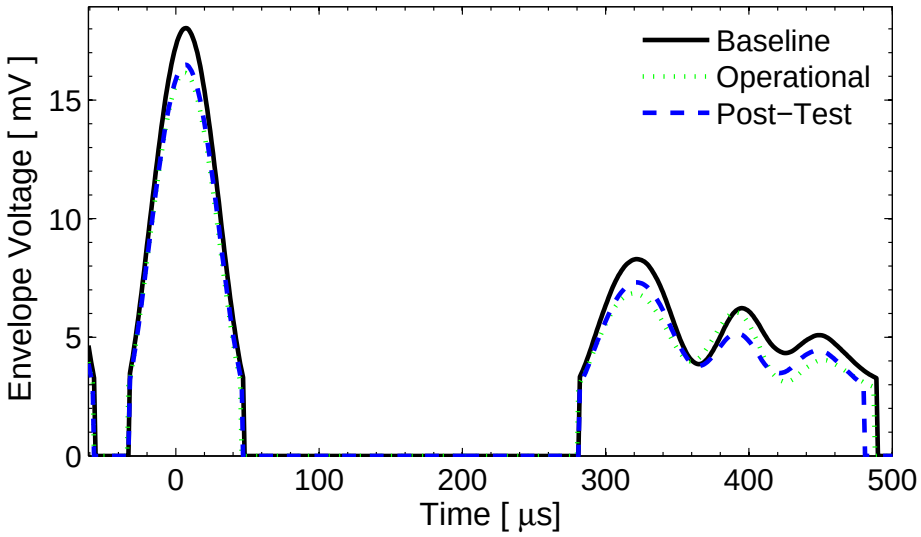

Figure B-38: Altitude test signal envelopes for node 2555.

Table B.19: Metric values and differences (deltas) of node 2555 for the altitude test.

	1^{st} wavepacket			2^{nd} wavepacket		
	Base	Op	Post	Base	Op	Post
TOF [μs]	7	6	7	322	320	322
ΔTOF [μs]	-	-1	0	-	-2	0
ΔTOF [%]	-	-14.3	0	-	-0.6	0
V [mV]	18.0	16.1	16.5	8.3	6.9	7.3
ΔV [mV]	-	-1.9	-1.5	-	-1.4	-1.0
ΔV [%]	-	-10.5	-8.6	-	-17.3	-11.7

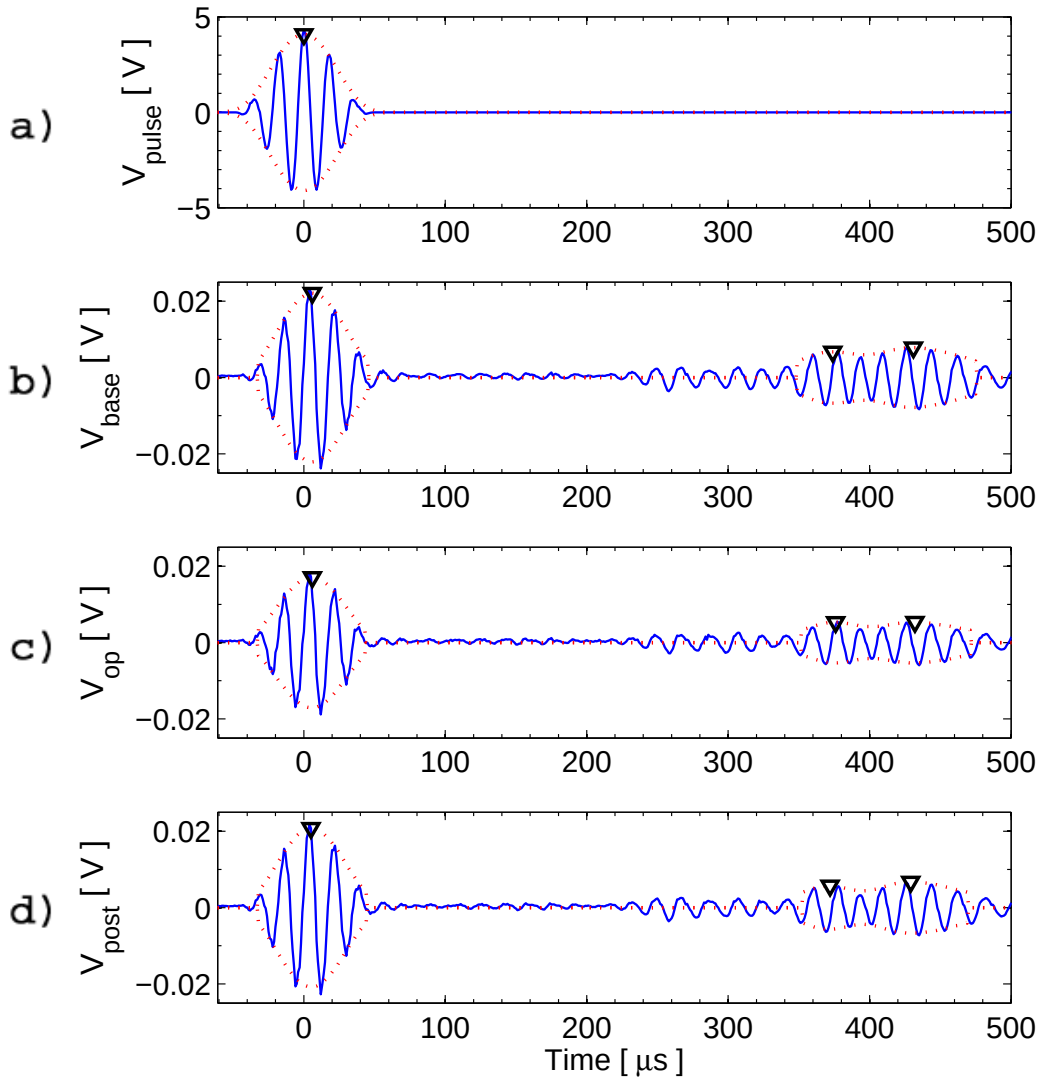

Figure B-39: Altitude test signals for node 2557, no clamps. a) Excitation pulse, b) baseline signal at 21°C and 101.3 kPa (time=0 hrs), c) operational signal at 21°C and 4.4 kPa (time=2 hrs), d) post-test signal at 21°C and 101.3 kPa (time=2.9 hrs).

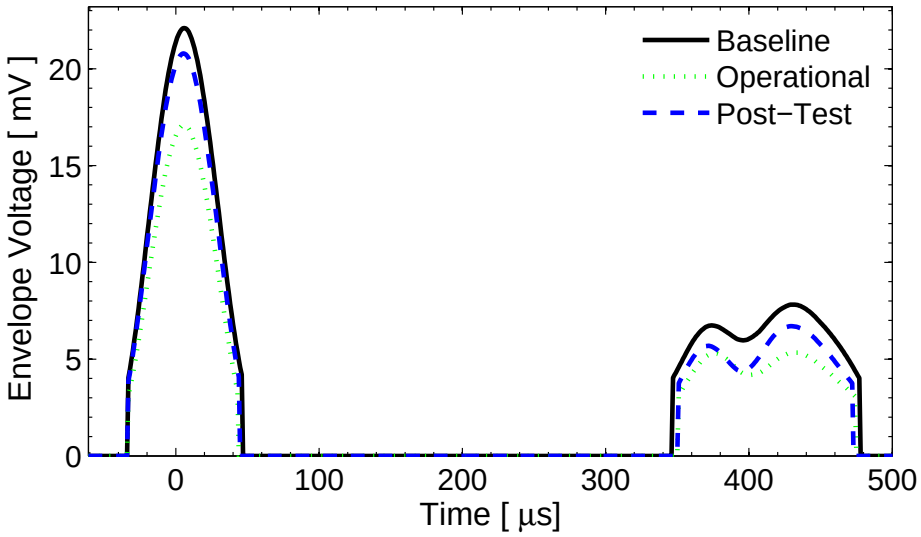

Figure B-40: Altitude test signal envelopes for node 2557.

Table B.20: Metric values and differences (deltas) of node 2557 for the altitude test.

	1^{st} wavepacket			2^{nd} wavepacket		
	Base	Op	Post	Base	Op	Post
TOF [μs]	6	6	5	374	376	372
ΔTOF [μs]	-	0	-1	-	2	-2
ΔTOF [%]	-	0	-16.7	-	0.5	-0.5
V [mV]	22.1	17.1	20.8	6.7	5.3	5.7
ΔV [mV]	-	-5.0	-1.3	-	-1.4	-1.0
ΔV [%]	-	-22.7	-5.9	-	-21.5	-15.6

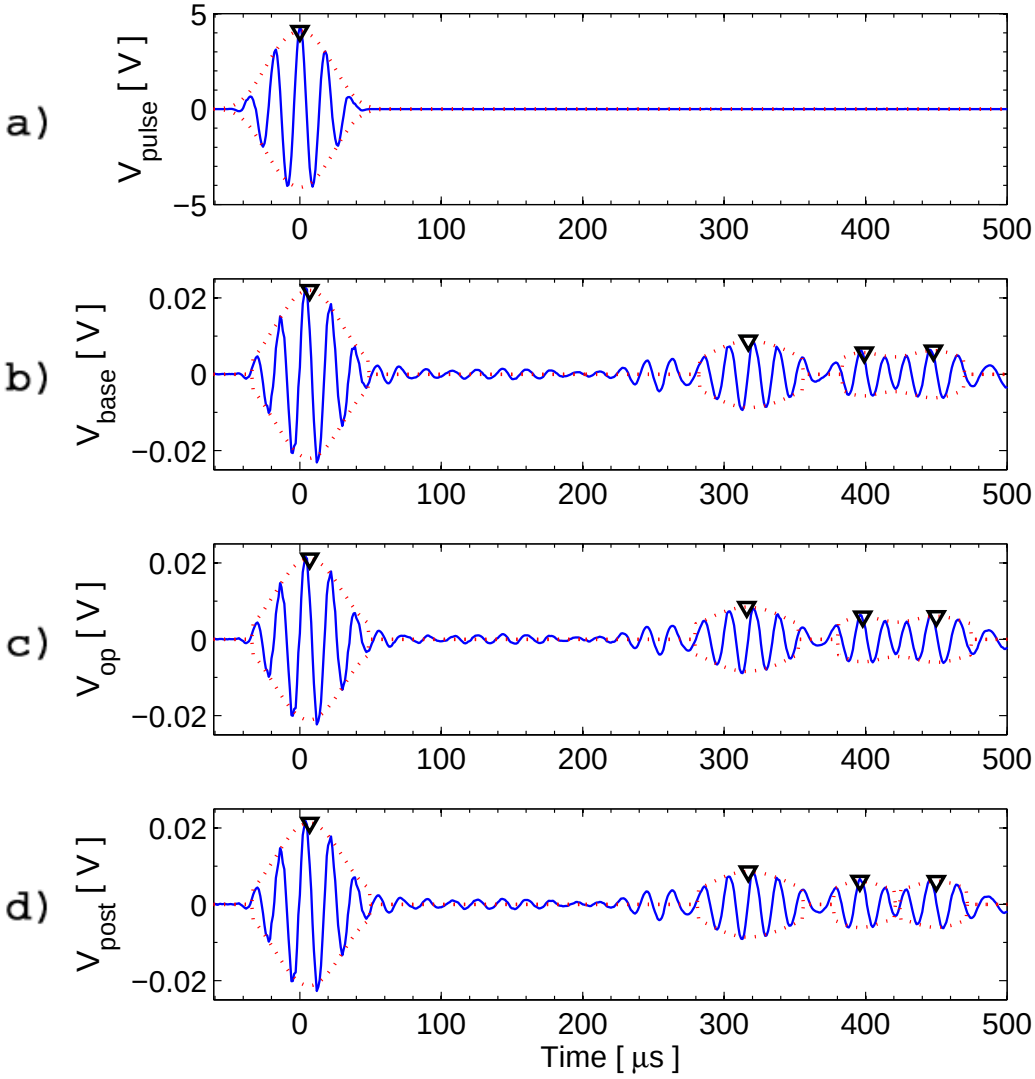

Figure B-41: Altitude test signals for node 2595, no clamps. a) Excitation pulse, b) baseline signal at 21°C and 101.3 kPa (time=0 hrs), c) operational signal at 21°C and 4.4 kPa (time=0.25 hrs), d) post-test signal at 21°C and 101.3 kPa (time=2.5 hrs).

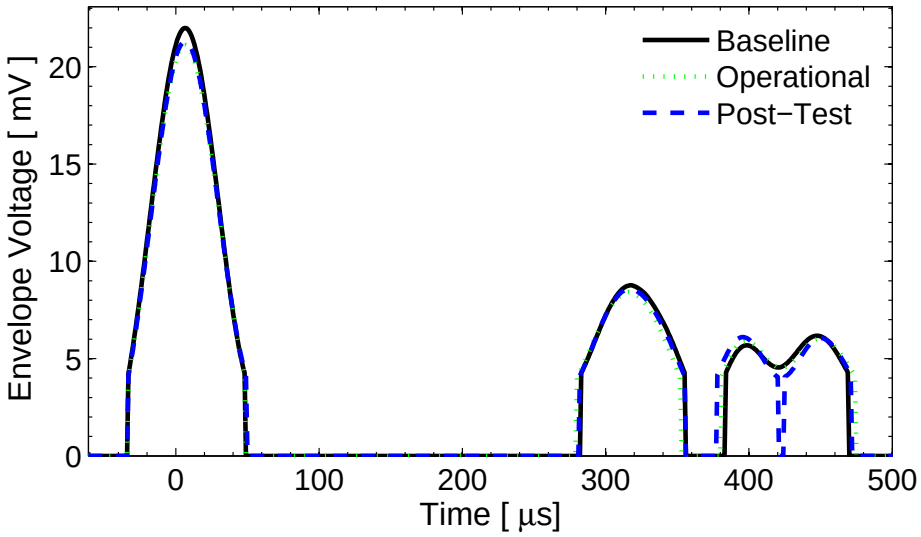

Figure B-42: Altitude test signal envelopes for node 2595.

Table B.21: Metric values and differences (deltas) of node 2595 for the altitude test.

	1^{st} wavepacket			2^{nd} wavepacket		
	Base	Op	Post	Base	Op	Post
TOF [μs]	7	7	7	317	316	317
ΔTOF [μs]	-	0	0	-	-1	0
ΔTOF [%]	-	0	0	-	-0.3	0
V [mV]	22.0	21.1	21.3	8.8	8.4	8.6
ΔV [mV]	-	-0.9	-0.7	-	-0.4	-0.2
ΔV [%]	-	-4.0	-3.2	-	-4.0	-1.9

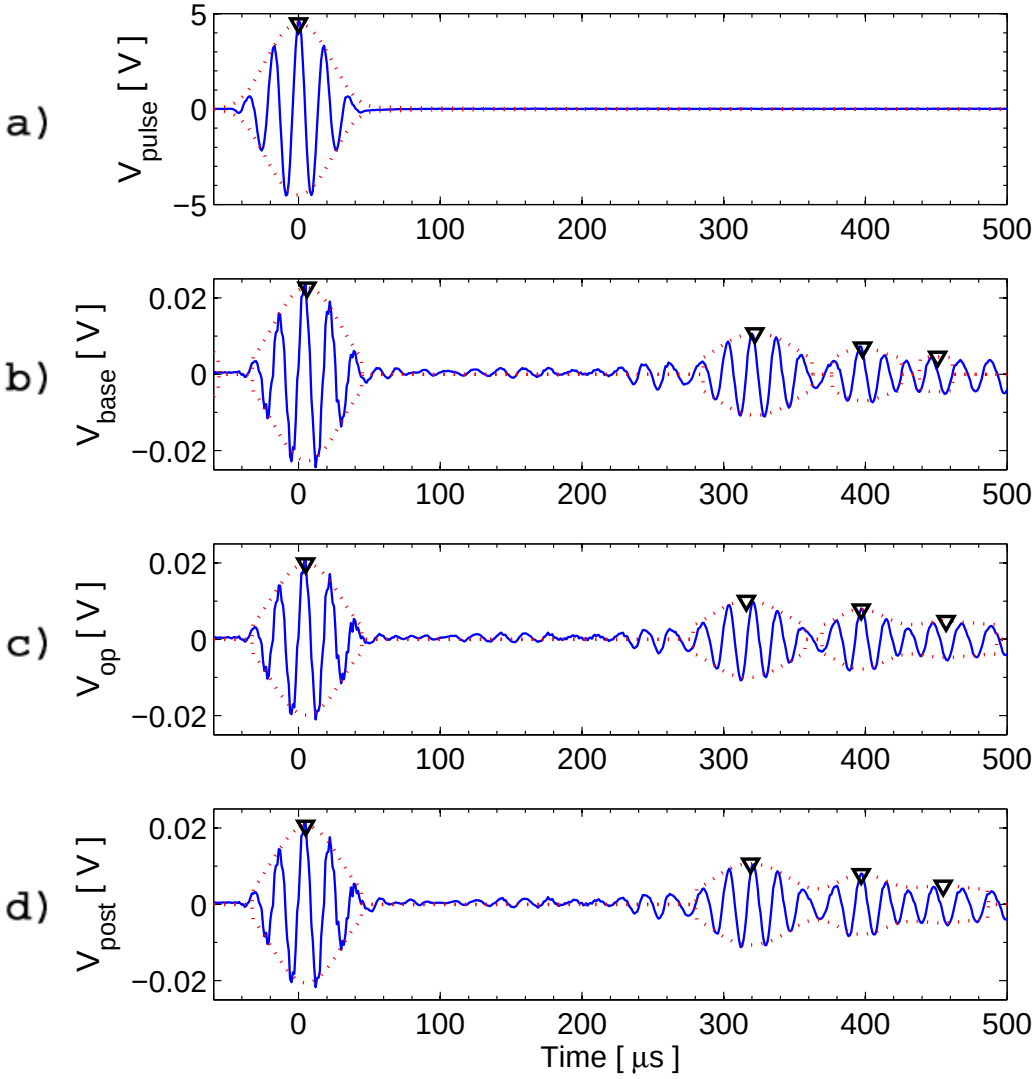

Figure B-43: Decompression test signals for node 0204, no clamps, data set 10. a) Excitation pulse, b) baseline signal at 21°C and 101.3 kPa (time=0 min), c) operational signal at 21°C and 4.4 kPa (time=21 min), d) post-test signal at 21°C and 101.3 kPa (time=31 min).

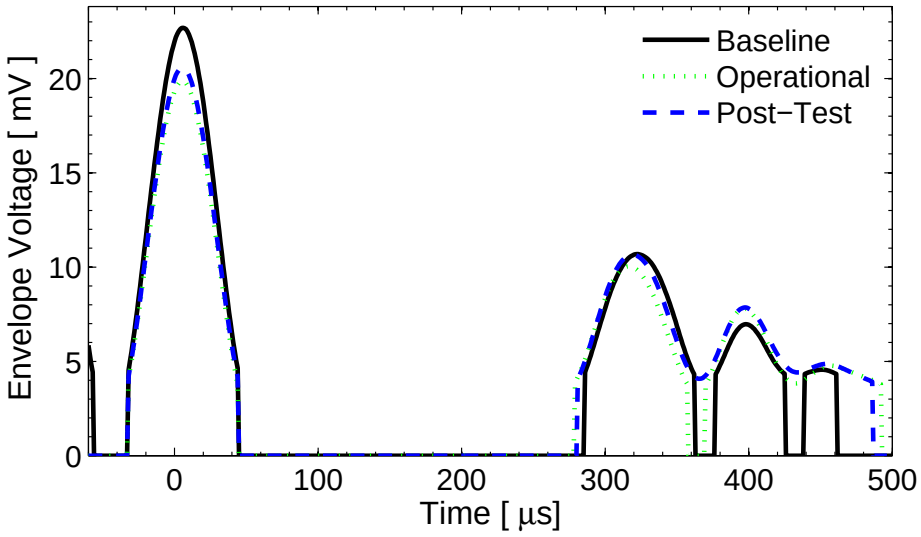

Figure B-44: Decompression test signal envelopes for node 0204.

Table B.22: Metric values and differences (deltas) of node 0204 for the decompression test.

	1^{st} wavepacket			2^{nd} wavepacket		
	Base	Op	Post	Base	Op	Post
TOF [μs]	6	5	5	322	316	319
ΔTOF [μs]	-	-1	-1	-	-6	-3
ΔTOF [%]	-	-16.7	-16.7	-	-1.9	-0.9
V [mV]	22.7	19.9	20.6	10.7	10.0	10.6
ΔV [mV]	-	-2.8	-2.1	-	-0.7	-0.1
ΔV [%]	-	-12.5	-9.3	-	-6.1	-0.3

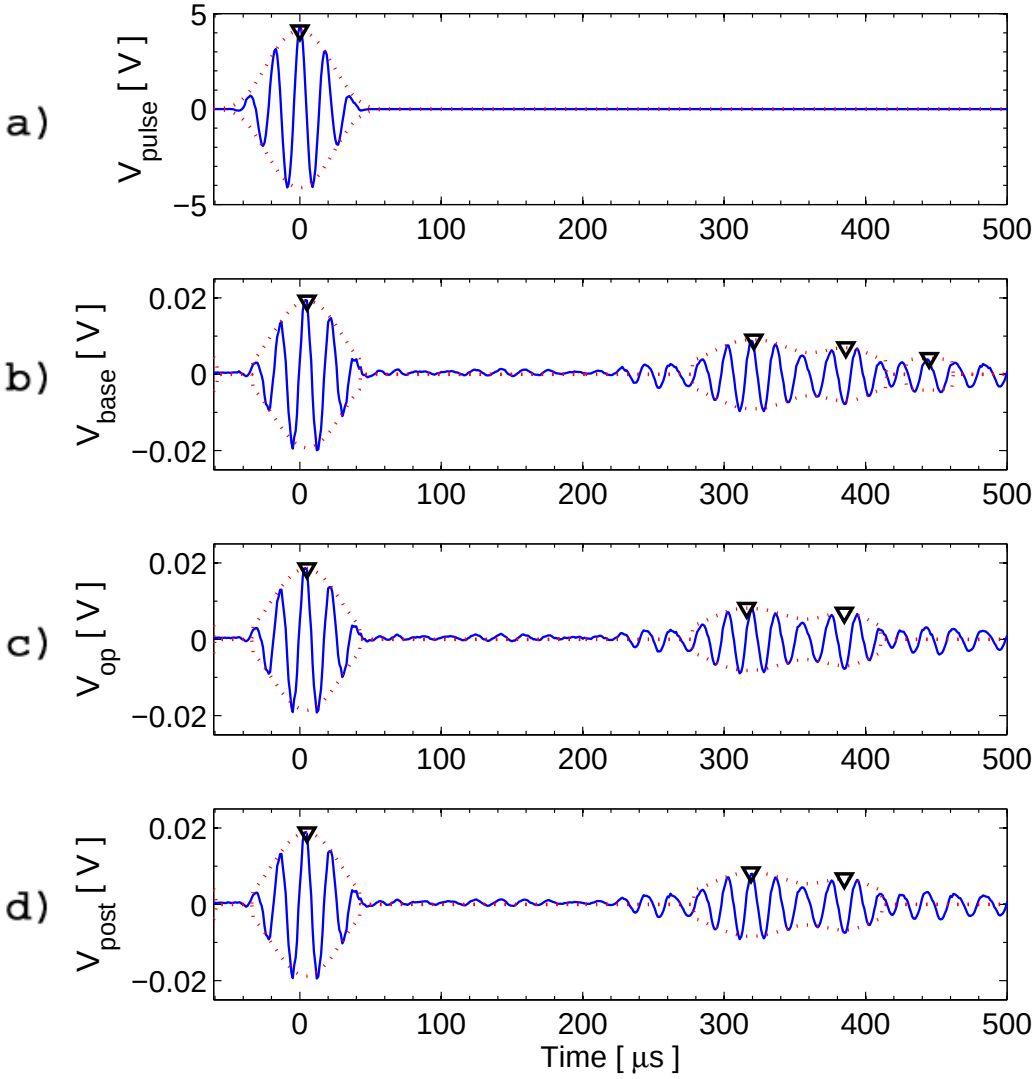

Figure B-45: Decompression test signals for node 2575, no clamps, data set 10. a) Excitation pulse, b) baseline signal at 21°C and 101.3 kPa (time=0 min), c) operational signal at 21°C and 4.4 kPa (time=21 min), d) post-test signal at 21°C and 101.3 kPa (time=34 min).

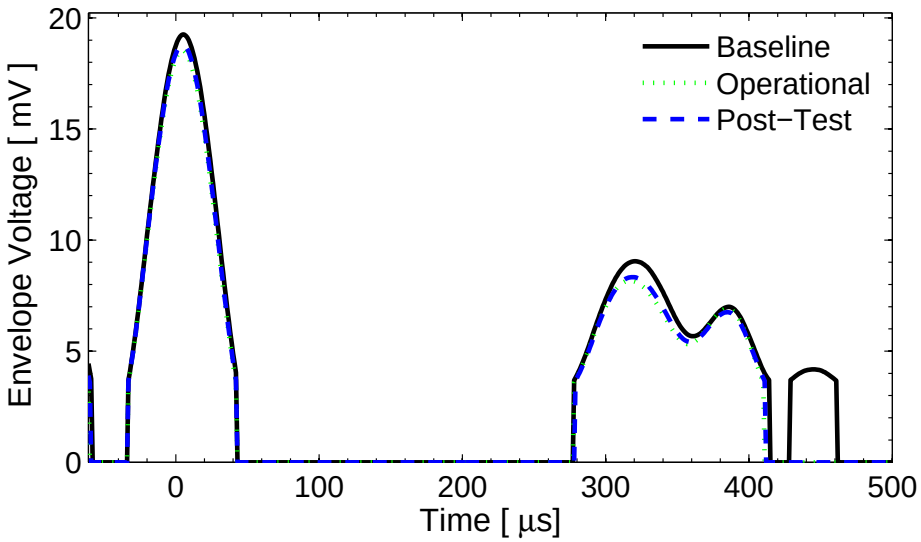

Figure B-46: Decompression test signal envelopes for node 2575.

Table B.23: Metric values and differences (deltas) of node 2575 for the decompression test.

	1^{st} wavepacket			2^{nd} wavepacket		
	Base	Op	Post	Base	Op	Post
TOF [μs]	5	5	5	321	316	319
ΔTOF [μs]	-	0	0	-	-5	-2
ΔTOF [%]	-	0	0	-	-1.6	-0.6
V [mV]	19.3	18.5	18.8	9.0	8.2	8.3
ΔV [mV]	-	-0.8	-0.5	-	-0.8	-0.7
ΔV [%]	-	-3.7	-2.4	-	-9.8	-7.9

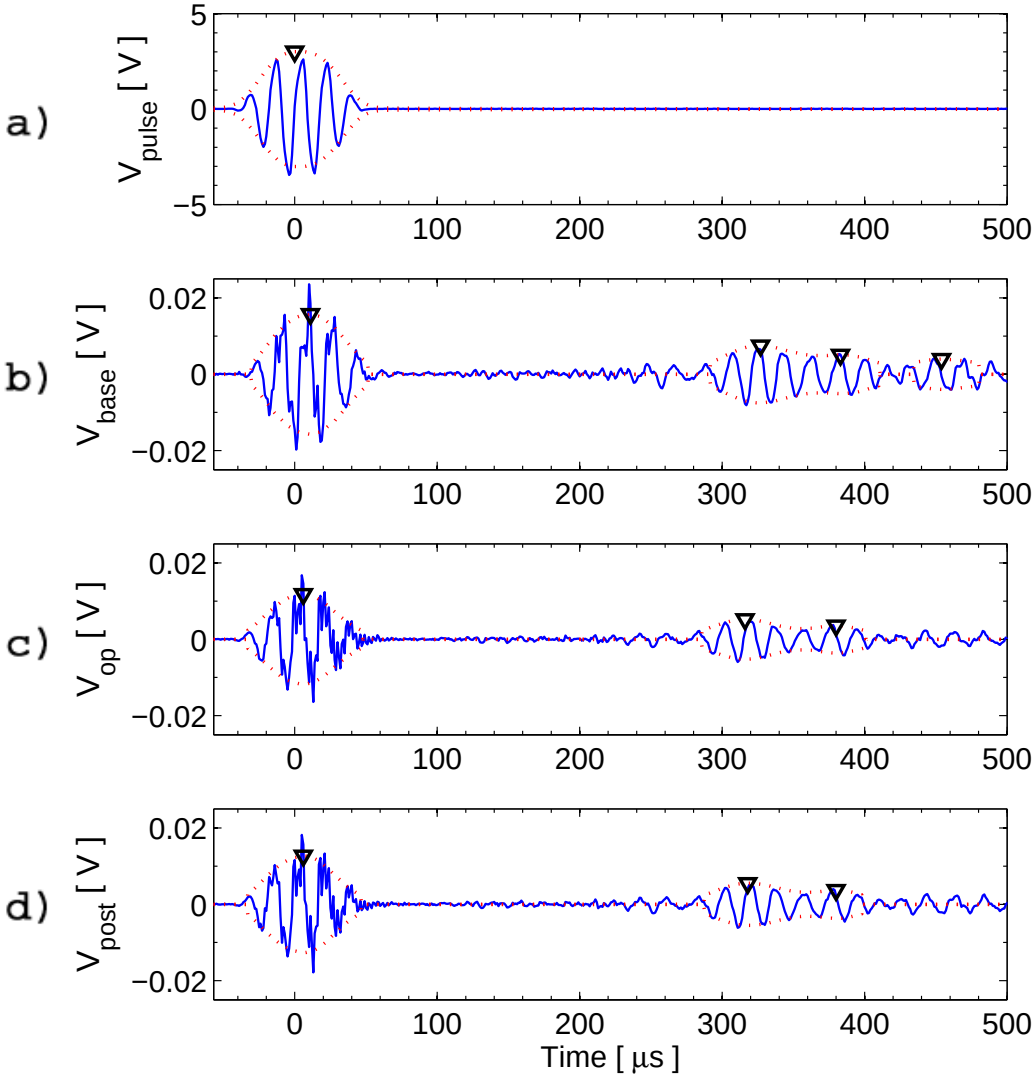

Figure B-47: Decompression test signals for node 2578, no clamps, data set 10. a) Excitation pulse, b) baseline signal at 21°C and 101.3 kPa (time=0 min), c) operational signal at 21°C and 4.4 kPa (time=20 min), d) post-test signal at 21°C and 101.3 kPa (time=30 min).

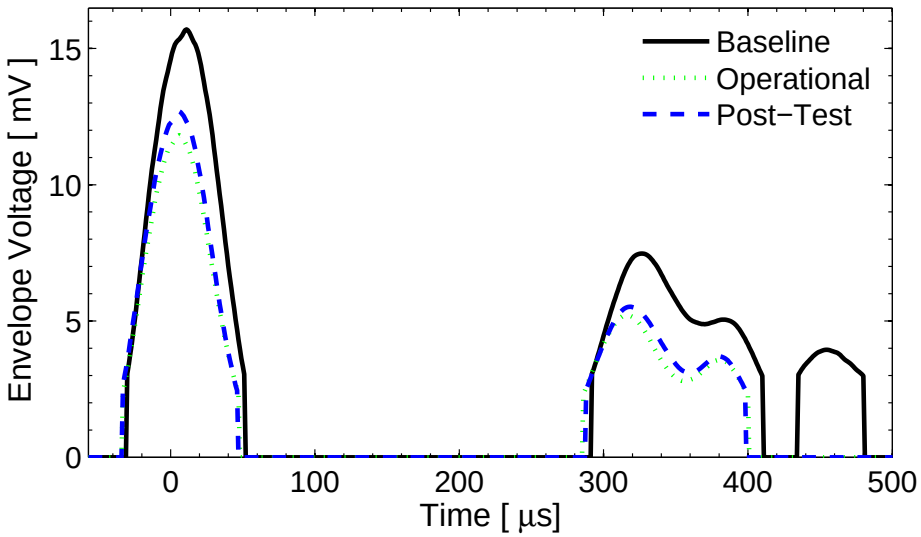

Figure B-48: Decompression test signal envelopes for node 2578.

Table B.24: Metric values and differences (deltas) of node 2578 for the decompression test.

	1^{st} wavepacket			2^{nd} wavepacket		
	Base	Op	Post	Base	Op	Post
TOF [μs]	11	6	6	327	316	318
ΔTOF [μs]	-	-5	-5	-	-11	-9
ΔTOF [%]	-	-45.4	-45.4	-	-3.4	-2.7
V [mV]	15.7	11.8	12.7	7.5	5.2	5.5
ΔV [mV]	-	-3.9	-3.0	-	-2.3	-2.0
ΔV [%]	-	-24.7	-19.2	-	-30.3	-26.1

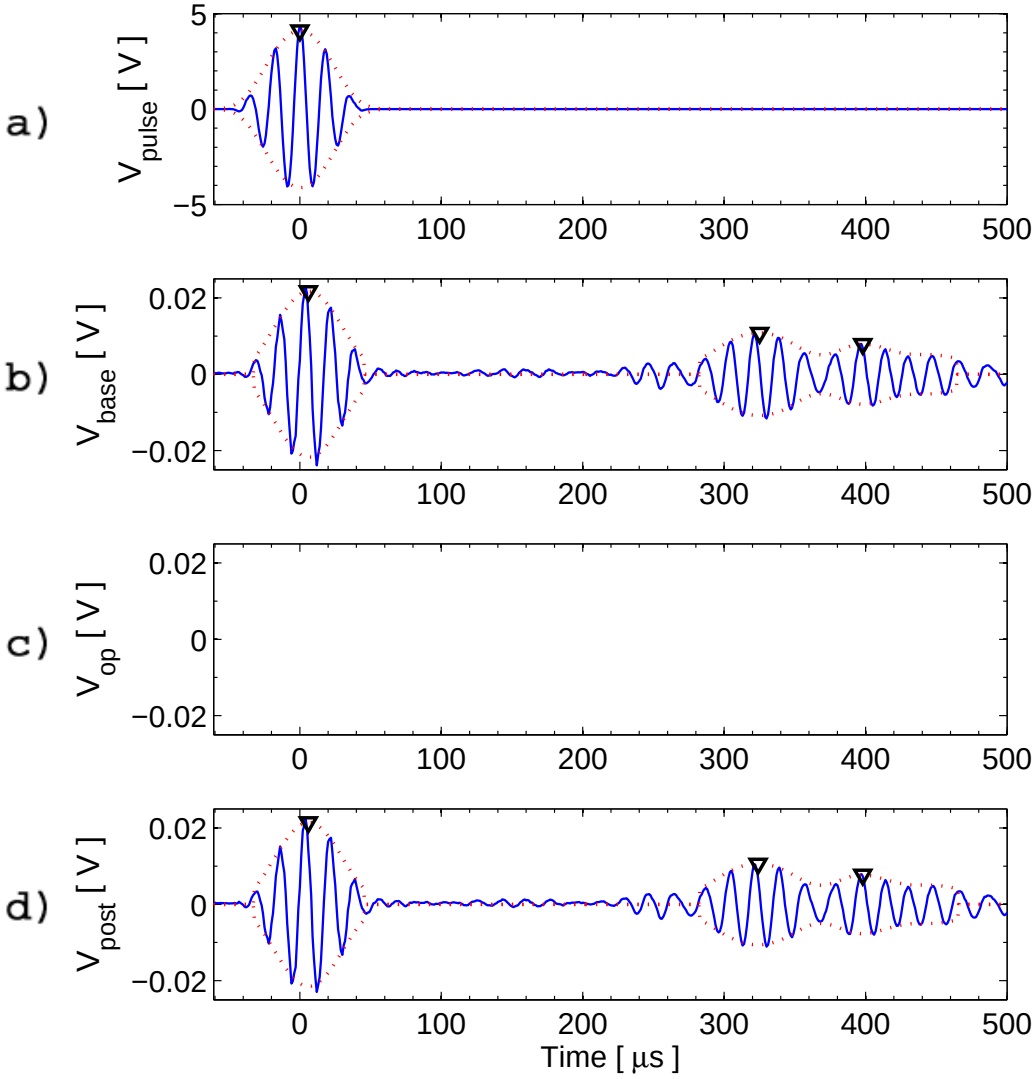

Figure B-49: Overpressure test signals for node 0011, no clamps, data set 10. a) Excitation pulse, b) baseline signal at 21°C and 101.3 kPa (time=0 min), c) operational signal, no data per test definition, d) post-test signal at 21°C and 101.3 kPa (time=20 min).

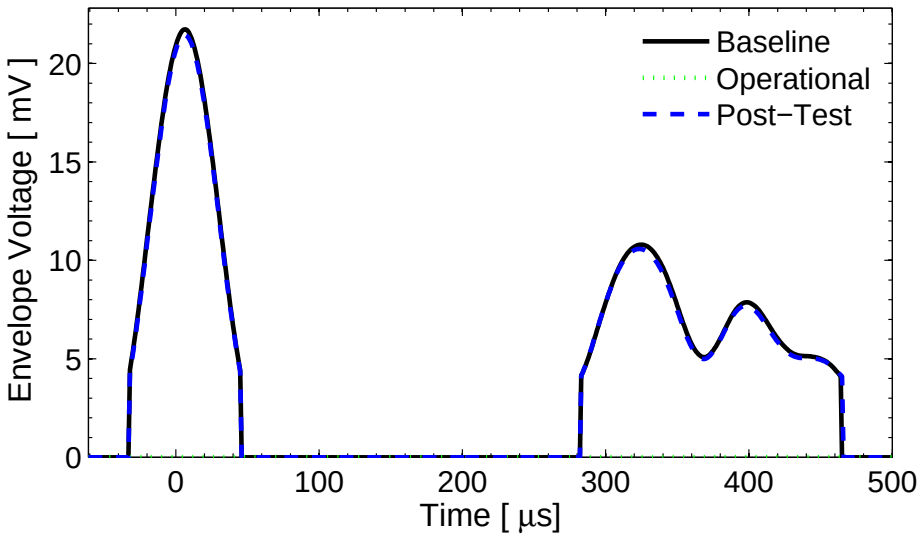

Figure B-50: Overpressure test signal envelopes for node 0011.

Table B.25: Metric values and differences (deltas) of node 0011 for the overpressure test.

	1^{st} wavepacket			2^{nd} wavepacket		
	Base	Op	Post	Base	Op	Post
TOF [μs]	6	-	6	325	-	324
ΔTOF [μs]	-	-	0	-	-	-1
ΔTOF [%]	-	-	0	-	-	-0.3
V [mV]	21.7	-	21.4	10.8	-	10.6
ΔV [mV]	-	-	-0.3	-	-	-0.2
ΔV [%]	-	-	-1.4	-	-	-2.0

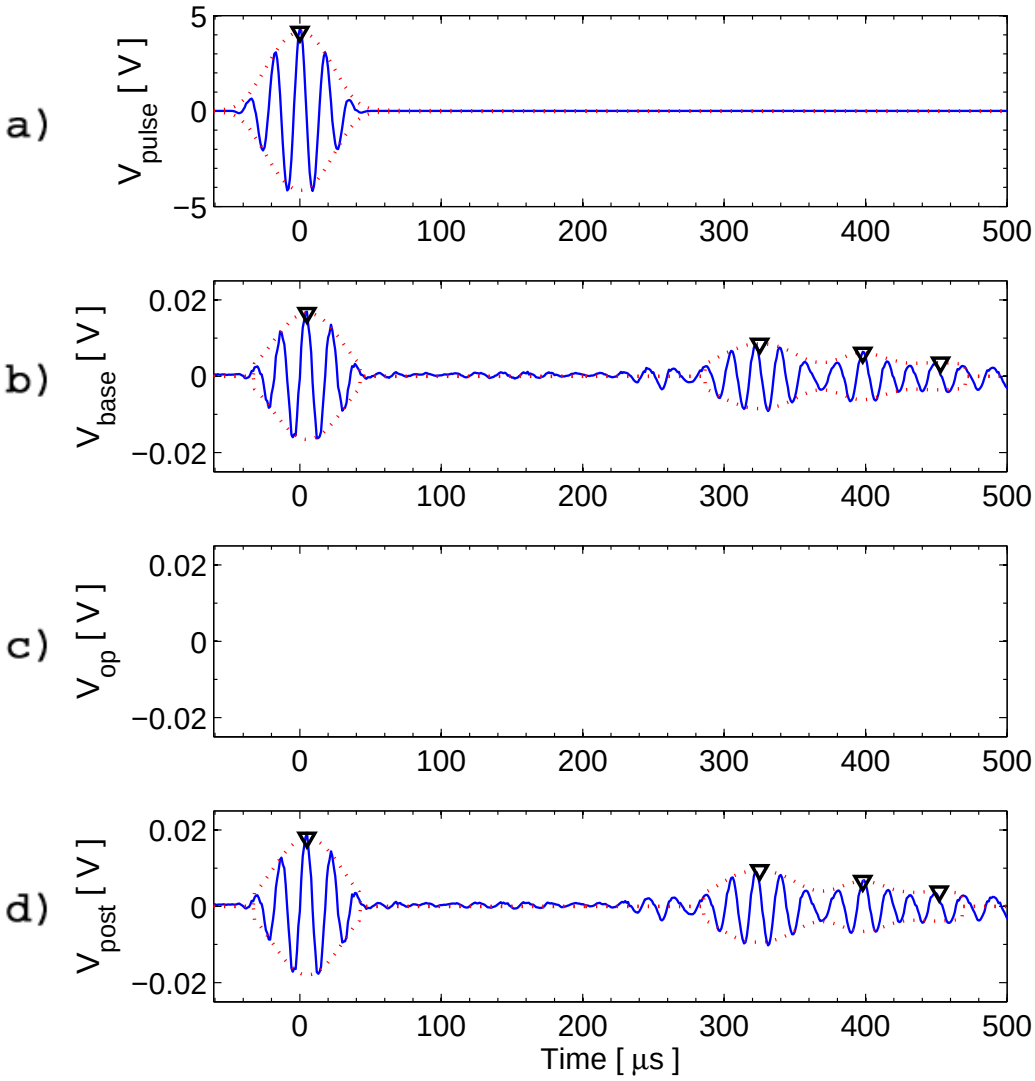

Figure B-51: Overpressure test signals for node 2586, no clamps, data set 10. a) Excitation pulse, b) baseline signal at 21°C and 101.3 kPa (time=0 min), c) operational signal, no data per test definition, d) post-test signal at 21°C and 101.3 kPa (time=20 min).

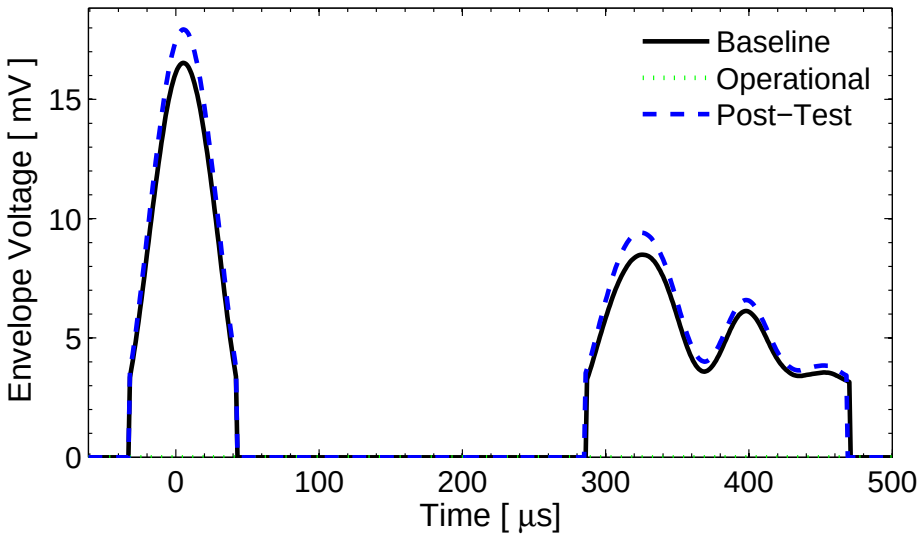

Figure B-52: Overpressure test signal envelopes for node 2586.

Table B.26: Metric values and differences (deltas) of node 2586 for the overpressure test.

	1^{st} wavepacket			2^{nd} wavepacket		
	Base	Op	Post	Base	Op	Post
TOF [μs]	5	-	5	325	-	325
ΔTOF [μs]	-	-	0	-	-	0
ΔTOF [%]	-	-	0	-	-	0
V [mV]	16.5	-	17.9	8.5	-	9.4
ΔV [mV]	-	-	1.4	-	-	0.9
ΔV [%]	-	-	8.5	-	-	10.9

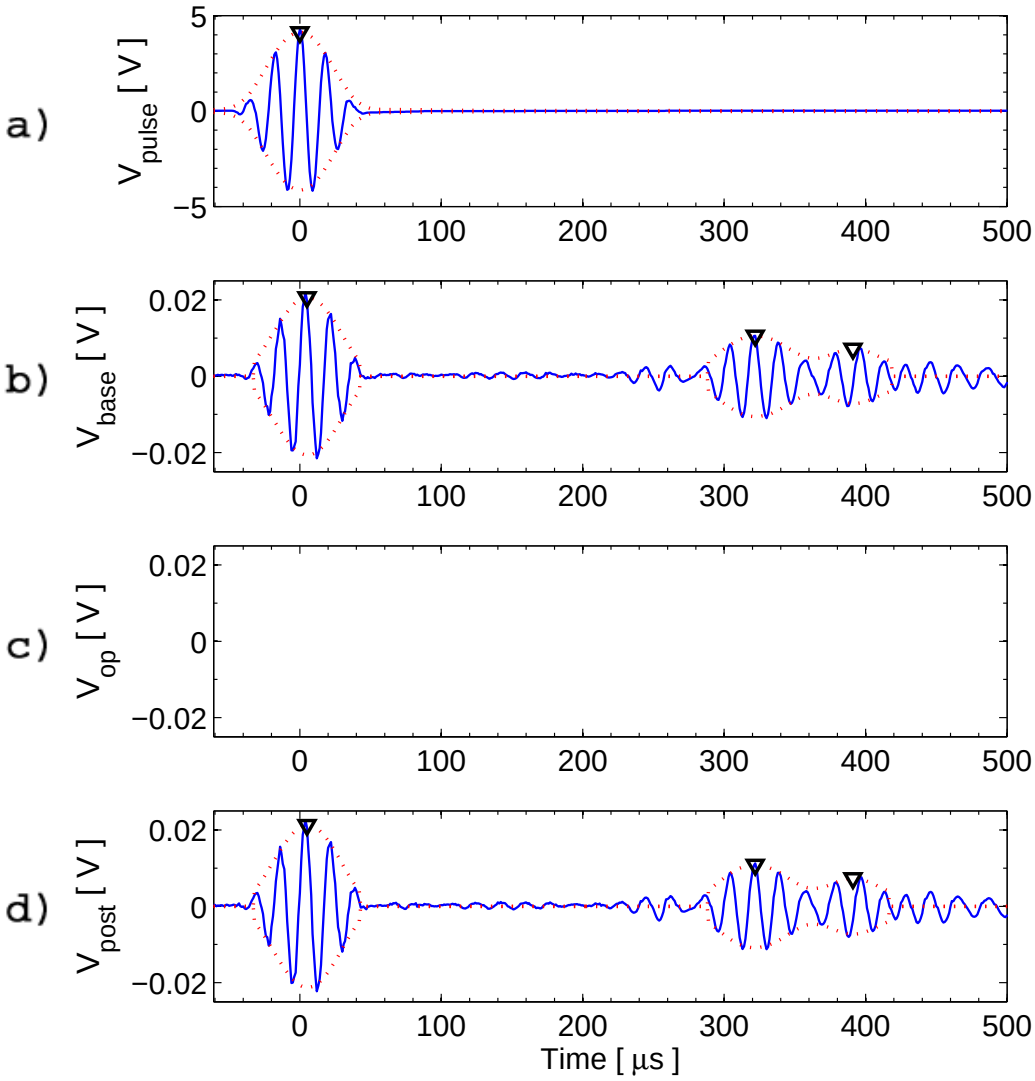

Figure B-53: Overpressure test signals for node 2601, no clamps, data set 10. a) Excitation pulse, b) baseline signal at 21°C and 101.3 kPa (time=0 min), c) operational signal, no data per test definition, d) post-test signal at 21°C and 101.3 kPa (time=20 min).

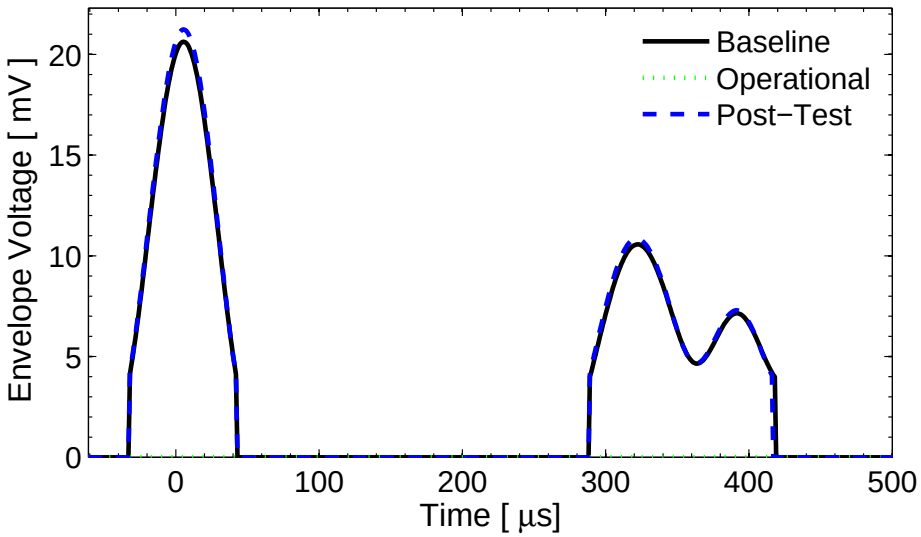

Figure B-54: Overpressure test signal envelopes for node 2601.

Table B.27: Metric values and differences (deltas) of node 2601 for the overpressure test.

	1^{st} wavepacket			2^{nd} wavepacket		
	Base	Op	Post	Base	Op	Post
TOF [μs]	5	-	5	322	-	322
ΔTOF [μs]	-	-	0	-	-	0
ΔTOF [%]	-	-	0	-	-	0
V [mV]	20.6	-	21.2	10.6	-	10.9
ΔV [mV]	-	-	0.6	-	-	0.3
ΔV [%]	-	-	3.0	-	-	2.7

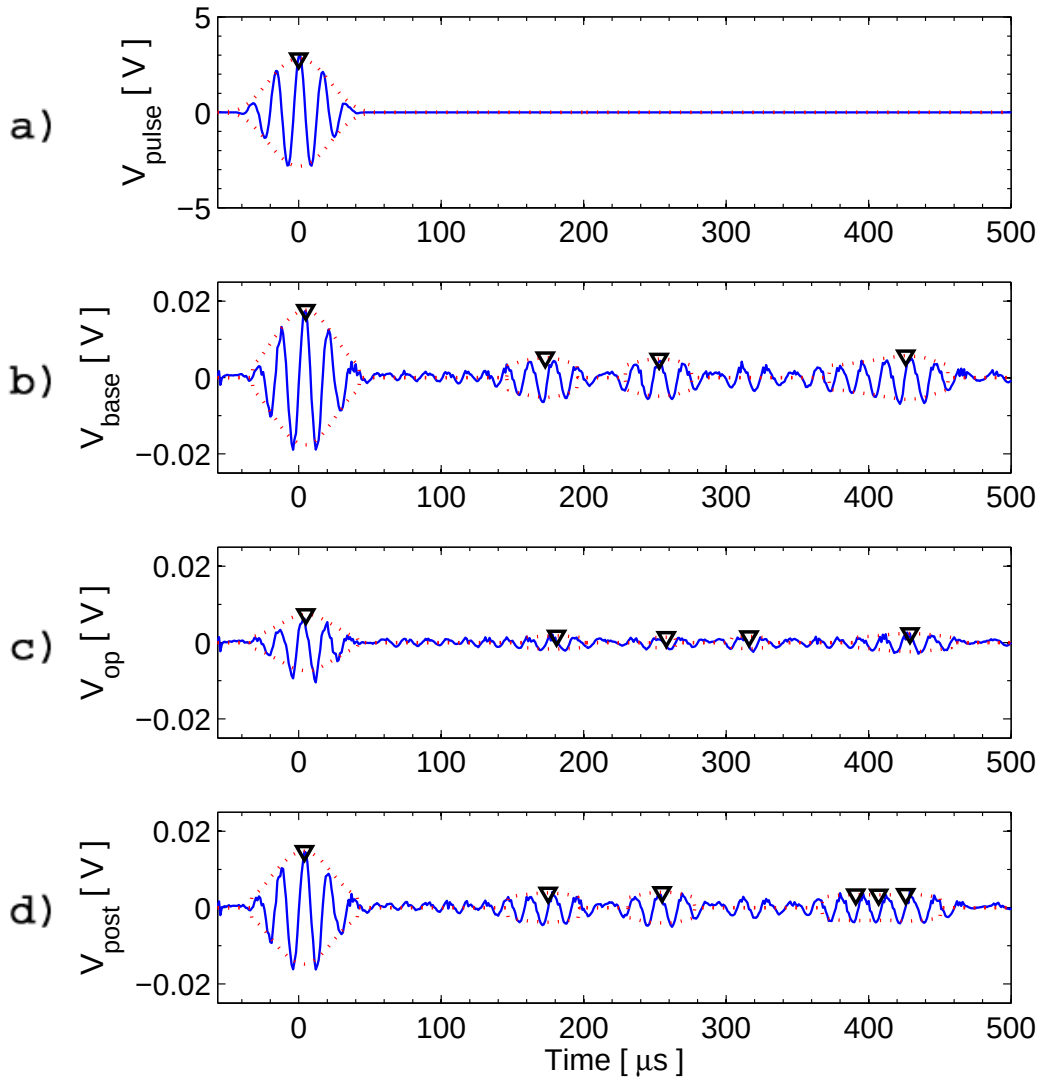

Figure B-55: Static-strain test signals for node 0017. a) Excitation pulse, b) baseline signal with no axial load (time=0 min), c) operational signal with 13.3 kN axial load (time=5.5 min), d) post-test signal with no axial load (time=14.5 min).

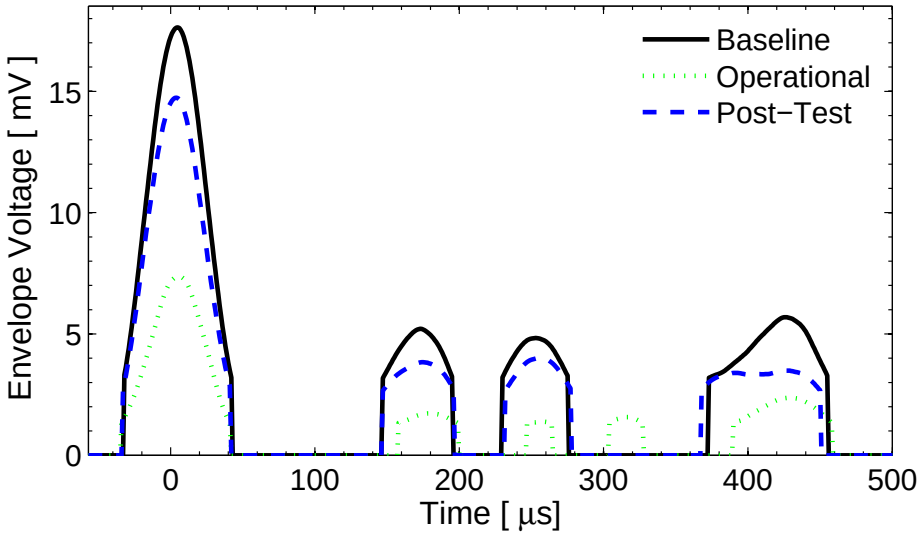

Figure B-56: Static-strain test signal envelopes for node 0017.

Table B.28: Metric values and differences (deltas) of node 0017 for the static-strain test.

	1^{st} wavepacket			2^{nd} wavepacket		
	Base	Op	Post	Base	Op	Post
TOF [μs]	5	5	4	173	181	175
ΔTOF [μs]	-	0	-1	-	8	2
ΔTOF [%]	-	0	-20.0	-	4.6	1.2
V [mV]	17.6	7.4	14.7	5.2	1.7	3.8
ΔV [mV]	-	-10.2	-2.9	-	-3.5	-1.4
ΔV [%]	-	-58.2	-16.4	-	-67.0	-26.4

Appendix C

Material Properties of 2024-T3 Aluminum Coupons

This appendix contains the material properties for the 2024-T3 aluminum samples used for this work. The specimens tested have the same geometry as the coupons used in the SHM tests. The experimental curves and results were obtained by placing two strain gages on an aluminum sample. One strain gage was aligned along the length of the sample and the other was at 90°. The strain gages were placed at the center of the sample. The sample was then placed in the MTS uniaxial tension-compression machine and stressed until yielding was observed. Load, displacement, and strain from both gages was collected by PC. Three samples were tested with the results shown in Figures C-1 and C-2. Average values for isotropic Young's modulus, Poisson's ratio, and 0.2% offset yeild stress are given in Table C.1. Also included in this appendix is the certified inspection report for the batch of aluminum from Alcoa.

Table C.1: Experimental material properties of 2024-T3 aluminum samples.

Coupon	Young's Modulus $[GPa]$	Poisson's Ratio	σ_y (0.2% offset) $[MPa]$
003	76.8	0.334	N/A^*
004	70.8	0.328	362
005	77.0	0.337	354
Average	**74.9**	**0.333**	**358**

*Coupon not tested to yield.

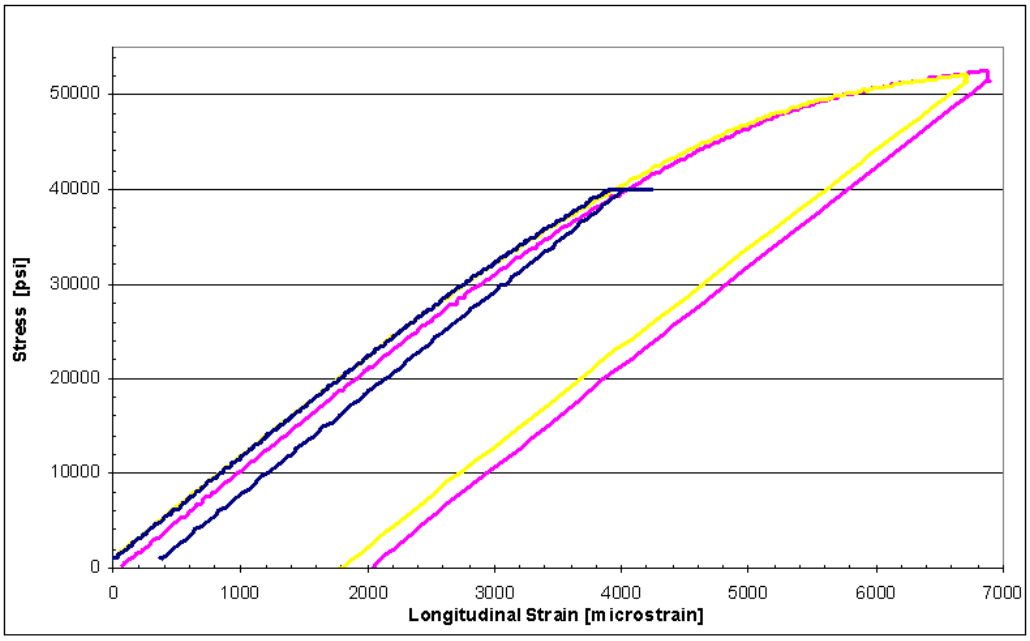

Figure C-1: Experimental stress-strain curves of three aluminum samples.

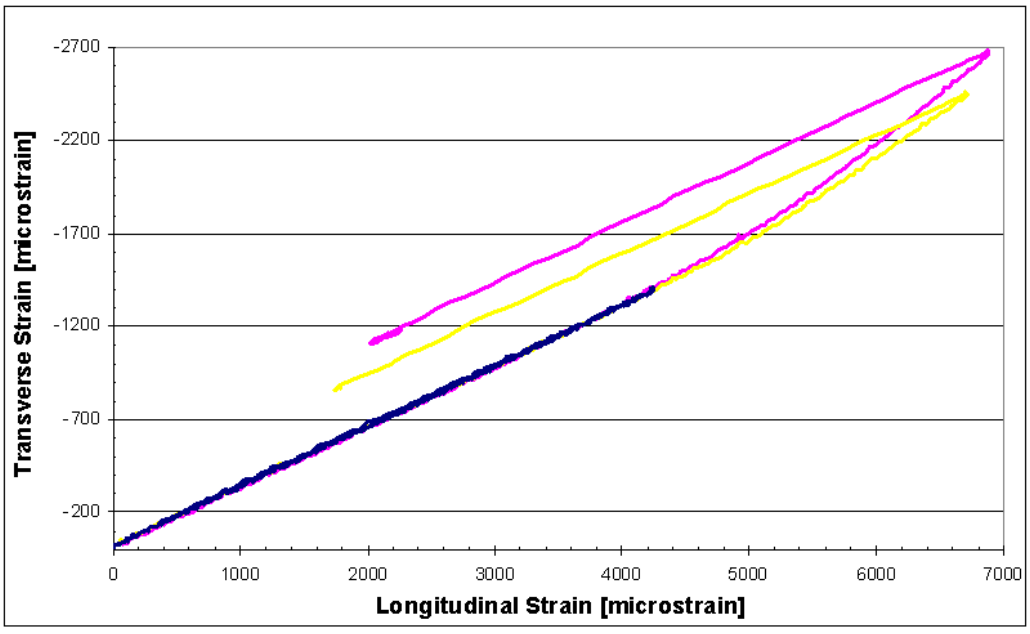

Figure C-2: Experimental transverse stain vs. longitudinal strain of three aluminum samples.

CERTIFIED INSPECTION REPORT **Alcoa Inc.** PITTSBURGH, PA DAVENPORT WORKS

Ship From: RIVERDALE, IA.

We hereby certify that the material covered by this certificate has been inspected with, and has been found to meet, the applicable requirements described therein, including any specifications forming a part of the description and that samples representative of the material met the composition limits and had the mechanical properties shown on the face of this sheet.
Per:

Mark J. Vrablec
Director of Manufacturing Davenport Works

Kenton P. Young
Quality Assurance Manager

Ship Date	B.L. No.	Invoice No.	Alcoa No. Item	Page 1
2005-09-30	84793	36154	DS-88597-2	

P.O. No./Govt Contract No. Customer

CF0030 C&B-WHS-SCHAUMBERG

Ship To: COPPER & BRASS SALES, INC.
415 STATE PARKWAY
SCHAUMBURG, IL 60195

Item Description
.1250 IN TK X 48.000 IN W X 144.000 IN LN CAT D 126185 (N) A/T 2024-T3 FLAT SHEET MILL FINISH {{ P/N 061913-0 }}. PER AMS-QQ-A-250/4 REV A & (EXCEPT OIL & MARKING) AMS4037 REV N & (EXCEPT MARKING) ASTMB209 REV 04 ((MARKED)) INTERLEAVED SKID WGT: 4500 LB QUAN TOL +/-10 % CQR D126185 REV 27 QRR 003140 CUST REQ 05-09-18 *** W/E 05-09-24 ***

Num	Package Ticket	Lot	Weight	Quantity	UOM	Pc Id/Serl
1	303320	455561	3845	45	PC	
2	306334	475461	3791	45	PC	
			7636	90		

Notes for CQR: D126185.27
PRODUCT PRODUCED AND MARKED TO THE REQUIREMENTS OF AMS-QQ-A-250/4 ALSO MEETS THE REQUIREMENTS OF QQ-A-250/4E, AMENDMENT 2.
PRODUCT PRODUCED AND MARKED TO THE REQUIRE- MENTS OF QQ-A-250/4E AMENDMENT 2 ALSO MEETS THE REQUIREMENTS OF AMS-QQ-A-250/4.

CQR: D126185.27 -Specification Limits

Tmpr	Dir		UTS KSI	TYS KSI	EL4D PCT
T3	Long Transv.	Max			
		Min	63.0	42.0	15

Chemical Composition		SI	FE	CU	MN	MG	CR	ZN	TI	Other Each	Other Total	Aluminum
	Max	.50	.50	4.9	.9	1.8	.10	.25	.15	.05	.15	
Alloy 2024	Min			3.8	.30	1.2						REMAIN

Lot: 455561 -Mechanical, Physical, Metallography, Quantometer Results

Tmpr	Dir	No. Test		UTS KSI	TYS KSI	EL4D PCT
T3	Long Transv.	5	Max	66.9	46.2	20.7
			Min	66.2	45.2	18.8

COPPER AND BRASS SALES
SOLD TO: MTT
DATE: 11/14 QTY: 45PC
CUSTOMER PO: clc
SHIPPER NO: 405845
BY:

CERTIFIED INSPECTION REPORT **Alcoa Inc.** PITTSBURGH, PA DAVENPORT WORKS

Ship From: RIVERDALE, IA.

We hereby certify that the material covered by this certificate has been inspected with, and has been found to meet, the applicable requirements described therein, including any specifications forming a part of the description and that samples representative of the material met the composition limits and had the mechanical properties shown on the face of this sheet.
Per:

Mark J. Vrablec
Director of Manufacturing Davenport Works

Kenton P. Young
Quality Assurance Manager

Ship Date	B.L. No.	Invoice No.	Alcoa No. Item	Page 2
2005-09-30	84793	36154	DS-88597-2	

P.O. No./Govt Contract No. Customer

CF0030 C&B-WHS-SCHAUMBERG

Lot: 455561 - Mechanical, Physical, Metallograpy, Quantometer Results (cont.)

Cast Number	Chemical	SI	FE	CU	MN	MG	CR	ZN	TI
H9217022	Actuals	.07	.16	4.7	.63	1.6	.01	.06	.03

Lot: 475461 -Mechanical, Physical, Metallography, Quantometer Results

Tmpr	Dir	No. Test		UTS KSI	TYS KSI	EL4D PCT
T3	Long Transv.	5	Max	67.2	45.9	20.3
			Min	66.4	45.2	18.7

Cast Number	Chemical	SI	FE	CU	MN	MG	CR	ZN	TI
H3461011	Actuals	.09	.10	4.7	.65	1.6	.00	.03	.03

Figure C-3: Certified inspection report for 2024-T3 aluminum from Alcoa.

Appendix D

AE-10 Epoxy Properties

This appendix contains the material properties of the AE-10 epoxy used to bond the nodes to the aluminum. The information is from the Vishay website [27].

The M-Bond brand AE-10 adhesive is a two-component, 100% solid epoxy system for general-purpose stress analysis. It is transparent with medium viscosity. A cure time as low as six hours at $+75°F$ $(+24°C)$ may be used. Elevated-temperature postcure is recommended for maximum stability, and/or tests above room temperature. The epoxy is claimed to be highly resistant to moisture and most chemicals, particularly when postcured. For maximum elongation, the bonding surfaces must be roughened. Cryogenic applications require very thin gluelines. The preferred room-temperature cure is 24-48 hours at $+75°F$ $(+24°C)$. The recommended post-cure is

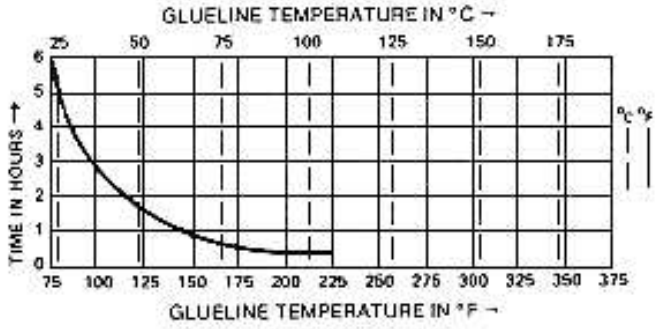

Figure D-1: AE-10 cure time vs. cure temperature [27].

2 hours at $25°F$ $(15°C)$ above the maximum operating temperature. The long term operating temperature range is $-320°$ to $+200°F$ $(-195°$ to $+95°C)$. The elongation capabilities of the AE-10 is 1% at $-320°F$ $(-195°C)$, 6% to 10% at $+75°F$ $(+24°C)$, and 15% at $+200°F$ $(+95°C)$. The adhesive has a shelf life of 12 months at $+75°F$ $(+24°C)$ and 18 months at $+20°F$ $(-7°C)$. If crystals form in the resin bottle, heat to $+120°F$ $(+50°C)$ for 30 minutes. Cool before mixing. The pot life of the mixed adhesive is 15 to 20 minutes at $+75°F$ $(+24°C)$. This can be extended by cooling jar or by spreading the adhesive on a clean aluminum plate. A clamping pressure from 5 to 20 psi (35 to 140 kN/m^2) should be used.

Appendix E

Shear Gel Properties

This appendix contains the shear gel information supplied by the manufacturer (Sonotech). This includes the product sheet and the material safety data sheet (MSDS).

SHEAR GEL shear wave couplant

ENVIRONMENTALLY BENIGN

Shear Gel provides coupling for shear wave generated by normal incidence (zero degree) shear wave transducers.

Temperature Operating Range:
40° to 90°F (4° to 32°C)

Benefits

- Environmentally benign formula

Safety

- Non-flammable, Non-irritating, orally nontoxic
- Contains NO naptha, oil, glycerine, hydrocarbons, heavy metals, harsh surfactants, glycol ethers, nitrites, silicones, petroleum distillates, dyes or fragrances

Removal

- Water-soluble; remove with warm water

Environmental Awareness

Sonotech developed environmentally benign couplants to minimize impact on the environment. Shear Gel contains biodegradable materials, safe for disposal. The likelihood of skin irritation has been reduced through the use of cosmetic grade ingredients.

Environmentally benign couplants are designed specifically for applications where couplant may not be removed by the inspector, may later be removed by weather, or could come into contact with animals, humans, and waterways.

Properties[1]

Viscosity	>4,000,000cps
Density	1.4 to 1.6 g/cc

[1] *At ambient temperature.*

Packaging
4 oz (100g) tube

SONOTECH® INC

774 Marine Drive, Bellingham, WA 98225-1530 *360-671-9121* *Fax 360-671-9024* *www.sonotech-inc.com*
sonotech@sonotech-inc.com *Order Phone: 800-458-4254* *Order Fax: 800-730-9024*

1/03 SI

SONOTECH®
774 Marine Drive
Bellingham, WA 98225-1530
360-671-9121 Fax: 360-671-9024
www.sonotech-inc.com

MSDS
Material Safety Data Sheet

	NFPA	HMIS
Health	0	0
Flammability	0	0
Reactivity	0	0
PPE		A

Section 1 - Material Identification
Product: SHEAR GEL®
Synonym: Ultrasonic Couplant
Manufacturer: Sonotech, Inc.
Date Prepared: 11/03
Emergency Phone: 800-458-4254 / 360-671-9121

Section 2 - Ingredients (>0.1% by WT)

Component	CAS
Proprietary	N/A

All required ingredients are listed on TSCA inventory.

Section 3 - Health Hazards

	Primary Route	Effect
Eyes	No	Transient irritation
Skin	Yes	None expected
Inhalation	No	None expected
Ingestion	No	None expected

Section 4 - First Aid
Eyes: Flush with water for 15 minutes.
Skin: Wash with water
Inhalation: N/A
Ingestion: Treat symptoms

Section 5 - Fire and Explosion Data
Flash Point: N/A
Upper Exposure Limit: None
Lower Exposure Limit: None
Extinguishing media: All standard firefighting media
Special Precautions: Not determined
Unusual Hazards: None

Section 6 - Accidental Release
Wipe up excess. Wash with water. Sprinkle with traction material if spill not cleaned immediately.

Section 7 - Storage and Handling
Storage & Handling Precautions: Store at room temperature. Material is sticky.

This Material Safety Data Sheet (MSDS) has been prepared in compliance with the Federal OSHA Hazard Communication Standard, 29 FR1910.1200. Sonotech believes this information to be reliable and up to date as of the date of this publication, but makes no warranty that it is. If this MSDS is more than three years old, you should contact Sonotech at the phone number provided above to verify that this sheet is current.

Section 8 - Exposure Controls
Respiratory Protection: Not required
Ventilation: Not required
Protective Gloves: Not required within operating range
Eye Protection: Not required within operating range
Other Controls: Not required within operating range (40° to 90°F)

Section 9 - Physical Data
Boiling Range: >220°F
Density: >1.0 g/cm³
Vapor Density: Not known
Vapor Pressure: N/A
Volatile Organic Compounds: None
Percent Solids: <2%
Solubility in water: Complete
Appearance & Odor: Dark brown, high viscosity, neutral odor

Section 10 - Reactivity Data
Stability: Stable
Hazardous Polymerization: Will not occur
Hazardous Decomposition Products: None known
Incompatibility: None known

Section 11 - Toxicology Information
Oral toxicity: Nontoxic
Skin irritation: Not determined
Eye Irritation: Not determined
Known / Suspected Carcinogens: None

Section 12 - Ecological Information
Not known

Section 13 - Disposal
Follow applicable federal, state, and local regulations

Section 14 - Transportation Information
Domestic Regulations: None
DOT Designation: None
Hazard Class: None
ID Number: None
Packing Group: None
International Regulations: None known

Section 15 - Regulatory Information
WHMIS: Not a Controlled Product
EPCRA 311/ 312 Categories: None

Appendix F

MATLAB Code for Data Analysis

This appendix contains MATLAB code used to produce the test profiles (Profile Code) and analyze the test data (Signal Analysis Code). The five files included are separated by the lines of %%%. The first profile code file requires the user to enter the time (x1) and corresponding test variable (y1) data to create the profile. The user then specifies the axes labels and the increments (ticks) of the axes. The entered information is then passed to the function ProfileMaker (second file shown) which creates the figures (*e.g.,* Fig. A-1).

The data analysis code consists of three files. The first file specifies the CSV file (filename = 'HC_0060.csv') to be analyzed, the data set number to read, the locations in the file of the baseline, operational, and post-test signals, and if the analysis should average the 10 data sets. These user inputs are passed to the function METImetric (second Data Analysis file), where the data file is read into MATLAB using the 'textread' function and then the signal analysis is preformed. The last function, waveplots, is called within METImetric and plots the wave signals (*e.g.,* Fig. B-1). The envelope plots (*e.g.,* Fig. B-2) are produced within METImetric. The signal analysis codes are discussed at the beginning of Chapter 5.

Profile Code

```
%%%%%%%%%%%%%%%%%%%%%%%%%%%%%%%%%%%%%%%%%%%%%%%%%%%%%%%%%%%%%%%%%%%%%%%%
x1          = [0 1 1.5 3.5 4.5];    %Time
y1          = [25 85 85 85 25];     %Test Variable
opX         = [min(x1) max(x1)];    %Equip. State Change
opY         = [1 1];                %0=off 1=on

x_lab       = 'Time [ Units ]';
y1lab       = 'Left Label [ Units ]';
y2lab       = 'Right Label [ Units ]';

xticks      = [0:1:5];
y1ticks     = [25:20:85];   %Ticks for left axis
```

```
y2ticks     = [0 1];        %Ticks for right axis
y2ticlab    = [];           %Labels for right ticks
discontL    = 1;            %1 if left axis is discont
discontR    = 0;            %1 if right axis is discont

ProfileMaker(x1,y1,opX,opY,x_lab,y1lab,y2lab,...
    xticks,y1ticks,y2ticks,y2ticlab,discontL,discontR);
%%%%%%%%%%%%%%%%%%%%%%%%%%%%%%%%%%%%%%%%%%%%%%%%%%%%%%%%%%%%%%%%%%%%%%%%%%%

%%%%%%%%%%%%%%%%%%%%%%%%%%%%%%%%%%%%%%%%%%%%%%%%%%%%%%%%%%%%%%%%%%%%%%%%%%%
function ProfileMaker(x1,y1,opX,opY,xlab,y1lab,y2lab,...
    xticks,yLticks,yRticks,yRticklabels,discontL,discontR)

figureX = figure('Position',[580 340 560 380]);
axesPos = [0.14 0.12 0.7 0.85];

axesR = axes(...
   'FontSize',13,...
    'Position',axesPos,...
  'Xtick',[ ],...
   'YDir','reverse',...
    'Ycolor','k',...
  'YAxisLocation','right',...
   'YMinorTick','off',...
    'YTick',yRticks,...
  'YTickLabel',yRticklabels,...
   'Parent',figureX);
axis(axesR,[0 max(x1) 0 1]);
ylabel(axesR,y2lab,'FontSize',14);
hold(axesR,'all');

axesL = axes(...
  'FontSize',13,...
  'Position',axesPos,...
  'XMinorTick','on',...
  'XTick',xticks,...
  'YMinorTick','on',...
  'YTick',yLticks,...
  'Parent',figureX);
axis(axesL,[0 max(x1)...
    (min(y1)-.1*(max(y1)-min(y1))) (max(y1)+.25*(max(y1)-min(y1)))]);
xlabel(axesL,xlab);
ylabel(axesL,y1lab);
box(axesL,'on');
hold(axesL,'all');
```

```
plot(x1,y1,'b','linewidth',2,'Parent',axesL);
plot(x1,y1,'k','LineStyle','none','Marker','x','MarkerSize',4.5);

%----Discontinuous y-Axis----
if discontL == 1
    annotation('line',[0.13 0.15],[0.14 0.145]);
    annotation('line',[0.13 0.15],[0.13 0.135]);
end
if discontR == 1
    annotation('line',[0.83 0.85],[0.14 0.145]);
    annotation('line',[0.83 0.85],[0.13 0.135]);
end
%----Equipment Operating Lines/Text----
xlims = get(gca,'xlim');
ylims = get(gca,'ylim');
XX  = 1.01*xlims(2);
ylimdiff= diff(ylims);
YY = .97*ylimdiff+ylims(1);
Ydif1 = YY-.035*ylimdiff;
Ydif2 = YY-.08*ylimdiff;
Ydif3 = YY-.115*ylimdiff;
text(XX,YY,'Equipment','FontSize',10,'Parent',axesL)
text(XX,Ydif1,'Operating','FontSize',10,'Parent',axesL)
text(XX,Ydif2,'Equipment','FontSize',10,'Parent',axesL)
text(XX,Ydif3,'Off','FontSize',10,'Parent',axesL)

Q = [min(x1) max(x1)];
W = .98*[YY YY];
E = .99*[Ydif2 Ydif2];

for i=1:length(opY)
    if opY(i)==1
      OPon(i)=W(1);
    else
      OPon(i)=E(1);
    end
end
plot(Q,W,'k:',Q,E,'k:','LineWidth',2);
stairs(opX,OPon,'k-','LineWidth',2.5);
end
%%%%%%%%%%%%%%%%%%%%%%%%%%%%%%%%%%%%%%%%%%%%%%%%%%%%%%%%%%%%%%%%%%%%%%%%%%%%
```

Signal Analysis Code

```
%%%%%%%%%%%%%%%%%%%%%%%%%%%%%%%%%%%%%%%%%%%%%%%%%%%%%%%%%%%%%%%%%%%%%%%%%%%%
filename = 'HC_0060.csv';     %Enter file to be read
setnum   = 1;                 %Enter the set number to analyze
%     [base  op  post]
loc = [ 5    17   35 ];
averaging = 0; %0=No avg, 1=avging
 [t_sigpeaks,v_sigpeaks,v_pulsepeaks,sig_env,pulse_env,...
  TOF,V,dTOF,dV,pdTOF,pdV]=...
  METImetric(filename,setnum,loc,averaging);
%%%%%%%%%%%%%%%%%%%%%%%%%%%%%%%%%%%%%%%%%%%%%%%%%%%%%%%%%%%%%%%%%%%%%%%%%%%%

%%%%%%%%%%%%%%%%%%%%%%%%%%%%%%%%%%%%%%%%%%%%%%%%%%%%%%%%%%%%%%%%%%%%%%%%%%%%
 % METImetric reads the CSV test file specified and produces
 % plots and metrics.

function [Ts,Peak_S,Peak_P,SE,PE,TOF,V,dTOF,dV,pdTOF,pdV]=...
    METImetric(filename,setnum,loc,avg)

 %----File Reader----
  % The CSV file is read in as strings and seperated first by rows
  % and then by columns. The size of the file is then determined.

[filerows] = textread(filename,'%s','delimiter','\n');
  for i=1:length(filerows)
     data(i,:) = strread(filerows{i},'%s','delimiter',',');
  end
  [rows columns] = size(data);
  clear file*;

%----Test Information----
 % The test headers are stored in the following variables.

 Test_Info= [data(1:12,1) data(1:12,2)];
 sets     = str2double(Test_Info(10,2));         %Sets per Acquire
 pts      = str2double(Test_Info(8,2));          %Points per Set
 t_step   = 1/(str2double(Test_Info(7,2))*1000); %t_step between pts
 t        = (t_step:t_step:t_step*(rows-2));     %Time [s]

 for i=1:3
  Pulse = 0;
  Signal= 0;
 %----Set Averaging----
  % If specified, the consecutive data sets can be averaged.
```

```
  if avg == 1
     Avg_Pulse = 0;
     Avg_Signal= 0;
     Pulse = str2double([data(3:rows,loc(i))]);
     Signal= -str2double([data(3:rows,loc(i)+1)]);
     for n=1:sets
         Avg_Pulse   = Avg_Pulse  + Pulse(1+pts*(n-1):pts*n);
         Avg_Signal  = Avg_Signal + Signal(1+pts*(n-1):pts*n);
     end
     P(:,i) = Avg_Pulse/n;
     S(:,i) = Avg_Signal/n;
  else
     P(:,i)   =  str2double([data((setnum-1)*pts+3:setnum*pts+2,...
      loc(i))]);
     S(:,i)   = -str2double([data((setnum-1)*pts+3:setnum*pts+2,...
      loc(i)+1)]);
  end

%----Zero Signals----
 % The pulse and signal voltages are zeroed to their
 % respective means.

   ZP(:,i)  = P(:,i) - mean(P(:,i));
   ZS(:,i)  = S(:,i) - mean(S(:,i));

%----Enveloping----
 % The Hilbert transform is used define the slowly varying amplitude
 % of the signal. A zero-phase filter is used as a low-pass filter
 % to elminate the noise in the envelope.

   M   = 20;                     %Averaging points for filter
   B   = ones(M,1)/M;            %Weighting coefficients. (All equal)
   h   = abs(hilbert(ZP(:,i)));  %Pulse envelope. h = abs(x + iH(x)).
   PE(:,i)  = filtfilt(B,1,h);   %Zero-phase filter. Pulse Envelope
   h   = abs(hilbert(ZS(:,i)));  %Signal envelope
   SE(:,i)  = filtfilt(B,1,h);   %Zero-phase filter. Signal Envelope

   [Peak_P(:,i), Tp(:,i)] = max(PE(:,i));
   [Peak_S(:,i), Ts(:,i)]   = max(SE(:,i));
   ts(:,i)  = t-Tp(:,i)*t_step;               %Shifted time

%----Threshold----
 % The threshold eliminates signal noise below the specified
 % value. If the signal is below the threshold, it's value
```

```
 % is set to zero.

   for k=1:pts
       if SE(k,i) < .18 * Peak_S(1,i)
           SE(k,i)=0;
       end
   end

%----Peak Finding----
 % The value and location of the peaks are determined from the
 % change in slope of the signal envelope. The length of the
 % wavepackets is also determined.

   n=1;
   m=1;
   dS(:,i) = diff(SE(:,i));
   dP(:,i) = diff(PE(:,i));
   for k = 1:pts-2
       if sign(dS(k,i))==1 & sign(dS(k+1,i))==-1
           Ts(n,i)=k+1;
           Peak_S(n,i)=SE(k+1,i);
           n=n+1;
       elseif sign(dS(k,i))==0 & sign(dS(k+1,i))==1
           sect_start(m,i) = k+1;
       elseif sign(dS(k,i))==-1 & sign(dS(k+1,i))==0
           sect_end(m,i) = k+1;
           m = m+1;
       end
   end

%----Time Shift----
 % The time is shifted to have the peak pulse voltage occur at
 % time zero. All TOFs are calculated relative to this occurance.

 Ts(:,i) = Ts(:,i) - Tp(:,i);

end

 for i=1:3
    for q=1:length(Ts(:,i))-1
        if Ts(q+1,i) < Ts(q,i)
            Ts(q+1,i) = NaN;
        elseif isnan(Ts(q,i))
            Ts(q+1,i) = NaN;
        end
```

```
    end
 end

%----Plots----
 ts      = ts*10^6;                        %Time [us]
 Saxis   = [ts(1,1) 500 -.025 .025];
 Paxis   = [ts(1,1) 500 -5 5];
 ylab   = 'V_p_u_l_s_e [ V ]';
 y1lab   = 'V_b_a_s_e [ V ]';
 y2lab   = 'V_o_p [ V ]';
 y3lab   = 'V_p_o_s_t [ V ]';
 xlab    = 'Time [ \mus ]';

 figure('Position',[5 65 600 700])
    waveplot(4,1,ts(1:pts,1),ZP(1:pts,1),PE(1:pts,1),0,...
     Peak_P(1),ylab,Paxis)
    waveplot(4,2,ts(1:pts,1),ZS(:,1),SE(:,1),Ts(:,1),...
     Peak_S(:,1),y1lab,Saxis)
    waveplot(4,3,ts(1:pts,2),ZS(:,2),SE(:,2),Ts(:,2),...
     Peak_S(:,2),y2lab,Saxis)
    waveplot(4,4,ts(1:pts,3),ZS(:,3),SE(:,3),Ts(:,3),...
     Peak_S(:,3),y3lab,Saxis)
    xlabel('Time [ \mus ]');

 figure('Position',[210 200 600 330])
    plot(ts(1:pts,1),1000*SE(:,1),'k',...
        ts(1:pts,2),1000*SE(:,2),'g:',...
        ts(1:pts,3),1000*SE(:,3),'b--',...
        'LineWidth',2)
    axis([Saxis(1) Saxis(2) ...
     0 1.05*1000*max(max(max(SE(:,1),SE(:,2)),SE(:,3)))]);
    xlabel('Time [ \mus]','FontSize',14);
    ylabel('Envelope Voltage [ mV ]','FontSize',14);

    set(gca,...
       'FontSize',13,...
       'XMinorTick','on',...
       'YMinorTick','on');
   legend('Baseline','Operational','Post-Test');
   legend('boxoff');

%----Metric Results----
 % The following data is passed back from the function. The data
 % includes the TOF of the first 2 wavepackets and the peak voltage.
 % The changes (deltas) from the baseline signal are calculated
```

```
  % and the percent change from the baseline is also calculated.

TOF  = Ts(1:2,:)
V    = Peak_S(1:2,:)*1000
dTOF = [Ts(1,:)-Ts(1,1) ; Ts(2,:)-Ts(2,1)]
dV   = [Peak_S(1,:)-Peak_S(1,1) ; Peak_S(2,:)- Peak_S(2,1)]*1000
pdTOF= [dTOF(1,:)/Ts(1,1) ; dTOF(2,:)/Ts(2,1)]*100
pdV  = [dV(1,:)/(Peak_S(1,1)*1000) ; dV(2,:)/(Peak_S(2,1)*1000)]*100
end
%%%%%%%%%%%%%%%%%%%%%%%%%%%%%%%%%%%%%%%%%%%%%%%%%%%%%%%%%%%%%%%%%%%%%%%%%%%

%%%%%%%%%%%%%%%%%%%%%%%%%%%%%%%%%%%%%%%%%%%%%%%%%%%%%%%%%%%%%%%%%%%%%%%%%%%
function []= waveplot(subps,subpN,t,y1,y2,t_peak,PEAK,ylab,ax)
subplot(subps,1,subpN)
   hold on;
    box on;
    plot(t,y1,'b','LineWidth',1)
    plot(t,y2,'r:','LineWidth',1.5)
    plot(t,-y2,'r:','LineWidth',1.5)
    plot(t_peak,PEAK,'kv','LineWidth',1.5)
    ylabel(ylab,'FontSize',14)
    axis(ax)
    set(gca,...
        'FontSize',13,...
        'XMinorTick','on',...
        'YMinorTick','on');
end
%%%%%%%%%%%%%%%%%%%%%%%%%%%%%%%%%%%%%%%%%%%%%%%%%%%%%%%%%%%%%%%%%%%%%%%%%%%
```